Control of the gravitational wave interferometric detector Advanced Virgo

Julia Casanueva Diaz

NNT: 2017SACLS209

THESE DE DOCTORAT
DE L'UNIVERSITÉ PARIS-SACLAY
PREPARÉE À L'UNIVERSITÉ PARIS-SUD

ÉCOLE DOCTORALE N°576
Particules Hadrons Énergie et Noyau : Instrumentation, Image, Cosmos et Simulation (PHENIICS)
Spécialité de doctorat : Astroparticules et Cosmologie

Par
Mme Julia Casanueva Diaz

Control of the gravitational wave interferometric detector Advanced Virgo

Thèse présentée et soutenue à Orsay, le 4 septembre 2017

Composition de jury:

M. Achille Stocchi *Professeur, Université Paris-Sud*	Président
M. David Shoemaker *Professeur, MIT*	Rapporteur
M. Carlo Rizzo *Professeur, Université Paul Sabatier*	Rapporteur
Mme Jaime Dawson *Chargée de recherche, CNRS*	Examinatrice
M. Patrice Hello *Professeur, Université Paris-Sud*	Directeur de thèse
M. Nicolas Leroy *Chargé de recherche, CNRS*	Co-directeur de thèse
Mme Maddalena Mantovani *Chargée de recherche, EGO*	Invitée

Laboratoire de l'Accélérateur Linéaire n°LAL 17-053

Acknowledgements

First of all I would like to thank David Shoemaker and Carlo Rizzo for accepting to review my work, and specially for the patience that it implies. Thank you as well to Jamie Dawson and Achille Stocchi for examining my work.

During these three years of thesis I had the chance to split my work between the VIRGO group at LAL and the VIRGO site in Pisa. It has been an extremely enriching experience in so many ways, and I would like to thank to all the people that have taught me something during this period, even if it might be a long list.

To Nicolas, for giving me this wonderful opportunity to discover the world of gravitational waves detectors in the first place. For always believing that I was capable of solving any problem even when I did not. For always finding time to discuss but letting me the freedom to try my ideas. In short, for you constant help and support, I want to thank you. I want to believe that I am a better scientist now, and it is also thanks you.

To Patrice and Fabien for sharing your wisdom with me, answering to all my numerous questions and to give me perspective to put in order my ideas.

To Dominique for your infinite patience and for introducing me in the world of feedback loops and noise injections. To Ivan and Vincent for all the time spent working at CALVA, I learnt a lot and I enjoyed it even more.

To all the members of the Virgo group at LAL: Marie-Anne, Florent, Valentin, Angelique, Sarah, Pierre et Imhene. Thank you for making me part of the group, it was very helpful, specially on the stressing moments!

I would also like to thank all the people on site that made the hard work of commissioning the best of the experiences.

To Eric, Gabriel and Matthieu, for opening me the doors of the Optics lab, even if during a short time. It was a pleasure to learn form you.

To Alain, for all the hours spent on the phone trying to make the SSFS work. I enjoyed every one of them.

To Paolo, for never give up on teaching me, even when I thought I did not need it. Grazie.

To Henrich, for always having his door open for me to ask any question. For always listen and consider what I had to say. I know a little bit more every time I walk out of your office.

To Diego, thank you for all your help and patience. The commissioning period has been stressful, and it was not always easy to work with me but I just hope that I was a good teammate because you sure were a good one.

To Madda, for all the time spent to discuss measurements and simulations. For all the plots, analysis and crazy matlab codes that we have worked on together. You have pushed me to work better and think faster. To do not make assumptions and to believe in my work. Thank you for taking the time to teach me, it was a pleasure and a honor.

And finally to all the people from the Commissioning crew: Bas, Dan, Franco, Annalisa, Antonino, Lucia... This work could not have been possible without all of you. You have teach me that with hard work the word impossible does not mean anything.

Finalmente quería agradecer a mis padres por su apoyo constante, no solo durante estos tres años, sino siempre. Si he llegado hasta aquí es sin duda alguna gracias a vosotros.

Contents

Résumé

L'existence des Ondes Gravitationnelles a été prédite par la Relativité Générale en 1916. Depuis, beaucoup d'efforts ont été faits pour les détecter. La première génération de détecteurs interférométriques d'Ondes Gravitationnelles sur Terre, LIGO et Virgo, a conclu sa prise de données en 2011 sans avoir effectué de détection. Plusieurs modifications ont été envisagées pour améliorer la sensibilité de la seconde génération de détecteurs d'un ordre de grandeur par rapport à la précédente.

La première détection d'une Onde Gravitationnelle provenant de la fusion de deux trous noirs par les détecteurs américains Advanced LIGO a été faite le 14 septembre 2015. La figure 1 montre le signal détecté par les deux détecteurs et sa comparaison avec la forme d'onde prédite par la Relativité Générale. On peut voir qu'elles sont en accord. Depuis, deux autres évènements de même nature ont été détectés, ce qui prouve que les détecteurs terrestres sont capables de faire des observations astrophysiques. L'incorporation du détecteur Advanced Virgo au réseau des deux détecteurs Advanced LIGO jouera un rôle clé dans l'estimation des paramètres des sources. Le commissioning d'Advanced Virgo a commencé en 2016 et Virgo a rejoint les détecteurs Advanced LIGO dans la prise de données scientifiques O2 du 1er au 25 août 2017.

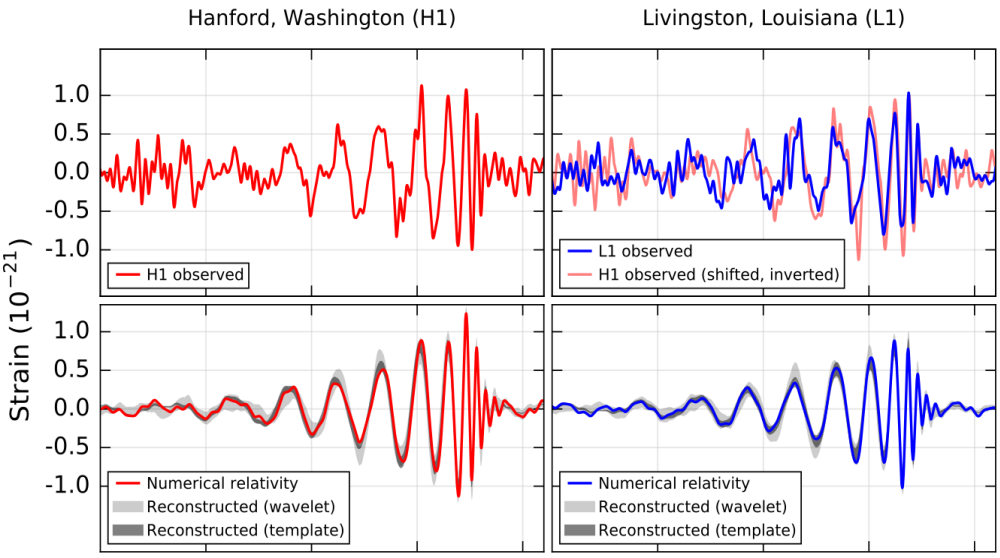

FIGURE 1: **Graphes superieurs:** Signal de l'onde gravitationnelle détectée par les détecteurs Advanced LIGO, à Hanford et Livingston respectivement, le 14 septembre 2015 (GW150914). **Graphes inferieures:** Forme d'onde théorique de l'onde gravitationnelle détectée dans le deux détecteurs.

Les améliorations effectuées sur l'interféromètre Virgo ont modifié significativement son fonctionnement, en particulier la stratégie de contrôle de l'interféromètre. L'objectif de cette thèse est l'implémentation des contrôles longitudinaux et angulaires nécessaires pour amener Advanced Virgo à son point de fonctionnement d'une

façon robuste et répétitive. L'utilisation de simulations et la mise en place concrète des différents contrôles a permis de comprendre et de relever les défis de ce nouvel instrument.

Dans le Chapitre 1 nous présentons les propriétés basiques des Ondes Gravitationnelles ainsi que les sources les plus intéressantes. Ensuite, nous expliquons le principe de détection basé sur l'interféromètre de Michelson dans le Chapitre 2. Nous introduisons également le concept de sensibilité des interféromètres et la configuration optique qui la maximise. Les principaux bruits limitant y sont aussi présentés. Nous donnons une description rapide du détecteur Advanced Virgo dans le Chapitre 3. Nous décrivons aussi dans ce chapitre les sous-systèmes les plus importants pour le sujet de cette thèse, avec les principales améliorations par rapport à la version précédente (Virgo+). En particulier, nous avons développé l'essentiel du travail présenté ici au sein du sous-système ISC (Interferometer Sensing and Control).

Le Chapitre 4 est focalisé sur les cavités Fabry-Perot et leurs propriétés optiques qui vont nous permettre de comprendre quels sont les premiers défis que nous allons devoir relever au cours du commissioning. Nous décrivons aussi les principes de base sur les techniques de contrôle longitudinal et angulaire, appliqués au cas des cavités Fabry-Perot des bras d'Advanced Virgo. Suite à l'augmentation de la finesse des cavités ainsi que du changement de la géométrie des faisceaux nous avons dû tenir compte de nouveaux effets lors de la création des systèmes de contrôle.

Ces finesses plus importantes introduisent des effets dynamiques qui nous obligent à utiliser une technique spéciale pour acquérir le contrôle longitudinal des cavités : le « Guided Lock ». Grâce aux simulations nous avons adapté cette technique aux besoins du commissioning. En particulier nous avons obtenu l'expression analytique qui relie le temps mis par la puissance transmise pour passer de 10% à 40% de sa valeur maximale à la vitesse de la cavité. La figure 2 montre cette relation, qui est linéaire entre le temps et l'inverse de la vitesse. Cette expression nous permet d'estimer la vitesse de la cavité en temps réel et directement en unités physiques (sans le besoin d'un facteur de calibration empirique). Avec cette technique nous avons réussi à acquérir le contrôle longitudinal des cavités des bras dans une période de temps très courte et de façon fiable.

Concernant la nouvelle géométrie des cavités des bras, elle a un impact sur le contrôle angulaire rendu plus complexe par une matrice d'actuation (qui relie les degrés de liberté angulaires avec les actionneurs) qui n'est pas diagonale. Nous avons simulé l'impact de l'alignement sur la puissance transmise et nous avons vérifié que la matrice d'actuation peut être extraite de cette information.

Le Chapitre 5 présente la configuration finale de l'interféromètre, connue comme Power Recycling Interferometer (PRITF). Elle est constituée de plusieurs cavités optiques et donc d'un nombre accru de degrés de liberté à contrôler (longitudinaux et angulaires). Ceci complique l'acquisition du contrôle du fait des couplages entre eux. Pour cette raison, il est très important de choisir des signaux d'erreurs indépendants pour chaque degré de liberté, c'est ce que nous appelons le sensing. Une fois que le point de fonctionnement a été défini, nous décrivons la stratégie d'acquisition de contrôle utilisée sur Virgo pour maintenir l'interféromètre dans cette position. Nous avons simulé les différentes étapes de ce processus pour vérifier la robustesse des signaux d'erreur utilisés dans le passé (étape Virgo+). Ensuite nous avons étudié le sensing optimal pour l'état final, en prennant en compte la précision et le couplage entre degrés de liberté. La figure 3 montre ces deux paramètres

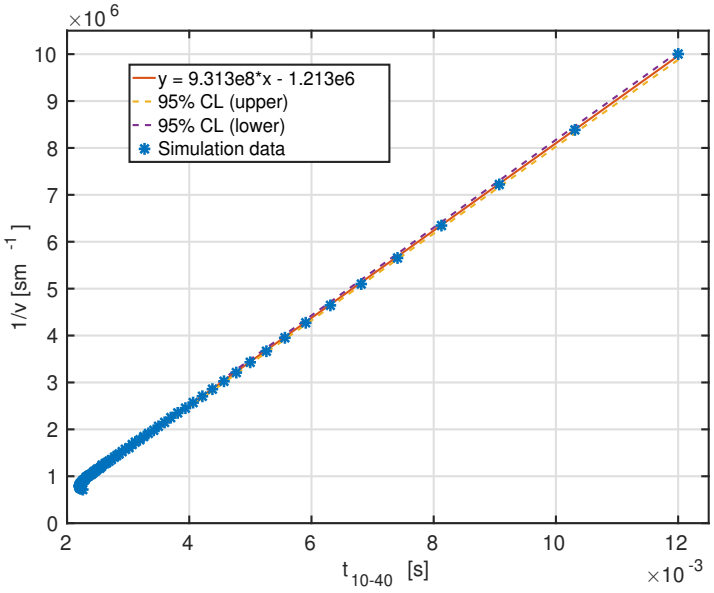

FIGURE 2: Les points bleus montrent la relation entre le temps et l'inverse de la vitesse de croisement de la résonance, donnée par la simulation. La courbe continue est l'ajustement de ces points. La légende montre l'expression analytique. Les lignes pointillées montrent les limites de confiance au 95% de l'ajustement. Ils représentent 1% du valeur de la simulation.

pour les signaux d'erreur optimaux dans l'état final. Ces études nous ont permis de mieux comprendre le processus d'acquisition du contrôle et nous ont donné une référence du comportement de l'interféromètre idéal.

Une des améliorations qui a eu un impact sur le contrôle global du PRITF est la stabilité de la cavité Fabry Perot qui recycle la puissance (« Power Recycling Cavity»). En particulier nous avons étudié la relation entre le désalignement et le gain optique. Nous avons vérifié que la cavité étant proche de l'instabilité, les modes d'ordre supérieur sont fortement couplés ce qui diminue drastiquement le gain optique, spécialement celui des bandes latérales. Ceci a un effet important sur la stabilité des contrôles et nous avons exploré une solution pour atténuer ce problème : l'utilisation d'une fréquence de modulation plus haute. La présence de l'asymétrie de Schnupp (différence de longueur macroscopique entre les deux bras du Michelson) fait que la finesse de la cavité de recyclage est inversement proportionnelle à la fréquence de modulation. Nous avons simulé l'impact de l'alignement sur le gain optique pour différentes fréquences de modulation en utilisant uniquement l'interféromètre Central (soit sans les cavités kilométriques). Nos résultats confirment que les hautes fréquences sont moins sensibles aux désalignements, ce que nous avons confirmé expérimentalement grâce à la cavité de basse finesse PRNI. Ces études nous ont permis de proposer un signal d'erreur alternatif pour contrôler l'interféromètre jusqu'à l'enclenchement du contrôle angulaire. Nous avons prouvé aussi que les contributions provenant des modes d'ordre supérieur ne commencent à être importants que très proche du point de fonctionnement.

Finalement nous avons aussi étudié l'impact des modes d'ordre supérieur sur la fonction de transfert optique du mouvement commun des cavités des bras et le signal d'erreur que nous pouvons utiliser pour le contrôler. Nous avons confirmé que tant les modes supérieurs que les bandes latérales créent des structures dans

cette fonction de transfert optique, qui devront être compensées par le contrôle correspondant pour éviter des instabilités.

Dans le chapitre final (Chapitre 6) nous présentons l'application des connaissances acquises grâce aux simulations dans le commissioning d'Advanced Virgo. Nous avons implémenté avec succès la technique du Guided Lock pour le contrôle des cavités des bras en utilisant la nouvelle méthode de calcul de la vitesse de la cavité en temps réel. Nous avons aussi enclenché le contrôle angulaire de ces cavités avec une technique de modulation mécanique des miroirs qui s'est révélée être très robuste.

Néanmoins, le commissioning n'a pas toujours été simple et nous avons trouvé différentes limitations expérimentales. En premier lieu le manque de fiabilité de la photodiode en réflexion de la cavité du bras nord nous a obligé à modifier le sensing, plus concrètement, en mettant en place la normalisation d'un des signaux d'erreur. Nous avons trouvé une combinaison alternative des signaux qui nous fournit une information directe sur l'état d'interférence du Michelson.

Un autre problème rencontré est que le miroir PR a un rayon de courbure qui rapproche la cavité de recyclage encore plus de l'instabilité. Ceci a engendré des fluctuations de gain optique d'un facteur 3 quand l'interféromètre se rapproche du point de fonctionnement. En pratique nous n'avons pas pu utiliser les signaux des photodétecteurs à quadrants ni un des signaux d'erreurs longitudinaux. Malgré tout, nous avons réussi à contrôler l'interféromètre en utilisant la solution proposée dans le chapitre précédant : des bandes latérales à plus haute fréquence. Cette solution a été un succès et nous a permis d'acquérir le contrôle longitudinal même en présence d'importantes fluctuations de gain optique. En ce qui concerne l'alignement, nous avons implémenté un contrôle basé sur la modulation mécanique, comme pour les cavités des bras.

En conclusion, le travail de commissioning fait pendant la dernière année avec les simulations préparatoires a permis d'amener l'interféromètre à son point de fonctionnement de façon fiable et robuste, ce qui était le but de ce travail de thèse. La figure 4 montre un exemple de d'acquisition du contrôle de l'interféromètre Advanced Virgo. Pendant la prise des données O2, le cycle utile a été supérieur à 80% avec un horizon moyen de détection de binaires d'étoiles à neutron autour de 26 Mpc. La sensibilité du détecteur Advanced Virgo a permis la première détection triple d'une Binaire des Trous Noirs le 14 août.

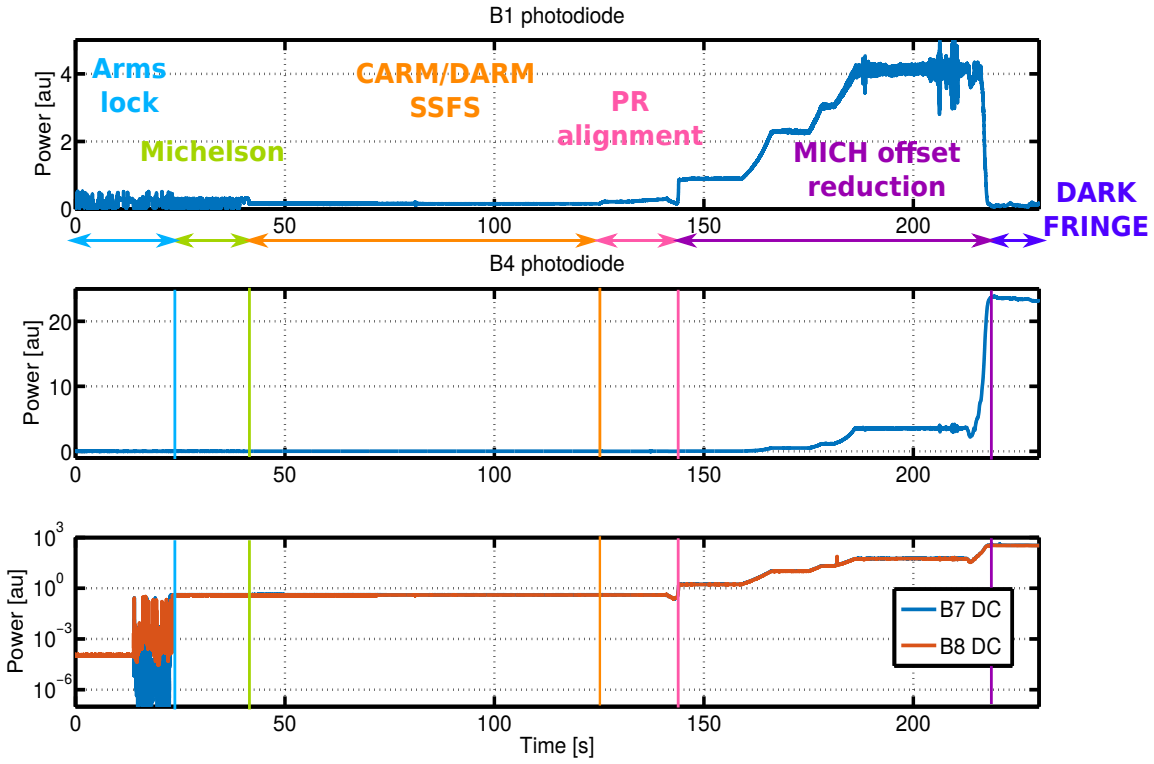

FIGURE 4: La stratégie de contrôle Variable Finesse est montrée ici, des le contrôle des cavités des bras jusqu'au changement de signal d'erreur du DARM en Fringe Noire. La figure montre la puissance dans le port asymétrique, dans la cavité PRC et en transmission des bras. Les différents étapes sont indiquées avec des couleurs différents.

Une fois le contrôle maîtrisé, il faut améliorer la sensibilité l'interféromètre. Or, il n'y a pas de contraintes explicites sur la précision des différents contrôles. Ce qui compte est alors le couplage des différentes boucles de contrôle avec la sensibilité qui peut dépendre des bruits présents et de la configuration optique de l'interféromètre. Donc pour atteindre la sensibilité nominale un processus itératif est nécessaire entre la chasse aux bruits techniques (ou autres) et l'amélioration des contrôles. En particulier, nous avons envisagé la possibilité d'utiliser pour les contrôles angulaires la même solution que pour ceux longitudinaux (une fréquence de modulation plus élevée). Ceci pourrait nous permettre d'utiliser les signaux d'erreurs nominaux pour les contrôles longitudinaux et diminuer ainsi le couplage avec la sensibilité.

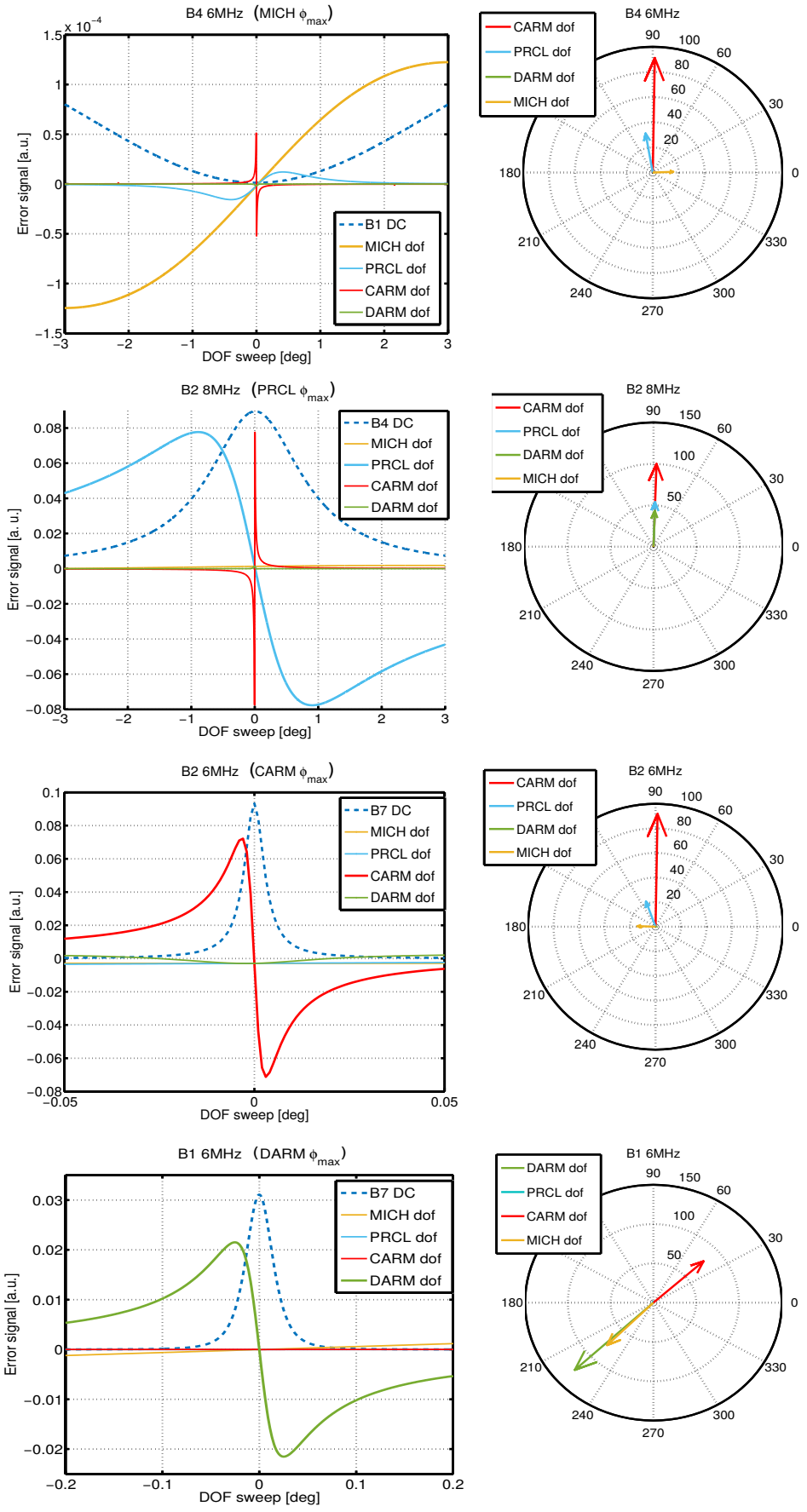

FIGURE 3: **Graphes à gauche:** Réponse du signal d'erreur au balayage des différents degrés de liberté. Pour chaque degré de liberté la phase de démodulation est réglée pour maximiser le degré de liberté a contrôler. **Graphes à droite:** Graphiques compas qui montrent pour chaque degré de liberté la phase de démodulation optimale et le gain optique correspondant.

Introduction

General Relativity predicted the existence of Gravitational Waves in 1916. Since then, a lot of attempts have been made in order to detect them. The first generation of ground-based interferometric gravitational wave detectors stopped the data taking in 2011 without making any detection. A series of upgrades were planned for the second generation of detectors in order to improve the sensitivity by an order of magnitude with respect to the one of Enhanced LIGO and Virgo+.

The first detection of a Gravitational Wave event by the Advanced LIGO detectors in 2015 September 14^{th} and the following detections have proved that it is possible to make astrophysical observations using ground-based detectors. The incorporation of Advanced Virgo to the network of detectors will play a key role on the parameters estimation of the sources. Advanced Virgo has been under commissioning during the last year and it joined the Advanced LIGO detectors in the Scientific Run O2.

The upgrades have affected the Advanced Virgo detector in many aspects, including the control strategy of the interferometer. The target of this thesis is the implementation of the longitudinal and angular controls necessary to bring Advanced Virgo to the target working point in a repetitive and robust way. This required not only commissioning work but also simulations to provide a better understanding of the new challenges. In this document I will present the simulation work I have developed and analysed, as well as the commissioning work to which I have contributed.

The basic properties of Gravitational Waves and the most interesting sources are presented in Chapter 1. Then the detection principle on Earth based on kilometric Michelson interferometer is described in Chapter 2, together with the optical configuration of the detector that maximizes the sensitivity. The limiting noise sources are also explained in this chapter. An overview of the most relevant subsystems of Advanced Virgo detector is given in Chapter 3 including the main upgrades with respect to Virgo/Virgo +. In Chapter 4 we present the basics needed for the following stages: Fabry-Perot optics, control theory, generation of error signals...

Chapter 5 describes the target optical configuration, defining the working point. The notions of sensing and driving are introduced, as well as the conditions they need to fulfil. We introduce the problematic linked to the stability of the Power Recycling Cavity and the solution proposed to deal with it. This chapter contains also a detailed study with the help of simulations of the control strategy used to reach the working point, focusing on the choice of sensing. This study is also applied to the final state of the interferometer.

Finally, the commissioning is described in Chapter 6. We give a timeline of the commissioning, highlighting the unexpected events that had an impact on the normal development of the activities on site and the main milestones achieved. A detailed description of the implementation of the longitudinal and angular controls is given: from the control of the first arm cavity to the global control at the target working point: full control of the Power Recycled Interferometer.

Chapter 1

Gravitational waves

The existence of Gravitational Waves (GW) is a consequence of GR and was predicted by Albert Einstein in 1916. This theory relates the curvature of the space-time with the energy matter distribution. GWs are perturbations of the metric (geometry of the space-time) that are caused by a movement of mass and which propagate at the speed of light. In this chapter we will describe their basic properties, as well as the most relevant sources [1] [2]. We will focus in particular in the ones that emit powerful GWs that can be detected by ground-based interferometric detectors.

The first detection of a GW was made on September 14^{th} of 2015 by the LIGO-Virgo collaboration with the two Advanced LIGO detectors [3]. It was emitted by the merger of a Binary Black Hole, providing the first direct proof of the existence of Black Holes. This event has marked the beginning of a new way of observing the Universe, and more detections have been done since then [4] [5]. We will briefly present their characteristics and the astrophysical implications of these detections.

1.1 Gravitational Waves

General Relativity links gravity to the curvature of the space-time manifold. This curvature is described by the metric $g_{\mu\nu}$. ***Einstein Equation*** relates the metric of the space-time with the energy/matter distribution so that:

$$R_{\mu\nu} - \frac{1}{2} g_{\mu\nu} R = \frac{8\pi G}{c^4} T_{\mu\nu} \tag{1.1}$$

where $R_{\mu\nu}$ is the Ricci tensor, which describes the space-time curvature, and R is the curvature. They are both function of the metric and its derivatives. G is the gravitation constant and c is the speed of light in vacuum. Finally $T_{\mu\nu}$ is the stress-energy tensor, which describes the matter distribution. It represents the source of the gravitational interaction.

In general Einstein equation can not be solved analytically. However it can be simplified in the weak field limit that is when the metric is close to the flat space one. This is a good approximation when we are far from the source, for example on Earth. In this case it we can linearize the Einstein Equation by writing the metric as:

$$g_{\mu\nu} = \eta_{\mu\nu} + h_{\mu\nu} \tag{1.2}$$

where $\eta_{\mu\nu}$ is the flat space Minkowski metric, which describes an infinite empty space without gravitation, and $h_{\mu\nu}$ is a small perturbation so that $|h_{\mu\nu}| \ll 1$.

General Relativity predictions do not depend on the choice of coordinates, so it can be proven that using *Lorenz gauge*, the Einstein Equation becomes:

$$\left(\nabla^2 - \frac{1}{c^2}\frac{\partial^2}{\partial t^2}\right)\overline{h}_{\mu\nu} = -\frac{16\pi G}{c^4}\left(T_{\mu\nu} - \frac{1}{2}g_{\mu\nu}T^k_k\right) \tag{1.3}$$

where $\overline{h}_{\mu\nu}$ is defined as:

$$\overline{h}_{\mu\nu} = h_{\mu\nu} - \frac{1}{2}\eta^{\mu\nu}h_{\mu\nu}\eta_{\mu\nu} \tag{1.4}$$

The term on the right side of Equation 1.3 represents the source of the wave. As we are working under the assumption that we are far from the source, we can neglect this term. Equation 1.3 then becomes a simple wave equation as in the electromagnetic case. The general solution can be written as a superposition of plane waves, and it describes the propagation of what we know as gravitational wave (GW):

$$h_{\mu\nu}(x) = A_{\mu\nu}e^{ik_\alpha x^\alpha} \tag{1.5}$$

where $A_{\mu\nu}$ is a 4x4 symmetric tensor that represents the spatial effect of a GW and k_α is the wave-vector.

The amplitude tensor has a priori 10 degrees of freedom (DOFs). A gauge called Tensor Traceless (TT) can be chosen so that only 2 DOFs remain. These DOFs are the two physical polarizations of the GW also known as plus (h_+) and cross (h_x). In this gauge the expression of a GW that propagates along the z-axis can be written as:

$$h^{TT}_{\mu\nu} = \begin{pmatrix} 0 & 0 & 0 & 0 \\ 0 & h_+ & h_x & 0 \\ 0 & h_x & -h_+ & 0 \\ 0 & 0 & 0 & 0 \end{pmatrix} e^{-i(\omega t - kz)} \tag{1.6}$$

where h_x and h_+ are the scalar amplitudes of the two polarizations, k is the wave-number and ω is the frequency of the GW.

It is interesting now to evaluate the **effect of the passage of a GW**. The distance between two masses, A(x_A, y_A, z_A) = (0,0,0) and B(x_B, y_B, z_B), infinitely close in the weak field approximation and in the TT coordinates can be calculated as:

$$L^2 = g_{\mu\nu}(x^\mu_B - x^\mu_A)(x^\nu_B - x^\nu_A) = (\delta_{ij} + h^{TT}_{ij})x^i_B x^j_B \tag{1.7}$$

where δ_{ij} is the Kronecker symbol and $x^i_B = L_0 n^i$, knowing that $\vec{n}$ is the unit spatial vector and L_0 is the initial distance between the masses.

This equation can be re-written as:

$$\begin{aligned} L &= \sqrt{L_0^2(\delta_{ij} + h^{TT}_{ij}n^i n^j)} \\ L &= L_0\sqrt{1 + h^{tt}_{ij}n^i n^j} \end{aligned} \tag{1.8}$$

so we can approximate

$$L \simeq L_0(1 + \frac{1}{2}h^{TT}_{ij}n^i n^j) \tag{1.9}$$

This expression indicates that the distance between two test masses is affected by the passage of a GW. If we define this change as $\delta L = L - L_0$ we obtain that for

an optimally oriented source:

$$\frac{\delta L}{L_0} = \frac{h}{2} \tag{1.10}$$

where h is the amplitude of the GW, also known as *strain amplitude*.

Equation 1.10 shows that the change on the distance between test masses induced by a GW is proportional to the amplitude of the GW. Moreover, from Expression 1.6 it can be deduced that this effect is differential. Figure 1.1 shows an example of the effect of a GW that goes through a ring of test masses perpendicularly.

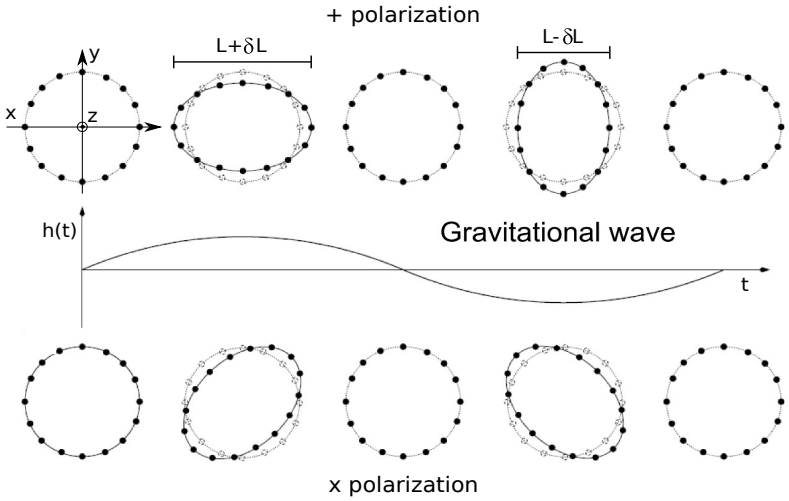

FIGURE 1.1: Effect of the plus and cross polarizations of a GW which propagates along the z axis through a ring of test masses. The evolution with time of the amplitude of the GW, h, is also shown.

The distance between the test masses contracts and then expands in one direction and the opposite in the perpendicular direction. The effect of the two polarizations is shown independently and we can see that it is rotated by $\pi/4$. Figure 1.1 also shows the amplitude evolution of the GW (h) with time.

1.2 Sources of Gravitational Waves

We are interested in the sources that emit GWs powerful enough to be detected by ground-based interferometric detectors. The power emitted by a source in form of GW is given by the *Einstein quadrupole formula*:

$$P_{GW} = \frac{G}{5c^5} \langle \dddot{I}_{mn} \dddot{I}^{mn} \rangle \tag{1.11}$$

where I_{mn} is the mass quadrupole moment of the source.

In order to estimate the power emitted by a source, the quadrupole moment can be roughly approximated as:

$$\dddot{I} \sim \epsilon \cdot \frac{M \cdot R^2}{T^3} \tag{1.12}$$

where ϵ is a mass distribution asymmetry factor ($\epsilon < 1$), M is the mass of the source, R is a characteristic length scale and T is a characteristic time scale.

Using the characteristic speed of the source $v = R/T$ and its Schwartzschild radius, $R_S = \frac{2GM}{c^2}$, Equation 1.11 can be re-written as:

$$P_{GW} \sim \frac{c^5}{G} \cdot \epsilon^2 \cdot \left(\frac{R_S}{R}\right)^2 \cdot \left(\frac{v}{c}\right)^6 \tag{1.13}$$

From this equation we can extract the conditions for a source to be a good emitter: it has to be **asymmetric** ($\epsilon \sim 1$), it has to be **compact** ($R_s/R \sim 1$) and **relativistic** ($v/c \sim 1$). With this information we can already predict which will be the most promising sources.

However, the emitted power is not the only parameter to take in account for evaluating the sources that could be detected by ground-based detectors. The **distance** of the sources from the Earth plays an important role since h decreases as 1/r. For this reason, the further a source is, the louder an event needs to be so that it can be detected.

Finally, the **rate** at which the transient events occur has also an impact on the detection probability. However, it is difficult to evaluate this parameter since it requires a knowledge of the processes that lead to the GWs emission that is not available yet such as population or structure formation among others.

Taking in account these considerations, the sources that are considered as potential candidates are presented below. Notice that normally they are classified in two groups: *continuous sources*, which comprises rotating neutron stars and stochastic background and *transient sources* such as compact binary coalescences or core collapse supernovae.

1.2.1 Neutron stars

Spinning neutron stars (NS) emit GWs if their mass distribution is asymmetric. The frequency of the emitted GWs will be at twice the rotational frequency. The amplitude of the GWs emitted depends on the asymmetry of the momenta of inertia of the NS, or eccentricity ε which, in turn, depends on the equation of state of nuclear matter.

Pulsars are a particular type of NS, which emit a periodic radio pulse. They are especially interesting because their rotational frequency can be precisely measured. This information allows the reconstruction of the GW signal which can be integrated over time in order to improve the Signal-to-Noise ratio (SNR).

The rotational frequency of the NS will decrease due to the energy loss in form of emitted GWs or electromagnetic radiation. This process is also known as spin-down. If we suppose that all the energy loss is due to the emission of GWs, we can put an upper limit on the eccentricity of the NS. Using the data from the first generation of GW detectors, LIGO and Virgo, we were able to put an upper limit below the spin-down limit on the eccentricity of two pulsars: Crab [6] and Vela [7].

1.2.2 Compact Binary Coalescence

Binary systems that emit GWs with amplitudes high enough to be detected by ground based detectors are composed of two neutron stars (NS), two black holes (BH) or a neutron star and a black hole. These systems emit GWs at twice the orbital frequency. Due to the loss of energy the orbit shrinks, increasing the orbital frequency until the two bodies merge.

These sources can not be considered as continuous since the frequency of the GW emitted is too low for being detected by ground detectors (mHz) until their coalescence. For this reason they can only be detected close to the merger, when the frequencies are within the detectors bandwidth (> 10 Hz) and increasing rapidly.

A useful parameter is the *BBH horizon*, which is the distance at which an optimally located and oriented binary system with two BHs of $10M_{\odot}$[1] each, would be detected with a SNR of 8. This magnitude is widely used to evaluate the sensitivity of the detectors, in the case of Advanced Virgo the nominal BBH horizon is 898 Mpc.

The signal emitted during this process is well modelled and a template bank is used for searching sources. The first detections of a GW were binaries black holes. We will enter into more details about them in the next section.

It is worth mentioning though, that the first indirect proof of the existence of GWs was provided by a binary far from coalescence. In 1974 R.A. Hulse and J.H. Taylor discovered a pulsar belonging to a binary system of neutron stars, also known as PSR B1913+16. The measurement of the evolution of its orbital frequency agreed precisely with the predictions of GR [8].

1.2.3 Bursts

This category contains the GW transients, which are the emissions that have a short duration compared to the observation time. The burst sources are in general not well understood, and in consequence not well modelled. For this reason the search of these signals is done by looking for an excess of power in the data.

A typical example of these events are Supernovae, which are the collapse of a star to form a neutron star or a black hole. However, they are not the only source of this type, cosmic strings are also bursts emitters, to give an examples.

1.2.4 Stochastic background

The signal can be the result of the incoherent sum of different sources emitting at the same time and frequency, transient or continuous, or it could have a cosmological origin. In the first case the sources can not be distinguished, and it can be shown that the signal follows a Gaussian distribution.

The search of such signals needs a very good understanding of the noise sources of our detector, since most of the noises have also a Gaussian shape. In order to separate noise from signal, correlation is used. It consists on combining the data from several detectors with uncorrelated noises to distinguish the signal from the noise.

1.3 GW150914: First detection

The 14^{th} of September of 2015 the first detection of a gravitational wave was made by the Advanced LIGO gravitational wave detectors, Hanford and Livingston, during their first Scientific Run [3]. The GW emitted came from the coalescence of a binary system of black holes of $30M_{\odot}$ each. During the process, the system emitted between 2.5 and $3.5M_{\odot}$ in GWs until the coalescence. The shape of the emitted GW, known as GW150914, is shown in Figure 1.2.

It can be seen in the figure that the frequency of the emitted GW increases at the same time as the amplitude during the *inspiral* phase, when the two BHs

[1] $M_{\odot}$ stand for solar mass, which is equivalent to $1.99{\cdot}10^{33}$ kg.

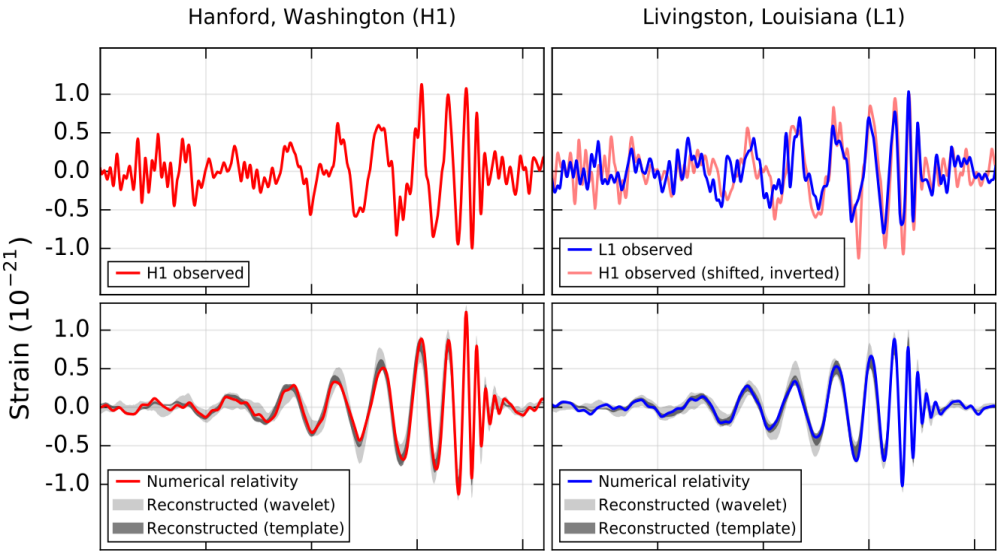

FIGURE 1.2: **Upper plots:** GW signal detected by the Advanced LIGO detectors in Hanford and Livingston respectively on September 14^{th} of 2015 (GW150914). **Lower plots:** Theoretical wave form of the detected GW in both detectors.

approach each other. Then the signal reaches a maximum that corresponds to the *merger* of both BHs. The detected signals are in very good agreement with the predicted wave form. This is because the SNR of the detection was very high: 25.

This event provided not only the first direct measurement of a gravitational wave but also interesting information concerning astrophysics. The experts were expecting BBH systems either at low masses (under $10M_\odot$) or at high masses (above $100M_\odot$). This detection proved that the intermediate range of masses is also populated.

During the first Scientific Run of the Advanced LIGO detector, another BBH was detected (GW151226) [4]. A third event was detected during the second Scientific Run, of the same nature as the previous ones (GW170104) [5]. The characteristics of the three detected events are summarized in Table 1.1.

	GW150914	GW151226	GW170104
Strain peak	10^{-21}	$3.4{\cdot}10^{-22}$	$5{\cdot}10^{-22}$
Distance [Mpc]	230-570	250-620	490-1318
Duration from 30 Hz [s]	0.2	1	0.25-0.31
Mass 1st BH [$M_\odot$]	32-41	11-23	25-40
Mass 2nd BH [$M_\odot$]	25-33	5-10	13-25
Energy emitted in GW [$M_\odot$]	2.5-3.5	0.8-1.1	1.3-2.6
Mass of the remnant BH [$M_\odot$]	58-67	19-27	44-54

TABLE 1.1: Characteristics of the three GW signals detected by the Advanced LIGO detectors.

Notice that the amplitudes of the GWs detected are extremely weak, which is the reason why building a detector was so challenging, as we will see in the next chapter.

Chapter 2

Ground based gravitational wave detectors

In the previous chapter we have introduced the basics about gravitational waves and their sources. In this one we will explain the working principle of ground based GW detectors. The fundamental noises that limit the sensitivity will be presented, as well as the upgrades added to the basic scheme in order to improve the detector sensitivity.

The effort to build GW detectors started back in the 60's with the so called Weber bar. It was a 1400kg aluminium bar and GWs were expected to excite its fundamental mechanical mode. In the same period, another detector configuration was proposed: using a Michelson interferometer. This detector would provide a wider detection frequency bandwidth [9]. It was sensitive to differential displacements which made this configuration the most promising one. The current GW detectors are the consequence of the refinement of the interferometric design.

Virgo detector was initially a french-italian project which started at the early 90's. The first design proposal was delivered to the funding agencies in 1992 and after some adjusting its construction was approved by 1995. The place chosen to build the experiment was the italian village of Cascina, in the province of Pisa. The construction started by the central building, and its commissioning started in 2001, while the construction of the long arm cavities was taking place in parallel. It was not until 2004 that the full interferometer was available to start the commissioning. The first scientific data taking, VSR1, took place in 2007 in parallel to LIGO S5 run.

Virgo detector and its optimized version Virgo + made four scientific runs in total between 2007 and 2011, three of them in coincidence with LIGO. As no detection was made with this first generation of GW detectors, it was decided to upgrade their design to increase the sensitivity. It was not until 2012 that the Advanced Virgo Technical Design was released and the installation started, ending in August of 2016. After one year of commissioning, the Advanced Virgo detector was operative and joined the 1st of August 2017 the Advanced LIGO detectors on the scientific data taking O2.

2.1 Detection principle

As presented in the previous chapter, the effect of a GW on Earth is a change on the distance between test masses that is proportional to the amplitude of the GW. The relationship is shown in Equation 1.10. Moreover this effect is differential, which makes a Michelson interferometer the ideal candidate. The particularity of this kind of detectors is that the mirrors of the interferometer are suspended in order to behave as test masses.

In a Michelson interferometer, the input beam is split in two with a Beam Splitter mirror (BS). Each of the beams travels a distance L and then is reflected back to the BS where they interfere. The interference depends on the phase difference between the beams ($\delta\phi$) due to the different optical paths traversed. This phase difference is related to the distance difference (δL) as:

$$\delta\phi = \frac{2\pi}{\lambda}\delta L = \frac{2\pi}{c}\nu\delta L \tag{2.1}$$

where λ is the laser beam wavelength and ν is the frequency of the laser beam.

Notice that $\delta\phi$ depends on the laser frequency as well. If this frequency fluctuates, as it is usually the case in practice, it will also contribute to $\delta\phi$. In this case we can not distinguish between length and frequency variation [10]:

$$\frac{\delta L}{L} = \frac{\delta\nu}{\nu} \tag{2.2}$$

For this reason the frequency stabilization of the laser will play a key role on the GW detection, since it can mimic the effect of a GW. However, in this part for simplicity we are going to consider the ideal case, where there is no frequency noise.

In this section we are not going to derive the equations of the Michelson interferometer, since we will do it in Section 5.1. Here we are interested only in the power arriving at the detection photodiode, in Michelson scheme of Figure 2.1.

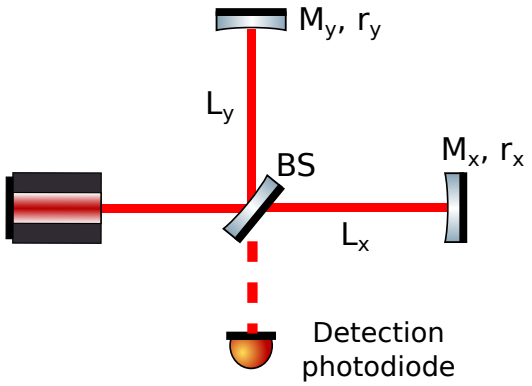

FIGURE 2.1: Scheme of a Michelson interferometer. The directions x and y are taken as the interferometer arms.

It can be shown that the detected power, P_{det}, is equal to [11]:

$$P_{det} = \frac{1}{4}\cdot P_0\cdot(r_x^2 + r_y^2)\cdot(1 + C\cdot\cos(2k\Delta L)) \tag{2.3}$$

where P_0 is the input power, $r_{x,y}$ are the reflectivities of the mirrors on the Michelson arms and $\Delta L = L_x - L_y$ is the length difference between the arms. C is the contrast, which is defined as:

$$C = \frac{P_{max} - P_{min}}{P_{max} + P_{min}} = \frac{2r_x\cdot r_y}{r_x^2 + r_y^2} \tag{2.4}$$

where P_{max} is the maximum power arriving to the detection photodiode (Bright Fringe), which happens when the interference is constructive. P_{min} is the minimum

power arriving to the detection photodiode (Dark Fringe), which happens when the interference is destructive.

The contrast depends on the reflectivity of the mirrors, and for totally reflective mirrors ($r_1 = r_2 = 1$ and no losses) it is 1. In this case P_{min} is 0 and P_{max} is the input power P_0.

As shown in Equation 2.3 the power detected depends on the optical path difference between the arms of the Michelson. Now if we consider the passage of a GW, the phase difference at the BS is:

$$\phi = \phi_0 + \delta\phi_{GW} = 2 \cdot k \cdot \Delta L_0 + 2 \cdot k \cdot (\delta l_x - \delta l_y) \tag{2.5}$$

where ΔL_0 is the static length difference between the arms. $\delta l_x = \frac{1}{2}hL$ and $\delta l_x = -\frac{1}{2}hL$ are the length differences induced by the passage of a GW on each arm.

The power detected can be re-written taking in account the effect of a GW. As the expected amplitude of GWs is very small, the small angle approximation can be used so:

$$P_{det} = \frac{P_0}{4} \cdot (r_x^2 + r_y^2) \cdot (1 - C \cdot [\cos(\phi_0) - \sin(\phi_0)\delta\phi_{GW}]) \tag{2.6}$$

From this expression we can calculate the variation of the detected power due to the passage of a GW optimally oriented:

$$\begin{aligned} \delta P_{det} &= \frac{P_0}{4} \cdot (r_1^2 + r_2^2) \cdot C \cdot \sin(\phi_0) \cdot \delta\phi_{GW} \\ &= \frac{P_0}{4} \cdot (r_1^2 + r_2^2) \cdot C \cdot \sin(\phi_0) \cdot (2 \cdot k \cdot h \cdot L) \end{aligned} \tag{2.7}$$

where L is the average length of the Michelson arms.

This equation shows that the detected power variation due to the passage of a GW is proportional to its amplitude. However, it depends not only on h but also on the reflectivity of the mirrors, on the input power, on the contrast, on the Michelson average length and on the interference condition. The optimization of these parameters is the key for detecting such a weak signal.

2.2 Interferometer sensitivity

As shown in the previous chapter, the typical amplitudes of the GWs we want to detect are very small when they pass through the Earth, $\sim 10^{-21}$. The *sensitivity* of a detector is the minimal signal that we are able to detect, in this case the minimal strain. The target is to maximize the signal caused by the passage of a GW, that is δP_{det} (see Equation 2.7).

In the absence of any noise, the interference condition that maximizes the sensitivity would be the *grey fringe*, meaning only half of the power arrives to the detection port (for an ideal contrast) [12]. In practice there are noises that limit the sensitivity and then the working point will be different.

In particular the lowest noise level that can be reached is the Quantum one. It has two contributions: *shot noise* and *radiation pressure*, that will be dominant at high frequencies and at low frequencies respectively. Notice however that a lot of research is being developed on a technique called *squeezing* that will allow to improve the sensitivity beyond the quantum limit at high frequency and/or at low frequencies in the near future [13].

For the moment though they can not be mitigated and we will focus on the shot noise, since it is going to limit the sensitivity at high frequencies. Then we will present the different noises that contribute at low frequency.

2.2.1 Shot noise

This noise is related with the quantum nature of light and affects to the power detected by a photodiode. The average number of photons, N, reaching a photodiode can be calculated as:

$$N = \frac{P_{det} \cdot T}{h_P \cdot \nu} \tag{2.8}$$

where T is the measurement time and h_P is the Planck constant.

Knowing that the measurement of the number of photons follows a Poisson distribution, the uncertainty is equal to $\sqrt{N}$. Then we can calculate the uncertainty on the detected power:

$$\sigma_P = \sqrt{N} \cdot \frac{h_P \cdot \nu}{T} = \sqrt{\frac{h_P \cdot \nu \cdot P_{det}}{T}} \tag{2.9}$$

At this point we can impose the condition for detecting a GW: $\delta P_{det} > \sigma_P$ which can be written as:

$$\frac{P_0 khL}{4}(r_x^2 + r_y^2)\sin(\phi_0) > \sqrt{\frac{h_P \nu}{T}\frac{P_0}{4}(r_x^2 + r_y^2)(1 + C\cos(\phi_0))/2} \tag{2.10}$$

So the smallest strain that we can detect due to the shot noise is:

$$h_{shot} = \frac{2}{k \cdot L} \cdot \sqrt{\frac{h_P \cdot \nu}{T \cdot P_0 \cdot (r_x^2 + r_y^2)}} \cdot \frac{\sqrt{(1 + C \cdot \cos(\phi_0))}}{C \cdot \sin(\phi_0)} \tag{2.11}$$

As mentioned before, the target is to tune the free parameters in order to improve the sensitivity of the detector. From Equation 2.11 it can be shown [11] that in the presence of shot noise the optimal interference condition is the Dark Fringe for a perfect interferometer, so $\phi_0 = (2n + 1)\pi$ with n any integer number. Considering also perfect reflective mirrors, the ideal sensitivity is:

$$\widetilde{h}_{shot} = \frac{2}{k \cdot L} \cdot \sqrt{\frac{h_P \cdot \nu}{P_0}} \tag{2.12}$$

The best sensitivity is obtained for a perfect interferometer with $C = 1$, but this is not possible in practice, so the real sensitivity is given by:

$$\widetilde{h}_{shot} = \frac{2}{k \cdot L} \cdot \sqrt{\frac{h_P \cdot \nu}{P_0 \cdot (r_x^2 + r_y^2)}} \cdot \frac{1}{\sqrt{1 - \sqrt{1 - C^2}}} \tag{2.13}$$

We can evaluate the sensitivity in the ideal case (Equation 2.12) for an interferometer with an infrared laser at 1064 nm, 25 W of input power and Michelson arms of 1 m. In this case $\widetilde{h}_{shot}$ is of the order of 10^{-17} $1/\sqrt{Hz}$. Clearly this sensitivity is not enough to detect GWs, so it needs to be improved. From Equation 2.12 two improvements can be deduced: an increase of the arms length, and an increase of the input power.

2.2.2 Improving the sensitivity

A significant **increase of the Michelson arms length** is needed in order to reach the sensitivity necessary for detecting GWs. However, it is not easy to build arms of more than 3-4 km. The solution found for this problem was to add Fabry-Perot cavities to the Michelson arms, as shown in Figure 2.2.

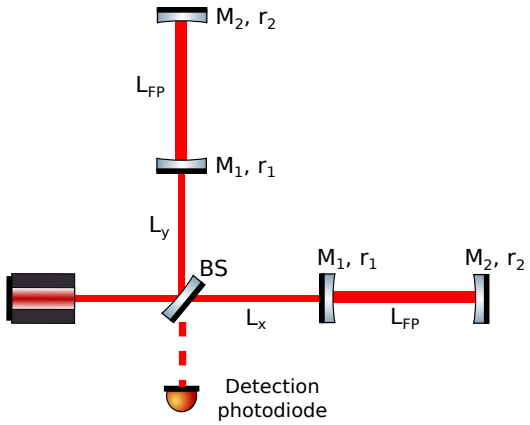

FIGURE 2.2: Scheme of a Michelson interferometer with Fabry-Perot cavities on its arms

A Fabry-Perot cavity is an optical resonator and when on resonance, the light is reflected back and forth inside the cavity, increasing the optical path travelled. These optical resonators will be described in detail in Chapter 4. The increase on the optical path due to the resonant cavity is related with a parameter called the *finesse* which is defined as:

$$\mathcal{F} = \frac{\pi \cdot \sqrt{r_1 \cdot r_2}}{1 - r_1 \cdot r_2} \tag{2.14}$$

where $r_{1,2}$ are the reflectivities of the input and end mirror respectively.

The extra phase accumulated due to a change on the length of a Fabry-Perot cavitiy is equal to:

$$\delta\phi_{FP} = 2 \cdot k \cdot \frac{2 \cdot \mathcal{F}}{\pi} \cdot \delta L \tag{2.15}$$

The effect of this δL on the phase is increased with respect to a single mirror by a factor $G_{FP} = \frac{2 \cdot \mathcal{F}}{\pi}$ usually known as *optical gain* of the cavity. However, the behaviour of a Fabry-Perot cavity depends on the frequency. The *storage time* is a parameter that gives the time needed to "fill" a resonant cavity. If the change on the length is faster than this time, its effects are attenuated by the cavity (it acts as a low-pass filter). Taking in account the frequency behaviour of the cavity we can write:

$$\delta\phi_{FP} = 2 \cdot k \cdot G_{FP} \cdot \frac{\delta L}{\sqrt{1 + \left(\frac{f}{f_c}\right)^2}} \tag{2.16}$$

where $f_c = \frac{c}{4\mathcal{F}L}$ is the *cut-off frequency* over which the effects start to be attenuated by the cavity. In the case of Advanced Virgo, for Fabry-Perot cavities of $\mathcal{F} \sim 450$ and arm lengths of 3 km the cut-off frequency is around 50 Hz.

Now we can repeat a reasoning analogous to the one in the previous section to evaluate the impact of the shot noise on the sensitivity when we add Fabry-Perot

cavities in the arms. The minimal strain that can be detected in this case is:

$$h_{shot} = \frac{1}{G_{FP}} \cdot \frac{1}{k \cdot L} \cdot \sqrt{\frac{h_P \nu}{P_0 \cdot (r_1^2 + r_2^2)}} \cdot \frac{1}{\sqrt{1 - \sqrt{1 - C^2}}} \cdot \sqrt{1 + \left(\frac{f}{f_c}\right)^2} \tag{2.17}$$

Comparing it to the expression in Equation 2.13 it can be seen that the sensitivity is improved by a factor G_{FP}, which in the case of the Advanced Virgo arm cavities is ~ 290.

The other parameter that can improve the sensitivity is the **input power**, P_0. Again it is not straightforward to increase the power of the laser since it arises technical problems, so an alternative was proposed: an additional mirror.

At Dark Fringe, the two beams that recombine at the BS are in destructive interference. This means that in the ideal case there is no light arriving to the detection photodiode. Instead, all the power is coming back towards the laser source. The idea was to add a mirror between the BS and the laser in order to recycle all the power that is coming back, as it can be seen in Figure 2.3.

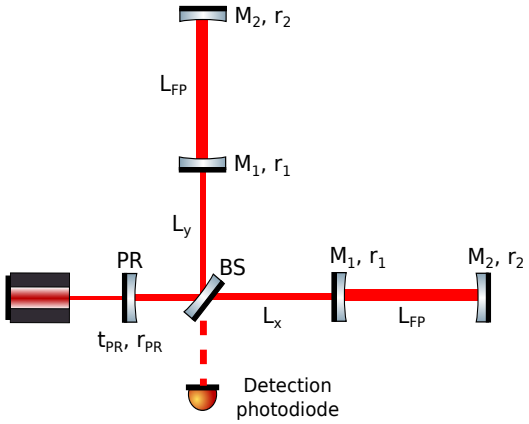

FIGURE 2.3: Scheme of a Michelson interferometer with Fabry Perot cavities on its arms and a power recycling mirror.

This way a new resonant cavity is created, the Power Recycling Cavity, and the effective power impinging on the BS is increased by the optical gain of the cavity G_{PR}. It can be calculated as:

$$G_{PR} = \left(\frac{t_{PR}}{1 - r_{PR} \cdot r_{MICH}}\right)^2 \tag{2.18}$$

where t_{PR}, r_{PR} are the transmission and reflectivity of the new mirror, also called Power Recycling mirror or PR, and r_{MICH} is the reflectivity of the Michelson enhanced by the presence of the Fabry-Perot cavities, which depends on the interference condition at the BS.

Knowing that the effective power is increased by G_{PR}, it is straightforward to evaluate the impact on h_{shot}:

$$h_{shot} = \frac{1}{G_{FP}} \cdot \frac{1}{k \cdot L} \cdot \sqrt{\frac{h_P \nu}{G_{PR} \cdot P_0 \cdot (r_1^2 + r_2^2)}} \cdot \frac{1}{\sqrt{1 - \sqrt{1 - C^2}}} \cdot \sqrt{1 + \left(\frac{f}{f_c}\right)^2} \tag{2.19}$$

In this case the sensitivity is increased by a factor $\sqrt{G_{PR}}$, which for Advanced Virgo is ~ 6.

Finally, it is foreseen to add an extra cavity to the Advanced Virgo detector in order to increase further the sensitivity. The target is to recycle the signal produced by the passage of a GW. For this purpose a mirror is added between the BS and the Detection photodiode as shown in Figure 2.4. This configuration is known as Signal Recycled or Dual Recycled.

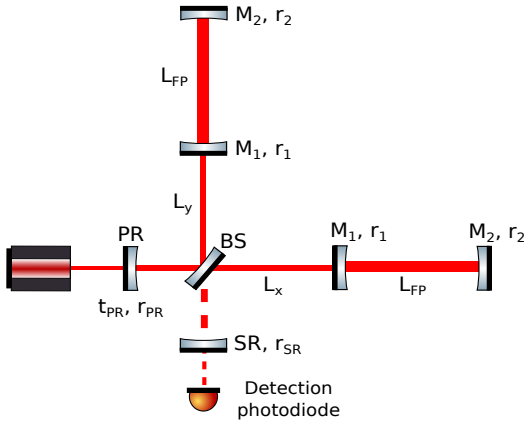

FIGURE 2.4: Scheme of a Michelson interferometer with Fabry Perot cavities on its arms, a power recycling mirror and a signal recycling mirror.

The interest of this configuration is that we can tune the shape of the sensitivity by changing the length of the Signal Recycling Cavity. In particular, there is a configuration called *detuned* that maximizes the sensitivity in the range of interest for BNS.

2.2.3 Limiting noises

So far we have only considered the shot noise which can not be mitigated. At low frequency though there are other noises that couple to the interferometer and that affect the sensitivity. Figure 2.5 shows an example of a sensitivity curve of Advanced Virgo with the contributions of the fundamental noises that typically limit the sensitivity.

The example shown in Figure 2.5 corresponds to the Advanced Virgo detector on its Dual Recycled configuration with 125 W of input power tuned for Binaries Neutron Stars. Even if it is not the current configuration, it is representative of the impact of the different noises to the sensitivity.

At high frequencies it can be seen that the Quantum noise dominates the sensitivity, in particular, the shot noise, as we had anticipated. At low frequencies though, there are different contributions. Here we will mention the most relevant [15]:

- **Quantum noise:** As mentioned before it comprises the shot noise (dominant at high frequencies) and the radiation pressure (dominant at low frequencies). The latter is the consequence of the force that the photons exert on the test masses, causing a displacement of the mirrors.

  This effect is more important when the power increases since the force is larger as well. Its behaviour depends on the frequency as $1/f^2$, which is

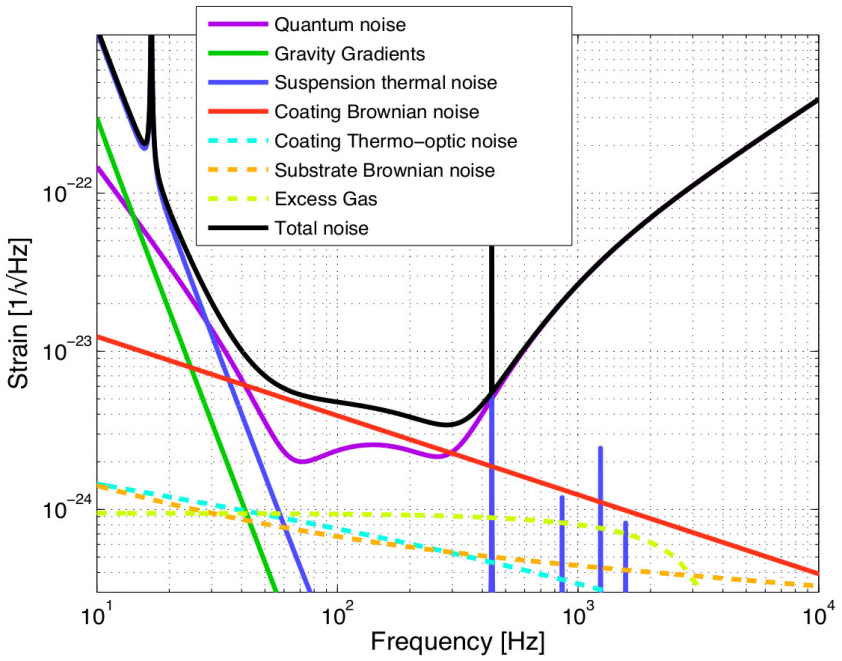

FIGURE 2.5: Sensitivity curve of the Advanced Virgo detector for its Dual Recycling configuration with 125 W of input power. The contributions from the main limiting noises are also shown [14].

the reason why it is more important at low frequencies. The impact can be reduced, in particular by increasing the mass of the mirrors, as it was done for Advanced Virgo, where their mass is 42 kg.

- **Thermal noises:** Both the test masses and the suspensions experience Brownian motions, since they operate at ambient temperature. In the case of the suspensions, this noise is attenuated by the pendulum above its resonance (0.6 Hz). At low frequencies it is the dominant contribution.

  Regarding the test masses, the coating noise is distributed over the mirror surface. Its effect can be minimized by increasing the beam size and so averaging over a bigger surface. For this reason the geometry of the arm cavities was modified for Advanced Virgo, in order to increase the beam size in both mirrors.

- **Seismic noise:** The ground motion has a big impact on the interferometer performance, and if it is not attenuated, it would dominate the sensitivity at low frequencies. However, as we mentioned previously, in order to behave as test masses the mirrors are suspended. A pendulum acts as a passive filter, that attenuates the noise above its resonance frequency as $1/f^2$. A complex suspension chain has been designed in order to attenuate completely the effect of the seismic noise above 10 Hz. It will be described in more detail in the next chapter, but it can be already seen in Figure 2.5 that it is so suppressed that it does not appear on the scale. As the mirrors are suspended, the residual seismic noise changes the position of the optics, sufficiently to spoil the working point. For this reason the position of the optics will need to be actively corrected as we will see in detail later.

Finally Figure 2.6 shows the nominal sensitivity for the Advanced Virgo detector on its current configuration (blue curve) as well as the ones expected after future upgrades.

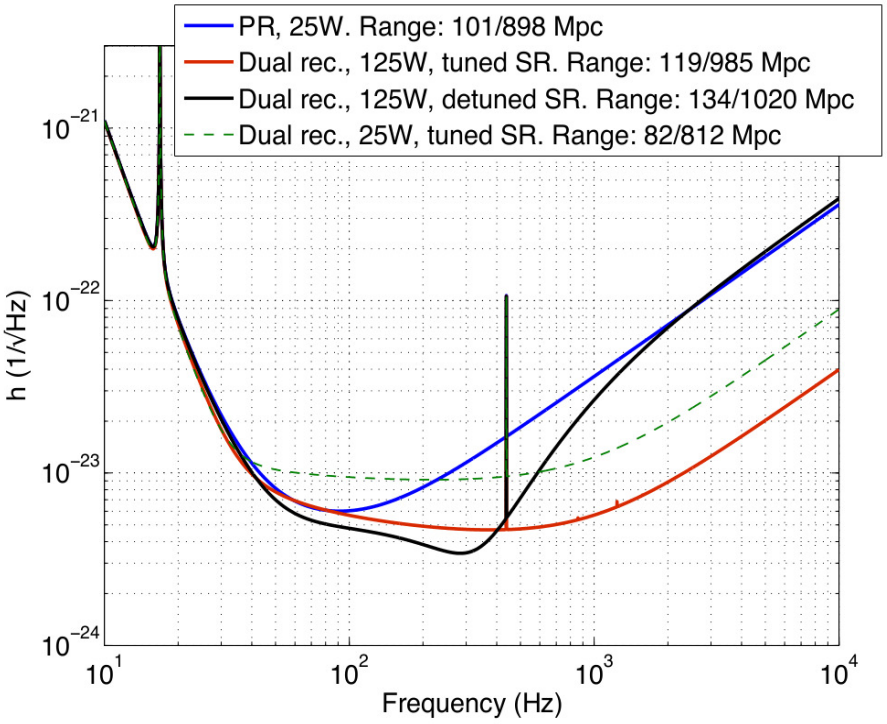

FIGURE 2.6: Sensitivity curves of Advanced Virgo for different configurations. The blue one is the configuration available so far, the rest of the curves correspond to future upgrades.

2.2.4 Homodyne detection vs. Frontal modulation

As we have mentioned, the seismic noise is attenuated in a very efficient way. However, the residual motion of the suspended mirrors is enough to bring the cavities out of resonance and the Michelson out of a Dark Fringe. For this reason, the position of the mirrors needs to be controlled to keep the target working point. I will not enter into details in this section, since this is the main topic of this thesis and it will be developed in the Chapters 4, 5 and 6. However we will give the basic knowledge to understand the type of detection scheme used in Advanced Virgo.

In order to keep the mirrors on their nominal positions, we need an error signal that provides this information. At the Dark Fringe the DC power at the detection photodiode has a quadratic shape, which means that it is symmetrical around the working point. A good error signal though needs to be bipolar[1] as we will see in Section 4.4.2, which is not the case. This means that it is necessary to find an alternative to generate an error signal.

The technique chosen was the **Pound-Drever-Hall technique** [16], which consists on modulating in phase the input beam in order to create *sidebands*. These sidebands appear at ± the modulation frequency and are chosen to be anti-resonant

[1] A bipolar signal has both positive and negative values.

inside the Fabry-Perot cavities of the arms. This way, they provide a phase reference to the carrier, which resonates, carrying information about the optical path inside the cavity and so of its length. The beating between the carrier and the sidebands provides the error signal, which is proportional to δL (and thus to h).

In order to build an error signal at the detection photodiode, the sidebands need to reach it, as they provide the phase reference. In the case of Advanced Virgo we need to take in account the Power Recycling Cavity. The sidebands frequency needs to be resonant as well inside it in order to reach the detection photodiode. Moreover, they need to reach the detection photodiode even in Dark Fringe, and for this reason the Schnupp asymmetry was implemented. It consists on adding a macroscopic length difference between the short Michelson arms, L_x and L_y so that the interference between the sidebands at the BS is not perfectly destructive unlike the carrier interference. Again, this will be described in more details in Chapter 5.

At this point we are able to keep the interferometer at Dark Fringe, and detect the passage of a GW. The sidebands provides a phase reference and the carrier carries information of the length difference between the Fabry-Perot arm cavities. However, this method depends strongly on the quality of the sidebands. This means that if they are noisy or largely unbalanced, there will be technical noises that will spoil the sensitivity such as phase and amplitude noise.

To avoid this, it was decided to change the read-out scheme in the Advanced GW detectors to *Homodyne detection* or *DC readout*. As it was mentioned before, it is not possible to use directly the DC power to control the interferometer in Dark Fringe. However, we can add a small offset to the arms, which means making one arm slightly longer than the other. This offset allows a small amount of carrier field to leak to the detection photodiode, which will play the role of phase reference. In this configuration the power detected is proportional to the length difference between the arms and so to h.

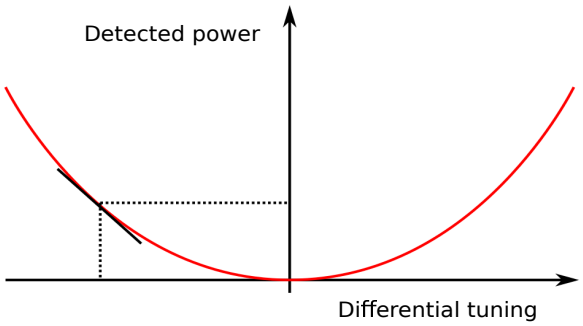

FIGURE 2.7: Variation of the power at the detection port as a function of a length difference between the arm cavities. [15].

Figure 2.7 shows the dependence of the power at the detection photodiode with respect to a differential detuning. It can be seen how in Dark Fringe the power is almost insensitive to a differential detuning, while it is almost linear when an offset is added. This behaviour does not depend on the value of the offset [15]. Of course, this offset needs to be smaller than the arms resonance, to keep them at their correct working point.

However, this method can be used only to control one degree of freedom (DOF), for the rest of longitudinal DOFs (there are four in total), the PDH technique is needed. This means that there will be sidebands leaking to the detection photodiode, spoiling the error signal. To prevent this, an extra Output Mode Cleaner was added before the detection photodiode. It is a resonant cavity whose target is to select only the carrier field.

Finally, due to the mistuning of the arm cavity lengths, the effect of radiation pressure is stronger, so it will be necessary to take it in account when designing the alignment control, as we will see later in Chapter 4.

Chapter 3

Advanced Virgo

Ground-based GW detectors are very complex optical systems and for this reason they are divided in different subsystems. Each of them takes care of a different topic but of course there are strong interactions between them. The Advanced Virgo detector is divided in the following subsystems: Optical Simulation and Design (OSD), Prestabilized Laser (PSL), Injection (INJ), Mirrors (MIR), Thermal Compensation Systems (TCS), Detection (DET), Interferometer Sensing and Control (ISC), Stray Light Control (SLC), Suspensions (SUSP), Vacuum (VAC) and Data Acquisition (DAQ). In this chapter we are going to present the relevant subsystems to have an overview of the detector and to give a context to the work I have done for the ISC subsystem [14].

The Advanced Virgo detector was designed to improve the sensitivity of the Virgo detector by one order of magnitude, which translates in three orders of magnitude in terms of volume of observable Universe. In this section we will also present the main upgrades that will allow this improvement.

3.1 OSD: Optical Simulation and Design

This subsystem takes care of the optical design of the interferometer. In order to improve the sensitivity, the optical design of the interferometer was modified for Advanced Virgo:

- **Increase of the finesse of the arm cavities:** In Virgo the finesse was 150 and in Advanced Virgo it is 450. The finesse has increased by a factor 3, which translates directly in to an improvement on the sensitivity as seen in the previous chapter.
- **Change of the geometry of the arm cavities:** In Virgo the Fabry-Perot cavities on the arms had the beam waist[1] on the input mirror. In order to minimize the coating thermal noise, their geometry was modified to maximize the size of the beam in both mirrors (see Figure 4.10 in Section 4.3.3).
- **Power Recycling Cavity marginally stable:** The change on the arms geometry obliged to adapt the geometry of the PRC in consequence. The new configuration is very close to instability which will have an important impact on the control of the interferometer as we will see in Section 5.2.2.
- **Heavier mirrors:** In order to decrease the thermal noise, which is inversely proportional to the mass, the mirrors of Advanced Virgo are thicker (20 cm) and heavier (42 kg). It also helps to decrease the radiation pressure noise, consequence of the new read-out scheme, as it was introduced in the previous Chapter (see Section 2.2.3).

[1] The waist is the point with the smallest size in a Gaussian beam.

- **Improvement of mirror coatings:** the mechanical losses in the coating of the mirrors determine their quality factor and so the displacement of the mirror surface due to its thermal vibration. To improve the thermal noise it is important to minimize them. For this purpose the coating of the mirrors of Advanced Virgo was done of a new material: Ta_2O_5, which is the best option known so far. Also the thickness of the different coating layers has been optimized to minimize mechanical losses.

- **Additional photodiode:** To monitor the power inside the Power Recycling Cavity, which requires the addition of a Pick-Off inside the cavity. This information will be useful in order to build error signals for the interferometer control, as it will be seen later.

For the study of the optical design there are a large variety of simulations that can be used. During my thesis the simulations that I have used are the following:

- **Finesse:** it is a modal code. It expands the electric field in a set of Hermite-Gauss modes in order to reproduce the behaviour of the optical system simulated [17]. It is ideal to study the steady state of the interferometer.

  It can also handle Higher Order Modes (HOMs) which means that the effects of mismatch and misalignments can be studied with this simulation. The only inconvenience is that when dealing with defects in marginally stable cavities (as it is the case for the PRC) it needs a lot of HOMs to converge into the good solution. This increases the calculation time too much to make it useful in some cases.

- **Optickle:** it is a simulation tool that allows to simulate the frequency behaviour of an optical system, including radiation pressure effects [18]. This simulation uses the plane wave approximation, so it does not take in account HOMs. It is usually used to simulate the optical response of different elements in the interferometer for the noise budget or to design control loops.

- **e2e:** this is a time domain opto-mechanical simulation based on a modal model [19]. It allows us to study dynamical effects, since it simulates also the mirrors suspensions and different noises can be added. It is useful to simulate the longitudinal control of the different DOFs, in particular the moment when they are engaged.

3.2 TCS: Thermal Compensation System

A marginally stable cavity, as the PRC, is very sensitive to the generation of HOMs, degrading quickly its performance when they are present. For this reason it is necessary to minimize the coupling of HOMs inside the interferometer in a more efficient way than in the past.

The target of the Thermal Compensation system is to deal with optical aberrations: both the manufacturing defects of the optics and the aberrations caused by thermal effects due to the power of the laser. In particular its key role is to assure that the PRC is effectively stable. The new system is composed of two actuators:

- **Ring Heater (RH):** it is a ring placed around the PR mirror and the input masses. Its role is to heat the optics in order to increase their radius of

curvature. This is specially critical when the High Power laser will be used, since it will induce a thermal lens in the optics that needs to be compensated.

- **Central Heating (CH):** the actuators are CO_2 lasers used to heat the center of two transmissive optics placed in front of the input masses, the Compensation Plates (CP). The target is to correct for aberrations in the arm cavities and differential defects (different behaviour on each arm).

3.3 SUSP: Suspensions

The mirrors of the interferometer are suspended, in order to behave as test masses. However, the seismic noise is a big problem in order to reach the target sensitivity, since it couples to the optics. For this reason the suspensions of Virgo are a very complex mechanical system. Figure 3.1 gives an overview of the whole chain, which is 9 m high.

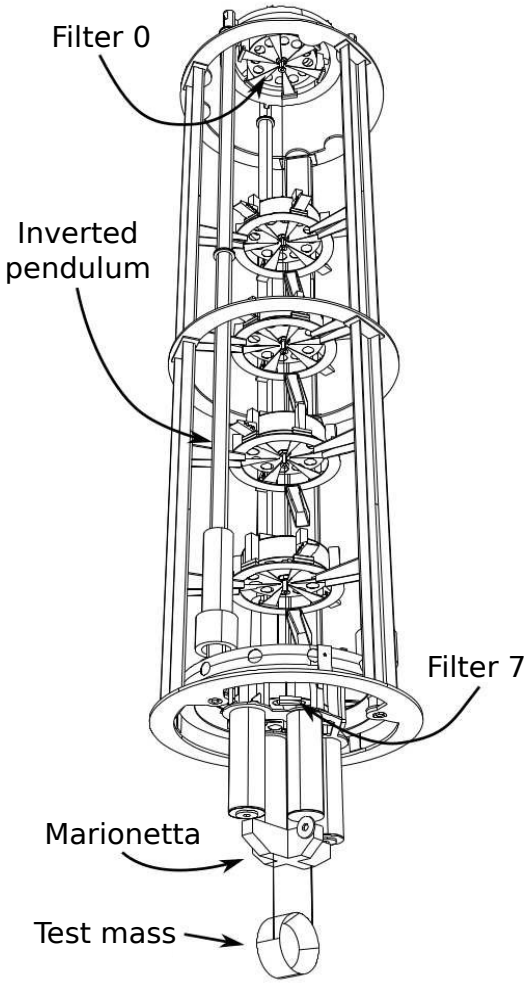

FIGURE 3.1: Mechanical scheme of the Superattenuator. Its aim is to isolate the test masses from the ground motion.

The top part is called *Superattenuator* and it is composed by six mechanical filters attached by metal wires and an inverted pendulum. The attenuation chain is based on the simple pendulum mechanism. An ideal pendulum attenuates all the

horizontal movements at frequencies above its resonant frequency, f_0, by a factor $(f/f_0)^2$. The total attenuation factor is the multiplication of the effect of each individual pendulum.

The last two stages are slightly different: the *marionetta* and the mirror itself. There are four magnets attached to each of them which are controlled by four coils. The angular and longitudinal position of the test masses can be controlled by acting on the current sent to the coils. To prevent the mirrors from moving freely, a preliminary control is engaged also known as *Local control (LC)*.

The error signals of these controls are built using *optical levers* obtained with red lasers and*Position Sensing Devices*, which monitor the angular and longitudinal positions of the mirrors. They provide only a local reference and in the target configuration the error signals are substituted to allow a more precise control.

For Advanced Virgo all the resonant frequencies are below 2.5 Hz, which means that the mirrors behave as free test masses in the horizontal direction above this frequency. The seismic noise is attenuated by 14 orders of magnitude above 10 Hz thanks to the suspension chain [20].

3.4 INJ: Injection

This subsystem is the interface between the laser and the interferometer. It plays an important role: it fixes the beam size, position and power to match the interferometer. It also controls some noise sources such as the frequency and power fluctuations, the beam jitter or the beam position fluctuations. Figure 3.2 shows a basic scheme of the different components of this subsystem from the laser source to the interferometer input.

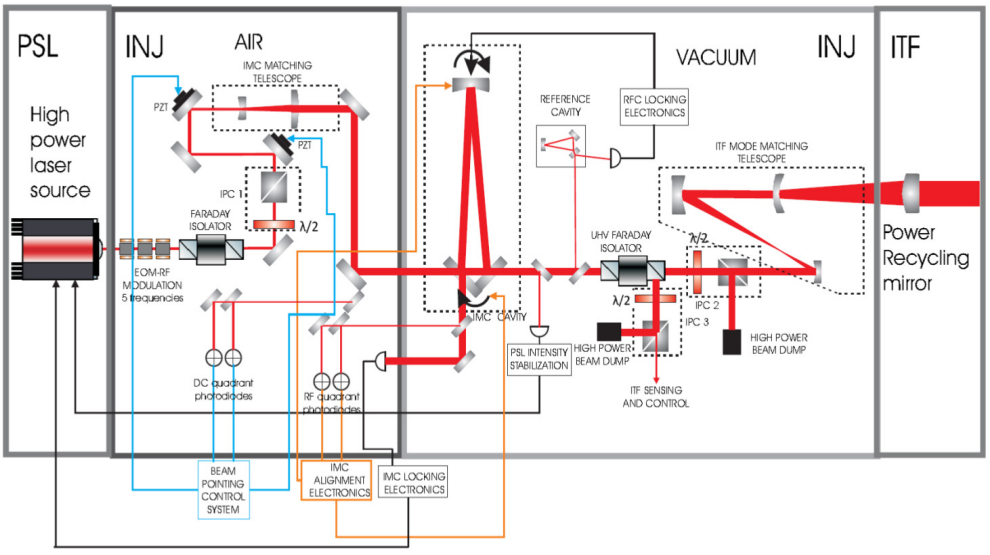

FIGURE 3.2: Scheme of the main elements of the Injection subsystem [21].

The bench under vacuum is suspended, with an attenuator similar to the one of the mirrors but smaller. The bench which is on air is not suspended, but the ground motion is passively damped by a special support and it could be actively corrected if needed.

- **Electro Optic Modulator (EOM):** it modulates in phase the laser beam to provide the sidebands used in the different controls of the interferometer. Currently there are six different modulation frequencies with a modulation depth of 0.1: 6MHz, 8MHz, 22MHz, 56MHz and 119MHz.
- **Faraday Isolator:** it prevents the beam coming back from the interferometer from reaching the laser.
- **Beam Pointing Control (BPC):** it acts on the beam position in order to reduce the beam jitter.
- **Input Mode Cleaner (IMC):** it is a triangular cavity of approximately 140 m and finesse 1000. It has two functions: to clean the beam from HOMs so that only the fundamental mode enters into the interferometer and to stabilize the frequency of the laser. Its end mirror is also suspended.
- **Power stabilization.**
- **Reference Cavity (RFC):** it is a smaller triangular cavity, ∼30 cm and finesse ∼900. It provides a frequency reference and it is used to stabilize the laser frequency at low frequencies.
- **Mode Matching Telescope:** it adapts the beam size and alignment to match the interferometer.

As it was mentioned in the previous chapter, the frequency noise couples directly to the strain that we want to measure (see Equation 2.2). For this reason a preliminary frequency stabilization is necessary before engaging the longitudinal control of the interferometer.

The Reference Cavity provides a frequency reference and it controls the length of the IMC at low frequencies, where the seismic noise is more important. At higher frequencies the IMC itself is a good reference. Then, there is a photodiode in reflection of the IMC that provides information about the deviation of the laser frequency from the length of the IMC. With this information the laser frequency is changed to follow continuously the IMC length. This first stage of frequency stabilization is also known as the *Pre-stabilization loop*.

3.5 DET: Detection

The role of this subsystem is to provide the error signals necessary for the different controls of the interferometer. There are 6 photodiodes for the longitudinal control and 12 quadrant photodiodes, placed in 5 detection benches, as it is shown in Figure 3.3.

Each photodiode monitors different signals from the interferometer: B1 the detection port, B2 the power reflected by the PRC, B4 the power inside the PRC, B5 the the reflected power by the North Arm cavity, B7 the transmitted power of the North Arm cavity and B8 the transmitted power of the West Arm cavity.

Regarding the quadrant photodiodes, they are used for the angular control of the interferometer. There are two per longitudinal photodiode, and they are placed 90° of Gouy phase away from each other, in order to extract useful error signals, as it will be explained in Section 4.5.2.

The case of the Detection bench is a particular one for several reasons. First of all there are two different informations extracted at it: the beam reflected from

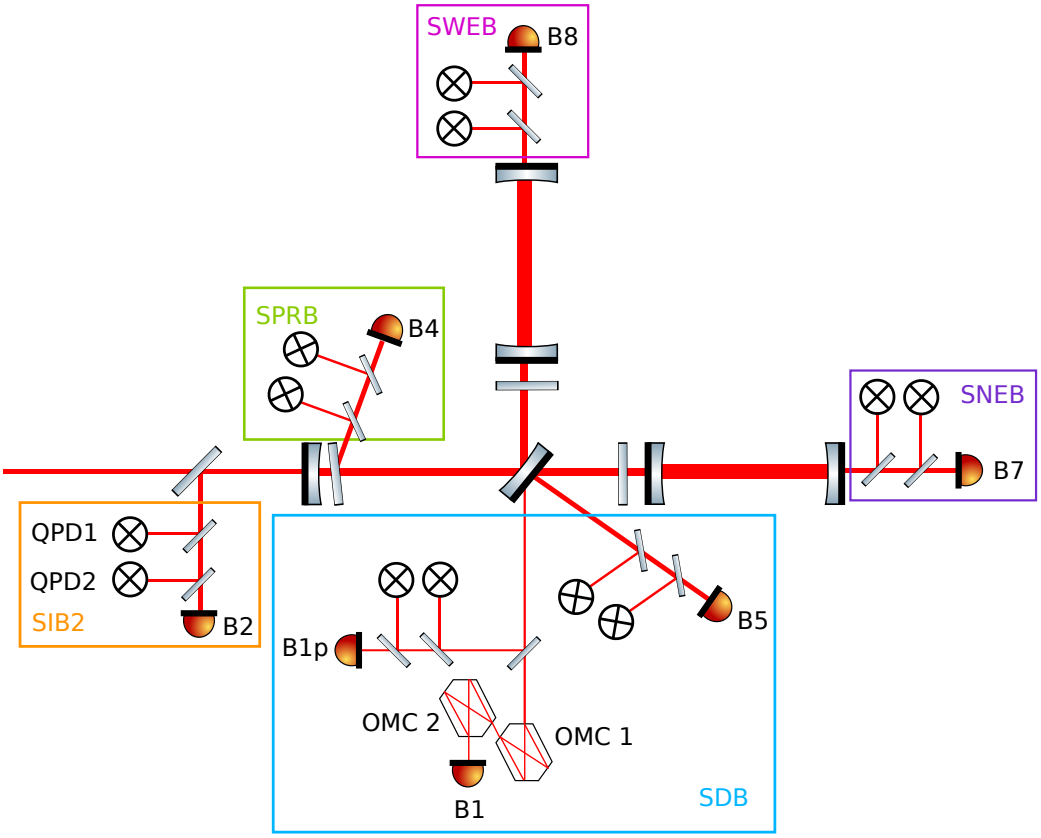

FIGURE 3.3: Scheme of the detection benches and the photodiodes used for the angular and longitudinal controls.

the North Arm cavity, B5 and the beam going to the detection port, B1. There is a wedge[2] at the Beam Splitter mirror in order to help separating both beams. Also, regarding the B1 beam, there are two identical Output Mode cleaners placed in series in order to provide the cleanest beam possible for the DC-readout. Their role is to select the fundamental mode and reject the Higher Order modes and to select the carrier wavelength only, rejecting the sidebands. For the longitudinal and angular controls we use the photodiodes placed before the OMCs. From now on when talking about the B1 photodiode we refer to the B1p one.

Finally, the PDH technique requires the treatment of the signal acquired by each photodiode. In particular it is necessary to *demodulate* the signals to build the error signals. It consists on multiplying each signal by a sine at the modulation frequency. In Virgo the demodulation was done analogically but in Advanced Virgo the demodulation is now done digitally. This allows more flexibility in the error signals available, allowing to demodulate at several different frequencies per photodiode.

In Virgo, one of the limiting technical noises was coming from diffused light. There were several measures in order to mitigate this noise, in particular the installation of *baffles*[3], which is the topic of the SLC subsystem. On its side, the Detection subsystem proposed to suspend the detection benches as well as to put

[2] A wedge in an optic element consists on introducing an angle between its two surfaces.
[3] The baffles are mechanical elements coated with a particular material which absorbs light.

them under vacuum. The suspension is very similar to the one used for the mirrors but smaller. It only has two mechanical filters and the inverted pendulum is shorter as well.

3.6 ISC: Interferometer Sensing and Control

As it was mentioned previously, even with the Local Controls engaged, the optics experience a residual motion that brings the interferometer out of its working point. For this reason an active control is needed to act on the optics and keep them on the desired position. In Advanced Virgo there are 4 longitudinal degrees of freedom (DOFs) and 16 angular DOFS to be controlled.

An active control or feedback loop needs an error signal to provide permanent information about the position of the optics with respect to the working point. The group of error signals used to control the DOFs is called sensing, and one of the tasks of this subsystem is to find the optimal one for each of them.

Then the error signal is sent to a controller or digital filter that calculates the correction needed to bring the mirrors to their working point. This correction is sent to the appropriate actuators: the coils that act on the magnets glued to the mirrors or to the marionetta. The design of the control filters and the choice of actuators or driving is as well a task of the ISC subsystem.

During my thesis I have participated to the design and commissioning of this subsystem. This has implied both simulation and implementation work on the longitudinal and angular loops, as well as on the Second Stage of Frequency Stabilization. The results of my work will be presented in detail in this document.

3.7 DAQ: Data Acquisition

This subsystem takes care of the exchange and processing of the data that are generated in the interferometer. The scheme shown in 3.4 gives a simplified overview of the DAQ subsystem. Some of its tasks are:

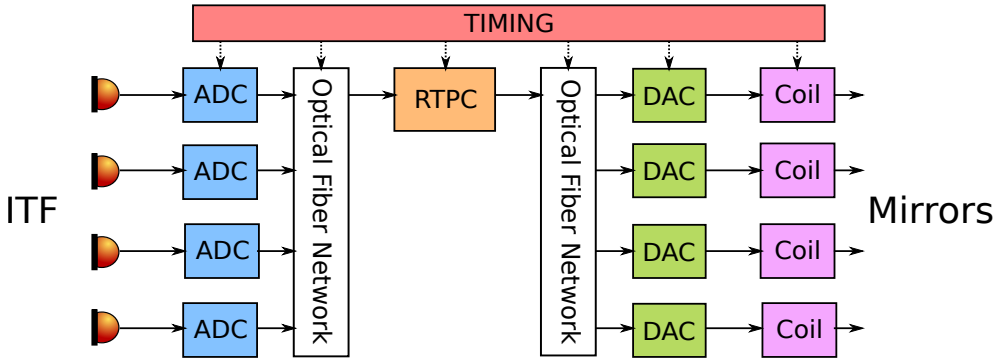

FIGURE 3.4: Scheme of the DAQ chain for the ISC part from the digitization of the photodiode signals until the analogic conversion of the corrections sent to the mirror actuators.

- **Digitization electronics** between the photodiodes electronics and both the Data Acquisition system and the control loops: Analog to Digital converters (ADC) and Digital to Analog converters (DAC). Their actuation is limited to ± 10 V.

- **Online software and communication between online processes.** This software allows to implement the digital control loops including the logic and the control filters, and to inject noise. This software runs in a series of real time computers (RTPCs) whose sampling frequency is 10 kHz. The communication between processes has an important role since any delay will have a direct impact on the stability of the controls, as we will see in the next chapter.

- **DAQ:** It collects all the information generated in the interferometer and it is used for monitoring its behaviour. The data are available online, but they are also stocked for offline analysis. This is specially useful during the commissioning period and there are three different data streams: *raw data*, which stores the data at 10 kHz during 6 months, *50 Hz data*, which stores the data at 50 Hz during 1 year, and *trend data*, which stores the data at 1 Hz during 3 years.

- **Timing system** to synchronize the ITF controls and the readout systems.

- **Cameras** for beam imaging at strategic places such as the detection benches and for the Local Controls.

- **SSFS DSP**. The Second Stage of Frequency Stabilization is a particular control loop which needs to work with a very low delay, which means at very high sampling frequency, $\sim$1 MHz. A specific Digital Signal Processor (DSP) is being developed to take care of this particular loop.

Chapter 4

Fabry-Perot cavities in Advanced Virgo

So far the working principle of the Advanced Virgo detector has been presented, as well as a detailed overview of its different subsystems. This chapter will give a detailed description of the Advanced Virgo Fabry-Perot arm cavities, introducing the basic concepts needed to understand the challenges of their commissioning. Starting from the general properties of a Fabry-Perot cavity, the aim is to present the particular problematic linked to their opto-mechanical characteristics and to motivate the choice of the experimental techniques that will be used to bring them to their optimal working point.

4.1 Basic properties

An optical resonator is an arrangement of mirrors that allows light to circulate in a closed path. The simplest kind of optical resonator consists of two reflecting mirrors facing each other at a distance L, and it is also known as *Fabry-Perot cavity*.

The complex amplitude of the electromagnetic wave resonating inside the cavity (E_{cav}) can be calculated as well as the one of the transmitted (E_{tr}) and reflected (E_{ref}) electromagnetic waves.

The convention that will be used here to indicate the phase shift of π that experiences the reflected field when travelling from the medium with the lower refraction index to the medium with the higher refraction index will be E_{ref} = -r $\cdot$ E_{in}.

For a cavity with two mirrors (M_1, M_2) with reflection coefficients r_1, r_2, transmission coefficients t_1, t_2 separated by a distance L (see Figure 4.1), the electromagnetic field at different points can be written as:

- $E_2 = t_1 \cdot E_1$ - $r_1 \cdot E_6$
- $E_3 = E_2 \cdot e^{ikL}$
- $E_4 = t_2 \cdot E_3$
- $E_5 = -r_2 \cdot E_3$
- $E_6 = E_5 \cdot e^{ikL}$
- $E_7 = r_1 \cdot E_1 + t_1 \cdot E_6$

where E_1 is the input field and k is the wavenumber.

It is worth saying that the reflected field, E_7, has two contributions: one coming from the directly reflected beam and the second one coming from the field inside the cavity being transmitted through the input mirror. This intra-cavity field is the result of the interference between the partial waves that are circulating inside the cavity. Every time a partial wave makes a round trip it acquires a phase

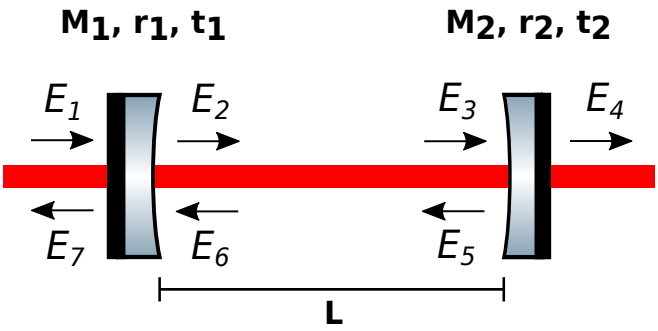

FIGURE 4.1: Scheme of a Fabry-Perot cavity. Notice that the reflective part of the mirror, its coating, is placed in the curved part.

shift of 2kL. The transmitted field instead is equal to the intra-cavity field after being transmitted through the end mirror.

Starting from the expressions above the equations of interest can be derived:

- Intra-cavity field (E_2):

$$E_{cav} = E_1 \cdot \frac{t_1}{1 - r_1 \cdot r_2 \cdot e^{2ikL}} \tag{4.1}$$

- Reflected field (E_7):

$$E_{ref} = E_1 \cdot \left[\frac{r_1 - r_2 \cdot (r_1^2 + t_1^2) \cdot e^{2ikL}}{1 - r_1 \cdot r_2 \cdot e^{2ikL}} \right] \tag{4.2}$$

- Transmitted field (E_4):

$$E_{tr} = E_1 \cdot \frac{t_1 \cdot t_2 \cdot e^{ikL}}{1 - r_1 \cdot r_2 \cdot e^{2ikL}} \tag{4.3}$$

However, these expressions are the complex amplitude of the respective fields while in practice the measurable quantity is the power. So starting from Equation 4.3 the power transmitted by a Fabry-Perot cavity can be written as:

$$P_{tr} = E_{tr} \cdot E_{tr}^* = P_{in} \cdot \frac{t_1^2 \cdot t_2^2}{1 + r_1^2 \cdot r_2^2 - 2 \cdot r_1 \cdot r_2 \cdot \cos(2kL)} \tag{4.4}$$

This expression is also known as the *Airy function* (see Figure 4.2) and it depends on the phase accumulated during one round-trip, *2kL*. This function contains all the relevant information that can be extracted from a Fabry-Perot cavity [22].

- **Resonance condition:** when the phase shift after one round trip corresponds to an integer multiple of 2π their interference is constructive and the cavity is on resonance.

$$\Delta\phi = 2 \cdot k \cdot L = n \cdot 2 \cdot \pi \tag{4.5}$$

Figure 4.2 shows that this phase shift corresponds to a maximum on the transmitted power. When substituting in Equation 4.1 and Equation 4.2 it can be seen that it also corresponds to a maximum of the intra-cavity power

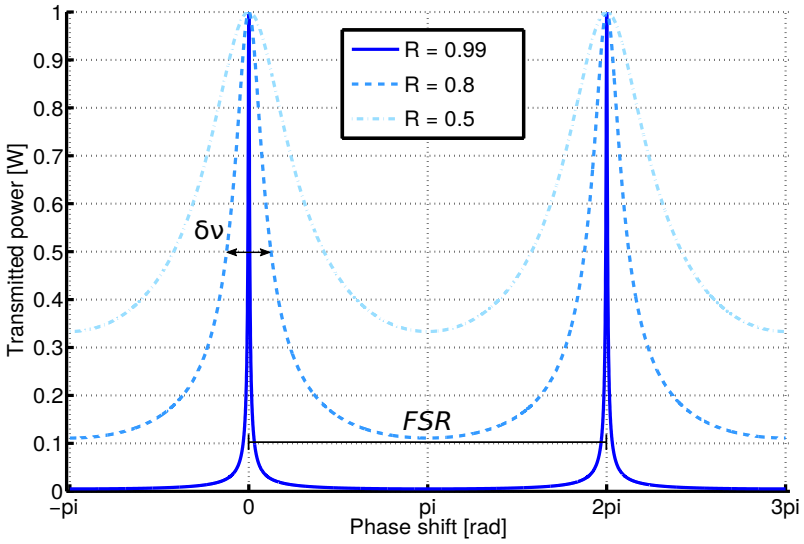

FIGURE 4.2: Power transmitted by a Fabry-Perot cavity as a function of the phase shift accumulated in a round-trip shows an Airy function. In the figure three different cavity configurations are shown: R=r_1^2=r_2^2=0.99, R=0.8, R=0.5. No losses were considered (T+R=1). $\delta\nu$ is the cavity linewidth and FSR the free spectral range.

and a minimum of the reflected power. As the aim of adding Fabry-Perot cavities on the arms is to enhance the optical path this is the working point on which we are interested, because it corresponds to the maximum number of round trips travelled by the light.

- **Free Spectral Range:** is the frequency difference between two consecutive resonances.

$$FSR = \Delta\nu = \frac{c}{2 \cdot L} \tag{4.6}$$

- **Linewidth:** it is the full width at half maximum (see Figure 4.2), and it is related to the pole frequency of the cavity such that f_p = FWHM/2. It can be calculated from the condition $P_{tr}(\omega_{1/2}) = \cdot P_{tr}(\omega = 0)/2$ obtaining:

$$\delta\nu = \frac{2 \cdot \omega_{1/2}}{2 \cdot \pi} = \frac{FSR}{\pi} \cdot \arccos\left(-\frac{1 + r_1^2 \cdot r_2^2 - 4 \cdot r_1 \cdot r_2}{2 \cdot r_1 \cdot r_1}\right) \tag{4.7}$$

where $\omega_{1/2}$ are the frequencies at which the power reaches half of its maximum value.

For cavities with high reflectivities ($r_1 r_2 \sim 1$) the small angle approximation for the cosine can be used:

$$\delta\nu \approx FSR \cdot \frac{1 - r_1 \cdot r_2}{\pi\sqrt{r_1 \cdot r_2}} \tag{4.8}$$

The linewidth depends on the reflectivities of the mirrors so that it becomes smaller when r_1 and r_2 become higher, meaning the light makes more round-trips inside the cavity.

- **Finesse:** it is the ratio between the free spectral range and the linewidth of the cavity.

$$\mathcal{F} = \frac{FSR}{\delta\nu} \approx \frac{\pi\sqrt{r_1 \cdot r_2}}{1 - r_1 \cdot r_2} \tag{4.9}$$

  This is an important parameter, and it can be used to re-write the expression of the transmitted power of the cavity, Equation 4.4:

$$P_{tr} = P_{in} \cdot \frac{t_1^2}{(1 - r_1 \cdot r_2)^2} \cdot \frac{t_2^2}{1 + \left(\frac{2\cdot\mathcal{F}}{\pi}\right)^2 \sin^2(kL)} \tag{4.10}$$

- **Storage time:** it is the mean time of storage of a photon inside a cavity before it escapes through one of the mirrors. It can be calculated from the relationship between the linewidth of the spectrum of an exponentially decreasing electromagnetic wave and the decay time:

$$\tau = \frac{1}{\pi \cdot \delta\nu} = \mathcal{F} \cdot \frac{2 \cdot L}{c \cdot \pi} \tag{4.11}$$

  As τ is related to the finesse of the cavity it can be used in order to measure it experimentally by suddenly stopping the power arriving to the cavity and measuring the exponential decay of the transmitted power.

4.1.1 Types of cavity

Depending on the field reflected by the cavity (Equation 4.2), in particular on its numerator, three types of cavity can be distinguished:

- *Undercoupled:* when r_1 - r_2·(1 - L_1) > 0
- *Critically coupled:* when r_1 - r_2·(1 - L_1) = 0
- *Overcoupled:* when r_1 - r_2·(1 - L_1) < 0

where L_1 are the losses at the input mirror, $r_1^2 + t_1^2 + L_1 = 1$. Figure 4.3 shows how the transmitted, reflected and intra-cavity fields change for each type of cavity. For a matter of simplicity the losses have been set to zero.

In a critically coupled cavity the power transmitted by the input mirror equals the cavity losses in one round-trip [23]. This means that at resonance all the input power is transmitted and no power is reflected, which is a good example of Impedance Matching.

Regarding the phase evolution of the electromagnetic fields it can be seen that in all cases the phase is almost constant when not resonant but it experiences a jump around the resonance. This property is very important as it will be seen later (see Section 4.4.2).

The configuration which is particularly interesting for the Advanced Virgo optical design is the overcoupled one. It is the configuration whose reflected field suffers the most violent phase change around resonance, which makes it very sensitive to length variations. Since this is the aim of having Fabry-Perot cavities on the arms, this is the configuration chosen for Advanced Virgo, with nominal transmission coefficients $T_{input} = 0.01375$ and $T_{end} = 4.4{\cdot}10^{-6}$, and nominal (maximum) losses of $37.5{\cdot}10^{-6}$. From Equation 4.9 the nominal finesse of the arm cavities can be calculated, $F_{arm} \approx 454$. Notice as well that this is the configuration which amplifies the most the stored power.

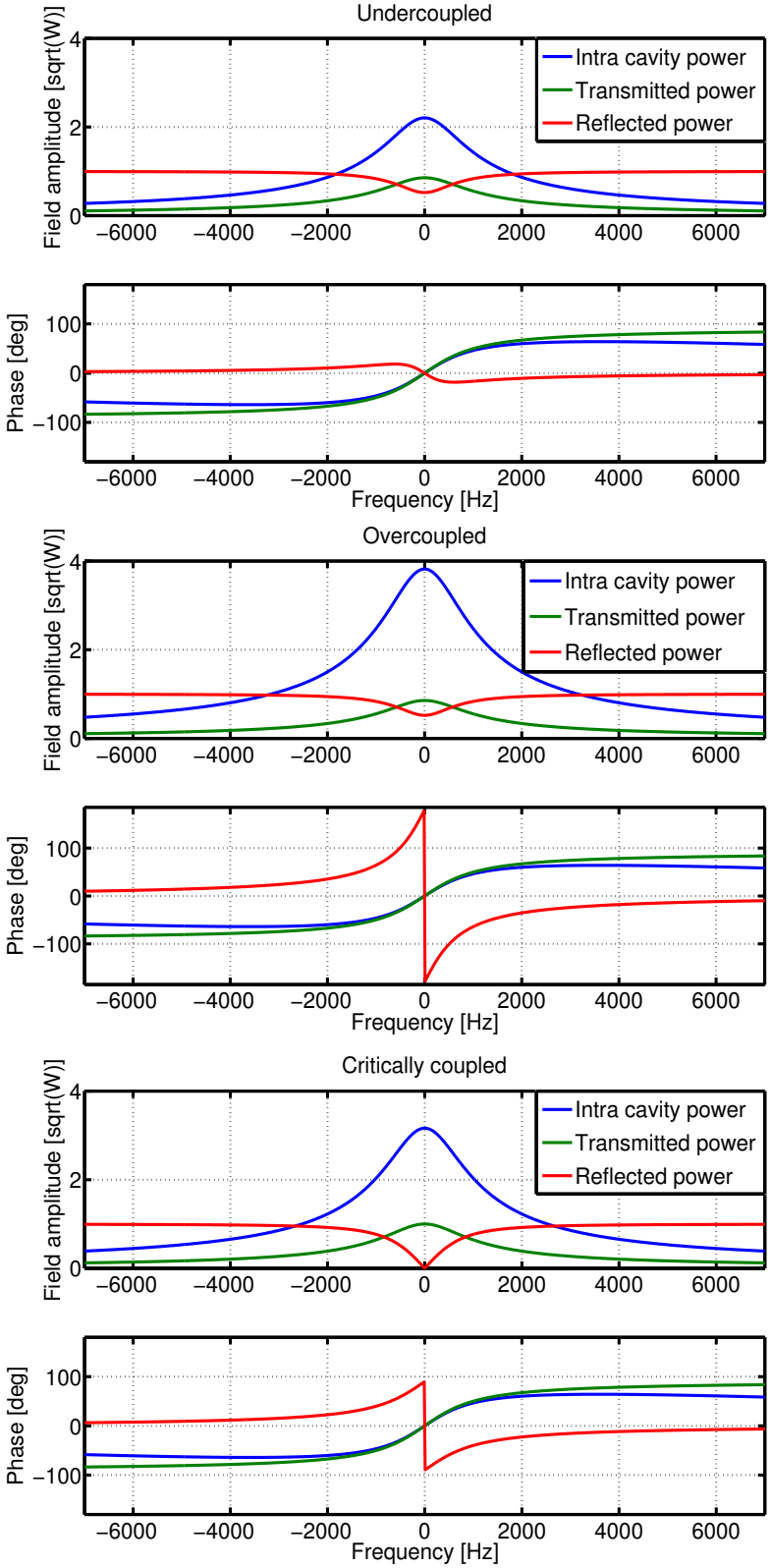

FIGURE 4.3: Intra-cavity, reflected and transmitted field amplitude and phase as a function of the laser frequency detuning. Three different cavities are presented, in all cases with $T_1+T_2=0.20$ (losses set to zero), from top to bottom: undercoupled, overcoupled and critically coupled.

4.2 Dynamical effects

So far the general features of Fabry-Perot cavities have been introduced. In this section the evolution of the electromagnetic fields of the cavity when a mirror is moving will be presented. It is specially relevant in our case because the mirrors are suspended and so free to move. Since seismic noise causes the mirrors to move by approximately 1μm rms with a velocity of $\sim 1\mu$/s, it is interesting to study the dynamical effects derived.

Let's suppose that one of the mirrors of the cavity is moving so that its position is given by the function X(t) as shown in Figure 4.4. The path traversed by the

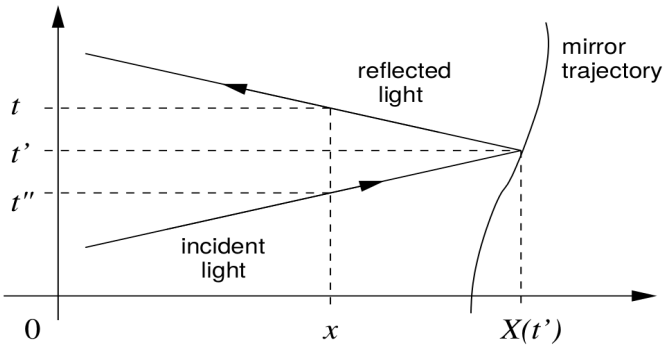

FIGURE 4.4: Reflected light from a moving mirror [24].

light is defined by the position of the mirror when the light arrives to its surface in which is given by X(t'). If a reference $\{x,\ t\}$ is defined, the additional optical path can be written [24]

$$\Delta x = X(t') - x = c \cdot (t - t') \tag{4.12}$$

This Δx translates into an additional phase of the electromagnetic field reflected by the mirror that can be seen as a frequency shift as a consequence of a transfer of energy from the mirror to the wave. This new frequency can be calculated by deriving the phase:

$$\phi(t) = \omega_0 \cdot t - 2 \cdot k \cdot X(t'); \qquad \phi'(t) = \omega_0 - 2 \cdot k \cdot \frac{dX}{dt'} \cdot \frac{dt'}{dt} \tag{4.13}$$

where ω_0 is the nominal frequency of the laser and k is the wavenumber. $\frac{dt'}{dt}$ can be derived from Equation 4.12 obtaining the final expression:

$$\phi'(t) = \omega_{new} = \frac{c - v_m(t')}{c + v_m(t')} \cdot \omega_0 \tag{4.14}$$

where v_m is the relative velocity of both mirrors or in other words, the cavity velocity.

This expression shows that the movement of a mirror of the Fabry-Perot cavity causes a Doppler effect on the circulating wave. For low velocity motions such as the ones expected for Advanced Virgo in free motion (around 1.5μm/s) the reflection can be considered as instantaneous (c » v_m and so t = t') and the

previous expression can be simplified by writing everything as a function of t:

$$\omega_{new} = [1 - 2 \cdot \frac{v_m(t)}{c}] \cdot \omega_0 \tag{4.15}$$

For a mirror speed of 1μm/s, the Doppler effect induced is very small (around 1Hz). However, this effect will accumulate on each round-trip and for high finesse cavities it can be of the order of magnitude of the linewidth causing dynamical effects. The total frequency shift induced by the Doppler effect can be calculated as the product of the $\delta\omega$ experienced in one round-trip times the effective number of round-trips made by a photon (N_{eff}). Knowing that N_{eff} is related to the storage time so that $\tau = 2 \cdot \frac{L}{c} \cdot N_{eff}$ we can write:

$$N_{eff} \cdot |\delta\omega| = \frac{|v_m(t)| \cdot \omega_0 \cdot \tau}{L} \tag{4.16}$$

The mirror velocity that makes the total Doppler shift equal to the linewidth of the resonance of the cavity can be calculated using Equation 4.16 and Equation 4.11:

$$v_{cr} = \frac{\lambda}{2 \cdot \tau \cdot \mathcal{F}} = \frac{\pi \cdot c \cdot \lambda}{4 \cdot L \cdot \mathcal{F}^2} \tag{4.17}$$

This expression gives the *critical velocity* of the mirror from which dynamical effects start to be relevant. For Advanced Virgo arm cavities, this v_{cr} is 0.4 μms^{-1}.

Now we are going to study how this dynamical effects impact the fields in the Fabry-Perot cavity. Let's suppose that both mirrors of a Fabry-Perot cavity are moving around the nominal length L, as shown in Figure 4.5. The total distance travelled by a photon at any time can be defined as:

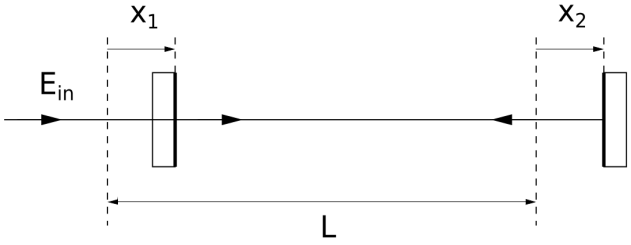

FIGURE 4.5: Scheme of a Fabry-Perot cavity whose mirrors are moving around a reference point [24].

$$d(t) = L + x_2(t - T) - x_1(t) = L + \xi(t) \tag{4.18}$$

where T is the time needed for a photon to go from one mirror to the other, T = L/c. The total distance can be written as a fixed part, which is the one that determines the interference conditions, and a variable part that affects the dynamics of the cavity.

Now the intra-cavity field can be re-written taking into account the variable optical path due to the mirror movement:

$$E_{cav}(t) = t_1 \cdot E_{in} + r_1 \cdot r_2 \cdot E_{in} \cdot e^{2ikd(t)} \tag{4.19}$$

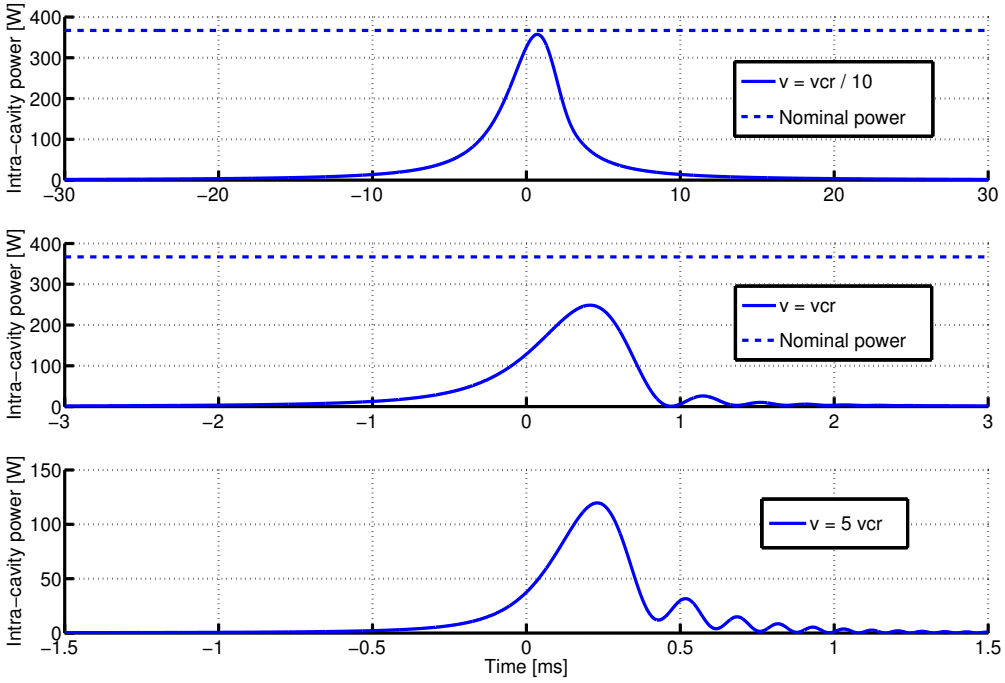

FIGURE 4.6: Intra-cavity power as a function of time for three different velocities of the cavity with respect to the critical velocity, v_{cr}. The dashed line represents the intra-cavity power reached by a cavity which is not moving and whose maximum power is reached at 0. Notice that the y-axis are not the same and so the maximum power of the peaks decreases considerably when the cavity velocity increases. Also the position if the maximum is shifted with respect to the static case.

In order to determine the total optical path, the number of round-trips made has to be considered, so we can write the Intra-cavity field expression after N round-trips:

$$E_{cav}(t) = t_1 \cdot E_{in} \sum_{n=0}^{N-1} (r_1 \cdot r_2)^n \cdot e^{-2ikS_n(t)} + E_{in} \cdot (r_1 \cdot r_2)^N \cdot e^{-2ikS_N(t)} \tag{4.20}$$

where S_n is the partial sum of the length traversed by the photons, or in other words, the total optical path after n round-trips:

$$\begin{aligned} S_n(t) &= \sum_{m=0}^{n-1} d \cdot (t - 2 \cdot T \cdot m) = v_m \sum_{m=0}^{n-1} [t - (2 \cdot m + 1) \cdot T] \\ &= v_m \cdot n \cdot t - v_m \cdot n^2 \cdot T \end{aligned} \tag{4.21}$$

Equation 4.20 can be simplified if we are in the *large-N limit*, which means for a number of round-trips N much higher than N_{eff}, when this expression becomes exact:

$$E_{cav}(t) = t_1 \cdot E_{in} \sum_{n=0}^{\infty} (r_1 \cdot r_2)^n \cdot e^{-2ikS_n(t)} \tag{4.22}$$

This expression can be re-written in order to take into account the general expression for the finesse of an optical cavity[1]:

$$\mathcal{F} = \frac{-2 \cdot \pi}{\ln(r_1 r_2)} \tag{4.23}$$

Including also the storage time (Equation 4.11) we can write:

$$E_{cav}(t) = t_1 \cdot E_{in} \sum_{n=0}^{\infty} e^{i(2kv_m T n^2 \; - \; 2kv_m tn) \; - \; 2Ln/c\tau} \tag{4.24}$$

This equation describes the behaviour of the intra-cavity field considering the mirror movement and so accounting for dynamical effects. Figure 4.6 shows the behaviour of the intra-cavity field for different velocities of the mirrors with respect to the critical velocity, v_{cr}.

The oscillations that appear once the resonance is passed when the speed of the cavity is above v_{cr} are known as *ringing*. Even when the cavity movement is very slow the resonance peak shape is changed and the power build-up in the cavity is not complete. The mirror movement impacts as well the transmitted and reflected fields.

4.3 Gaussian optics

4.3.1 Generalities and definitions

So far we have only considered the axial properties of the electric field on a Fabry-Perot cavity, describing them as a function of the frequency and the position along the optical axis, z. However in order to have a more complete description of the optical resonator we need to consider the transverse beam geometry. Now, in order to do this we will describe the spatial part of the electric field as:

$$E(x, y, z) = u(x, y, z) \cdot e^{-ikz} \tag{4.25}$$

where *u(x,y,z)* is a complex scalar wave amplitude that describes the transverse beam shape. In order to find a solution for *E(x,y,z)* we need to solve the scalar wave equation:

$$[\bigtriangledown^2 + k^2] \cdot E(x, y, z) = 0 \tag{4.26}$$

Substituting Equation 4.25 on the wave equation we obtain:

$$\frac{\partial^2 u}{\partial x^2} + \frac{\partial^2 u}{\partial y^2} + \frac{\partial^2 u}{\partial z^2} - 2 \cdot i \cdot k \cdot \frac{\partial u}{\partial z} = 0 \tag{4.27}$$

This expression can be simplified for our particular case in which our source is a laser beam. Lasers are a special type of electromagnetic waves characterised by their low diffraction [23]. This means that their width in the transverse plane, w is smaller than a characteristic length along the propagation axis, l, where the properties of the beam do not change much. For this special case when w/l is small it can be considered that *u(x,y,z)* varies very slowly with z and so the second derivative in z can be neglected. This is called *paraxial approximation* which leads

[1] When presenting the basic properties of Fabry-Perot cavities in Section 4.1, the expression of the finesse for cavities with high reflectivities was introduced for being the most commonly used. Here we use the general expression instead, valid for no matter which type of cavity [25].

to the *paraxial wave equation*:

$$\frac{\partial^2 u}{\partial x^2} + \frac{\partial^2 u}{\partial y^2} - 2 \cdot i \cdot k \cdot \frac{\partial u}{\partial z} = 0 \tag{4.28}$$

Solving *u(x,y,z)* for this equation will give an expression that describes the transverse properties of a paraxial beam. The simplest solution is a Gaussian function and it is given by

$$u(x, y, z) = \sqrt{\frac{2}{\pi}} \cdot \frac{1}{w(z)} \cdot \exp(i\Psi(z)) \cdot \exp\left(-ik\frac{x^2 + y^2}{2R(z)} - \frac{x^2 + y^2}{w^2(z)}\right) \tag{4.29}$$

where *w(z)* is the *beam size*, which is the transverse distance where the intensity of the beam is reduced to 1/e of the maximum at a given point z, *R(z)* is the *radius of curvature* of a wavefront intersecting the axis at a position z and $\Psi(z)$ is an extra phase shift along the z-axis called the *Gouy phase*. Their expressions will be written later on.

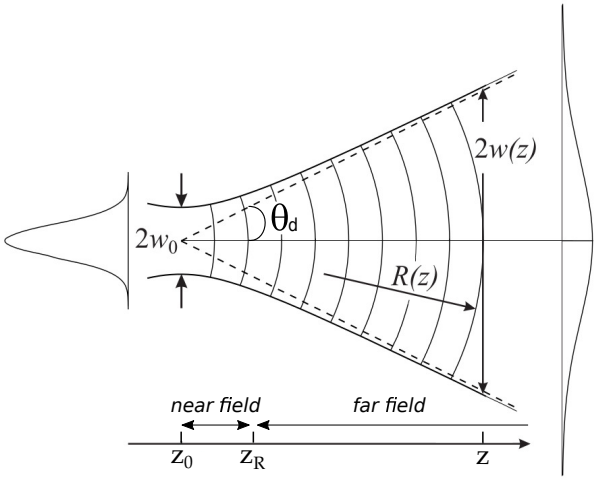

FIGURE 4.7: Evolution of a Gaussian beam along the z-axis (modified from [22]).

From this expression it can be understood that the transversal intensity profile is a 2D Gaussian distribution, which gives the name to the beam that describes, *Gaussian beam*. However, there is another representation that gives useful information about the evolution of a Gaussian wave, which is the beam size as a function of the position along the optical axis and it is shown in Figure 4.7. For a given wavelength λ the Gaussian beam profile is completely determined by two parameters: *beam waist* w_0, which is the minimum beam size, and z_0 which is the *beam waist position* on the optical axis.

A Gaussian beam can be divided along the z-axis in two sections (see Figure 4.7) separated by a parameter called *Rayleigh range,* z_R which can be related to the waist:

$$z_R = \frac{\pi \cdot w_0^2}{\lambda} \tag{4.30}$$

These two regions are: *near field*, when $z_R > z$, which is the region around the beam waist and *far field*, when $z_R < z$, which is the region far from the waist where the transverse expansion of the beam becomes more noticeable.

At this point some useful parameters of Gaussian beams can be defined:

- Beam size, *w(z)*:

$$w(z) = w_0 \cdot \sqrt{1 + \left(\frac{z - z_0}{z_R}\right)^2} \tag{4.31}$$

  which in the far-field (z » z_R, z_0) becomes

$$w(z) \approx w_0 \cdot \frac{z}{z_R} = \frac{z \cdot \lambda}{\pi \cdot w_0} \tag{4.32}$$

- Radius of curvature, R(z):

$$R(z) = z \cdot \left[1 + \left(\frac{z_R}{z}\right)^2\right] \tag{4.33}$$

- Divergence, θ_d: angle between the optical axis and the beam size in the far-field.

$$\theta_d = \arctan\left(\frac{w_0}{z_R}\right) \approx \frac{w_0}{z_R} \tag{4.34}$$

- Gouy phase, $\Psi(z)$: it describes the extra longitudinal phase that acquires a Gaussian beam with respect to a plane wave.

$$\Psi(z) = \arctan\left(\frac{z - z_0}{z_R}\right) \tag{4.35}$$

4.3.2 Higher Order Modes

The pure Gaussian solution of the paraxial equation that has been described in the previous section is not the only possible solution for Equation 4.28. Instead it can be found a special set of functions (infinite, countable and complete) that are an exact solution of the paraxial wave equation and which are called **T**ransverse **E**lectromagnetic **M**odes (TEM). Indeed the product of two Hermite polynomials ($H_m(\sqrt{2}\frac{x}{w})$, $H_n(\sqrt{2}\frac{y}{w})$) and a Gaussian function to describe u_{nm}(x,y,z) gives an exact solution of the paraxial wave equation and forms a set of TEM called *Hermite-Gauss modes*. The general expression is given by:

$$\begin{aligned} u_{nm}(x,y,z) &= u_n(x,z) \cdot u_m(y,z) \\ &= (2^{n+m-1}\ n!\ m!\ \pi)^{-1/2} \cdot \frac{1}{w(z)} \cdot \exp(i(n+m+1)\Psi(z)) \cdot \\ &\quad H_n(\sqrt{2}\frac{x}{w}) \cdot H_m(\sqrt{2}\frac{y}{w}) \cdot \exp\left(-ik\frac{x^2+y^2}{2R(z)} - \frac{x^2+y^2}{w^2(z)}\right) \end{aligned} \tag{4.36}$$

where n and m are the indexes that define the Hermite polynomials, which are called *mode numbers* and refer to the number of zeros of the polynomial in the corresponding direction (x or y). The first two Hermite polynomials are:

$$H_0(x) = 1; \quad H_1(x) = 2 \cdot x \tag{4.37}$$

Using these expressions the rest of the Hermite polynomials can be calculated with the recurrence relation

$$H_{n+1}(x) = 2 \cdot x \cdot H_n(x) - 2 \cdot n \cdot H_{n-1}(x) \tag{4.38}$$

Hence, the TEM_{00} corresponds to the Gaussian profile that was described in the previous section. The TEMs that have n+m > 0 are also called *Higher Order Modes* (HOMs), where n+m represent the order of the mode. As previously mentioned these mode numbers represent the number of zeros on the Hermite polynomials. This translates in a dark fringe on the transverse profile of the beam. Figure 4.8 shows the intensity distribution of different TEMs. Notice as well that the phase shift for the HOMs due to the propagation on the z-axis is higher than for the TEM_{00} and it is given by $\psi =$ (n+m+1) $\Psi(z)$.

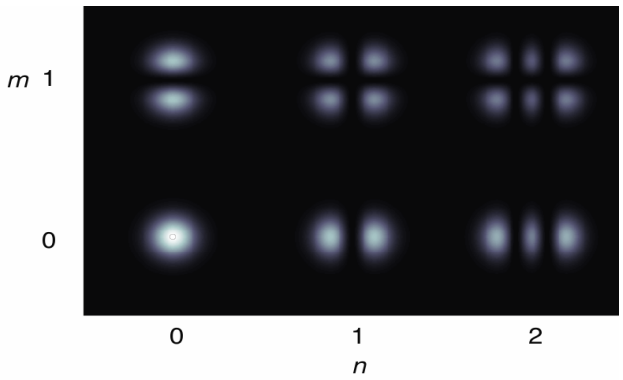

FIGURE 4.8: Intensity profile of several Hermite-Gauss HOMs, u_{nm}. As the order increases, the intensity peak decreases and the surface increases. The TEM_{00} has the smallest intensity profile [23].

Regarding a linear optical resonator with two concave mirrors, such as the one of Advanced Virgo, the eigenfrequencies of the HOMs depend on the radius of curvature of the mirrors as well as the length of the cavity. They are given by the following expression [22]:

$$\nu_{mnq} = \frac{c}{2 \cdot L} \cdot \left[q + \frac{(m+n+1)}{\pi} \cdot \arccos\left(\sqrt{\left(1 - \frac{L}{R_1}\right)\left(1 - \frac{L}{R_2}\right)} \right) \right] \tag{4.39}$$

where q is an integer that indicates all the possible resonance conditions. Notice that for m = n = 0, so the TEM_{00} or *fundamental mode*, we find the axial modes that depend only on the optical length.

Figure 4.9 shows a length scan of one FSR of the North arm cavity of Advanced Virgo. Due to the residual seismic noise, the length of the cavity changes permanently, crossing the resonance condition of the different HOMs. The fundamental mode is the highest peak since it has the strongest coupling to the cavity. Figure 4.9 shows as well HOMs up to order 7, which reach less power since they couple more weakly. The presence of HOMs indicate that the beam is not perfectly adapted to the cavity (misalignment, mismatch, other optical defects and so on). Since the scan is done by the free mirrors, there is ringing on all of the peaks due to the high mirror velocity.

The Hermite-Gauss modes are not the only set of TEM that solve the paraxial equation. Another set commonly used are the *Laguerre-Gauss modes*, that uses the Laguerre polynomials. The choice of basis depends on the physical phenomena to be studied. For example Laguerre-Gauss are often used to study the mode-matching, that is how the beam size matches the cavity geometry. The Hermite-Gauss basis is used instead to study the alignment of a cavity. In Section 4.5 it will be explained how these HOMs are originated by the cavity.

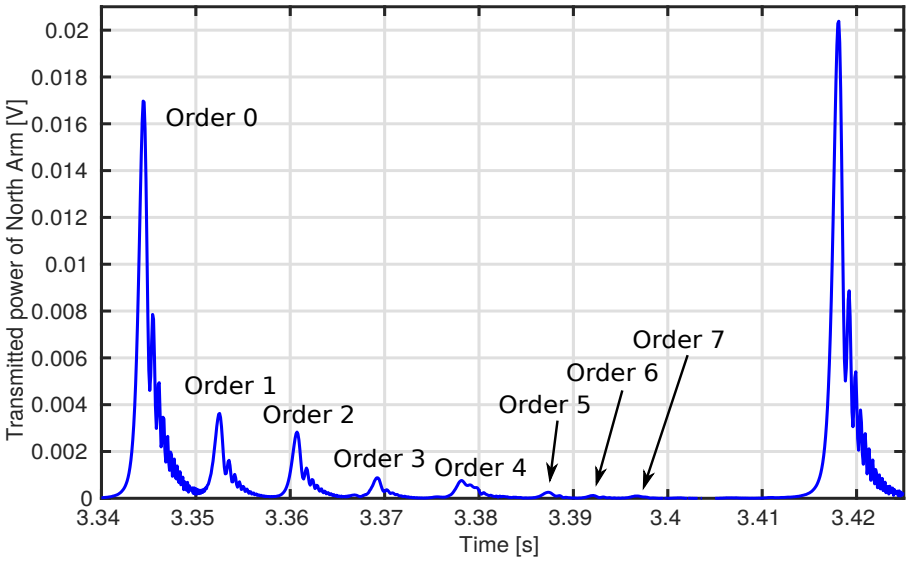

FIGURE 4.9: Transmitted power during a scan of the North Arm Cavity length. The two highest peaks correspond to the fundamental mode, meanwhile the smaller peaks are the HOMs. The closer peak to the TEM_{00} correspond to the first HOM, the second closer to the second HOM and so on. HOMs can be seen up to the seventh order, even if the two last are very small.

4.3.3 Stability of a resonator

As it was explained at the beginning of this Section 4.3, a Gaussian beam is defined by its waist w_0 and its position z_0. For a Gaussian beam to be resonant in a Fabry Perot cavity the radius of curvature of the mirrors (RoC) has to be matched exactly to the wavefront of the Gaussian beam when impinging on them. This way the mirrors will reflect the beam exactly as when it arrived but with reversed wavefront, curvature and direction.

Taking into account the previous consideration, for a given optical resonator with mirrors of RoC R_1 and R_2 and separated by a length L, the parameters that match the Gaussian beam to the optical resonator can be calculated (see Figure 4.10). In particular, it is convenient to write these parameters as a function of the *resonator g parameters*:

$$\begin{aligned} g_1 &= 1 - \frac{L}{R_1} \\ g_2 &= 1 - \frac{L}{R_2} \end{aligned} \tag{4.40}$$

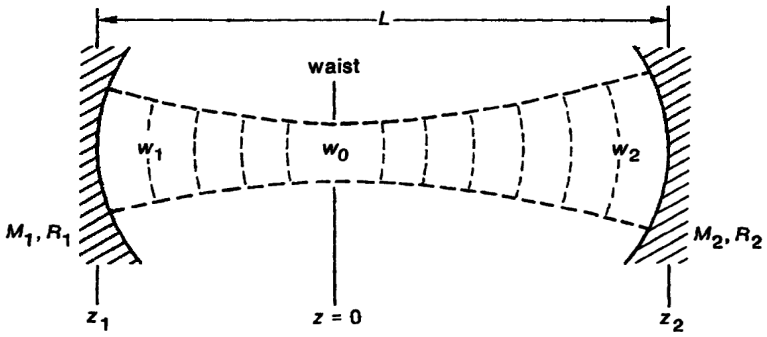

FIGURE 4.10: Scheme of a Fabry-Perot cavity with a Gaussian beam matched to it [26].

It can be proven [26] that in order to obtain real and finite solutions for the Gaussian beam parameters (w_0) and the spot sizes on the mirrors (w_1 and w_2 at the mirror positions z_1 and z_2) the g parameters need to fulfill the following stability condition:

$$0 \leq g_1 \cdot g_2 \leq 1 \tag{4.41}$$

This expression can be written as well as a function of the Gouy phase, Ψ_G, knowing its relationship with the g parameters, $\Psi_G = \arccos(g_1 \cdot g_2)$ as [27]:

$$\pi \leq \Psi_G \leq 0 \tag{4.42}$$

Every optical resonator is characterized by its g parameters and when the previous condition is fulfilled the mirrors form a *stable periodic focusing system*. This stable resonator will have associated a unique set of Gaussian TEM. If this condition is not fulfilled, the mirrors will form an *unstable periodic focusing system* and no Gaussian beam will fit properly into this cavity. With these g factors a stability diagram can be designed as shown in Figure 4.11. All the resonators are represented by a point on this diagram, those who fall within the shadowed region are stable and those which do not are unstable.

4.4 Longitudinal motion Control

In the previous sections the basics of Fabry-Perot cavities have been presented, as well as the particular characteristics of the Advanced Virgo Arm cavities. As mentioned on Section 2.2.2, the aim of having Fabry-Perot cavities on the arms is to increase the sensitivity by maximizing the optical path travelled by the light that resonates inside them. This happens only when the cavities are on a resonance position for the fundamental mode, which will be our desired working point. However, the seismic noise causes the suspended mirrors to move and in consequence the length of the cavity is changing permanently if not controlled. This means that a *longitudinal control* of the cavity is needed in order to actively correct its length and to keep it on resonance. Also, as shown in Equation 2.2 the fluctuations on the frequency of the laser will be seen as length changes and so the control will have to correct for them as well.

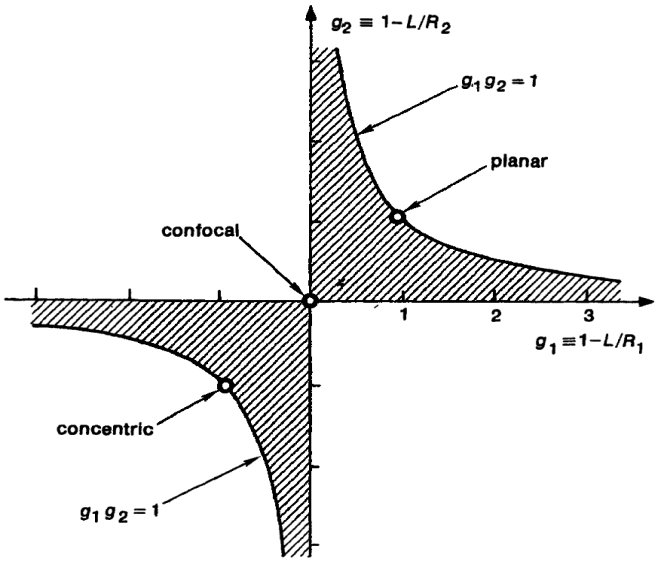

FIGURE 4.11: Stability diagram. It represents the *g-factor* $= g_1 \cdot g_2$ as a function of g_1 and g_2. Each type of cavity can be characterized by a point in this diagram, if it stays within the shadowed region the cavity is stable, meanwhile if it stays outside this region, the cavity will be unstable. [26].

4.4.1 Feedback control loops

Basically, what is needed is information about the cavity length variation to be able to bring it back continuously to its working point. The process of taking the output of a system and feed it back to its input in order to keep it always at a given working point is called a *feedback control loop* [28].

Control theory is widely used in many different domains from engineering to biology, and it has been extensively studied [29]. When applied to Linear Time-Invariant systems, such as the ones we find in interferometric detectors, frequency-domain techniques can be used to understand and predict the behaviour of very complex systems.

A physical system can be characterized by its ability to accept an input parameter and produce an output in response. When the system is linear, the output and input are related by a linear expression. Moreover, if the response of the system is the same independently of the time, we say that it is a *linear time-invariant system (LTI)*. These systems can be described by a differential equation of the type:

$$a_0 \cdot x(t) + a_1 \cdot \frac{dx(t)}{dt} + a_2 \cdot \frac{d^2x(t)}{dt^2} + ... + a_n \cdot \frac{d^n x(t)}{dt^n} = b_0 \cdot y(t) \tag{4.43}$$

where *y(t)* is the input of the system, also known as *forcing funtion* and *x(t)* is the output or *response function*. A well known example of a second order Linear Time-Invariant system is the damped Harmonic Oscillator.

Differential equations of high order can be very complicated to solve in the time domain. Frequency-domain techniques such as the Laplace transform allow us to find the time response of such complex systems, by solving the differential

equation on the s-domain. The Laplace transform is defined by:

$$\mathcal{L}\{f(t)\} = F(s) = \int_0^\infty f(t) \cdot e^{-st} dt \tag{4.44}$$

where $s = \sigma + i\omega$. The integral is single-sided, which makes it perfect to analyse physical systems starting at t=0, because it can take into account initial conditions.

The behaviour of a LTI system on the s-domain is characterized by its *Transfer function (TF)*, which is the ratio between its output and its input both in the s-domain:

$$G(s) = \frac{Output(s)}{Input(s)} = \frac{X(s)}{Y(s)} \tag{4.45}$$

The main advantage of solving a differential equation on the s-domain is that the TF of LTI systems can be described by rational functions, which simplifies considerably the task:

$$G(s) = k \cdot \frac{(s - z_1) \cdot (s - z_2) \cdots (s - z_{N-1}) \cdot (s - z_N)}{(s - p_1) \cdot (s - p_2) \cdots (s - p_{D-1}) \cdot (s - p_D)} \tag{4.46}$$

where *G(s)* is the TF of the system. All the z_i's that cancel the numerator of the TF are called *zeros*, and all the p_i's that cancel the denominator of the TF are called *poles*. Moreover for real (physical) systems, the poles and zeros are real or complex conjugate pairs.

This way of writing a transfer function is commonly referred to as *zpk*, because with the zeros, the poles and the gain (k) you have all the information needed to reconstruct the TF.

In order to simplify the visualization of the shape of a TF, it can be written as a product of, at most, second order polynomials. A first order zero / pole at a given frequency f_0 can be written as [10]:

$$\begin{aligned} Z_1(s) &= s - 2\pi \cdot f_0 \\ P_1(s) &= \frac{1}{s - 2 \cdot \pi \cdot f_0} \end{aligned} \tag{4.47}$$

A simple zero is also known as *differentiator* because in the time domain it derives the input value. On the other hand a simple pole is also called *integrator* because in the time domain it integrates the input value.

A second order zero / pole at f_0 can be written as [10];

$$\begin{aligned} Z_2(s) &= s^2 + \frac{2 \cdot \pi \cdot f_0}{Q} \cdot s + (2 \cdot \pi \cdot f_0)^2 \\ P_2(s) &= \frac{1}{s^2 + \frac{2 \cdot \pi \cdot f_0}{Q} \cdot s + (2 \cdot \pi \cdot f_0)^2} \end{aligned} \tag{4.48}$$

where Q is the quality factor. Notice that a quality factor of 0 will give you a simple zero / pole and a quality factor higher than 0.5 will give you different overshoots before falling as f^2 / f^{-2}, as it can be seen on Figure 4.12.

An example of a system described by a second order pole is the damped Harmonic Oscillator, whose behaviour is determined by the value of its Q: overdamped for $Q < 0.5$, underdamped for $Q > 0.5$ and critically damped for $Q = 0.5$.

This way of writing TF is called *second order section (SOS)* and it is the most commonly used because it is very intuitive to understand the global behaviour of a system from it.

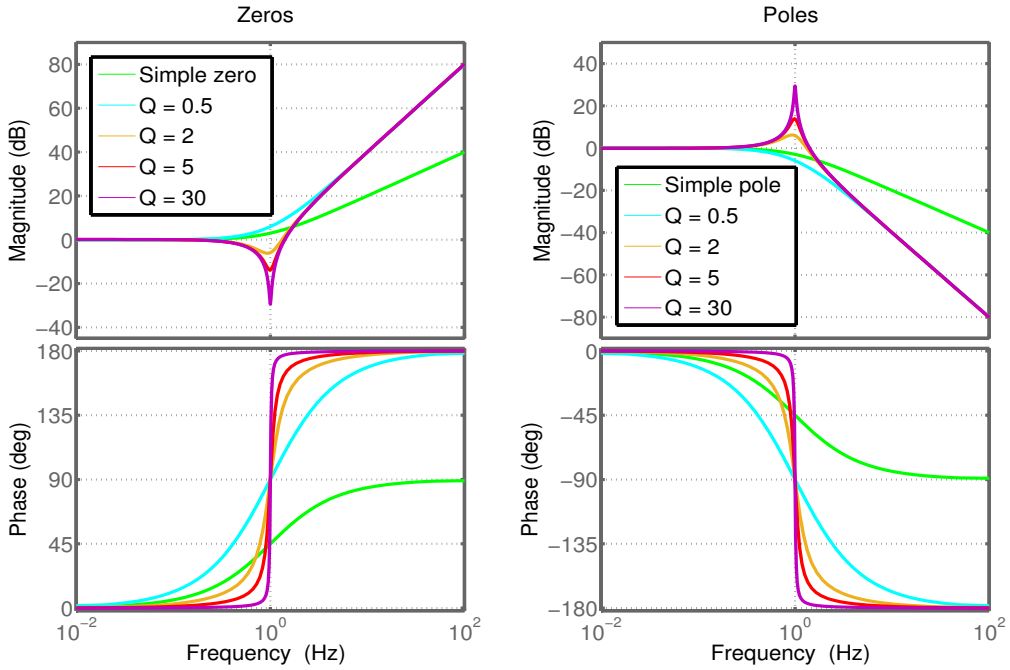

FIGURE 4.12: **Left picture:** Transfer function of a second order system described by a zero with different Q. **Right picture:** Transfer function of a second order system described by a pole with different Q.

An important information provided by the TF of a system concerns its stability. A system is *stable* if, given an arbitrary function as input, the system experiences a transient which reduces with time, leaving the system back to a quiescent state. On the contrary, a system is *unstable* if for an arbitrary input, the system experiences a transient that increases with time, never returning to a quiescent state. This happens when the denominator of the TF goes to zero.

Arm cavity feedback system

Control theory can be applied now to our system of interest: the longitudinal control of a Fabry-Perot cavity. In order to actively correct the position of the mirrors to be permanently on resonance, that is, implement a feedback loop to control the length of the cavity, several elements are needed:

- **System to be controlled or *plant*** .
- **Error signal**: a signal that provides constant information about the parameter to be controlled, in our particular case the length of the cavity and how far it is from resonance. An important characteristic of a good error signal is the bipolarity, meaning that it changes sign around the point of interest, giving information about the sense of the movement. In the case of a Fabry-Perot cavity it is called PDH signal, and it will be explained in detail in the next Section 4.4.2.

- **Feedback filter or corrector**: it is used to calculate the correction needed to bring back the cavity to resonance.
- **Actuator**: it is an element that acts on the plant by applying the correction calculated by the filter and so recovering the working point. In the case of Advanced Virgo the actuators are the coils that act on the magnets which are placed on the mirrors. Their TF is a simple pole given by its particular RLC circuit. However, as the coils act on the mirror movement we need to consider also the mechanical TF of the mirror (see Section AdV).

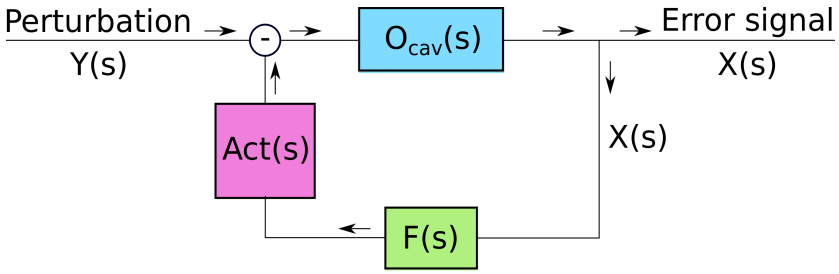

FIGURE 4.13: Scheme of a feedback loop controlling an optical cavity. In the case of the arms of Advanced Virgo the optical cavity is the Fabry-Perot on the arms, the filter calculates the correction needed to bring the cavity on resonance from the error signal and the correction is sent to the coils that act on the magnets placed on the mirror 3.3.

A scheme of this feedback loop can be seen on Figure 4.13. Considering the input function, Y(s), as a perturbation that brings the plant out of its working point and the output function, X(s), as the error signal, it is straightforward to calculate the Transfer Function of the system:

$$TF_{FP}(s) = \frac{X(s)}{Y(s)} = \frac{O_{cav}(s)}{1 + O_{cav}(s) \cdot F(s) \cdot Act(s)} \tag{4.49}$$

This equation gives us the behaviour of the system in *Closed loop*, that is with the feedback loop active. The aim of a feedback loop is to keep the system in a given working state, it will correct for or suppress any perturbation that brings the system out of its working point. As a consequence, the signals of the system in closed loop will be reduced with respect to the uncontrolled state. This suppression factor is called *Closed loop gain* and it gives information about how effective is the control loop, in this case in keeping the cavity in resonance:

$$CL_{gain} = \frac{1}{1 + O_{cav}(s) \cdot F(s) \cdot Act(s)} \tag{4.50}$$

Figure 4.14 shows the transfer function of each element of the loop for the Advanced Virgo arm cavities and its Closed loop gain. It can be understood from the CL_{gain} that the system will be able to act to reduce the input up to a given frequency, which is called *Unity Gain Frequency (UGF)*, where it becomes 1.

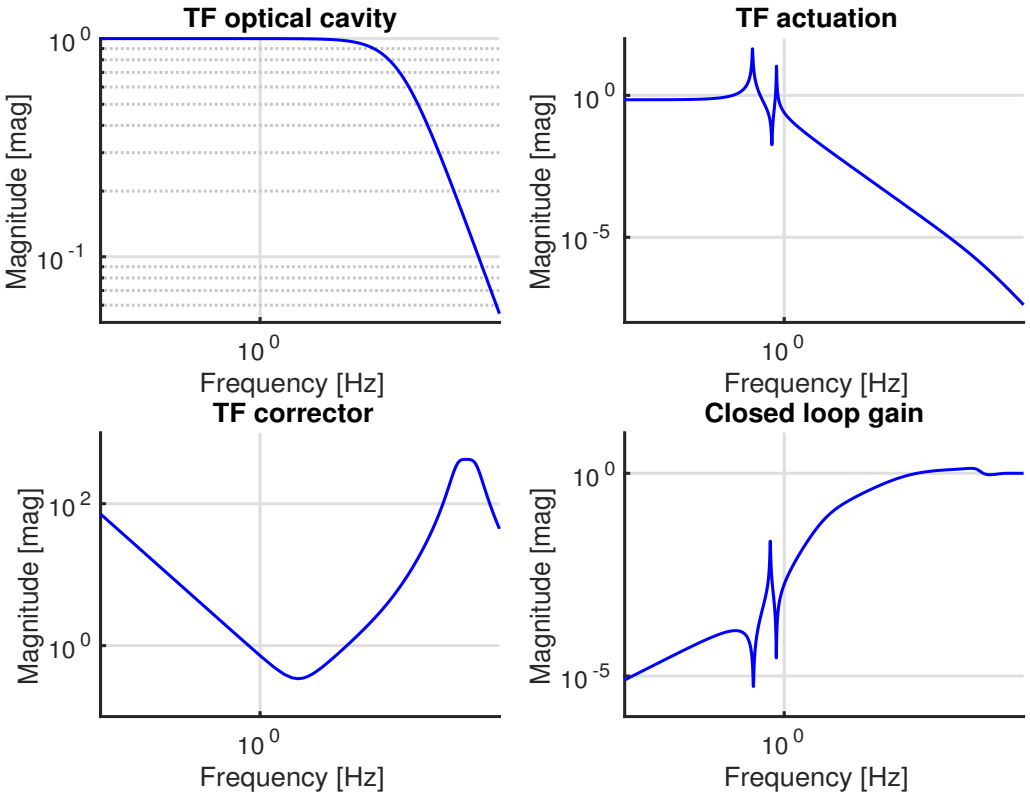

FIGURE 4.14: **Up-left picture:** Transfer function of a Fabry Perot cavity of 3km (normalized). **Up-right picture:** Transfer function of the actuation of AdV including the coil and the mechanics of the suspension of the mirror, which explains the two resonances that are visible. **Down-left picture:** Transfer function of an example of stable corrector for this system. **Down-right picture:** Suppression factor of the system.

Regarding the stability, it can be seen on the denominator of Equation 4.49 that whenever the product $O_{cav}(s) \cdot F(s) \cdot Act(s)$ becomes -1, the TF will be infinite, that is, the system will become unstable. This product of the individual TF of the elements of the system is called *Open loop Transfer Function* (OLTF), which corresponds to the system when the feedback is disconnected from the input. Figure 4.15 shows the OLTF of the feedback loop of one of the arm cavities of Advanced Virgo.

In order to determine the stability of a feedback system from its OLTF, two points are needed: the **UGF**, which corresponds to the frequency where the amplitude, also called gain, becomes 1, and the **180° crossover**, which is the closest frequency to the UGF at which the phase becomes ±180° (see Figure 4.15). With these two points two parameters can be determined:

- **Phase margin:** is calculated as, phase at the UGF - (±180°), depending on the sign of the ±180° crossover. If this value is **positive** the system will be stable, otherwise, it will be unstable. The absolute value also gives you information about how much phase margin you have before becoming unstable. For the nominal arm cavities of AdV (T_{input} = 0.01375, T_{end} = $4.4{\cdot}10^{-6}$ and $L_{1,2}$ = $37.5{\cdot}10^{-6}$) the phase margin is: -115.4 - (-180) = +64.6°.

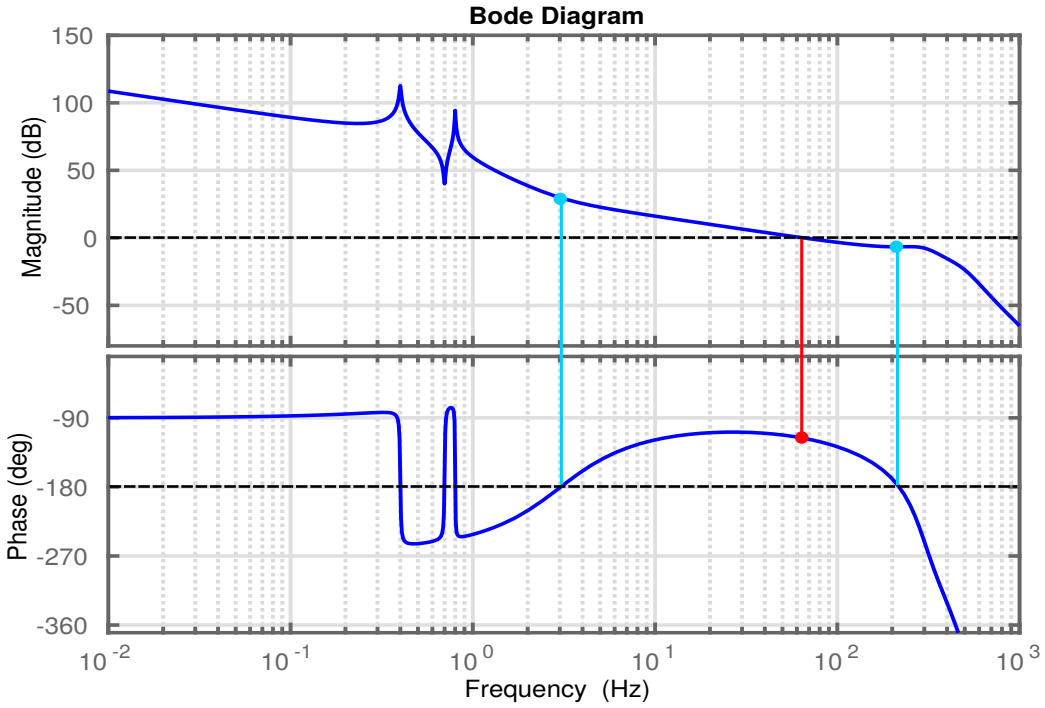

FIGURE 4.15: Gain and phase of the Open Loop of the Advanced Virgo arm cavities showing the UGF which is at 65 Hz (red bars) and the 180° crossover points at 2.8 Hz and 215 Hz (blue bars). This type of representation is also known as Bode plot.

- **Gain margin:** it is given by the values of the amplitude at both ±180°. It gives you as well information of your stability margin. In our particular case the amplitude stability range is: [36.1 0.46]. This means that you can decrease the gain by a factor 36 or increase it by a factor 0.46 and still remain stable.

A figure that provides more complete information about the stability behaviour of the system is the Nichols plot [10]. It is the representation of both the amplitude and the phase of the system OLTF for each frequency, see Figure 4.16. The red point gives you the instability of the system: when the amplitude is 1 and the phase is -180°. The stability condition in this representation requires that the system crosses the unity gain axis between -180° and 0.

From this representation is much straight forward to extract the stability margins (in red the phase margin and in blue the gain margin). Moreover, the different grids gives an extra information about the amplification of the system for each frequency. This is important because even if your system is stable, if it is too close to the instability area the input will be enhanced instead of reduced. This enhancement is called an *overshoot* and depending on your system and in the perturbation sources or noises it might cause the system to oscillate making it unstable in practice. Normally the convention is to avoid the 6 dB region where the perturbation is enhanced by a factor 2.

The equivalent representation in the time domain is the *step response* of the system. It is important because it gives you its behaviour at the moment of closing

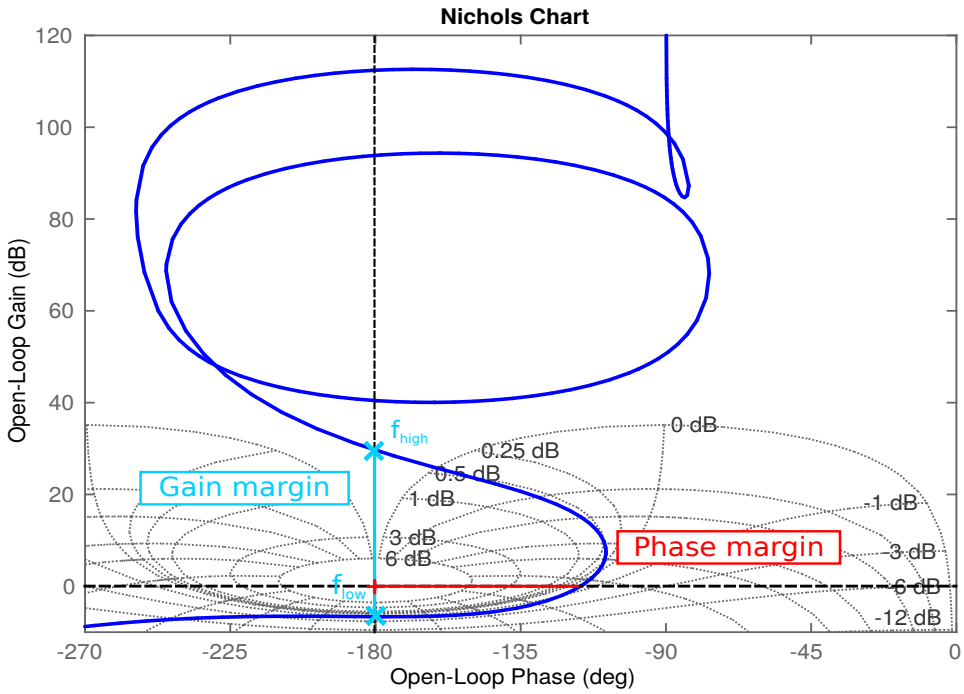

FIGURE 4.16: Nichols plot of the system, showing the gain and the phase of the OLTF for each frequency. The gain and phase margins are shown in blue and red respectively. The frequencies that indicate the gain stability limits (low and high) are shown by a blue cross. The grid indicates the behaviour of the system in Closed Loop.

the control loop. Ideally the response would be a step, but depending on how close is our system from the instability area, a transient oscillation will take place, at the frequency which is closer to the instability.

An example of a system too close to the instability area is shown in Figure 4.17. The Nichols plot shows that the system passes very close to the 6dB curve, in the region between 150-200 Hz. An overshoot of more than 2 can be seen on the CL_{gain} around this frequency region, which means that the movement is enhanced instead of reduced on that region. Also an oscillation on the step response can be seen, from which the frequency that is causing the instability can be extracted (T $\sim$0.006s, f $\sim$170 Hz).

A very simple example has been presented here, but this Laplace analysis of feedback loops is very powerful, allowing to make a much more detailed analysis by considering more elements or adding noise sources.

4.4.2 Length Sensing: PDH technique

The basics to control a Fabry-Perot cavity has been presented in the previous section. In particular the control scheme used for the 3 km cavities of Advanced Virgo. One key element is the error signal that contains the information about the length of the cavity with respect to the resonance point. An ideal error signal fulfils several conditions: it is **bipolar**, that means that it changes sign depending

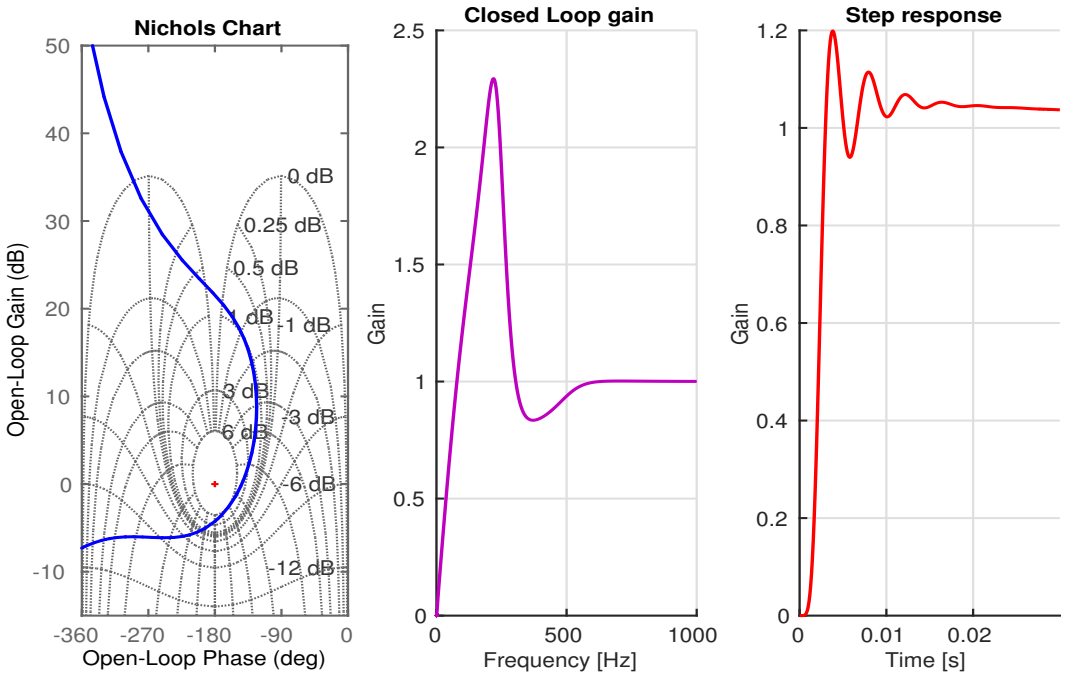

FIGURE 4.17: **Left picture:** Nichols plot for the previously studied system, but with a higher gain, which brings the frequency range 150-200 Hz closer to the instability region. **Central picture:** Closed Loop gain of the system. There is an overshoot of more than 2 in the critical frequency region. **Right picture:** Step response of the system when engaging the feedback loop. We can see a transient oscillation with a period of 6 ms, corresponding to a frequency of ∼170Hz as expected. Notice that it converges to 1 outside the zoom that is shown in the figure.

on which side of the working point we are; it is **linear**, meaning it is proportional to the parameter we want to measure; and it **crosses zero** at the desired working point.

In order to obtain an error signal with all these requirements the Pound-Drever-Hall technique (PDH) is used [16]. It was invented to control the frequency of a maser with respect to a reference optical cavity, based on a microwave technique [30]. Instead in the gravitational waves detectors it is used to control the cavity length with respect to the wavelength of the laser which has been previously stabilized. It takes advantage of the fact that the phase of the electromagnetic field entering into the cavity changes its value around the resonance point (see Figure 4.3 in Section 4.1.1) and that it is not the case out of resonance, where the phase is almost constant.

PDH technique consists of adding *sidebands* around the main field or *carrier* with a frequency that is chosen to be *anti-resonant* in the FP cavity while the carrier is resonant. This way they act as phase reference for the carrier which enters into the cavity, and carries information about the cavity length. The **beating between sidebands and carrier** is the error signal we are interested in because it gives the phase difference between them.

The sidebands are created by modulating in phase the laser beam using an

Electro Optical Modulator (EOM). It consists of a crystal that changes the propagation properties of electromagnetic radiation by applying an electric field [22]. In our particular case a sinusoidal radio-frequency signal of frequency Ω is applied affecting the phase of the electromagnetic field as:

$$E_{EOM} = E_0 \cdot e^{(i\omega_0 t + m\cos(\Omega t))} \tag{4.51}$$

where ω_0 is the laser frequency and m is the modulation depth. This field can be re-written in terms of Bessel functions using the Jacobi-Anger expansion at first order [10]:

$$E_{EOM} = E_0 \cdot e^{i\omega t}\left[J_0(m) - J_1(m)\cdot e^{-i\Omega t} + J_1(m)\cdot e^{i\Omega t}\right] + ... \tag{4.52}$$

where J_i are the Bessel functions of first kind.

The term in J_0 corresponds to the carrier and the terms in J_1 correspond to the two first sidebands created, one shifted in frequency from the carrier by Ω (upper sideband) an the other one by -Ω (lower sideband). The points in the expression refer to the higher order sidebands at integer multiples of the modulation frequency. As m is often small they have a much smaller amplitude so over the first order they can be neglected, as it is shown in Figure 4.18. For example in Advanced Virgo the modulation depth is 0.1 which means that $J_0 = 0.9975$, $J_1 = 0.05$, $J_2 = 0.0012$ and $J_3 = 2{\cdot}10^{-5}$.

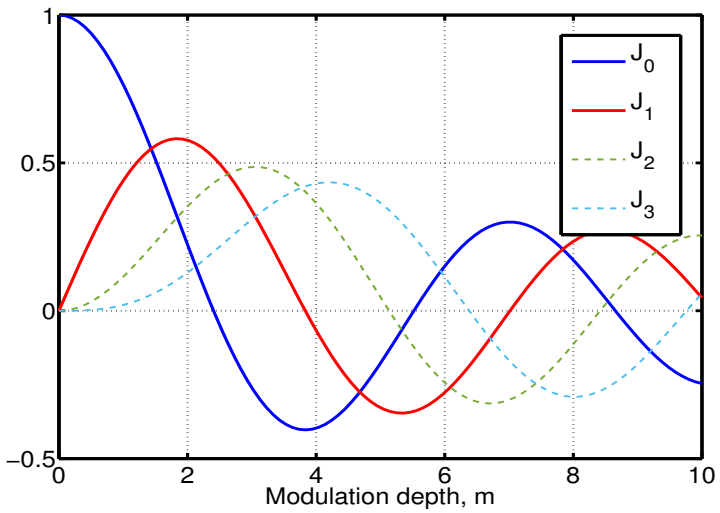

FIGURE 4.18: Bessel functions of first kind from 0 order to 3rd order. In our case the variable is the modulation depth, and it can be understood from the graph that at low m, J_2 and J_3 have negligible values.

Now the expression of the error signal in reflection of the cavity can be calculated:

$$\begin{aligned} E_{refl} &= E_0 \cdot e^{i\omega t}\left[J_0(m)\cdot r^c - J_1(m)\cdot r^- \cdot e^{-i\Omega t} + J_1(m)\cdot r^+ \cdot e^{i\Omega t}\right] \\ P_{refl} &= P_{in}\Big[J_0(m)^2\cdot|r^c|^2 + J_1(m)^2\cdot\left|r^+\right|^2 + J_1(m)^2\cdot\left|r^-\right|^2 \qquad (DC) \\ &\quad + e^{-i\Omega t}\cdot J_0(m)\cdot J_1(m)\cdot\left(-r^c\cdot r^{+*} + r^{c*}\cdot r^-\right) + cc \qquad (\Omega) \\ &\quad + e^{-2i\Omega t}\cdot J_1(m)^2\cdot r^-\cdot r^{+*} + cc\Big] \qquad (2\Omega) \end{aligned} \tag{4.53}$$

where r^c, r^+ and r^- are the reflection coefficients for the carrier, upper and lower sideband respectively. The complex conjugate for the reflection coefficients is defined as r^* and cc stands for complex conjugate of the previous expression.

In the expression of the reflected power, Equation 4.53, three terms can be distinguished: the first one in DC, which corresponds to the static power in reflection of the cavity; the second term at the modulation frequency, which corresponds to the beating between sidebands and carrier that we are interested in; and a third term which oscillates at twice the modulation frequency, which corresponds to the beating between sidebands.

In order to isolate the term which contains the relevant information, the power is multiplied by the signal used to generate the modulation frequency. This process is also known as *demodulation of the error signal*. The resulting signal will have a term in DC which is the one containing the beating, and terms in Ω, 2Ω and 3Ω. As we are interested in the DC term as it will be shown to be an excellent error signal, a low-pass filter is applied to the demodulated signal. The scheme of the process is shown in Figure 4.19.

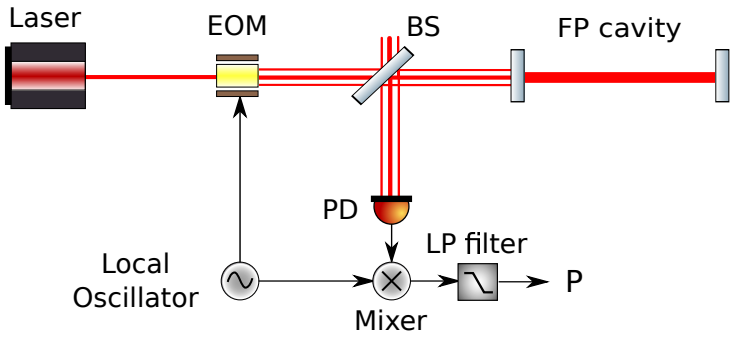

FIGURE 4.19: Scheme of the PDH technique. The laser is modulated in phase by an EOM, adding sidebands at the modulation frequency. The carrier field resonates in the cavity while the sidebands are reflected because they are anti-resonant. The photodiode detects the reflection of the cavity and the power is multiplied by the modulation frequency. A low pass filter is applied to this demodulated signal, obtaining the desired error signal.

Depending on the phase of the demodulation signal, that is whether we multiply by a sine or a cosine, the information obtained will be different. Ideally only one of them will be significant and the other will be zero. The signal obtained from multiplying by a sine is called *in-phase* (PDHp) and the one obtained from multiplying by a cosine is called *quadrature* (PDHq):

$$\begin{aligned} PDH_p =& P_{in} \cdot J_0(m) \cdot J_1(m) \cdot \Im(r^{c*} \cdot r^{-} - r^{c} \cdot r^{+*}) \\ PDH_q =& P_{in} \cdot J_0(m) \cdot J_1(m) \cdot \Re(r^{c*} \cdot r^{-} - r^{c} \cdot r^{+*}) \end{aligned} \tag{4.54}$$

In practice there are delays due to cables and electronics in the demodulation process. This means that it is needed to consider a more general case where the demodulation signal, either a cosine or a sine, needs to include an arbitrary phase such as: $\cos(\Omega t + \phi_{mod})$ or $\sin(\Omega t + \phi_{mod})$. At the end of the process this demodulation phase, ϕ_{mod}, needs to be tuned to separate the information provided by the in-phase and the in-quadrature projections.

It is worth noticing that the phase modulation introduces an effect called Residual Amplitude Modulation via the EOM. This amplitude modulation occurs at the frequency of the phase modulation, and so it couples to the PDH error signals, changing their zero-crossing. It can couple to the strain sensitivity, and for this reason there are important requirements on the EOM performances. An

analytical expression of this error signal can be obtained starting from the reflectivity of the carrier (see Equation 4.2). First let's consider that the carrier is on resonance (see Equation 4.5) and that a longitudinal deviation from resonance δl is applied. The reflectivity then becomes:

$$r^c = \left[\frac{r_1 - r_2 \cdot e^{2ik\delta l}}{1 - r_1 \cdot r_2 \cdot e^{2ik\delta l}} \right] \tag{4.55}$$

Notice that the losses have been neglected.

The reflectivity for the sidebands is slightly different because they have been chosen to be anti-resonant when the carrier is resonant. This means that the phase shift accumulated by the sidebands when propagating along the arm will be an odd multiple of π. Taking into account a longitudinal deviation from resonance δl we can write:

$$r^{\pm} = \left[\frac{r_1 + r_2 \cdot e^{2ik\delta l}}{1 + r_1 \cdot r_2 \cdot e^{2ik\delta l}} \right] \approx 1 \tag{4.56}$$

As the sidebands are anti-resonant in the arm cavity, the reflectivity can be approximated to one if no losses are considered, as shown in Figure 4.3.

There should be a term in $\pm 2\frac{\Omega}{c}\delta$l which can be neglected because Ω is normally of the order of MHz and δl of the order of a wavelength ($\sim 10^{15}$Hz). When both the upper and the lower sidebands are anti-resonant, they have the same reflectivity which is approximately 1. Taking this approximation into account we can write [12]:

$$r^{c*} \cdot r^{-} - r^{c} \cdot r^{+*} = -2 \cdot \Im(r^c) \tag{4.57}$$

Finally the analytical expression of both PDH projections can be solved for the reflectivities previously calculated using Equation 4.57:

$$\begin{aligned} PDH_p &= 4 \cdot P_{in} \cdot J_0(m) \cdot J_1(m) \cdot r_2 \cdot t_1^2 \cdot \frac{\sin(2k\delta l)}{1 + r_1^2 \cdot r_2^2 - 2 \cdot r_1 \cdot r_2 \cdot \cos(2k\delta l)} \\ PDH_q &= 0 \end{aligned} \tag{4.58}$$

Even if the sidebands are poorly transmitted by the cavity, for being anti-resonant, there is some beating in transmission that creates also a PDH signal. It can be used for locking purposes, but it will have a lower signal-to-noise ratio. It differs from Equation 4.58 in a factor $2\frac{t_2}{t_1}$ instead of the term $4r_2$ [31].

Figure 4.20 shows both projections of the error signal and the transmitted power of the AdV arm cavity, including the resonance of the carrier and of the sidebands. The in-phase signal fulfils the conditions for an ideal error signal: it is linear around the region of interest, it crosses zero at the resonance and it is bipolar around the working-point. Notice that it is also a good error signal at the sidebands resonance, but its slope has opposite sign.

On the other hand, the in-quadrature projection is zero at resonance, but a peak can be seen where the upper and lower sideband are resonant respectively. This is because it is sensitive to amplitude variations, that is to the absorption of the Fabry-Perot cavity. At the carrier resonance there is no structure because the beat note between carrier and each sideband is dephased by π.

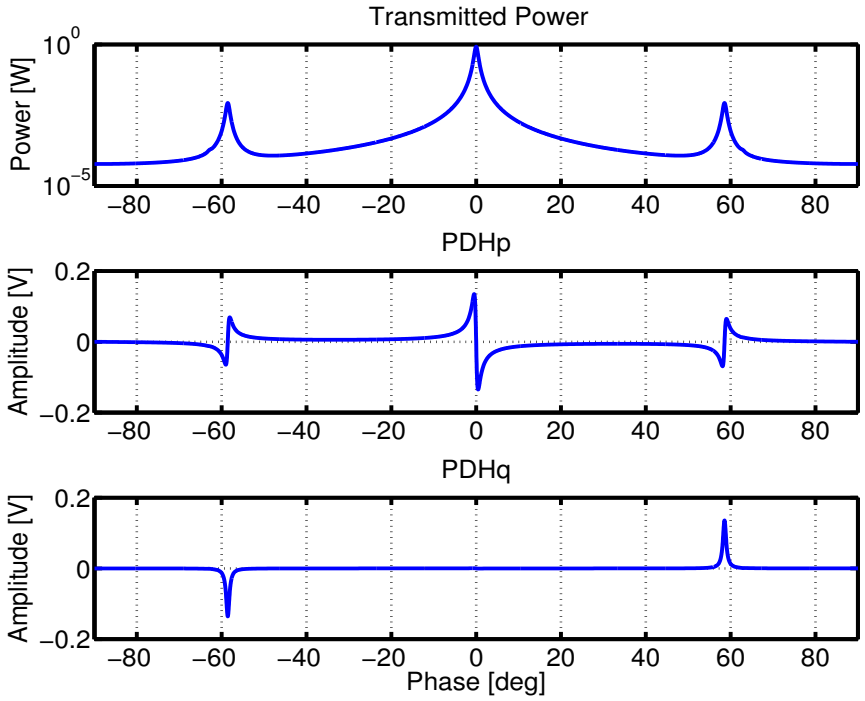

FIGURE 4.20: **Upper picture:** Transmitted power of a Fabry Perot cavity such as the one of AdV. **Central picture:** In-phase projection of the PDH signal. **Lower picture:** In-quadrature projection of the PDH signal.

Notice however that the error signal is only linear in a limited region around resonance and so outside this region it can not be used. It can be shown that the width of the linear region is equal to the linewidth of the cavity [31] as it can be seen in Figure 4.21.

Another interesting feature of the error signal is its slope in the linear region because it gives us the sensitivity of the error signal to a longitudinal displacement. It can be obtained from the derivative of 4.58 evaluated at the origin [10]:

$$\frac{dp}{d(\delta l)} = -J_0(m) \cdot J_1(m) \cdot P_{in} \cdot r_2 \cdot \frac{8 \cdot F}{\lambda} \tag{4.59}$$

This expression shows that the slope of the error signal depends on the finesse of the cavity. This means that an increase of this parameter will translate in an

increase of the sensitivity. However, this would also mean a smaller linewidth and so a narrower linear region. A compromise between both parameters is the key of a good control of the cavity length.

If we consider that the photodiode transfer function is flat and equal to one it can be shown that the slope of the error signal is equal to the value of the optical transfer function of the cavity (as a function of displacement) at low frequency [23]. For this reason, from now on we will refer to the slope of the error signal as its *Optical Gain (OG)*.

This Optical Gain can be calculated from the intra-cavity power (Equation 4.1) and can be related to the finesse of the cavity as [32]:

$$OG = \left(\frac{t_1^2}{(1 - r_1 r_2)^2} \right) = \left(\frac{(1 + \zeta) \cdot \mathcal{F}}{\pi} \right) \tag{4.60}$$

where the value of ζ depends on the type of cavity: $1 < \zeta < 0$ for an overcoupled cavity, $\zeta = 0$ for a critically coupled cavity and -1 $< \zeta <$ 0 for an undercoupled cavity.

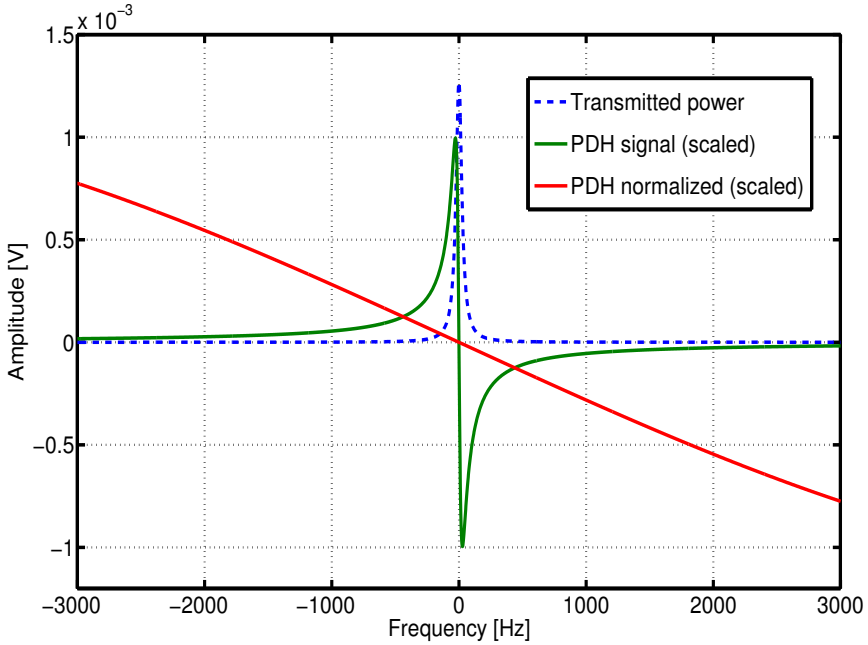

FIGURE 4.21: The dashed curved represents the power transmitted by the cavity and the blue continuous line is the correspondent PDH signal for an AdV arm cavity with 1 W of input power. It crosses zero at the resonance and that is linear around this point. The red line shows the PDH signal normalized and this increases the width of its linear region.

Linearisation of the error signal

As it was just mentioned the error signal can only be used within its linear region. However there is a way to increase the width of this region by processing the error signal. Equation 4.58 shows that the linear region is limited by the denominator which for small displacements behaves as δl^2. Now, the PDH can be re-written in

terms of transmitted cavity power (Equation 4.4)

$$PDH_p = 4 \cdot J_0(m) \cdot J_1(m) \cdot r_2 \cdot \frac{P_{tr}}{t_2^2} \sin(2k\delta l) \tag{4.61}$$

This means that normalizing by the transmitted power it is possible to remove the limitation on the linear region [33]. The linearised PDH then becomes:

$$PDH_{lin} = \frac{PDH_p}{P_{tr}} = \frac{4 \cdot J_0(m) \cdot J_1(m) \cdot r_2}{t_2^2} \sin(2k\delta l) \tag{4.62}$$

Notice that both expressions are linear for small deviations from resonance, but they have different slopes.

Figure 4.21 shows the comparison between the PDH signal with and without linearisation. The linear region is now much wider, which increases the range of use of the error signal, simplifying the lock acquisition.

However in real life linearisation implies that far from resonance we are dividing by a very small number which is affected by electronic noise or shot noise and this limits the linear range that can be reached in practice.

4.4.3 Lock acquisition: Guided Lock

So far the basics of the control loop used to keep the FP cavities on resonance has been presented as well as how to study its performance once closed. However, in the case of Advanced Virgo the dynamics of the cavities has to be considered, as introduced on Section 4.2, because it will have an impact on the shape of the error signal, preventing the control to be engaged.

As it has been seen in the previous section, the error signal is linear only within a restricted region. Its width is equal to the linewidth of the FP cavity (when non linearised), which for Advanced Virgo is ∼2.4 nm. The mirrors displacement when the Local Control is active is approximately 1 μm RMS (see Section AdV), which means that the cavity will pass through several resonances per second. The control loop needs to be closed during one resonance crossing, and the success of this action will depend on the velocity of the cavity. There are several factors that determine the velocity threshold above which the lock can not be engaged [34]:

- **Control bandwidth:** the reaction time of a control loop is determined by its bandwidth (B). In order to acquire lock, the loop needs to react faster than the time to cross a resonance:

$$v_{max,B} < \frac{\lambda}{2 \cdot \mathcal{F}} \cdot 2 \cdot \pi \cdot B \tag{4.63}$$

- **Actuation force:** the lock acquisition is also limited by the maximum force that can be applied. The time needed to stop the mirrors which are moving with a linear momentum mv by applying the maximum force available has to be smaller than the resonance crossing time. This puts another threshold on the mirror velocity:

$$v_{max,F} < \sqrt{\frac{\lambda}{2 \cdot \mathcal{F}} \cdot \frac{F_{max}}{m}} \tag{4.64}$$

- **Fabry-Perot cavity dynamics:** the field needs some time in order to reach a stationary state. If the cavity changes its length due to a mirror movement

before its build-up is completed, the ringing effect will start to distort the fields, spoiling the error signal as well (see section 4.2).

$$v_{max,cr} < \frac{\lambda}{2 \cdot \mathcal{F}} \cdot \frac{c \cdot \pi}{2 \cdot L \cdot \mathcal{F}} \tag{4.65}$$

These threshold velocities can be estimated for the Advanced Virgo Fabry-Perot arm cavities. They are shown in Table 4.1 together with the corresponding ones of Virgo+ for comparison.

	Units	Virgo +	Advanced Virgo
Mirror mass	kg	20	42.3
Control bandwidth	Hz	100	100
Maximum force per coil-pair	mN	2.9	2.5
Finesse	–	150	450
$v_{max,B}$	$[\mu ms^{-1}]$	2.23	0.74
$v_{max,F}$	$[\mu ms^{-1}]$	0.72	0.26
$v_{max,cr}$	$[\mu ms^{-1}]$	3.71	0.14

TABLE 4.1: Threshold velocities calculated for the Virgo + and Advanced Virgo Fabry-Perot cavities.

In the case of Advanced Virgo the three velocities become critical. Regarding the maximum force that can be applied, there are 4 coil-pairs available for each cavity, so this factor is no more critical. Moreover, the first two requirements can be relaxed by linearising the PDH signal as explained in the previous section 4.4.2. This would increase the width of the linear region as well as the threshold velocity.

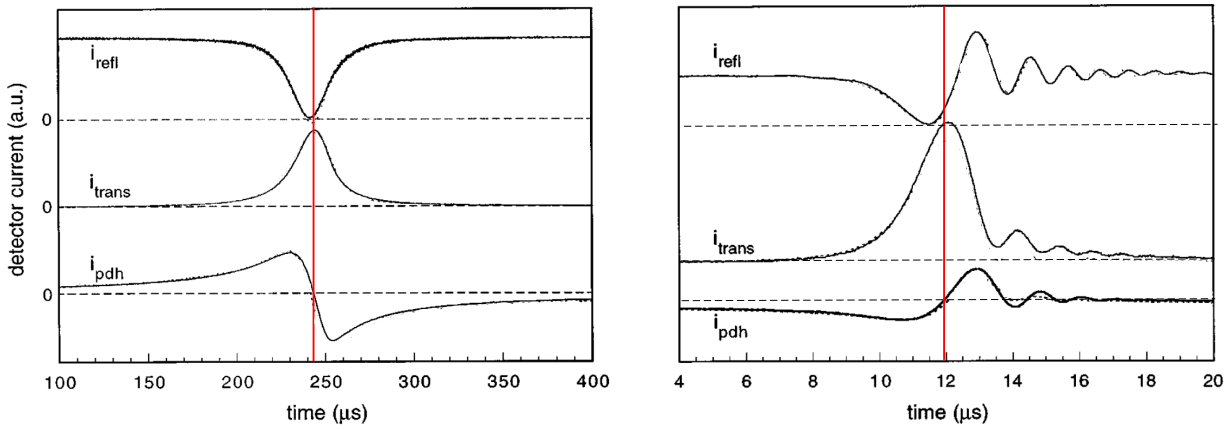

FIGURE 4.22: Reflected, transmitted and PDH signal photodetector currents of a Fabry-Perot cavity with a storage time of 1.8μs. The red line shows the zero-crossing of the PDH signal. **Left picture:** no ringing present, v « v_{cr} **Right picture:** ringing effects are present, v » v_{cr} [35].

However, linearisation does not solve the problem of the ringing effect, which distorts the fields in a way that can not be compensated by normalization. Figure 4.22 shows a PDH signal for a cavity that moves faster than its critical velocity. It can be observed that the linear region is smaller than usual, it is asymmetric around zero and the zero-crossing does not coincide with the resonance. With

a PDH like this the lock acquisition becomes almost impossible and so a special strategy needs to be adopted: *Guided Lock*.

Guided lock

Guided lock was first tested at the 40-m laboratory in Caltech [36], and improved further in TAMA [37]. It was already implemented as well in Virgo+ as a feasibility test, even though at the time there were no ringing effects present [34]. The basic principle of the Guided Lock is to **estimate the velocity at which a resonance is crossed in order to give a single extended impulse to the mirror with the maximum force available sending it back to the same resonance with an opposed and smaller velocity than the initial one**. If this velocity is smaller than the critical one, the error signal no more suffers from ringing and the linear control is engaged. Otherwise another pulse can be applied in order to further calm the cavity.

The locking sequence for one of the arm cavities has been simulated using a time-domain simulation tool, e2e 3.1, and it is shown in Figure 4.23. A pulse is applied after the first resonance peak is crossed that sends the cavity back to the resonance. A second pulse is applied with the opposite force to further reduce the velocity until the linear controller can be engaged.

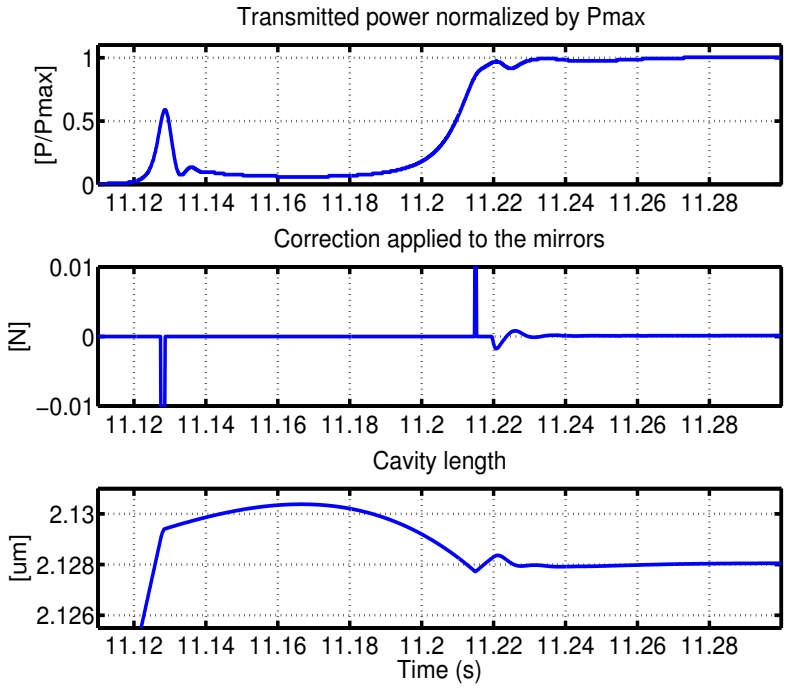

FIGURE 4.23: e2e simulation of a lock engagement sequence using the Guided Lock technique. **Upper picture:** Transmitted power normalized by the maximum power on the cavity. **Central picture:** Correction sent to the mirrors in units of force. **Lower picture:** Cavity length variation.

The aim is to calculate the duration of the pulse so that the mirror is stopped and accelerated in the opposite direction with a velocity smaller than the initial one. Knowing the mass of the mirrors (m_{mirr}) and the maximum force that can

be applied to them (F_{max}), the maximum acceleration that can be achieved can be calculated as $a_{max} = F_{max}/m_{mirr}$. With this information the time that the impulse needs to be applied in order to reach a given velocity can be defined as:

$$t_{pulse} = \frac{v_{ini} + v_{fin}}{a_{max}} \tag{4.66}$$

where v_{ini} is the initial velocity and $v_{fin} = \epsilon \cdot v_{ini}$ where ϵ is a value between 0 and 1.

One important factor to consider is the time needed for the cavity to go back to the resonance. If the final velocity is too low, the mirror takes a longer time to return to the resonance. During this time the seismic noise is able to change the acceleration of the cavity introducing uncertainty on the final velocity or even changing the direction of the mirrors motion. From the tests done in Virgo+, the final velocity was chosen to be $v_{fin} = 0.3\ \mu ms^{-1}$ and as the seismic noise is not expected to have increased, this value will be kept for the Advanced Virgo cavities lock.

The main challenge of this technique is the velocity estimation, that needs to be done online, in order to react on time. When there is no dynamical effects the velocity of the cavity can be calculated from the derivative of the PDH signal on its linear region. However, this is not true anymore when the ringing is present, and a power-law correction needs to be applied [37]:

$$v_{cav} = C \cdot \left(\frac{\partial PDH_{lin}}{\partial t} \right)^{P} \tag{4.67}$$

where C is a calibration factor and P accounts for a power-law correction. Time domain simulations have been performed in [38] in order to determine up to which velocity of the cavity the estimation of the velocity is good without the need of a power-law correction. The simulations concluded that for the error signal linearised in reflection the approximation is valid up to $\pm 3\ \mu ms^{-1}$.

Nevertheless, in practice the lock acquisition of the two arm FP cavities is done simultaneously, which means that their signals will be mixed at the photodiodes in reflection. Thus the error signal to be used preferably is the one in transmission. Simulations tell that in this case, the approximation is valid up to $\pm 1.5\ \mu ms^{-1}$. However due to the low SNR the data lose significance even before this value. Together with the difficulty of finding the right calibration factor at the early stage of commissioning, we looked for an alternative way of calculating the speed online.

The dynamical effects on FP cavities were introduced on Section 4.2 and Figure 4.6 shows the shape of the intracavity power at three different cavity speeds. Although the ringing effect is visible, it is not the only distortion. The rising of the resonance peak also changes with the speed, becoming less steeper when the velocity increases. A new idea was then explored: to use the time that the transmitted power takes to go from 10% of its maximum power to 40% of its maximum power (t_{10-40}) to calculate the velocity of the cavity.

This method has two advantages: first of all the *velocity of the cavity is calculated before reaching the resonance*, which increases the reaction time and so the possibilities of slowing down the cavity with only one pulse. Second, *the rising time that is measured is already in physical units*, which removes the need of calibration, decreasing a potential source of uncertainty.

Using the equation of the transmitted power when dynamical effects are present (Equation 4.24) a simulation was made in order to determine if it exists a relationship between t_{10-40} and the velocity of the cavity. Figure 4.24 shows that it exists a linear relationship between t_{10-40} and the inverse of the velocity of the cavity which allows to calculate the velocity with an accuracy of 1%.

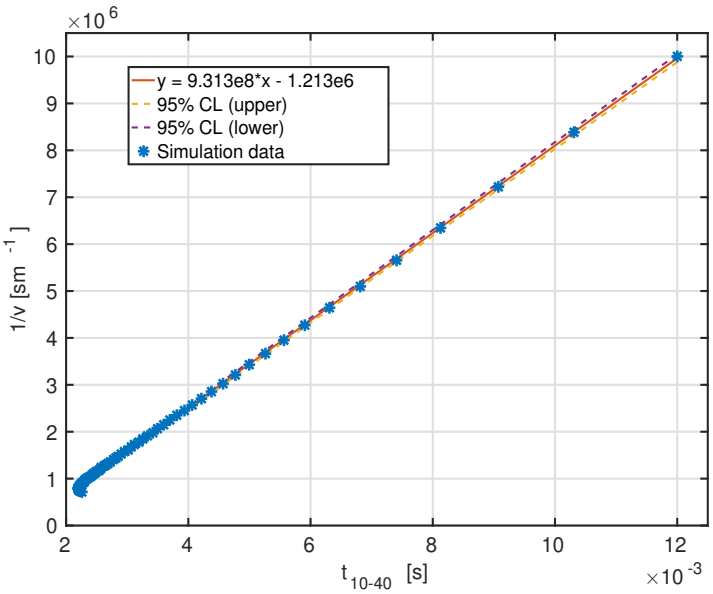

FIGURE 4.24: The blue points show the relationship between t_{10-40} and the inverse of the resonance crossing velocity given by the simulation. The straight line is the fit of these points whose expression is shown in the legend. The dashed lines shows the 95% confidence limits of the fit. They represent 1% of the simulation value.

This way of estimating the velocity is limited by the speed at which the cavity does *not have enough build-up* to reach 40% of the maximum power, which in our case is 1.4 μms^{-1}. It is worth to mention as well the *local loss of linearity* around 1.2 μms^{-1} that can be seen in Figure 4.24. It is not a major problem because it only affects a small range of velocities (from 1.2 to 1.4μms^{-1}), introducing an error of 20% in the worst case. Both parameters can be improved when using the time between 10% and 30% of the maximum power, which would increase the range of validity of this approximation. However, for our particular case the range given by t_{10-40} is enough to engage a lock.

Notice as well that this way of estimating the velocity, unlike the one that uses the derivative of the error signal, does not indicate the sign of the velocity. However this information can be extracted from the sign of the PDH signal, which changes when crossing the resonance. So its sign when the power build-up is starting will determine the sign of the impulse that will bring the cavity back to the same resonance. The experimental results after the implementation of this lock strategy are shown in Section 6.2.2.

4.5 Angular motion Control

So far we have considered only the longitudinal motion of the cavity, in order to keep the fundamental mode resonant. However this is only true if the input beam is properly aligned to the cavity axis. When this is not the case the electromagnetic field couples to higher order modes. The *optical axis* of a cavity with two spherical mirrors of RoC R_1 and R_2 is defined as the line that intersects both center of curvatures, as shown in the plot on the left of Figure 4.25.

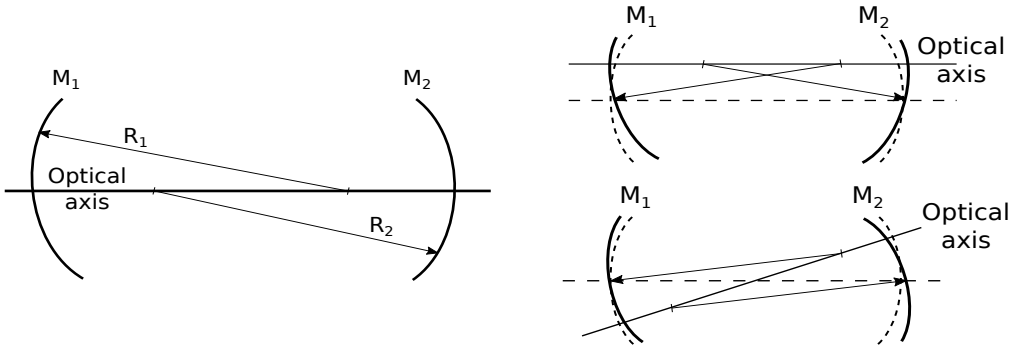

FIGURE 4.25: **Left picture:** Scheme of the optical axis for a Fabry-Perot cavity with spherical mirrors. **Up-Right picture:** Optical axis shift. **Down-Right picture:** Optical axis tilt.

There are four parameters to describe the alignment of a cavity: **2 rotations** (around the horizontal axis of the mirror, θ_x or around the vertical axis, θ_y) and **2 transverse translations** (Δx, Δy). It can be shown [39] that when there is a shift of the input beam and/or of the cavity axis (δ_x) as shown in the Up-Right plot of Figure 4.25, the first HOM is coupled:

$$E(x+\delta_x) = A \cdot H_0(x-\delta_x) \approx A \cdot \left[H_0(x) + \frac{\delta_x}{w_0} \cdot H_1(x) \right] \tag{4.68}$$

Modes with order higher than 2 have not been taken into account. This approximation stands if δ_x is much smaller than w_0. This equation is written for a displacement on the x-axis, but a displacement on the y-axis will have an identical expression.

For a tilt of the input beam and/or the cavity axis (α_x), as shown in Figure 4.25 Down-Right, the HOM coupling can be calculated as for the shift. However, this time a phase change has to be taken into account. This can be understood due to the fact that the wave-front is spherical and so the phase distribution when a tilt is present changes with respect to the on-axis. For this case the assumptions are:

$$|E(x+\alpha(x))| = |E(x')| \cdot cos(\alpha_x)^{-1}; \qquad \phi(x) = k \cdot x \cdot sin(\alpha_x) \tag{4.69}$$

It can be shown for this case as well [39] that the first HOM is coupled, but this time with 90° of phase shift. Again, this expression is valid for angles much smaller than the divergence angle of the beam, θ_d (see Equation 4.34).

$$E(x+\alpha_x) \approx A \cdot [H_0(x) + i \cdot \frac{k \cdot \alpha_x \cdot w_0}{2} \cdot H_1(x)] = A \cdot [H_0(x) + i \cdot \frac{\alpha_x}{\theta_d} \cdot H_1(x)] \tag{4.70}$$

As in the shift case, Equation 4.70 is equivalent for a tilt α_y.

4.5.1 Alignment coordinates

As mentioned before, a misalignment can occur by changing the input beam and/or the cavity axis direction. Depending on the nature of the misalignment and on the cavity optical configuration, the HOMs generated will be different. A change on the angular position of one mirror could modify the cavity axis both in rotation (tilt) and in translation (shift). However, from the control point of view it is more convenient to work in a coordinate system that decouples the two DOF to be controlled. For this reason we want to move from the mirror basis to the tilt / shift one because they are the eigenvectors of the optical cavity. Due to the high finesse of the cavity the allowable mirror misalignments to maintain closed the longitudinal control are in the micro-radians regime, thus in the following we will use the *small angle approximation*.

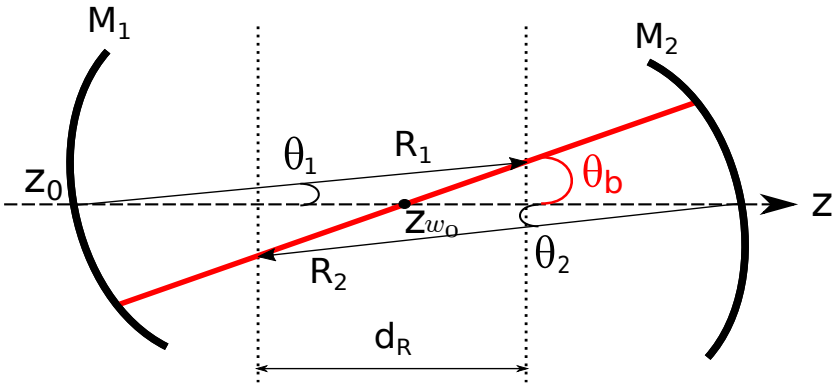

FIGURE 4.26: Scheme of a cavity with its optical axis tilted.

First we will study the **tilt** case. The equation of the optical axis can be written as a function of the optical parameters of the cavity. We are going to consider as zero-coordinate, z_0 the position of the input mirror, as seen in Figure 4.26. Some useful parameters can be extracted from it:

- Distance between radius (d_R):

$$d_R = R_1 - (L - R_2) \tag{4.71}$$

- Beam waist position (z_{w_0}):

$$z_{w_0} = d_R/2 + (L - R_2) = \frac{R_1 - R_2 + L}{2} \tag{4.72}$$

- Optical axis slope (m_{oa}):

$$m_{oa} = \frac{R_1 \cdot \theta_1}{d_R/2} \tag{4.73}$$

- Y-intercept of the optical axis (b_{oa}):

$$b_{oa} \approx -z_{w_0} \cdot m_{oa} \tag{4.74}$$

At this point the optical axis expression can be written:

$$y = m_{oa} \cdot z + b_{oa} = m_{oa} \cdot z - m_{oa} \cdot z_{w_0} = m_{oa} \cdot (z - z_{w_0}) \tag{4.75}$$

In order to know the combination of mirror movements needed to make a pure tilt we solve the optical axis equation for a given point (z = L - R_2, y = $\theta_2 R_2$) obtaining the following relationship:

$$\theta_2 = -\frac{R_1}{R_2} \cdot \theta_1 \tag{4.76}$$

This equation gives the relationship between the angular displacement of both mirrors in order to produce a pure tilt of the optical axis.

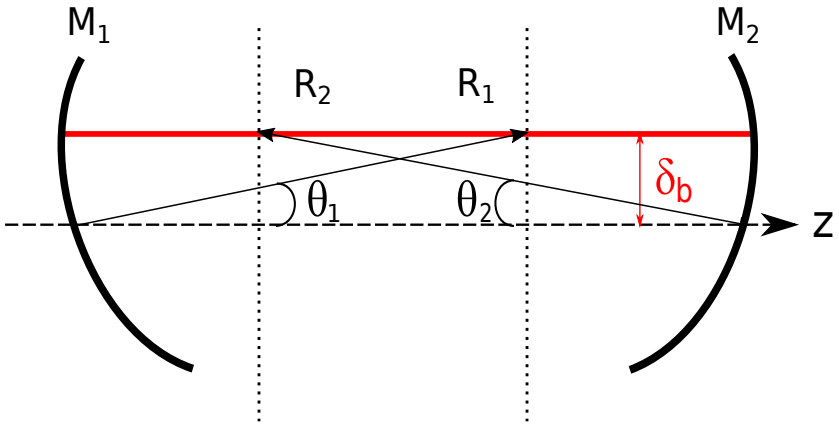

FIGURE 4.27: Scheme of a cavity with its optical axis shifted.

This reasoning can be repeated for a pure **shift** of the optical axis. In this case the equation of the optical axis becomes easier because the slope is zero. A scheme of this configuration is shown in Figure 4.27. To obtain the relationship between the mirrors angular movement we only need two points of the line:

$$y = \theta_1 \cdot R_1 = \theta_2 \cdot R_2 \tag{4.77}$$

With this information we can build the matrix that changes from the mirror basis to the cavity eigenvectors:

$$\begin{pmatrix} \theta_b \\ \delta_b \end{pmatrix} = \begin{pmatrix} 1 & -R_1/R_2 \\ 1 & R_1/R_2 \end{pmatrix} \cdot \begin{pmatrix} \theta_1 \\ \theta_2 \end{pmatrix} \tag{4.78}$$

where θ_b is the tilt of the optical axis and δ_b is the shift of the optical axis.

For the moment the matrix contains only the information about the ratio between the single mirrors misalignments (θ_1 and θ_2), and how they couple into tilt and shift. However, there is a units problem (the shift DOF is expressed in μrad) and so the values do not have a physical meaning. Nevertheless, it is convenient to have the same "fake units" in order to compare the coupling between them. The real matrix will be written at the end of this section.

An additional interest on the tilt / shift coordinate system arises when working at high power. In this case the light beam exerts a torque upon the mirrors eigenvectors due to the *radiation pressure* [40]. This effect is equivalent to an optical spring connecting the two mirrors and which modifies its mechanical transfer function. When taking into account radiation pressure the tilt coordinate corresponds

to the (+) mode or hard mode because it increases the frequency of the pendulum, making the system stiffer. On the other hand, the shift coordinate corresponds to the (-) mode or soft mode because it decreases the frequency, making the system softer [41].

The stiffness of the optical spring for each mode can be calculated such as [42]:

$$\begin{aligned} \kappa_+ &= \frac{2 \cdot P_{in} \cdot L}{c \cdot (g_1 \cdot g_2 - 1)} \cdot \frac{(g_1 + g_2) + \sqrt{(g_1 + g_2)^2 + 4}}{2} \\ \kappa_- &= \frac{2 \cdot P_{in} \cdot L}{c \cdot (g_1 \cdot g_2 - 1)} \cdot \frac{(g_1 + g_2) - \sqrt{(g_1 + g_2)^2 + 4}}{2} \end{aligned} \tag{4.79}$$

As for a classical spring, the resonance frequency can be obtained as $f = 1/2\pi \cdot \sqrt{k/m}$. The angular control will have to adapt to these new values of the mechanical TF of the mirrors. Their value depends on the input power. If one of them becomes negative, the system will be unstable and it will depend on the control filter to maintain the stability. This was the case of the shift of the arm cavities in Virgo+. In the new configuration, the DOFs are stable even at high power (200 W), which simplifies the design of the angular control.

Arm cavity alignment simulation

A simulation of the misalignment impact on the transmitted power of one of the arm cavities of Advanced Virgo has been made using Finesse [17]. Starting from the ideal alignment, a scan of different misalignments around the horizontal axis of both mirrors (θ_x) has been done. The objective was to quantify the evolution of the transmitted power as a function of the misalignment. The result of the simulation can be seen in Figure 4.28. Notice that only θ_x has been simulated, because we expect an equivalent behaviour around the vertical axis θ_y.

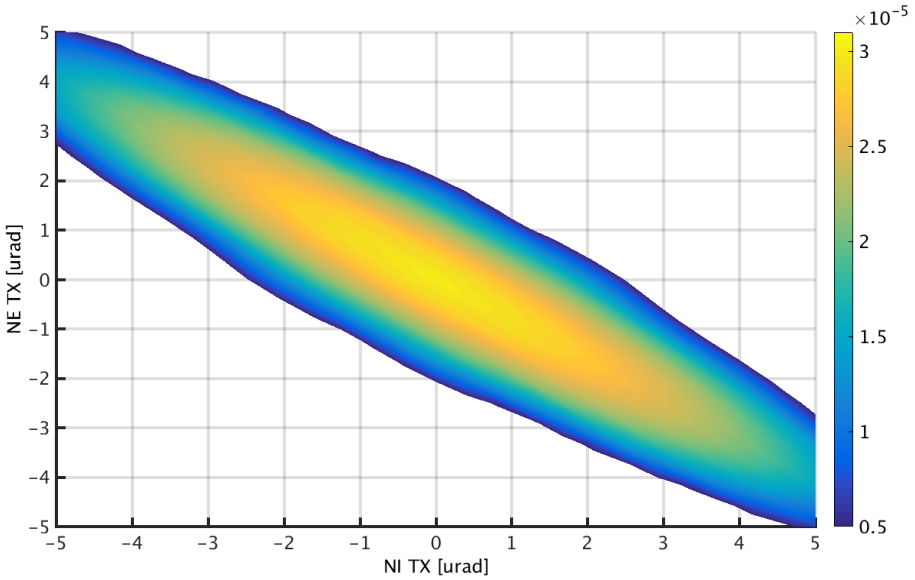

FIGURE 4.28: Finesse simulation result of the transmitted power of an arm cavity as a function of the NI and NE mirrors misalignment on θ_x. The power distribution is represented in a color scale which goes from blue (minimum power) to yellow (maximum power).

From Figure 4.28 it is clear that in the coordinate system of the mirrors both degrees of freedom are very coupled. The fact that the ellipse is inclined implies that the two variables plotted are coupled. The ellipse axis on this figure represents the tilt and the shift coordinates and it can be seen already that one is much more critical than the other.

The ratio between them can be estimated by comparing the misalignment needed to lose a given amount a power while doing a pure tilt or a pure shift, using the change of basis matrix presented above, in "fake units". From the simulation we know that the pure tilt needed to decrease the power to $2.5 \cdot 10^{-5}$W is approximately 2.3 ± 0.4 μrad and the pure shift needed is 10 ± 0.4 μrad. The total ratio Shift/Tilt is then 4.3 ± 0.9. The uncertainty on this calculation comes from the limited number of points simulated. It is clear now that the cavity is more sensitive to a tilt than to a shift. From the control point of view this means that the most critical degree of freedom is the tilt of the cavity, which should be controlled first.

The same plot can be represented in the coordinate system tilt / shift mentioned in the previous section, although now it is more interesting to put them in SI units. Starting with the tilt, the calibration can be derived from the slope of the optical axis equation (Equation 4.74). For an angular movement of 1 μrad of the input mirror the optical axis of the cavity is tilted by:

$$\theta_b = \theta_1 \cdot \frac{2 \cdot R_1}{R_1 - L + R_2} = 27.6 \quad [\mu rad] \tag{4.80}$$

where $R_1 = 1420$ m and $R_2 = 1683$ m are the nominal RoC of the mirror.

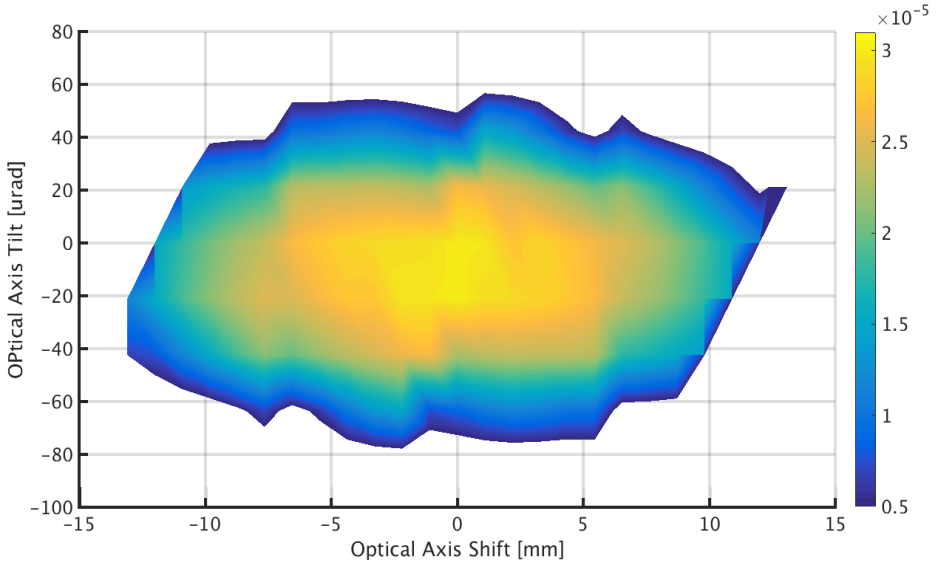

FIGURE 4.29: Simulation result of the transmitted power of an arm cavity on the tilt / shift basis having the tilt calibrated in micro-radians and the shift in millimeters. The power distribution in Watts is represented in a color scale which goes from blue (minimum power) to yellow (maximum power).

The calibration factor for a pure shift can be derived from Equation 4.77 instead. For an angular movement of 1 μrad of the input mirror the optical axis of

the cavity is shifted by:

$$\delta_b = \theta_1 \cdot R_1 = 1.42 \quad [mm] \tag{4.81}$$

Now the change of basis matrix can be written in SI units:

$$\begin{pmatrix} \theta_b \ [\mu rad] \\ \delta_b \ [mm] \end{pmatrix} = \begin{pmatrix} 27.6 & -27.6 \cdot R_1/R_2 \\ 1.42 & 1.42 \cdot R_1/R_2 \end{pmatrix} \cdot \begin{pmatrix} \theta_1 \ [\mu rad] \\ \theta_2 \ [\mu rad] \end{pmatrix} \tag{4.82}$$

Figure 4.29 shows the scan of the cavity alignment on the tilt / shift basis.

4.5.2 Automatic alignment

Once the length of the cavity is controlled, the mirror's relative position is fixed to keep the cavity on resonance. However, this does not guarantee that the cavity axis and the input beam are well aligned. If this is not the case there will be HOMs generated (see Section 4.5) which might couple inside the cavity spoiling the quality of the field that resonates.

This is not the only effect of the alignment on the cavity behaviour. An additional problem arises if the optical axis is not well centered inside the cavity, which means perpendicular to the mirrors and centered on their rotation axis. The mirrors are subject to alignment drifts due to the fact that they are suspended. When this occurs and the optical axis is miscentered, the angular movement will cause a change on the length of the cavity (see Figure 4.30) spoiling the resonance and adding noise to the longitudinal control. This coupling between angular and

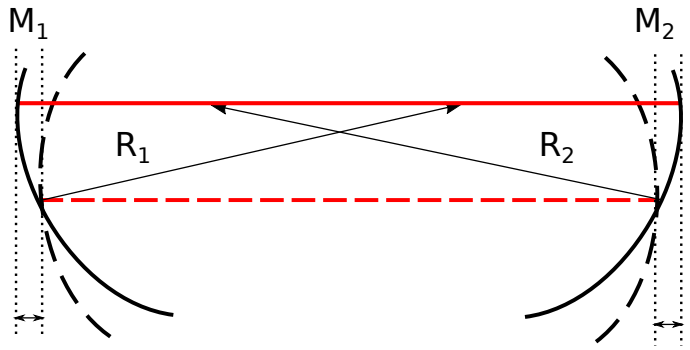

FIGURE 4.30: Coupling between the angular movement of the mirrors of the cavity with the length of its optical axis when a misalignment is present.

longitudinal motion can be approximated to first order to [41]:

$$\delta L(f)_{cav} = d(f) \times \theta_{mir}(f) = d^{RMS} \cdot \theta_{mir}(f) + d(f) \cdot \theta_{mir}^{RMS} \tag{4.83}$$

where d is the miscentering of the beam with respect to the rotation center of the mirror and θ_{mir} is the misalignment of the mirror with respect to the centered position.

This means that the drift of the angular dofs and their working point need to be controlled in order to maintain the cavity alignment and to minimize the coupling to the cavity length. Typically three different alignment techniques have been used in gravitational waves interferometric detectors. They can be separated in two groups depending on the kind of modulation used to produce an error signal:

Mechanical modulation

It consists of adding a *tilting oscillation* to the mirrors of the FP cavity in both degrees of freedom θ_x and θ_y with different frequencies $\omega_i^{(x,y)}$ and $\omega_e^{(x,y)}$. This technique takes advantage of the fact that spherical mirrors are insensitive to rotations around their center. When the cavity is aligned the angular oscillations do not produce any effect, they are invisible. However, it can be shown [43] that when a misalignment is present, these lines can be seen in the transmitted power. An error signal can be obtained from demodulating the transmitted power at these particular frequencies, $\omega_i^{(x,y)}$, $\omega_e^{(x,y)}$, which for small amplitudes of the oscillations depends linearly on the misalignment of the cavity.

Due to the angular-longitudinal coupling in the presence of a misalignment and a miscentering, the same principle can be applied to the longitudinal corrections of the cavity. When the cavity is aligned there is no coupling to the cavity length and so the longitudinal lock is not perturbed. However, a misalignment will couple the tilting oscillations of the mirrors to the cavity length, and so the frequencies $\omega_i^{(x,y)}$ and $\omega_e^{(x,y)}$ will appear on the longitudinal corrections sent to the mirrors.

This technique is very easy to implement although it gives information about the misalignment of the cavity in the single mirror coordinate system. The preliminary alignment of the AdV arm cavities is done with this technique because it provides a good initial working point without a very complex commissioning. However, the typical performances of this type of alignment are 0.5 mm of accuracy in the centering of the beam. In terms of single mirror alignment it translates in $\sim$0.5 μrad. This is very high if we take in account that the requirements of the alignment of the arm cavities mirrors are $\sim$2 nrad. They are calculated so that the power fluctuations induced by the residual misalignment are lower than 10^{-3}.

Regarding the global alignment of the interferometer it implies the use a big number of different oscillation frequencies, whose amplitudes need to be tuned high enough to be visible but low enough to stay in the linear range of the error signal. For this reason it is only used at the early stages of the alignment process, being substituted by a less invasive and more precise technique further on during the lock acquisition. The requirements for the global alignment will be discussed in more detail in Section 5.4.

Phase modulation: Anderson and Ward techniques

There are two different techniques that use instead frequency modulation. They are also known as *wave-front sensing techniques* because they measure the spatial distortion of the beam phase distribution due to the presence of misalignments.

The first one was developed by **Anderson** in 1984 [39]. It consists of adding a phase modulation at the frequency of the alignment HOMs (TEM_{10} and TEM_{01}), which in the case of a linear cavity is the same for both horizontal and vertical misalignments, ω_1. For a perfect alignment there is only TEM_{00} present, which is on resonance inside the cavity. In this case, the alignment sidebands are not resonant on the cavity.

Instead, when a misalignment is present there will be HOMs excited that will be mostly reflected by the cavity, just as the sidebands of the TEM_{00}. However, the sideband of the HOMs has been chosen at the same frequency as the carrier of the fundamental mode and so the upper one will be resonant in the cavity. This means

that on the presence of a misalignment the **transmitted field** can be written as:

$$E_{tr} = E_0 \cdot H_0(x) \cdot e^{-i\omega_0 t} + E_1 \cdot A_1 \cdot H_1(x) \cdot e^{-i[(\omega_0+\omega_1)t+\phi_1+\phi_0]} \tag{4.84}$$

where E_0 is the amplitude of the on-axis mode, E_1 is the amplitude of the sideband at ω_1 and ϕ_0 is a constant factor that accounts for the phase difference between the fundamental mode and the off-axis one, and the length traversed. From Equations 4.68 and 4.70 we can write:

$$\begin{aligned} A_1 &= \left[\left(\frac{\delta_x}{w_0}\right)^2 + \left(\frac{\alpha_x}{\theta_d}\right)^2\right]^{1/2} \\ \phi_1 &= \arctan\left(\frac{\alpha_x}{\theta_d} \cdot \frac{w_0}{\delta_x}\right) \end{aligned} \tag{4.85}$$

A photodetector in transmission would so detect:

$$\begin{aligned} P_{tr} = &|E_0 \cdot H_0(x)|^2 + |E_1 A_1 \cdot H_1(x)|^2 \\ &+ 2 \cdot A_1 \cdot E_0 \cdot E_1 \cdot H_0(x) \cdot H_1(x) \cdot \cos(\omega_1 t + \phi_1 + \phi_0) \end{aligned} \tag{4.86}$$

However $H_0(x)$ and $H_1(x)$ are orthogonal functions and so the integral of their product is 0. This means that the interference term, which is the one that contains information on the alignment, will disappear since the photodiode integrates the signal over all its surface. Instead, a *split detector* is needed because it divides the plane of the detector in two and so the signal can be constructed as the difference of both halves. Figure 4.31 shows an example of the transmitted electric field when a horizontal misalignment is present. It is clear from it how the difference between the two halves would give you information of the TEM_{10} only, since the fundamental mode is an even function an it will not contribute.

In particular the difference of both halves of the detector can be demodulated at ω_1 as for the PDH error signal in order to extract the relevant information. The error signals obtained after this process are [39]:

$$\begin{aligned} Q_I &= A_1 E_1 \cos(\phi_1) = E_0 E_1 \frac{\delta_x}{w_0} \\ Q_Q &= A_1 E_1 \sin(\phi_1) = E_0 E_1 \frac{\alpha_x}{\theta_d} \end{aligned} \tag{4.87}$$

where Q_I is the in-phase error signal and Q_Q is the in-quadrature one.

As usual, only the horizontal misalignment has been analyzed, but the same reasoning can be applied to the vertical one. However in practice this means that the photodetector has to be divided in four parts in order to obtain signals in both directions, receiving the name of *quadrant photodiode*.

The main advantage of this method is that by tuning the demodulation phase you can decouple the information about tilt and shift. This means that all the information needed to close a loop can be extracted from a single quadrant photodiode. However the disadvantage is that a different modulation frequency is needed for each degree of freedom, which in the case of the global alignment of the interferometer becomes too demanding.

Instead the **Ward** technique takes advantage of the existing modulation that is used for the longitudinal lock. A **photodiode in reflection** of the cavity will

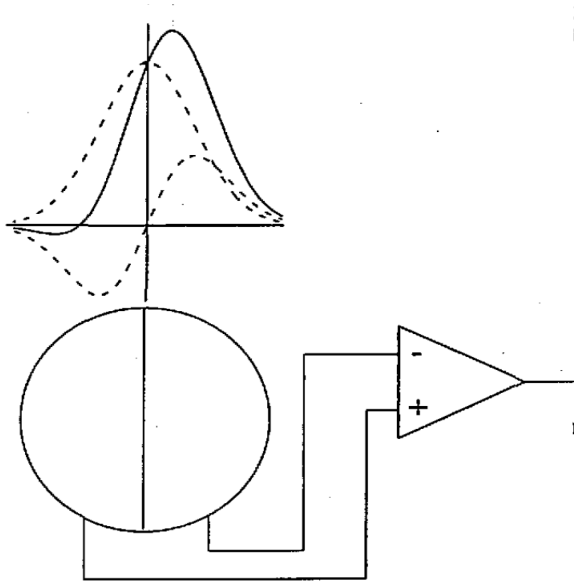

FIGURE 4.31: The plot in the upper part of the figure shows three lines: two dashed lines that correspond to the transverse profile of the TEM_{00} (the symmetrical one) and of the TEM_{01} (the one that crosses zero at the origin) and a continuous line that corresponds to the total electric field as a linear combination of both contributions. An example of a split photodiode is shown in the lower part of the figure, each half is acquired independently and then the demodulation of their difference becomes the error signal [44].

see the sidebands of the TEM_{00} and some of the carrier of the TEM_{00}. In the presence of a misalignment the off-axis modes will be reflected, as well as their sidebands. This means that the signal detected will be the beat note between all these fields as follows [44]:

$$\begin{aligned} P_{ref} = & \left(E_{00}^{c*}E_{10}^{c} + E_{00}^{+*}E_{10}^{+} + E_{00}^{-*}E_{10}^{-}\right) + cc \\ + & \left(E_{00}^{c*}E_{10}^{+} + E_{00}^{-*}E_{10}^{c} + E_{00}^{+}E_{10}^{c*} + E_{00}^{c}E_{10}^{-*}\right) e^{i(\Omega t+\Psi(z))} + cc \\ + & \left(E_{00}^{+}E_{10}^{-*} + E_{00}^{-*}E_{10}^{+}\right) e^{i(2\Omega t+\Psi(z))} + cc \end{aligned} \tag{4.88}$$

where $\Psi(z)$ is the Gouy phase, Ω is the modulation frequency and $E^{+\backslash -}$ represents the upper or lower sidebands.

This expression has a DC term, one at the demodulation frequency and another at twice the demodulation frequency, as in the PDH error signal case. This time we are also interested in the term at Ω so the error signal can be demodulated at this frequency in order to extract the relevant information. Notice that, as in the previous technique, due to the orthogonality of $H_0(x)$ and $H_1(x)$ a split detector will be needed.

However, in this case, as for the PDH technique, all the information is on one projection of the error signal. This means that in principle the information about tilt and shift is mixed. In order to separate both degrees of freedom the dependence of the error signal on the Gouy phase will be used. This can be understood easily from geometrical considerations [45]. At the beam waist, the wave fronts are approximately plane. In this configuration, a tilt will be sensed

as a phase gradient. However, a shift will produce no phase gradient and so a quadrant placed there would not sense anything. On the other hand, at a distance z in the far field of the beam, the radius of curvature converges to z in all cases as it can be seen in Equation 4.33. This means a tilt will not create a phase gradient while a lateral displacement will. Both cases are shown in Figure 4.32.

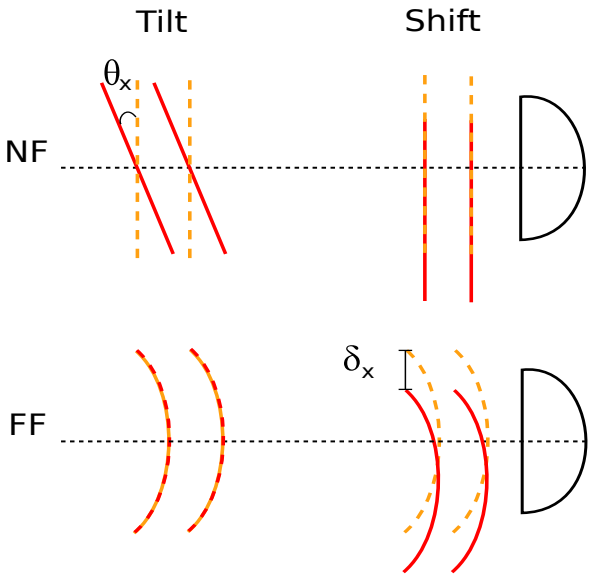

FIGURE 4.32: **Upper picture:** Wave-front of the beam seen by a photodetector placed in the near field of the beam (NF) in the presence of a tilt and a shift respectively. **Lower picture:** Wave-front of the beam seen by a photodetector placed in the far field of the beam (FF).

So even if the error signal contains information both on the tit and the shift, they can be decoupled by using two quadrants: one on the waist of the beam ($\Psi(z) = 0°$) and another one in the far field ($\Psi(z) = 90°$). This technique is the one chosen for the global alignment of the interferometer because even if it requires two quadrants it is the less invasive since it does not impose any extra modulation frequency.

4.6 Summary

The purpose of having Fabry-Perot cavities on the arms of the AdV detector is to increase the optical path travelled by the light that resonates inside them. It has been shown that this condition is maximized in a particular position, called the resonance, specially for the overcoupled optical cavities. However the AdV arm cavities have the particularity of having their mirrors suspended. This translates in a residual motion both in the longitudinal and the angular degrees of freedom which oblige to actively control them to reach the correct working point and avoid a coupling between them. This active control or feedback that brings back the cavity permanently to its working point needs an error signal containing information on the deviation of the dofs from the nominal position.

In the case of the longitudinal control this error signal is produced using the PDH technique. However, the high finesse of the cavity (450) together with the

longitudinal movement of the uncontrolled mirrors produce dynamical effects that distort the error signal. This can be solved by designing an adapted control strategy or lock acquisition, the Guided Lock. This technique tries to slow down the cavity around a resonance until the dynamical effects disappear and the feedback can be engaged normally.

Regarding the angular control there are several techniques that provide information on the misalignment of the cavities, that is on the presence of Higher Order Modes. The easiest to implement is the one using mechanical modulation, which is the one that will be used at the early stages of the global lock acquisition. This technique does not provide the best accuracy but it fixes a good and robust alignment working point that allows the commissioning to move forward.

When it comes to the global alignment of the interferometer the Ward technique will be used because it is less invasive and it provides error signals that decouple the information about the cavity angular degrees of freedom, tilt and shift. For doing this it uses the reflected field of the cavity that is detected by a couple of split photodetectors or quadrant photodiodes placed in strategical places of the laser beam, the waist and the far field.

The characteristics of the full interferometer configuration as well as the global control strategies of both longitudinal and angular degrees of freedom will be discussed in the next chapter.

Chapter 5

Power Recycled Interferometer

In the previous chapter we have introduced the problematic that faces the commissioning of the Advanced Virgo arm cavities. The next step in the commissioning process concerns the Power Recycling configuration of the interferometer (PRITF) and it will be presented here. Notice that this is the target configuration for the first Scientific Run of Advanced Virgo.

The aim is the same as for the cavities, that is, to control the interferometer both longitudinally and angularly. However the full configuration involves several optical cavities bringing new problems of coupling between error signals and thermal transients, increasing the difficulty of finding a lock acquisition scheme, even if at this early stage the thermal transients are not yet relevant.

In this chapter we will define the working point of the PRITF, both for the carrier and for the sidebands. The lock acquisition procedure used in the past to reach the working point will be presented, as well as a detailed study of each of its steps and its validity for the Advanced Virgo optical design. This study will be done using different simulations, in order to find the most convenient set of error signals both during the lock acquisition and in the target configuration, adapting the old sensing when necessary.

Also the optical configuration of the Power Recycling Cavity (PRC) requires a special consideration for being marginally stable. The implications of this fact will be explained as well as the strategies proposed to deal with it.

5.1 PRITF optical configuration

The Advanced Virgo detector is formed by several optical cavities as it was explained in Chapter 2. When all the mirrors are controlled simultaneously we say that the interferometer is on its Power Recycling configuration (PRITF). Figure 5.1 shows the scheme of this configuration with all the lengths that need to be controlled. For simplicity the angular *degrees of freedom (DOFs)* have not been included. They will be presented in a dedicated section (see Section 5.4).

The FP cavities on the arms have been already presented in the previous chapter as well as their longitudinal and angular lock strategies. So far we have considered them independently, however when it comes to the full interferometer the PRC mixes everything, as it will be shown in this section, and it is more convenient to define a *Common* degree of freedom that controls the average length of the arms and a *Differential* one that controls the relative length difference between the arms. This is important because the Differential DOF is the one that will be sensitive to the passage of a GW (see Chapter 2). The cavities longitudinal degrees of freedom can be defined as:

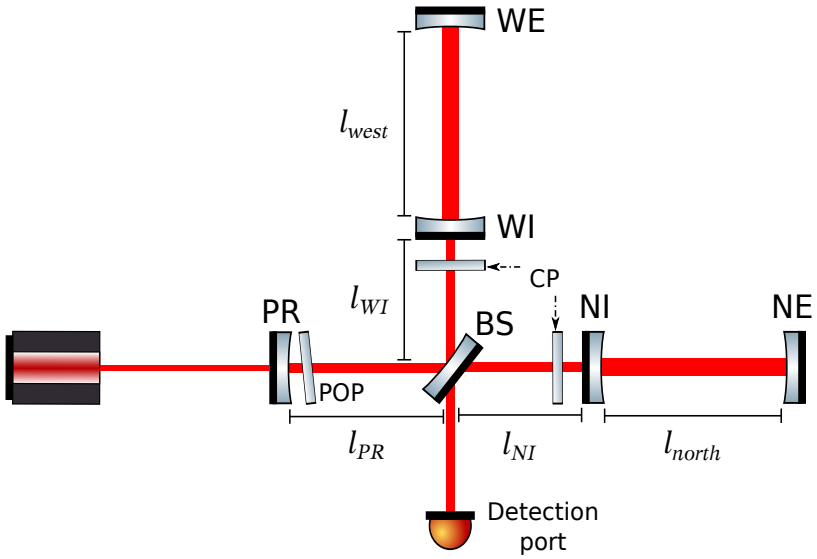

FIGURE 5.1: Scheme of the PRITF with all the lengths that needs to be controlled.

$$\begin{aligned} CARM &= \frac{l_{north} + l_{west}}{2} \\ DARM &= \frac{l_{north} - l_{west}}{2} \end{aligned} \tag{5.1}$$

where $CARM$ stands for the arm's Common DOF and $DARM$ for the arm's Differential one.

Another degree of freedom to be controlled is the Michelson interferometer, which depends on the length difference between the two short arms ad it is defined as:

$$MICH = l_{NI} - l_{WI} \tag{5.2}$$

Finally the last length to be controlled is the one of the PRC which depends on the distance between the Power Recycling Mirror (PR) and the Beam Splitter (BS) and the average length between the BS and the Input Mirrors such as:

$$PRCL = l_{PR} + \frac{l_{NI} + l_{WI}}{2} \tag{5.3}$$

These are the four DOFs that need to be controlled. In order to reach the maximum sensitivity, they need to be controlled in a particular position or **working point**.

- The **carrier field has to be resonant inside the arm Fabry-Perot cavities**, as seen in the previous chapter.
- The **carrier field has to be resonant inside the PRC** in order to enhance the effective input power as much as possible, as explained in Chapter 2, and reach the arms.
- As introduced in the previous chapter, the control strategy of the arms is based on the PDH technique, that uses RF sidebands as a phase reference to

build the error signal. For this reason, **the sidebands can not be resonant inside the arm cavities**.

- This implies that also the **sidebands have to be resonant inside the PRC**, otherwise, they would not reach the arm cavities.
- A phase reference is also needed to build up an error signal for PRCL. For this reason it is necessary to use a **modulation frequency that is not resonant inside the PRC**.
- The chosen detection technique that is explained in Chapter 2 requires the **Michelson DOF to be in destructive interference at the detection port** (see Figure 5.1), that is to be tuned at a *Dark Fringe (DF)*.

Finally, an offset is added to the MICH DOF in order to allow the **DC readout** explained as well in Chapter 2. The passage from RF to DC readout has been already studied in [46]. In the following we will consider only the global control of the PRITF until reaching the DF. Taking this into account the field equations for the PRITF can be calculated at its working point.

5.1.1 Electric field equations in Dark Fringe: carrier

As seen in Section 4.1 the arm Fabry-Perot cavities can be characterized by their reflectivity, their transmission and their Finesse or Optical Gain (see Equations 4.2, 4.3 and 4.9). This means that effectively they can be treated as equivalent mirrors, which simplifies the calculations of the electric field for the PRITF configuration.

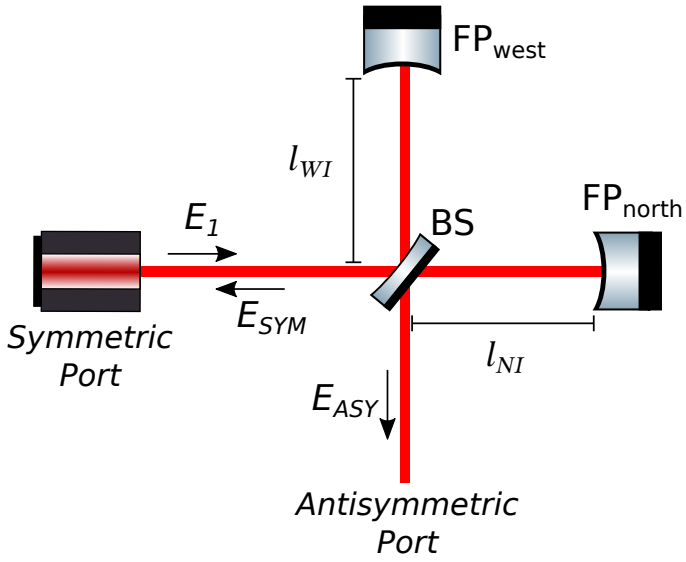

FIGURE 5.2: Scheme of a Michelson interferometer with Fabry Perot cavities as equivalent mirrors.

Let's consider then a simple Michelson interferometer, as shown in Figure 5.2, whose mirrors reflectivity and transmission are the ones of the Fabry-Perot arm cavities. In this case the field that arrives to the Detection port or *Antisymmetric port* and to the *Symmetric port* can be written as:

$$E_{ASY} = E_1 \cdot \frac{r_{FP}}{2} \cdot \left(e^{2ikl_{NI}} - e^{2ikl_{WI}} \right) \tag{5.4}$$

$$E_{SYM} = -E_1 \cdot \frac{r_{FP}}{2} \cdot \left(e^{2ikl_{NI}} + e^{2ikl_{WI}}\right) \tag{5.5}$$

where r_{FP} is the reflectivity of the Fabry-Perot arm cavities (see Equation 4.2), l_{NI} is the distance between the BS and the NI mirror and l_{WI} the one between BS and WI mirror. The BS reflectivity and transmission have been considered as $t_{BS} = r_{BS} = \frac{1}{\sqrt{2}}$.

From these equations it can be understood that the Antisymmetric port will be sensitive to the phase difference between the short Michelson arms while the Symmetric port will be sensitive to common phase changes. In order to simplify the working point definition it is useful to define two lengths:

$$\begin{aligned} L_+ &= \frac{l_{NI} + l_{WI}}{2} \\ L_- &= \frac{l_{NI} - l_{WI}}{2} \end{aligned} \tag{5.6}$$

Using these expressions, Equations 5.4 and 5.5 can be re-written as:

$$E_{ASY} = i \cdot E_1 \cdot r_{FP} \cdot e^{2ikL+} \cdot \sin(2kL_-) \tag{5.7}$$

$$E_{SYM} = -E_1 \cdot r_{FP} \cdot e^{2ikL+} \cdot \cos(2kL_-) \tag{5.8}$$

The argument of the sine and the cosine in these expressions defines the interference condition, and so the working point. It depends on the wavenumber and on the length L_-, which is proportional to the MICH length that needs to be controlled.

The chosen **working point is the Dark Fringe**, which means that there is no carrier that arrives to the Antisymmetric port. The microscopic interference condition can be then defined as:

$$\sin(2kL_-) = 0 \quad \longrightarrow \quad 2 \cdot k \cdot L_- = \pi \cdot n \tag{5.9}$$

where n is an integer number.

In terms of the degree of freedom to be controlled this means:

$$MICH = \frac{\pi \cdot n}{k} = n \cdot \frac{\lambda}{2} \tag{5.10}$$

Finally we can calculate the reflectivity and the transmission of a Michelson interferometer, enhanced with Fabry-Perot cavities, in Dark Fringe:

$$\begin{aligned} t_{ASY} &= 0 \\ r_{SYM} &= -r_{FP} \cdot e^{2ikL_+} \end{aligned} \tag{5.11}$$

The same exercise of considering the FP cavities as an equivalent mirror can be done now with the Michelson interferometer. It can be considered as a mirror whose reflectivity and transmission varies as a function of the interference condition. Following this reasoning, the full interferometer can be modelled as a single FP cavity whose input mirror is the Power Recycling Mirror and whose end mirror is the enhanced Michelson, as shown in Figure 5.3.

An analogous analysis as the one done in Section 4.1 for a simple FP cavity can be applied in this case in order to calculate the most relevant fields:

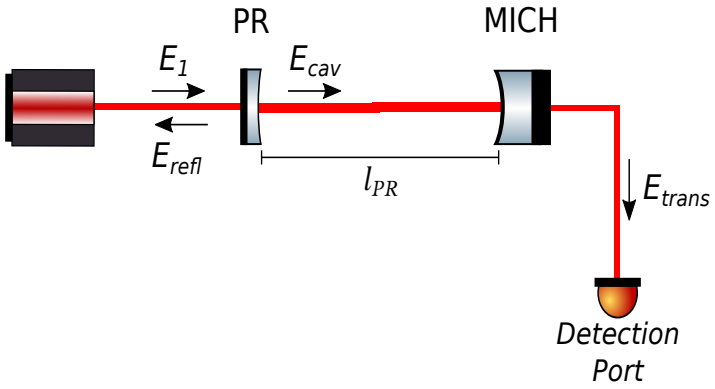

FIGURE 5.3: Scheme of the whole PRITF configuration simplified as a Fabry-Perot cavity. The input mirror is the PR and the end mirror is the Michelson interferometer enhanced by the Fabry Perot arm cavities.

- Intra-cavity field: it contains the optical gain for the carrier

$$E_{cav} = E_1 \cdot \frac{t_{PR}}{1 - r_{PR} \cdot r_{SYM} \cdot e^{2ikl_{PR}}} \tag{5.12}$$

- Reflected field: signal that comes back to the Symmetric port

$$E_{refl} = E_1 \cdot \frac{r_{PR} + r_{SYM} \cdot \left(r_{PR}^2 + t_{PR}^2\right) \cdot e^{2ikl_{PR}}}{1 - r_{PR} \cdot r_{SYM} \cdot e^{2ikl_{PR}}} \tag{5.13}$$

- Transmitted field: signal that gets to the Detection port

$$E_{trans} = E_1 \cdot \frac{t_{PR} \cdot t_{ASY} \cdot e^{ikl_{PR}}}{1 - r_{PR} \cdot r_{SYM} \cdot e^{2ikl_{PR}}} \tag{5.14}$$

These expressions contain all the information of how the PRITF behaves. It is worth mentioning that they depend either on r_{SYM} or on t_{ASY}, which depend as well on the FP arm cavities behaviour, showing that the four DOFs are strongly coupled.

Finally the working point can be fully determined by forcing the **carrier to be resonant on the Power Recycling Cavity**. Again, this happens when the intra-cavity field is maximum, and if we write E_{cav} in the DF configuration (using Equation 5.11) it is straightforward to obtain the resonance condition for the PRC:

$$E_{cav} = E_1 \cdot \frac{t_{PR}}{1 + r_{PR} \cdot r_{FP} \cdot e^{2ik(l_{PR}+L_+)}} \tag{5.15}$$

where $(l_{PR} + L_+)$ corresponds to the PRCL DOF previously defined in Equation 5.3. Now we can impose the resonance condition that maximizes this expression:

$$e^{2ikPRCL} = 1 \quad \longrightarrow \quad 2 \cdot k \cdot PRCL = 2 \cdot n \cdot \pi \tag{5.16}$$

where n is an integer number. Notice that the resonance condition is positive because the reflectivity of the FP cavities when the carrier is resonant is negative (see Equations 4.55 and 4.56).

This resonance condition, restricts the length of the PRC so that the carrier is resonant when:

$$PRCL = n \cdot \frac{\lambda}{2} \tag{5.17}$$

At this point we can evaluate the nominal optical gain, reflectivity and transmission of the carrier inside the PRC when the full ITF is controlled at its working point: As the PRC is overcoupled we can calculate the finesse from the OG, using

OG^c_{PRC}	R^c_{PRC}	T^c_{PRC}
37.91	0.9995	0

TABLE 5.1: Optical parameters of the Power Recycling Interferometer for the carrier. Not all the power is reflected due to the losses in the different optics involved

Equation 4.60, $\mathcal{F} = 59.5$. The pole of the PRC is at a higher frequency than for the arm cavities, $f_{PRC} = 100kHz$.

5.1.2 Sidebands behaviour: Schnupp asymmetry and PRC length

Now that the working point of the carrier in the PRITF configuration has been defined, it is necessary to take into account the role of the sidebands. As explained in Section 4.4.2, sidebands are used as a phase reference in the control of the arm cavities, either in reflection or in transmission. This imposes a condition on their frequency, since they need to be **resonant on the PRC** in order to reach the input mirrors.

It is easy to write the intra-cavity field of the PRC for the sidebands, by replacing k with their wavenumber $k' = k \pm \frac{\Omega}{c}$, always under the assumption that the carrier is in Dark Fringe and resonant inside the PRC:

$$E^s_{cav} = E_1 \cdot \frac{t_{PR}}{1 + r_{PR} \cdot r^s_{FP} \cdot \cos\left(\pm\frac{2 \cdot \Omega L_-}{c}\right) \cdot e^{\pm 2i\frac{\Omega}{c}PRCL}} \tag{5.18}$$

The resonance condition for the sidebands can be defined then as:

$$e^{\pm 2i\frac{\Omega}{c}PRCL} = -1 \quad \longrightarrow \quad 2 \cdot \frac{\Omega}{c} \cdot PRCL = (2 \cdot n + 1) \cdot \pi \tag{5.19}$$

where n is an integer number, and Ω is the modulation frequency, $\Omega = 2\pi f_1$

The PRC microscopic length is fixed already by the carrier resonance condition (see Equation 5.17) and now we can define the the sidebands resonance condition which will stablish the relationship between the allowed modulation frequencies and the macroscopic PRC length, such as:

$$\nu_{mod} = (2 \cdot n + 1) \cdot \frac{c}{4 \cdot PRCL} \tag{5.20}$$

AS the PRCL is conditioned by the mirrors towers position, the first possible frequency is the one used in Advanced Virgo for the longitudinal control, $f_1 =$ 6.270777 MHz. Once this value has been fixed, we can choose the value of the sideband used to control the PRC, $f_2 = f_1 \cdot 4/3$. Its value was only conditioned by the IMC length, which was fixed in turn to allow the passage of the 6 MHz.

Moreover, in order to have an **error signal at the Detection port**, a phase reference is needed and so the sidebands must reach the Antisymmetric port even in Dark Fringe. This implies that the interference condition of the Michelson interferometer can not be destructive for the sidebands at the same time as for the carrier. This can be easily understood by writing Equations 5.7 and 5.8 for the sidebands wavenumber, *k'*:

$$E^s_{ASY} = i \cdot E_1 \cdot r^s_{FP} \cdot e^{2ik'L_+} \cdot \sin\left(\pm\frac{\Omega\Delta_S}{c}\right) \tag{5.21}$$

$$E^s_{SYM} = -E_1 \cdot r^s_{FP} \cdot e^{2ik'L_+} \cdot \cos\left(\pm\frac{\Omega\Delta_S}{c}\right) \tag{5.22}$$

where $\Delta_S = l_{NI} - l_{WI}$.

In the previous section the microscopic interference condition for MICH has been established in Equation 5.10. However, a macroscopic length Δ_S can be defined to change the interference condition of the sidebands without spoiling the carrier one. This parameter is also called the *Schnupp asymmetry*. In Virgo it had a value of 0.84 m, but for Advanced Virgo it has been reduced to 0.23 m. This change was motivated by a future upgrade which implies the installation of a new mirror between the BS and the Detection port, forming a new resonant cavity, the Signal Recycling Cavity. The studies showed [47] that in order to optimize the performance of this new configuration the Schnupp Asymmetry needed to be smaller to avoid back-coupling of this new cavity to the other DOFs. Ideally, the target value was 5cm which would cause a back-coupling lower than 10%. However, 0.23 m was the lowest value that could be reached given the towers position which implies approximately 60% of back-coupling.

Notice as well that the value of the electric field at the symmetric and anti-symmetric ports depends on the value of the modulation frequency. This means that each sideband will see a different Finesse of the PRC since the reflectivity of the effective end mirror will change. In particular, higher frequencies will be more transmitted to the ASY port and so they will see a lower finesse. Table 5.2 shows the optical gain of the PRC for different sideband frequencies at the working point.

Modulation frequency	OG^s_{PRC}
6 MHz	77.16
56 MHz = f_1 x 9	13.25
131 MHz = f_1 x 21	1.05

TABLE 5.2: Optical gain of the Power Recycling Interferometer for different sidebands frequency, where f_1 is the main modulation frequency, 6.27 MHz.

It can be seen that the 6MHz sidebands experience a higher OG than the carrier inside the PRC. This is because they are not resonant inside the arms and so they see a higher reflectivity $r^s_{FP} > r^c_{FP}$. Figure 5.4 shows a scan of the PRC including the contributions of the sidebands at the working point. The 6, 56 and 131 MHz are resonant at the same time as the carrier while the 8 MHz resonates has a different resonance condition. The sidebands are not perfectly superposed because their interference condition is not exactly the same due to the Schnupp asymmetry.

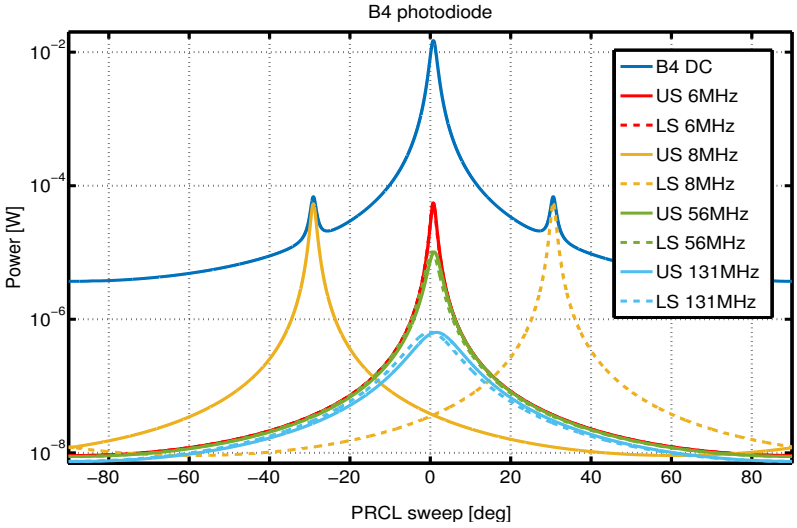

FIGURE 5.4: Simulation of the total power and contribution from the different sidebands to the power inside the PRC (B4 photodiode) for a sweep of the PRC length at the working point.

5.1.3 Summary: Working point

In this section we have defined the target working point for the PRITF configuration, and the microscopic lengths of the different DOFs. The carrier fixes these lengths which are gathered in Table 5.3. The role of the sidebands is to provide a phase reference in order to build up good error signals: one for the arm cavities, f_1, one for the PRC, f_2, and a macroscopic length difference in the short arms for the Michelson, Δ_S. These conditions are also shown in Table 5.3.

Carrier			Sidebands		
MICH	**PRCL**	**Arm L**	$\mathbf{f_1}$	$\mathbf{f_2}$	$\mathbf{\Delta_S}$
$n \cdot \frac{\lambda}{2}$	$n \cdot \frac{\lambda}{2}$	$n \cdot \frac{\lambda}{2}$	$(2n+1) \cdot \frac{c}{4 \cdot PRCL}$	$f_1 \cdot \frac{4}{3}$	0.23 cm

TABLE 5.3: Resonance conditions of the longitudinal DOFs to reach the working point for the carrier and for the sidebands.

Once at this working point, the Optical Gain of the carrier and the first sideband, f_1, is shown in Table 5.4. In order to illustrate the effect of the Schnupp asymmetry, the Optical Gain inside the PRC of two modulation frequencies with a higher value are also shown in Table 5.4 for comparison.

	Carrier	6 MHz	56 MHz	131 MHz
OG_{PRC}	37.91	77.16	13.25	1.05

TABLE 5.4: Optical Gain of the PRC for the carrier and for different modulation frequencies, all of them resonant inside the PRC.

5.2 Longitudinal control

So far the desired working point for the PRITF has been defined, as well as the frequency of the sidebands needed. Now we are going to address the problem of how to control the system to reach this working point. As mentioned in the previous chapter, the mirrors move due to the seismic noise and so an active control is needed in order to keep the relevant lengths at the desired values.

However, this configuration is more complex than the single FP cavity, because there are several coupled DOFs to be controlled simultaneously and independently. For this reason the choice of the error signals (sensing) and the way of applying the correction calculated (driving), need a careful study. In the target working point we need a sensing with very high sensitivity, so a high SNR, and during the lock acquisition it is more important to have robust error signals, that are well decoupled between them. A detailed analysis of the sensing will be presented, based on the results of simulations done with Optickle and Finesse 3.1.

5.2.1 Final State: Sensing and driving

In this configuration there are several photodiodes available and so several potential error signals for each degree of freedom. Figure 5.5 shows all the photodiodes available and their location. The ideal ones are chosen based on the following criteria:

- **Maximize the slope**: the precision of the lock is given by the slope of the error signal. It has to be as high as possible in order to maximize the Signal to Noise Ratio (SNR) and so to be more sensitive to deviations from the working point. Notice that, as it was shown in Equation 4.59, the OG value is **proportional to the power and to the finesse**.

- **Linear region**: a good error signal has to measure how far the DOF is from the working point. This is true on the region where it is linear with respect to the longitudinal displacement. For this reason it is important to maximize the width of the linear region.

- **Zero-crossing**: the control loop will bring the system at the position where the error signal is zero. For this reason the zero-crossing of an error signal has to point to the desired working position.

For a single FP cavity the first two conditions are complementary, that is, a high slope implies a narrower linear region and vice versa. However, the PRITF is a more complex example with several coupled cavities whose interactions do not always behave as expected. For this reason we will consider these two parameters independently in our analysis.

These are the criteria that are used to choose the ideal error signal for each DOF. However, there is one more consideration that needs to be taken into account: **the coupling between DOFs**. It is a crucial issue because the error signals are used to calculate the length correction needed to bring the different DOFs back to their working point independently. If the error signal can not decouple the information about the DOF that needs to control from the other ones, the loop will move the system away from the good working point.

Typically, two parameters are used in order to determine the coupling between DOFs at a given sensor. The first one is the **demodulation phase** that provides the optimal error signal for a given DOF (ϕ_{max}) which is the one that fulfils the

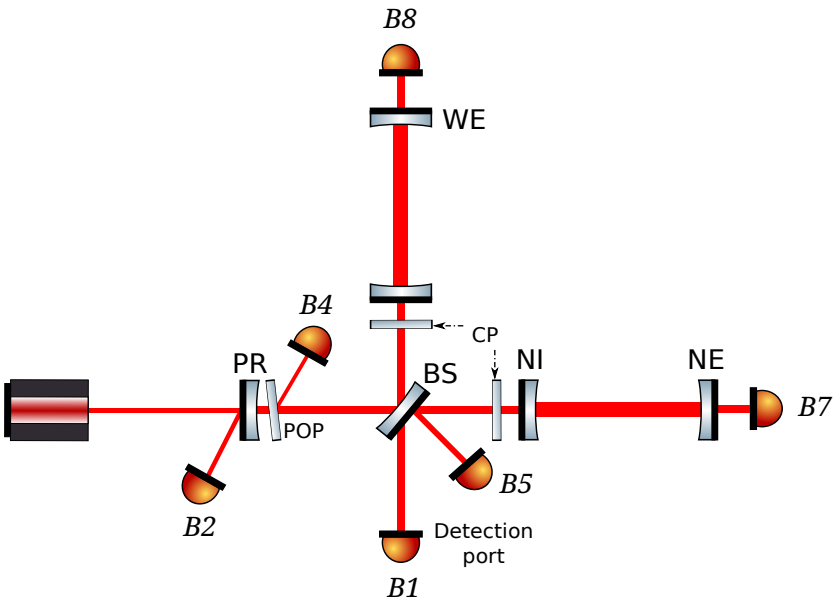

FIGURE 5.5: Scheme of the Power Recycling Interferometer showing the position of the longitudinal photodiodes.

best the three conditions that were just presented. The second one is the **Optical Gain** at this demodulation phase. With these parameters we can build a **compass plot** that presents the optimal OG at the corresponding demodulation phase for each DOF. Ideally the slope scales linearly with the demodulation phase and so it is a very visual way to understand the contribution of each DOF for a given ϕ, and so the coupling between DOFs for all demodulation phases.

Ideally we want the DOFs to be completely decoupled. This means that at a given sensor the information is distributed so that a basis can be found where the interesting DOF is all in the in-phase projection (P) and all the information about the other DOFs is in the in-quadrature projection (Q). In practice their ϕ_{max} have to be 90° apart. However, this requirement is very stringent and there are circumstances under which the coupling exists but can be neglected, for example if one of the DOFs is completely dominant.

A careful study of the optimal **sensing at Dark Fringe** has been done using the simulation tool Finesse (see Section 3.1). The target was to check whether the sensing scheme used in Virgo+ is still valid in the present configuration also considering the new photodiode available to monitor the Intra-cavity power, B4 (see Section 3.5).

The first step was to find the good working point in the simulation, that is:

- **MICH**: minimum of B1 photodiode DC signal, which indicates that the interferometer is in Dark Fringe.
- **PRCL**: maximum of B4 photodiode DC signal, which indicates the resonance of the recycling cavity.
- **Arm cavities**: maximum of B7 and B8 DC signals respectively, which indicates the resonances of the arm cavities.

At this position, the **demodulation phase** was optimized in the model at each photodiode for each DOF in order to obtain the best error signals possible. Already

at this stage, the error signals that do not have a **good zero crossing** (due to offsets or even double zero-crossings), or that are not **linear** around the working point can be excluded as candidates. Then, the remaining possible signals are classified depending on their **OG** (from the highest to the lowest one). Once this is done, the **cross-coupling** between DOFs is checked starting from the best candidate, until finding an error signal that fulfils all the conditions. In order to obtain realistic results we have taken into account the attenuation due to the telescope of each photodiode.

A summary of the best error signals is presented in Table 5.5, together with the error signals used in Virgo+ for comparison. They have been chosen following the process just described.

	MICH	PRCL	CARM	DARM
Virgo+	B5 6MHz	B2 8MHz	B5 6MHz	B1 6MHz
Advanced Virgo	B4 6MHz	B2 8MHz	B2 6MHz	B1 6MHz

TABLE 5.5: Error signals used for the longitudinal control of the different DOFs in Dark Fringe in Virgo+ and the optimal ones for Advanced Virgo. The first term is the photodiode name and the second one the demodulation frequency.

For both DOFs, PRCL and DARM, the error signals used in Virgo+ are still the best option for the Advanced Virgo configuration. Instead for the MICH DOF the B4 photodiode is less coupled to the other DOFs than B5. For CARM, the best candidate is B2 photodiode, which shows a higher OG and less coupling.

Figure 5.6 shows the chosen signals and it can be seen that they fulfill all the conditions to be good error signals. Concerning the coupling, the corresponding compass plots are shown as well as the contribution from the other DOFs to the error signals chosen. There is a lot of information on this Figure 5.6 and we will try to clarify its meaning by analysing it in more detail.

Notice that, unless indicated, the signals showed in these plots are the ones coming directly from the interferometer; no attenuation due to the optical benches has been considered. This is important to compare photodiodes between them but not for evaluating the coupling to a single photodiode.

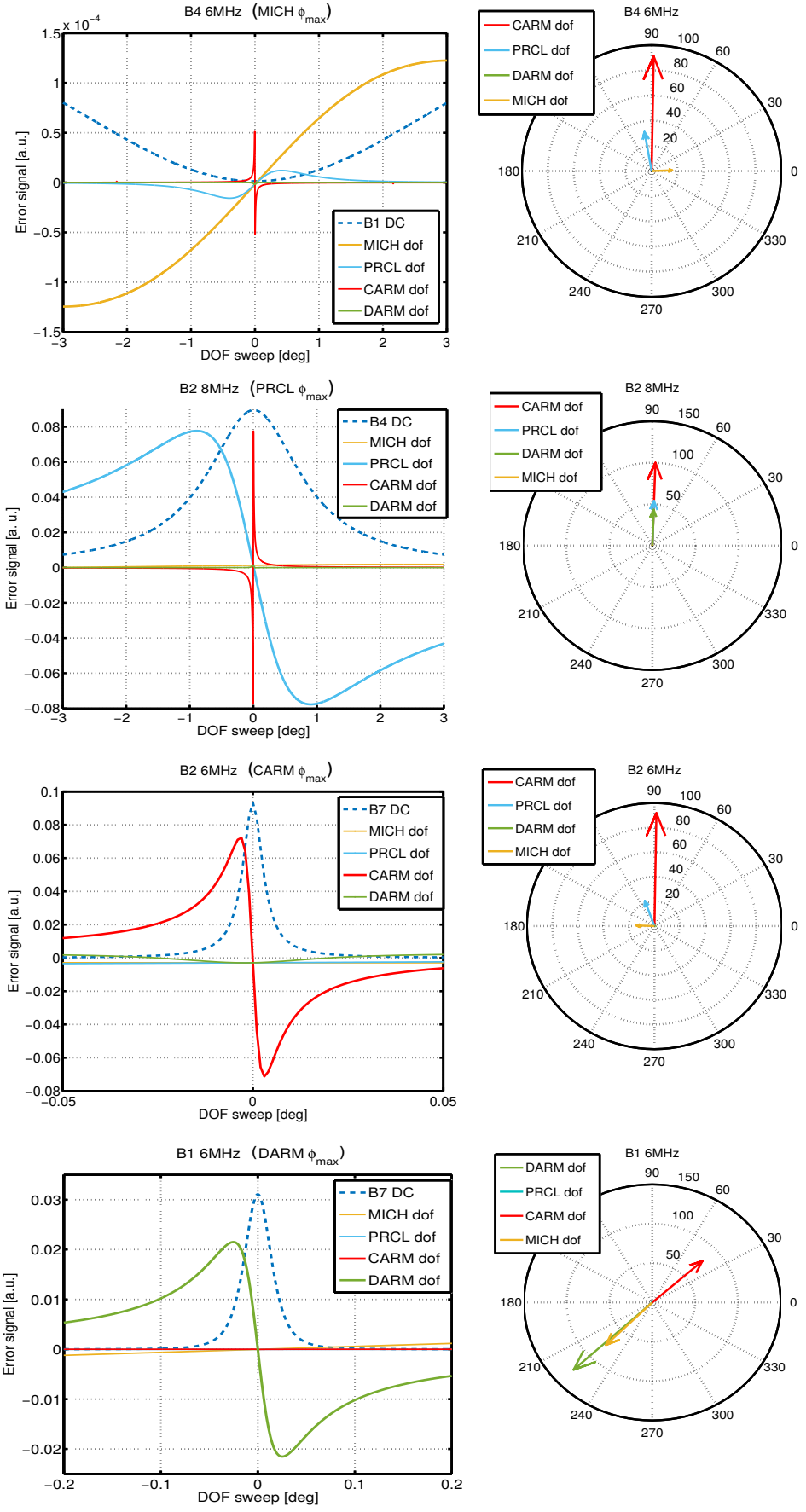

FIGURE 5.6: **Left plots:** Error signal response to the sweep of the different DOFs. For each error signal the demodulation phase tuned for the DOF to be controlled. The relevant DC powers are shown in dashed as an indication of the working point. **Right plots:** Compass plots that show for each DOF the optimal demodulation phase and the corresponding OG.

First interesting thing to notice in Figure 5.6 is that in the compass plots **CARM is the dominant signal**, which means that all the photodiodes see (with better or worse error signals) the common degree of freedom. This is a particular case, because the seismic noise is not the only contributor but also the frequency noise of the laser. As it was mention in Chapter 2, the cavities are unable to distinguish between a change on the length of the laser or on the length of the cavity. For this reason both noise sources are mixed in the CARM DOF.

Since the frequency noise typically extends up to the kHz region, a mechanical control only is not sufficient to compensate for it and so the corrections are sent to the laser itself. However, this loop is quite complex because it involves as well the Input Mode Cleaner and the Reference Cavity and we will enter into details in the next section (see Section 5.3). For the present analysis is enough to know that the CARM DOF will be controlled with a very high bandwidth, ∼20 kHz. For this reason we can consider that in the region of interest (∼100 Hz) it is suppressed by a factor equal to the gain of the loop in this region. This means a factor 1000 during the lock acquisition and a factor 10^8 (80 dB) in DF with the final optimized filter [46]. In practice this means that it is negligible in all cases.

The plots on the left side of Figure 5.6 give a lot of interesting information as well. Each error signal is maximized for the relevant DOF by tuning the demodulation phase, ϕ_{max}. Then, a sweep of the length of all DOFs around their working point is made, in order to see better the contribution of the non-interesting DOFs to the error signal. In fact they show that the **compass plots are not enough to understand if the DOFs are coupled or not**.

A good example of this is the error signal for PRCL, B2 8MHz. The compass plot shows that all the DOFs are very coupled, since their maximum OG is attained for the same demodulation phase. However, we have checked in the plot on the left that MICH and DARM DOFs are not good error signals: they do not cross zero and they are not linear. As their value is very small with respect to the amplitude of the PRCL contribution, their coupling can be neglected.

The information given by the compass plot is misleading because the demodulated signal is not a good error signal for these DOFs and so it does not behave as a PDH signal. In such a complex optical configuration, there are non-trivial couplings between DOFs and often the sidebands are not balanced, which causes complex interactions between the sidebands and the carrier. An example of a misbehaviour of this type is shown in the right plot of Figure 5.7.

This type of signal changes dramatically with the demodulation phase and so their slope do not scale properly and a compass plot in this case is meaningless. The DOFs whose contribution behaves this way do not couple strongly to the relevant DOF, since they do not cross zero at the working point and so they do not modify the nominal OG. However, as they are non-zero at the working point, they introduce an offset, changing the zero-crossing position and as a consequence the working point. Depending on the value of this offset, the distortion caused by the contribution of the other DOFs can spoil the error signal. This means that we need to consider two sources of coupling: when the **signal that couples crosses zero**, it affects the OG of the error signal and when it **does not cross zero** it modifies the error signal zero-crossing by adding an offset.

Taking into account these considerations, the only error signal which is still coupled to a DOF is B2 8MHz, which sees the variations of CARM. However this is not worrying, first of all because CARM is strongly suppressed and second, because the coupling is unilateral which means that CARM error signal does not see PRCL

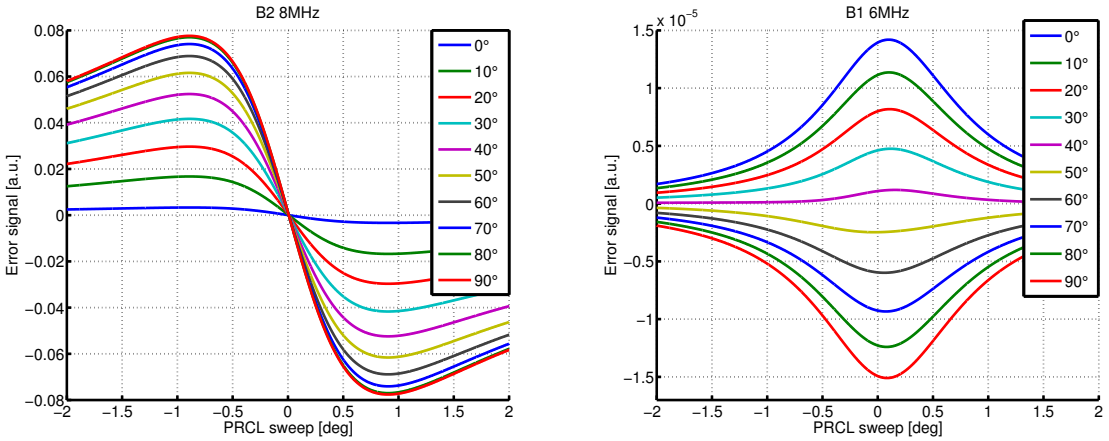

FIGURE 5.7: Response of two error signals to a sweep of the PRC length for different demodulation phases. **Left plot:** B2 8MHz, good PDH error signal. **Right plot:** B1 6MHz, bad error signal whose behaviour depends strongly on the demodulation phase.

DOF. So as long as CARM is controlled in first place, this coupling will not become a problem.

Table 5.6 shows the sensing matrix for the working point of the PRITF configuration. It shows the Optical Gain (W/m) of the chosen error signals when they are optimized for the interesting DOF. CARM is a special case as it was already mentioned and so the OG shown is the one in-loop, supposing a suppression of 10^8 in DC, which is a conservative factor. The cells marked with a line represent the DOFs which do not contribute to the sensing matrix, since they do not couple to the OG because they are not linear around the working point.

	DARM	MICH	CARM in-loop	PRCL
B1 6MHz	$\mathbf{6.7 \cdot 10^{-3}}$	$-2.3 \cdot 10^{-5}$	–	–
B4 6MHz	–	$\mathbf{-2.8 \cdot 10^{-7}}$	$9.3 \cdot 10^{-5}$	$\mathbf{-2.4 \cdot 10^{-7}}$
B2 6MHz	–	–	$\mathbf{0.13 \cdot 10^{-8}}$	–
B2 8MHz	–	–	$-0.14 \cdot 10^{-8}$	$\mathbf{6.9 \cdot 10^{-4}}$

TABLE 5.6: Sensing matrix of the Power Recycling Interferometer on its working point. The values in bold represent the most relevant contributions to each error signal.

The most relevant contributions are shown in bold and it can be seen that the sensing matrix is triangular. This means that it can be diagonalized and so the control will be able to decouple all the DOFs. In this case we have taken into account the optical benches attenuation of each photodiode.

Once the sensing is fixed, and so the optimal error signal has been chosen for each DOF, we need to consider how to **actuate on the system (driving)**. So far the error signals are decoupled so that each of them provides information about one DOF only. However, it is necessary to preserve this decoupling when applying the corrections, which is the role of the *driving matrix*.

The driving matrix carries the information about which mirrors need to be moved, and how much they need to be moved in order to act on each DOF independently. This way we know how and to which mirrors the corrections calculated by the control filter of each DOF need to be applied.

As the geometry of the interferometer has not changed, the driving matrix used in Virgo+ is still valid for Advanced Virgo [46]. The strategy chosen was to leave the Input Mirrors swinging freely and apply the corrections needed to the other mirrors:

	DARM	CARM	MICH	PRCL
NE	-1/2	-1		
WE	1/2	-1		
BS			$1/\sqrt{2}$	
PR			-1/2	-1

TABLE 5.7: Driving matrix of the Power Recycling Interferometer [46].

5.2.2 PRC stability vs. alignment: 131MHz

As it was anticipated in the introduction the Power Recycling cavity needs a special consideration due to its optical configuration. The conditions for an optical cavity to be stable were explained in Section 4.3.3. The PRC of Advanced Virgo is very close to the limit of stability, in particular $1-g_1g_2 = 0.19\cdot10^{-5}$, which is equivalent to $\Psi_G = 2$ mrad. This situation is worsened by the mirror imperfections since they scatter light from the fundamental mode to the HOMs.

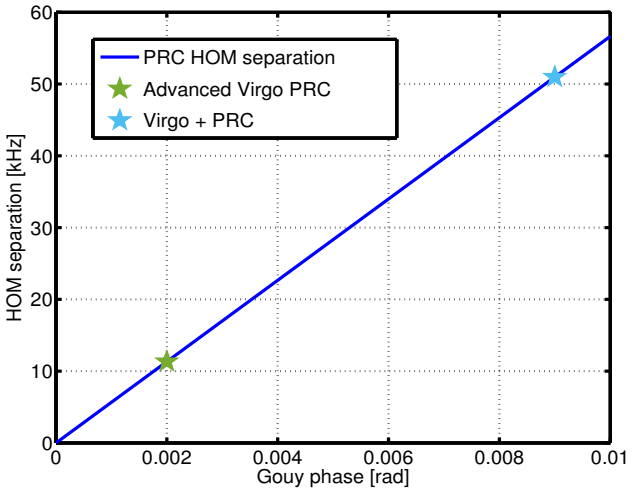

FIGURE 5.8: HOM separation in the PRC as a function of its Gouy phase. The Advanced Virgo and Virgo+ PRC configurations are shown for comparison.

The consequence of being so close to the instability region is that the frequencies of the HOMs are very close to the fundamental mode. In this case, in the presence of HOMs (due to a misalignment or to a mismatch for example) they will

couple very strongly to the optical cavity, diminishing the power in the fundamental mode. Figure 5.8 shows the relationship between the HOM separation for the PRC and the Gouy phase of the cavity. On it they are marked the Advanced Virgo configuration as well as the Virgo+ one. The separation decreases with the Gouy phase, until becoming a degenerate cavity when reaching instability.

The frequency separation between HOMs has been calculated from Equation 4.39, and for the PRC is 11.3 kHz. When compared to its linewidth which is 210 kHz it is obvious that the coupling is going to be very important. Figure 5.9 shows the power distribution between the fundamental mode and the different HOMs on the B4 photodiode for a scan of the PRC length at the working point. Only the first four orders are shown, but it is clear that the coupling of the HOMs inside the interferometer is very important.

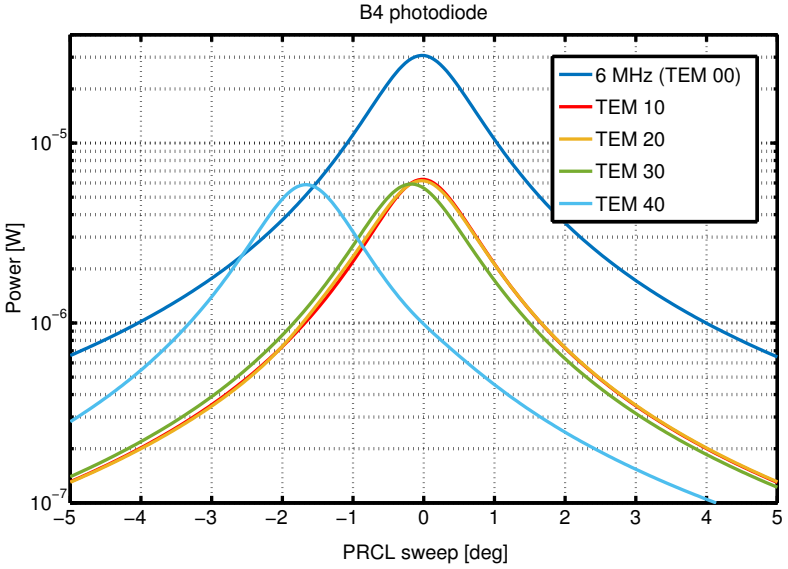

FIGURE 5.9: Simulation of the power impinging on B4 for a scan of the PRC length around the working point when there are HOMs present in the input beam. The distribution of the power between the fundamental mode and the HOMs is shown explicitly.

In practice this will have an impact on the stability of the control loop. The longitudinal control filter is designed for the nominal Optical TF, however as the power in the fundamental mode will change so will do the DC value of the Optical TF. If the power fluctuations are larger than the amplitude margin of the filter, the control will become unstable, causing the loop to saturate and open.

This could be a problem in case of fluctuations such as the ones of the alignment DOFs when only the Local Controls (LC) are engaged. In order to evaluate the impact of the alignment on the optical gain, several Finesse simulations of the Central Interferometer (CITF) configuration were done. This configuration consists in misaligning the end mirrors to "remove" the arm cavities, which leaves only the two central DOFs, MICH and PRCL, to be controlled as shown in Figure 5.10. It is simpler than the PRITF one, but sufficient to study the behaviour of the carrier and the sidebands inside the PRC, which is our target, as we will see now.

For the sidebands the CITF configuration is equivalent to the PRITF one, scaled by the fact that they see the reflectivity of the input mirrors instead of the

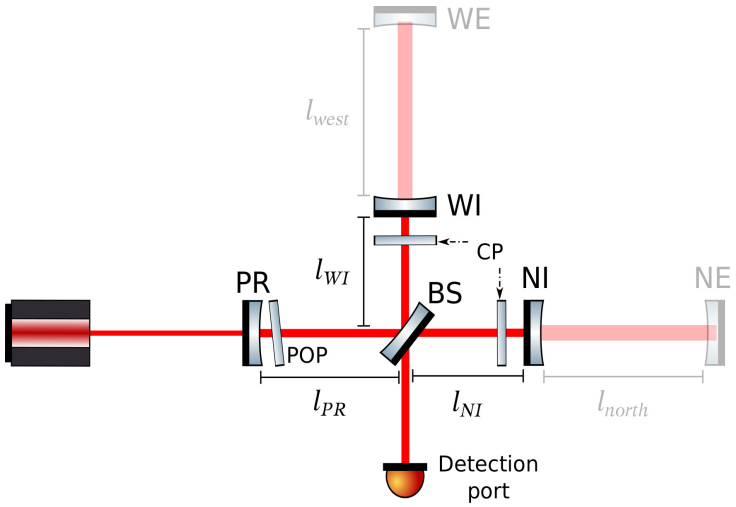

FIGURE 5.10: Scheme of the Central Interferometer with the relevant lengths to be controlled.

reflectivity of the FP cavities out of resonance, and so they see a lower finesse of the PRC. The carrier sees as well the reflectivity of the input mirrors, which raises slightly its finesse inside the PRC instead, see Table 5.8.

Modulation frequency	OG^s_{PRC}
Carrier	49.3
6 MHz	47.91
56 MHz = 6 x 9 MHz	10.80
131 MHz = 6 x 21 MHz	1.00

TABLE 5.8: Optical Gain of the CITF for the carrier and the different sidebands frequency.

The main difference with respect to the PRITF configuration is that when the carrier is resonant inside the arms it acquires an extra phase π due to the cavity reflectivity that makes it resonant on the PRC at the same time as the sidebands (see Figure 4.3). But this is not the case anymore for the CITF and so the carrier and the sidebands do not resonate at the same time inside the PRC. This is not a problem although it obliges us to study them separately.

The first study showed that indeed the impact of the alignment was very strong, with a loss of 80% of the OG in the presence of a misalignment of 0.15 μrad on the PR mirror [48]. The Local Controls are not precise enough to control the mirrors with a 0.1 μrad precision so it was necessary to look for a solution to deal with these power fluctuations. We expect the same behaviour for a misalignment of the input mirrors.

Several years ago there was a proposition of taking advantage of the dependence of the PRC finesse on the sidebands frequency due to the Schnupp asymmetry. The idea was to add a higher frequency modulation that would see a lower finesse inside the PRC because it would be less sensitive to optical aberrations [47]. This can be understood very easily from the energy conservation in an optical cavity, $r^2 = 1 - t^2 - L$. In a high finesse cavity the transmission is very low, and so

any energy loss from coupling to HOMs will have a big impact in the reflectivity and as a consequence, in the effective finesse. On the contrary, in a low finesse cavity, where the reflectivity is already dominated by the losses, the impact of any extra loss will be smaller, and so the OG (which is related to the finesse) will not change a lot.

We wanted to explore the use of the same solution to cope with the natural misalignment of the PRC when not controlled angularly (only by the LC). This time we made a simulation on the CITF adding several modulation frequencies with higher values (all of them multiples of f_1 to be resonant inside the PRC) to determine how effective was this solution. Table 5.9 shows the loss of OG with the PR mirror misaligned by 1 μrad with respect to the ideal alignment for different modulation frequencies and for different photodiodes:

	Carrier lock OG loss (%)	Sideband lock OG loss(%)
B1 6 MHz	91.3	91.5
B1 56 MHz	–	83.0
B1 131 MHz	–	65.3
B2 6 MHz	91.8	91.7
B2 56 MHz	–	83.7
B2 131 MHz	–	68.1
B4 6 MHz	91.6	91.5
B4 56 MHz	—	83.3
B4 131 MHz	–	65.7

TABLE 5.9: Optical Gain loss in different photodiodes due to a 1μrad of misalignment of the PR mirror. Notice that the 56 MHz is $9f_1$ and the 131 MHz is $21f_1$ and so they are all resonant inside the PRC.

The table has two columns corresponding to two different configurations. The first one when the carrier is resonant inside the PRC and so the sidebands are not and they act as phase reference. The second one is the most interesting, which is when the sidebands are resonant inside the PRC. This time is the carrier that acts as a phase reference since it is not resonant in the cavity.

Only the values at 6 MHz are shown in the first case, since it is the behaviour of the carrier that matters, and so all the sidebands give the same value. As predicted in [48] there is a dramatical OG loss. In the second case a difference in the OG loss between the different sidebands can be seen. As expected, using a higher frequency decreases the OG drop, confirming the effectivity of this solution. Finally, the OG loss is very similar for the carrier lock and for the 6 MHz one, since their OG is also similar ($OG^c_{CITF} = 49.3$, $OG^s_{PRC} = 47.91$).

In conclusion, the marginally stable nature of the PRC makes it too sensitive to misalignment to keep a stable feedback control. However, this issue can be mitigated by building the error signals with a higher modulation frequency. This solution can be adopted in order to engage the lock, while the alignment is not controlled yet. This sensing will provide a stable lock, even if it will be less precise, since the OG will be lower. Once the longitudinal control is engaged, it will be possible to close the alignment loops necessary to stabilize the OG of the 6 MHz

sideband inside the PRC. Then, the control can be handed-off to the nominal error signal, improving the precision of the lock.

5.2.3 Lock acquisition strategy: Variable Finesse

So far the target working point has been defined, as well as the DOFs that need to be controlled in order to reach it. However, initially all the mirrors are freely moving and in order to engage the lock, all the four lengths have to be within their linear range simultaneously which does not happen very often by chance. Moreover, the actuation does not have enough dynamic to stop all the mirrors at the same time, the seismic and frequency noises are to high. This obliges us to use an alternative lock strategy, as it was done for the arm cavities.

The *Variable finesse* method is the control strategy that was implemented for Virgo and Virgo + [31]. It consists in engaging the control of the ITF far from its working point, in an intermediate interference condition of the Michelson that is reached by adding an offset to its error signal. This reduces the PRC finesse as well as the impact of the coupling between the different DOFs. From this point, and with all the four DOFs already controlled, the MICH offset is slowly reduced until reaching dark fringe. The advantage of this method is that the target working point is attained by passing through a series of steady-states where all the control loops are already closed. This technique is called variable finesse because the change in the interference condition of the Michelson changes the reflectivity of the compound end mirror of the PRC, changing as well its finesse.

Even though the lock acquisition is simplified by starting from a PRC with a lower finesse, it is still very challenging to engage the control of the four DOFs at the same time, especially due to the coupling between them, as it was introduced in the previous section (see Equations 5.13).

This problem is solved by misaligning the PR mirror at the beginning of the lock sequence. This way there are only three DOFs to be controlled, and they can be more easily decoupled. The arm cavities are brought to resonance and the Michelson is controlled at its Half-Fringe, where $R_{SYM} = T_{ASY} = 0.5$. At this point the PR mirror is aligned and its control is engaged. It is at this stage when the coupling between DOFs starts to be relevant, distorting the error signals. Once all the lengths are controlled, the offset on the MICH length is slowly decreased until reaching the Dark Fringe.

In order to better illustrate the control strategy, the whole process was simulated using Optickle. Starting far from their working point the mirrors are brought to the correct position following the variable finesse lock strategy. The evolution of the power impinging on the different photodiodes during the lock sequence is shown in Figure 5.11.

With the information provided by the simulation, we are going to describe each stage of the lock strategy in detail, together with the problems that will be faced during the process and potential solutions.

- **Steps 1 and 2:** The lock sequence starts when the **cavities are brought to resonance** by acting on the end mirrors while all the others are moving freely and the PR mirror is misaligned. The photodiodes in transmission of the arms pass through several peaks, which correspond to resonances of the carrier and the sidebands, until reaching the working point where the power

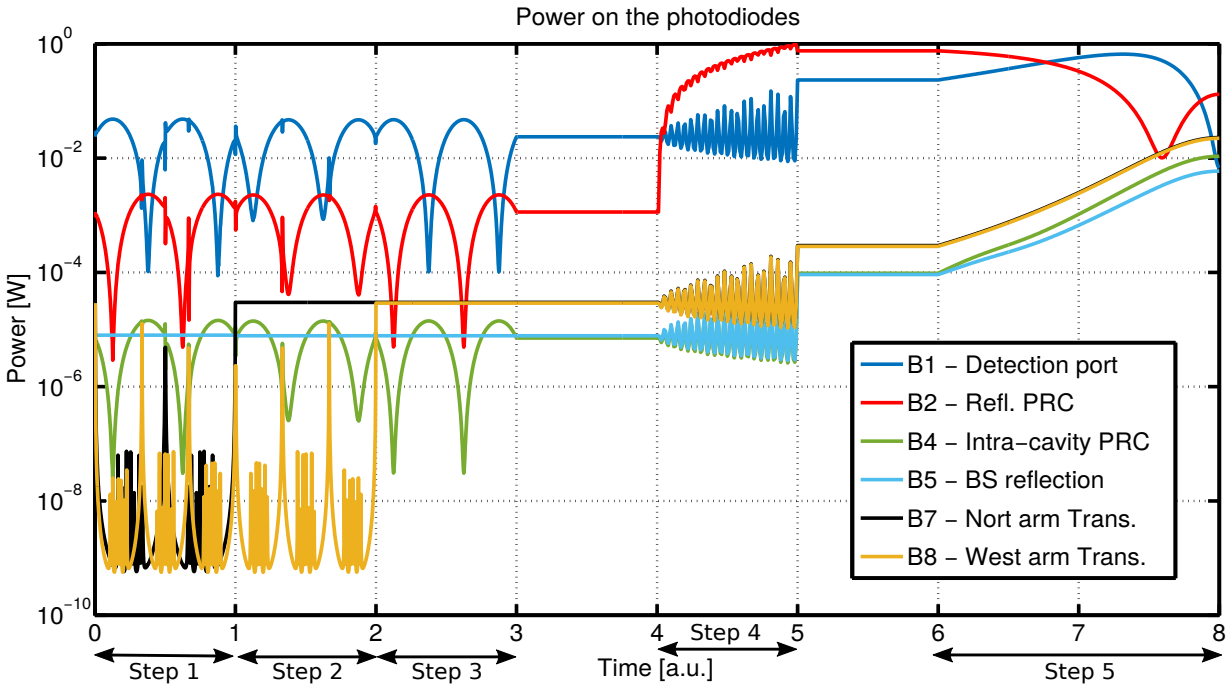

FIGURE 5.11: Simulation of a lock acquisition sequence. The power impinging in the photodiodes during the different stages is shown in the plot. The horizontal axis has arbitrary units. This is because the duration of each step was chosen arbitrarily so that the signals behaviour during the sequence could be understood.

stabilizes at the maximum of a carrier resonance. It is the transmission of each cavity which is used as error signal at this stage.

- **Step 3:** During this step the **Michelson is locked on its Half-Fringe**. As the PR mirror is misaligned, B2 and B4 photodiodes are equivalent, except for their amplitude which is much lower for B4 due to the low reflectivity of the Pick-off-Plate (POP). Also notice that the B1 photodiode has the opposite behaviour, as expected, since the it monitors the differential phase between the arms while B2 and B4 monitor the common phase.

  It is worth mentioning that during these three first steps, the B5 photodiode reads an almost constant power. This is because it receives the power reflected by the North arm cavity before it interferes with the beam that comes from the West cavity. As the reflectivity of the arm cavities is very high, the reflected power remains almost constant independently of the PRC length.

  Also in this step the **change of basis from arm cavities to CARM and DARM** takes place. This is important because the DARM DOF is the one sensitive to the passage of a GW. Also, once in this basis a more stringent control on the Common DOF can be engaged by acting on the laser frequency, the ***Second Stage of Frequency Stabilization (SSFS)*** (Section 5.3). It helps to improve the sensitivity and it reduces the coupling of CARM to the other DOFs.

- **Step 4:** The following step is the most critical one, the **PR mirror alignment**. During this transition the power impinging in all the photodiodes oscillates strongly as we pass through different resonances. Also during the

process there is an increase of power of a factor 10 in all the photodiodes except for B2, where it is a factor 100, as the power build-up increases. The OG of the error signals scales with the power, and so it will fluctuate strongly which will make it difficult for the control loop to remain stable during the transition. In order to mitigate this effect, it is necessary to **normalize all the error signals** by the corresponding fluctuating power before aligning the PR mirror (already from Step 3).

- **Step 5:** Once the PRC is controlled, the **Michelson offset is slowly reduced towards Dark Fringe**. During this process the arm cavities transmission and the power inside the PRC increase until reaching their maximum. This is because the finesse of the PRC increases while we become closer to the DF and so does the intra-cavity power. However the transmission (B1) and the reflection (B2) of the PRC have a more complex behaviour.

  As the Michelson interference condition changes, the equivalent end mirror of the PRC changes its reflectivity. At the beginning the PR mirror has a bigger reflectivity than the end mirror so the cavity is under-coupled. However, while going towards DF the end mirror reflectivity increases until reaching the critically-coupled condition. In this configuration there is a minimum in the reflected power as shown in Figure 5.11 around 7.5. It is not exactly zero due to the presence of the sidebands.

  As the MICH offset keeps on decreasing, the cavity pass to an over-coupled configuration, and the reflectivity increases at the same time that the transmitted power reaches a minimum in the DF where there is no carrier at the ASY port, only the sidebands leakage due to the Schnupp asymmetry.

Harmonic demodulation: 3Ω error signal

It is worth mentioning that during the MICH offset reduction the powers change again significantly. However this process is done in a controlled way, so it can be as slow as required, which leaves time to retune the gains of the control loops in order to compensate the power changes. So during this step it is not necessary to normalize the error signals, although it can simplify the process.

The PRCL control loop is slightly different though. The change on the optical parameters during this last step makes the system pass through some critical conditions such as the critically-coupled configuration where $r^c_{PRC} = 0$ or the moment where the recycling gain inside the PRC is the same for the carrier and for the sideband, $r^c_{PRC} = r^s_{PRC}$. As it is presented in [49], when passing close to these situations the error signals used for the control can suffer from large amplitude fluctuations or even change signs, which can not be compensated.

An extra problem is the coupling between CARM and PRCL in the photodiode in reflection (B2). As it was previously showed in Equation 5.13, the reflectivity of the PRC depends on the microscopic lengths of the arm cavities and of the interference condition of the Michelson and so will do the PDH error signal [49]. The coupling between DOFs in this photodiode has been already seen in Figure 5.6.

For these reasons it is convenient to generate the PRCL error signal using the 3Ω *demodulation* proposed and tested in TAMA [49] and that is used as well in LIGO control scheme [50]. It consists in demodulating the photodiode signal at 3Ω. The target of this technique is to extract the information needed about the PRC length avoiding the contributions from the carrier and the first sideband which depend strongly on the optical parameters of the PRC. The 3Ω error signal

depends instead on the second and third order sidebands as it is shown in the following expression:

$$\begin{aligned} PDHp^{3\Omega} = & - J_0(m)\cdot J_3(m)\cdot OG_c^2\cdot r_{PRC}^{3\Omega}\cdot |r_{FP}^{c'}|\cdot CARM \\ & - J_1(m)\cdot J_2(m)\cdot OG_\Omega^2\cdot r_{PRC}^{2\Omega}\cdot r_{FP}^{\Omega}\cdot \cos\left(\frac{\Omega\Delta_S}{c}\right)\cdot PRCL \\ & - J_0(m)\cdot J_3(m)\cdot \left(OG_c^2\cdot r_{PRC}^{3\Omega}\cdot r_{FP}^{c}\right. \\ & + \left. OG_{3\Omega}^2\cdot r_{PRC}^{c}\cdot r_{FP}^{3\Omega}\cdot \cos\left(\frac{3\Omega\Delta_S}{c}\right)\right)\cdot PRCL \end{aligned} \tag{5.23}$$

where OG_* are the optical gain inside the PRC of the different elements, r_*^* are the reflectivities of the PRC or the arm cavities for the carrier and the different sidebands, and Δ_S is the Shcnupp asymmetry.

This error signal works well because the odd multiples of the sideband are resonant inside the PRC but not the even multiples. They accumulate an extra π phase inside the PRC that makes them anti-resonant, as shown in Equation 5.20. According to this, the second order sideband is not resonant inside the PRC and can act as phase reference, while the third order sideband is resonant but less sensitive to the optical parameters than the carrier and the first order sideband.

Now the error signal not only depends on the reflectivity of the PRC for the carrier but also on the one of the second and third order sidebands, which do not disappear and so they fluctuate less during the MICH offset reduction. Simulation done in [49] showed that the amplitude of the 3Ω error signal remains almost constant while changing the cavity configuration. Moreover, with the 3Ω signal, the coupling of CARM is decreased by a factor 30 for Schnnup asymmetries lower than 0.4 m, which is our case.

Variable finesse, was used for controlling Virgo and Virgo+. The different steps of this procedure are summarized in Table 5.10.

Step 1	North arm lock
Step 2	West arm lock
Step 3	Michelson locked in HF Change to CARM/DARM Engage the SSFS
Step 4	PR alignment
Step 5	MICH offset reduction
Step 6	MICH hand-off to DF

TABLE 5.10: Summary of the different steps of the lock acquisition sequence, Variable Finesse.

The particular error signals used for each DOF have changed during time for various reasons, from design changes to commissioning limitations. A detailed study on the validity of the error signals used in the past is presented below, together with some alternatives for those which do not work in a robust way, always from the information provided by the Finesse simulations.

Notice, though, that the analysis presented here is slightly different from the one done in Section 5.2.1. The target is to bring the interferometer to its working position in a controlled way. This means that the priority is not so much a good

SNR, but more a good controllability, and so to decouple the DOFs as much as possible.

5.2.4 Step 3: Recombined configuration

The case of the MICH longitudinal control is particular because we are controlling it far from its working point in the steady state. The RF signals are not valid so far from the Dark Fringe so an alternative error signal is needed. However, looking at the power on B1 it can be seen that the signal is linear between Bright Fringe and Dark Fringe. In Virgo, B1 DC was used as an error signal, normalized by B5 DC, and then an offset was added to bring the zero-crossing to the Michelson Half-Fringe.

As it was explained, normalization is very important to survive to Step 4, when the PR mirror is aligned. In the past, the B1 DC was normalized using B5 DC because it is a good probe of the power inside the interferometer. We have used the Finesse simulation to check whether this combination is still the best, especially taking into account the addition of the B4 photodiode which monitors the intra-cavity power of the PRC.

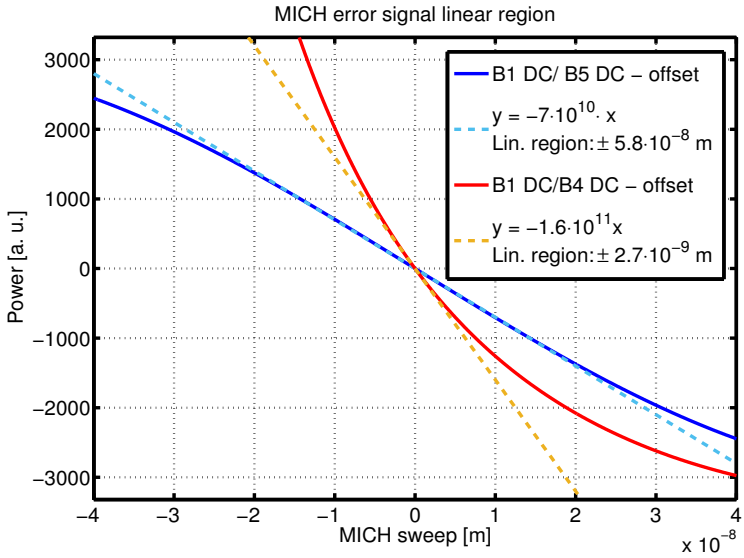

FIGURE 5.12: Comparison of two normalizations of B1 DC, with B4 DC and with B5 DC. The continuous lines are their response to a sweep of the Michelson DOF. The dashed lines are the fit of the linear region of the error signals.

The simulation shows that normalizing by B4 DC power is a good candidate, but the B5 DC normalization is still the best option because even though its OG is one order of magnitude lower, its linear region is one order of magnitude wider (see Figure 5.12). The linear region has been evaluated as the range within which the error signal deviates less than 10% from the linear fit.

Also during this step we pass from controlling the arm cavities independently to control the Common and Differential lengths. Since the arm cavity lengths are decoupled on the photodiodes, that is, B7 sees only the North arm length and B8 sees only the West arm length, it is easy to build a normalized error signal for the Common and Differential DOFs based on Equation 5.1:

$$\begin{aligned} CARM &= \frac{B7\ 6MHz}{B7\ DC} + \frac{B8\ 6MHz}{B8\ DC} \\ DARM &= \frac{B7\ 6MHz}{B7\ DC} - \frac{B8\ 6MHz}{B8\ DC} \end{aligned} \tag{5.24}$$

These error signals were also used for the lock acquisition in Virgo. The advantage is that the linear region is very large due to the normalization of the error signals, it increases from an interval of 0.5° to an interval of 35° (always from a simulation point of view, in real life the noise will limit before). The disadvantage is that the transmitted power is very low and so in practice the SNR will be limited by the noise of the sensors.

However the CARM error signal built with B7 and B8 is too noisy for the frequency stabilization, since its bandwidth will be much larger. An error signal with a better SNR is needed, and in the past B5 photodiode was used for this purpose. In Advanced Virgo it is forseen to use the B4 photodiode as error signal. In this case there is not much flexibility because the SSFS control loop is a particular one (it runs at very high sampling frequency) and special hardware is needed for reading the photodiode signals. However this error signal does not need normalization to survive the PR alignment since the control loop has an enormous gain margin (a factor 100) as it will be seen in the next Section 5.3.

Also using B4 6MHz for CARM is not incompatible with using it for MICH as well, since they are separated by 90°, as it can be seen in Figure 5.6. Moreover, it could be convenient to do this in order to avoid the coupling of phase noise. The phase noise is normally coming from the mis-tuning of the demodulation phase or a change on the phase of the modulation frequency. Let's consider that the error signal we want to use for CARM is on the P projection. As it is in closed loop, its value will be kept at zero. If you have an offset in the Q projection, as it is usually the case due to an unbalance of the sidebands, the phase noise will make it rotate around the Y-axis, which will cause a coupling to the P projection and so to the error signal we are interested in, as shown in Figure 5.13. If instead we use the Q projection as an error signal for MICH, it will be zeroed by the control loop, minimizing the coupling of the phase noise [10].

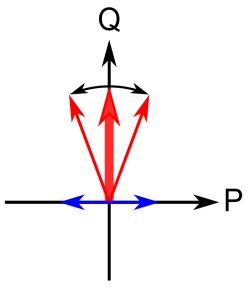

FIGURE 5.13: Coupling mechanism of the phase noise into an error signal [10].

It is also useful to check the coupling between the three DOFs. Figure 5.14 shows the chosen error signals optimized for the interesting DOF and how they behave when the other DOFs are not in their working point.

The same photodiodes are used for sensing CARM and DARM, but there is only one demodulation phase per photodiode to be tuned. In the case showed in Figure 5.14 the demodulation phase of the photodiodes, ϕ_{max}, was tuned for the Common mode and kept for both error signal combinations. Notice however that when optimizing per DARM the ϕ_{max} is almost the same so we can choose to optimize the phase with respect to any of them. These error signals are perfectly decoupled from the other DOFs as well as B4 6MHz for CARM.

However, this is not the case for the MICH error signal, to which DARM is strongly coupled. At this stage this is not a problem because DARM error signal does not sense MICH DOF and so there is no problem as far as DARM is controlled first. Also notice that when it comes to the Michelson DOF, the working point is not critical. It is not important to know exactly the fringe offset, but to start at a low PRC finesse and then increase it until reaching the working point.

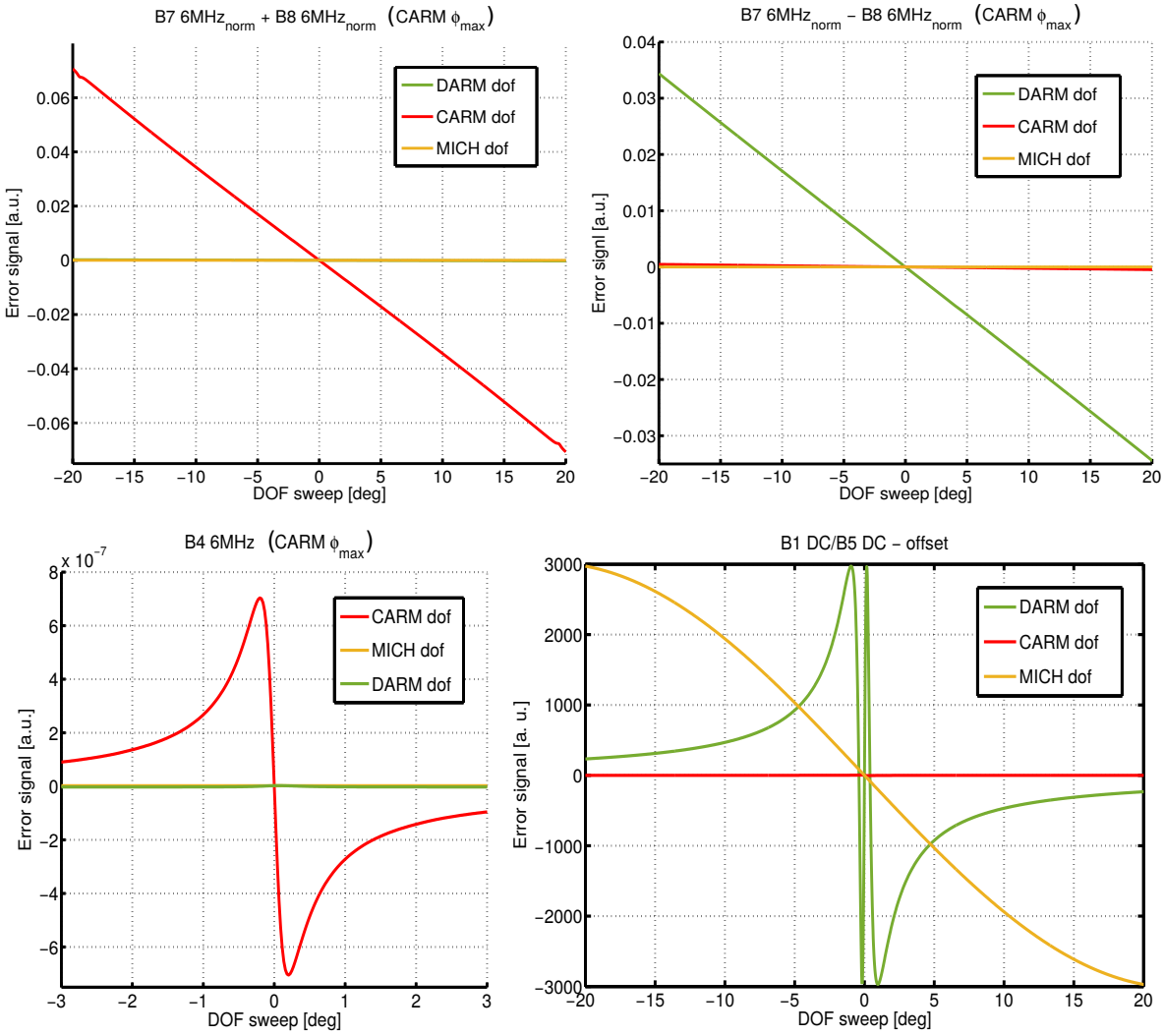

FIGURE 5.14: Response of an error signal to the different DOFs with the demodulation phase, ϕ_{max}, tuned for the interesting one. **Upper-Left plot:** CARM error signal. **Upper-Right plot:** DARM error signal. **Lower-Left plot:** CARM error signal for the SSFS. **Lower-Right plot:** MICH error signal.

5.2.5 Step 4: PR alignment

Regarding the alignment of the PR mirror, we have checked first if the error signals chosen for Step 3 were still valid after the alignment of the PR mirror. Let's start

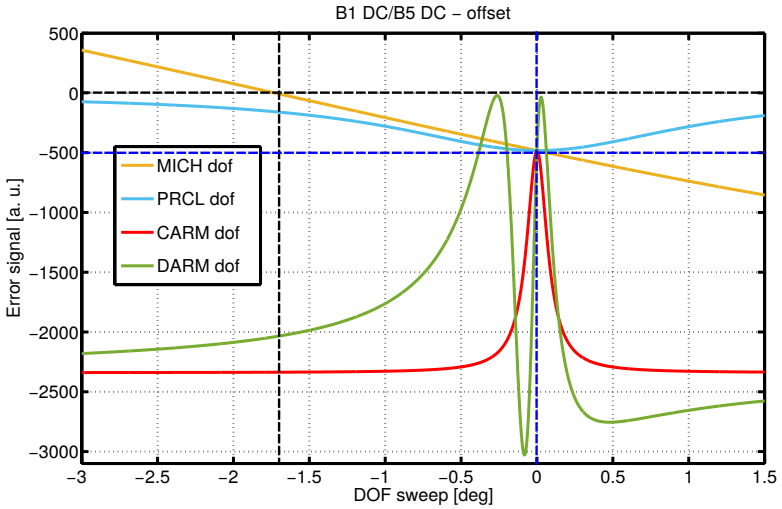

FIGURE 5.15: Response of the MICH error signal B1 DC / B5 DC to a sweep of the different DOFs.

by MICH error signal, B1/B5 DC - offset, which is shown in Figure 5.15. There are a few interesting things that can be deduced from this plot. First of all, notice that the zero-crossing of the MICH error signal is not anymore at zero (Half-Fringe) but it has shifted by ∼1.7°, as shown by the black dashed line. In terms of fringe it is negligible (0.9% deviation from the Half-Fringe) but not in terms of coupling.

Around zero (the vertical dashed blue line), which represents the working point of the rest of DOFs, the coupling of PRCL and CARM to the MICH OG is negligible for being at the maximum of a parabola (quadratic coupling). However, as the zero-crossing of MICH has been slightly shifted, they have a very big value around zero (500) as shown by the horizontal blue line, and so they will introduce an enormous offset. However, by tuning the offset of the MICH error signal properly, and so tuning their value to 0, the PRCL and CARM coupling can disappear. However, the DARM DOF is still very coupled to this error signal which means that its robustness will depend on the DARM error signal behaviour.

The DARM and CARM error signals built from B7 and B8 photodiodes are shown in Figure 5.16. The CARM error signal, B7 6MHz$_{norm}$ + B8 6MHz$_{norm}$, is still a good error signal, with negligible coupling with the other DOFs.

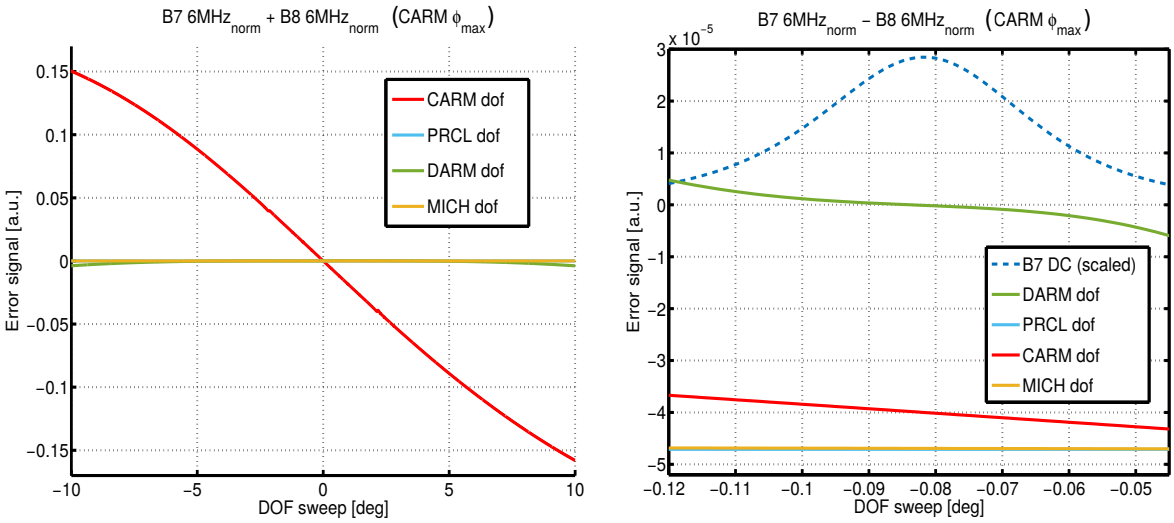

FIGURE 5.16: Response to a sweep of the different DOFs of the error signals for CARM and DARM built with the photodiodes in transmission of the arm cavities with the demodulation phase optimized for CARM. As mentioned before, their demodulation phases are optimized for CARM DOF (CARM ϕ_{max}).

This is not the case for the DARM error signal, B7 6MHz$_{norm}$ - B8 6MHz$_{norm}$, though. The transmission of the North cavity is shown in dashed in order to indicate the position of the resonance, which has slightly changed after the alignment of the PR mirror. In principle this is not worrying, as far as the working point provided by the error signal is in agreement with the resonance position, as it is the case.

However, the coupling of the other DOFs can not be neglected, they would introduce a big offset. Together with the coupling of DARM into the MICH error signal makes this error signal not an ideal option. We have looked for alternative error signals that would solve this problem, in particular in the B1 photodiode since it is the chosen one for the Dark Fringe and so a natural candidate. Figure 5.17 shows the B1 signal demodulated at 6 MHz and 131 MHz normalized by B1 DC.

First of all notice that even though the working point of DARM is shifted when the PR mirror is aligned, it is not the case for the other DOFs. This means that we have to evaluate the coupling of the DOFs around their respective working point because we are assuming that all the DOFS are controlled at this stage.

Taking this into account, MICH and PRCL introduce a static offset in both error signals. However this offset is small enough so that the zero-crossing stays within the linear region of the error signal. The main difference between both signals is the coupling of CARM. It is quadratic in the case of the 131 MHz and so it contributes to the offset as MICH and PRCL, however in the case of the 6 MHz signal it couples strongly to the OG. Also the 131 MHz has a higher OG because the sidebands are more transmitted to the ASY port.

In conclusion, the B1 photodiode signals demodulated at 131 MHz and 6 MHz are a good alternative for controlling the DARM DOF during the PR alignment if the coupling predicted by the simulation for the B7 6MHz$_{norm}$ - B8 6MHz$_{norm}$ is confirmed experimentally and is a problem.

Regarding the error signal for the SSFS control loop, Figure 5.18 shows that

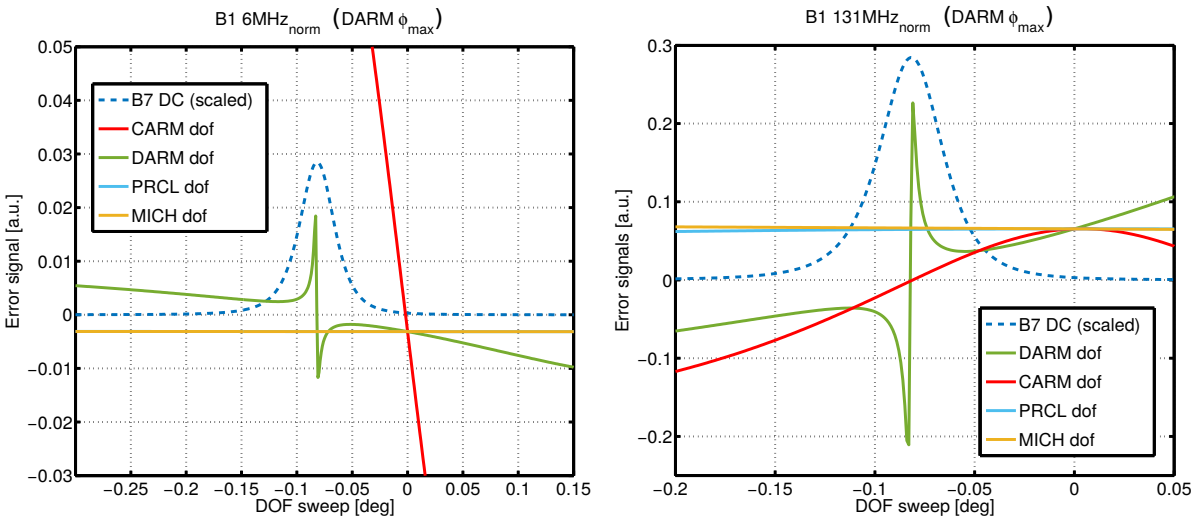

FIGURE 5.17: Response of the B1 6MHz and 131MHz to a sweep of the different DOFs with the demodulation phase optimized for DARM (DARM ϕ_{max}).

B4 6MHz is decoupled from both MICH and PRCL. DARM DOF couples quite strongly instead, but if this becomes a problem, the SSFS could be engaged after the alignment of the PR, when the DARM loop is already stable and we can tune the good working point by adding an offset.

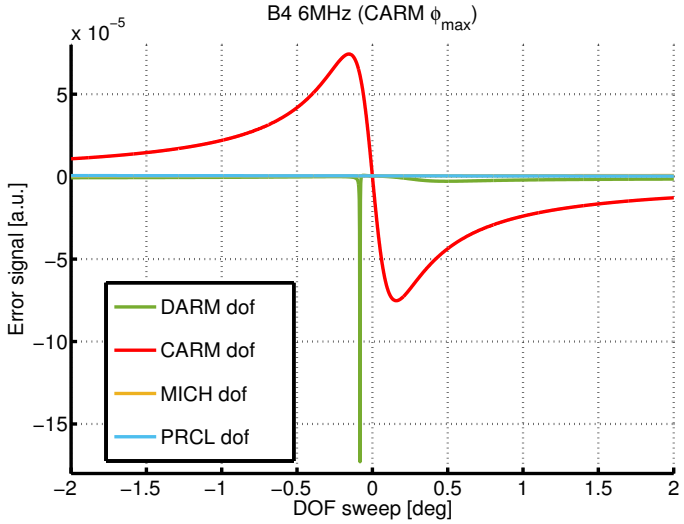

FIGURE 5.18: Response of the B4 6MHz error signal for a sweep of the different DOFs with the demodulation phase tuned for CARM (CARM ϕ_{max}).

Finally Figure 5.19 shows the two potential error signals for the PRC, the 8 MHz that will be used in the Dark Fringe, and the 3Ω that was used in Virgo during the MICH offset reduction.

It can be understood from the plots that the 8 MHz error signal sees the CARM DOF, even though the coupling is not very significant, especially taking

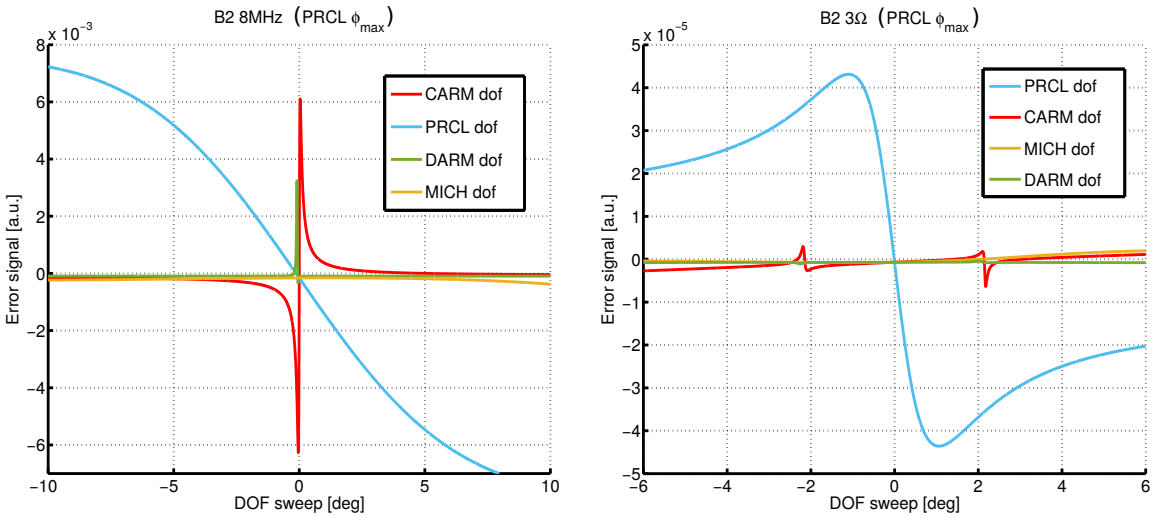

FIGURE 5.19: Response of B2 6MHz and 3Ω error signals for a sweep of the different DOFs with the demodulation phase tuned for PRCL (PRCL ϕ_{max}).

into account that it is very suppressed. DARM DOF also couples slightly by adding an offset, but as the PRCL resonance is very wide, it is not a fundamental problem.

However, it is worth noticing that the 3Ω error signal is completely decoupled from the other DOFs, which makes it a better candidate. The only inconvenient is that due to the coefficients $J_2(m)$ and $J_3(m)$ that affect this error signal (see Equation 5.23) the OG is very low, which in practice can translate in a noisy error signal (low SNR). Again, this is not necessarily a problem because here the priority is the robustness and not the sensitivity.

This error signal does not need normalization because it is engaged once the PR is aligned and so once the power has reached a maximum.

5.2.6 Towards Dark Fringe: MICH offset reduction

So far we have discussed few options of potential error signals that are likely to survive the alignment of the PR mirror. In this section we are going to study how these error signals evolve during the MICH offset reduction, as well as their coupling.

The first thing to look at is the **demodulation phase evolution**. As it was already mentioned in Section 4.4.2, in practice the demodulation phase needs to be tuned in order to project all the relevant information in-phase (P) or in-quadrature (Q) of the error signal. A demodulation phase badly tuned will translate in a loss of OG due to a leak of the relevant information to the other projection.

This means that on top of the change in OG due to the MICH offset reduction, there might be further fluctuations due to a shift on the optimal demodulation phase, as it has been observed experimentally in the past. In principle, as the process is very slow, this gain fluctuations can be compensated, or the demodulation can be re-tuned when necessary during the lock acquisition procedure as it was done in Virgo and Virgo+. However, we are looking for more violent changes such as sign changes, that are hard to deal with and we will try to avoid them.

Figure 5.20 shows the OG variation due to a bad tuning of the demodulation phase. In other words, the change that the OG would suffer if the demodulation

phase is tuned at Step 4 and not further adjusted during the MICH offset reduction. This variation is expressed relative to the optimal demodulation phase ϕ_{max} at each point. In the plot on the right side it is shown the evolution of the optimal demodulation phase with respect to the initial point. The simulation has been made for different offsets between Step 4 (Half-Fringe) and Dark fringe, including the Critically-Coupled point.

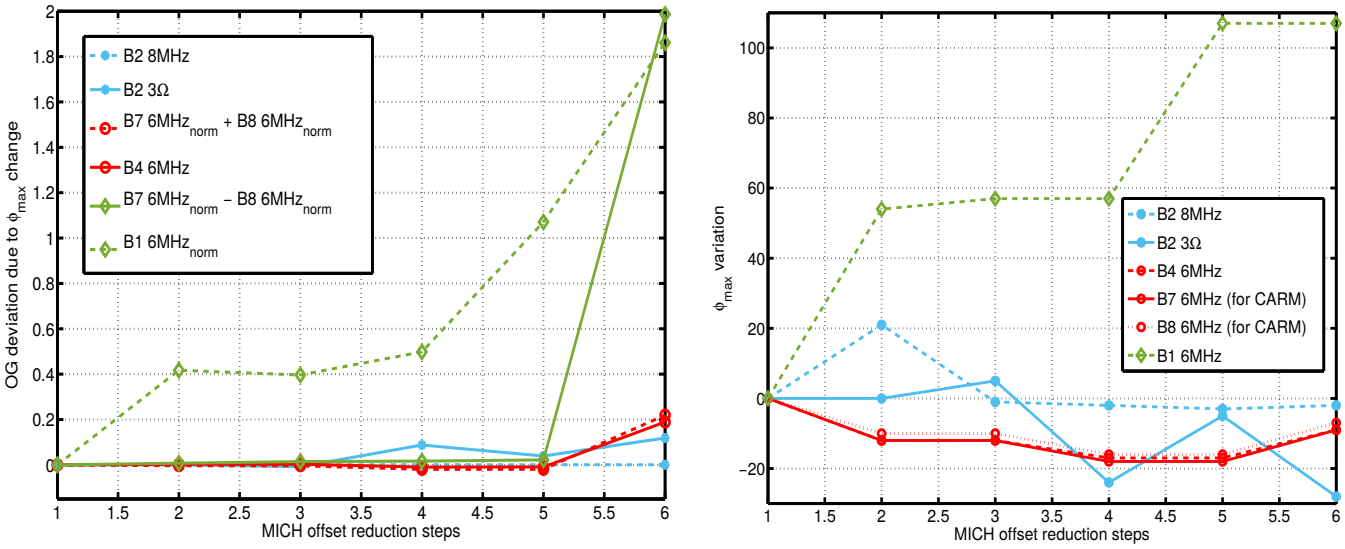

FIGURE 5.20: **Left plot:** Relative OG deviation from the ideal one with the optimal demodulation phase, when keeping the initial ϕ_{max} during the MICH offset reduction. **Right plot:** Variation of the optimal demodulation phase with respect to the initial one during the offset reduction. The steps are chosen arbitrarily towards the Dark Fringe in a non-linear way: starting from 0.7 fringe (6) to DF (1) passing through the critically coupled point (5).

As we can see in the left plot of Figure 5.20, most of the error signals stay within a 20% of OG change, with fluctuations of the demodulation phase of 20°, which is negligible. The DARM error signals though, suffer a big variation of the OG and it can be seen in the plot on the right that the optimal demodulation phase suffers from big fluctuations. This can be understood from the unbalance between the sidebands due to the Schnupp asymmetry, and which is sensed by the differential DOFs. The upper and the lower sideband do not have the same interference condition, and so they are not symmetrical at the carrier resonance, which has an impact on the error signal. Figure 5.21 shows the power on the upper and lower sideband at 6MHz in the B1 photodiode at different MICH offsets. They are unbalanced at 0, the carrier resonance, except at DF, where they are very close to being identical.

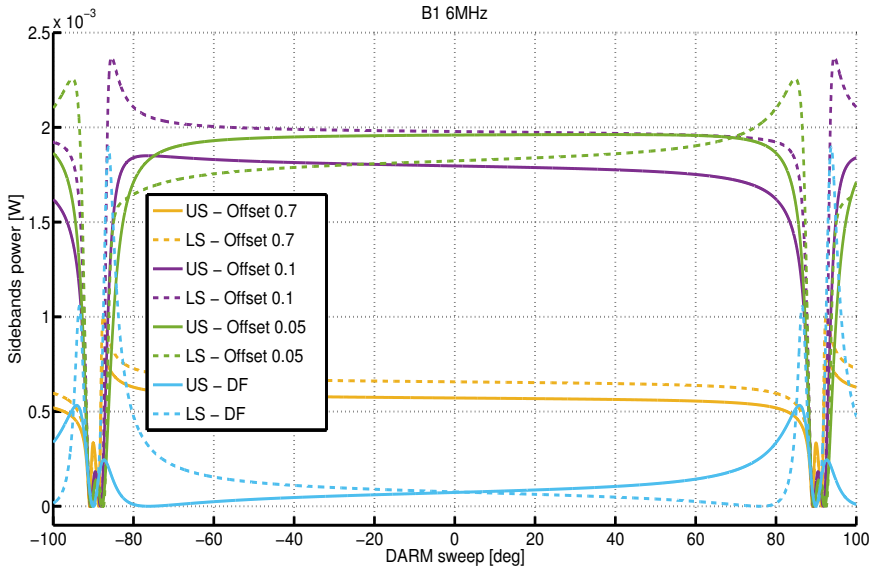

FIGURE 5.21: Power of the upper and lower sidebands (UL and LS) at 6MHz in the B1 photodiode for different MICH offsets.

For this reason the DARM DOF error signals have a more complicated behaviour than the other DOFS. The MICH DOF does not experience this problem because it uses DC powers as error signals. The alternative error signals for DARM proposed to minimize the coupling of the other DOFs, B1 6MHz and B1 131 MHz, change sign during the offset reduction as we can see in Figure 5.22.

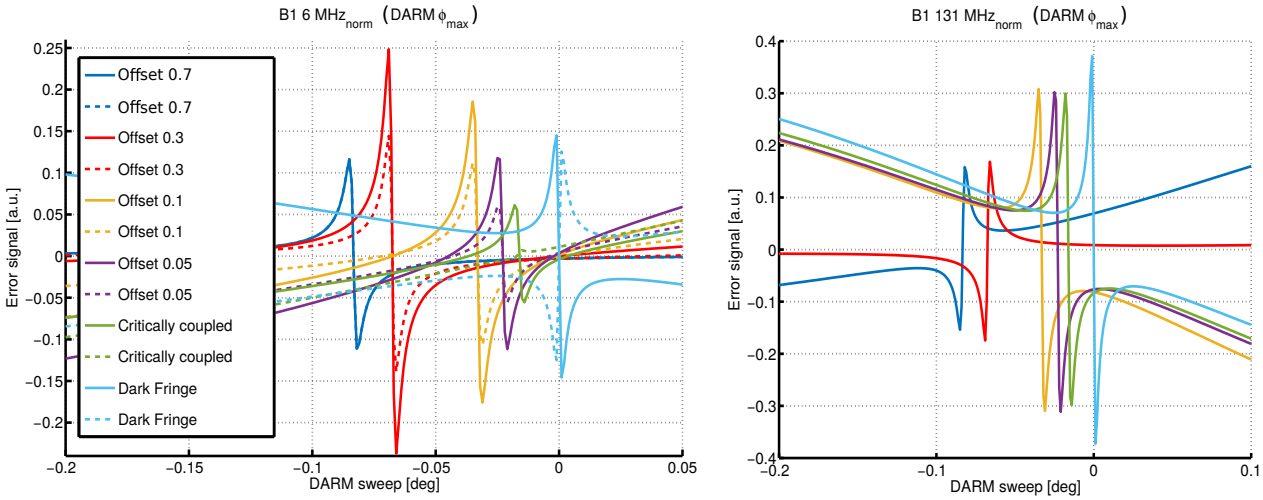

FIGURE 5.22: Response of the B1 6MHz and 131MHz error signals to a sweep of DARM for different MICH offsets from Step 4 (Half-Fringe) to DF. The continuous lines correspond to the error signals whose demodulation phase is optimally tuned. The dashed lines correspond to the error signal tuned with the initial demodulation phase.

The B1 131 MHz can be ruled out, because it changes sign independently of the demodulation phase, and this can not be compensated. In the right plot the

error signal has an opposite slope after the two first points.

The case is slightly different for the B1 6 MHz, because the sign change depends on the demodulation phase. In the left plot of Figure 5.22 there are two sets of signals, the continuous lines which represent the error signals with the optimal demodulation phase at each MICH offset, and the dashed lined which correspond to the error signals obtained by keeping the initial demodulation phase. In this case the change in the slope occurs only when the demodulation phase is detuned, and so it could be avoided by tuning the phase at the last stages of the MICH offset reduction process.

So after exploring the alternatives to the DARM error signal B7 6MHz$_{norm}$-B8 6MHz$_{norm}$ we found that B1 6MHz could be used, knowing that the first one is very coupled to the other DOFs but that the second one needs a careful tuning of the demodulation phase.

Finally it is also interesting to study the **evolution of the coupling** of the most promising error signals. In order to evaluate it, we have taken as a reference for each DOF and at each MICH offset, the maximum of the linear region of the error signal. This way it is easier to evaluate whether the offset induced by the other DOFs is significant or not.

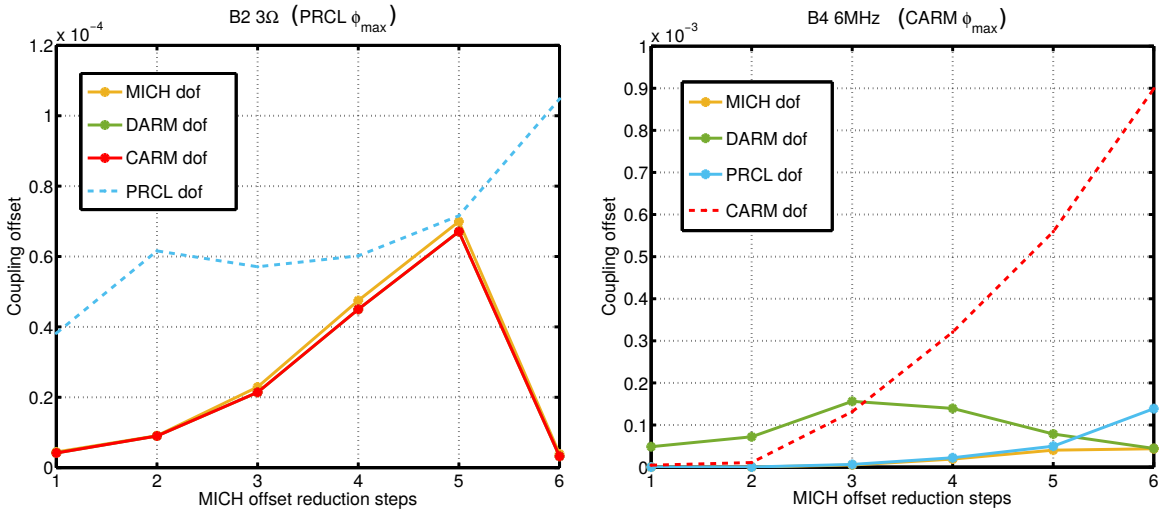

FIGURE 5.23: Coupling evolution of the Common DOFs during the MICH offset reduction. The continuous lines are the offsets produced by the non-interesting DOFs to the error signal tuned for the interesting DOF at several MICH offsets. The dashed line represents the maximum of the linear region of the error signal for the interesting DOF, providing a reference.

The offset induced by the other DOFs has been evaluated by taking the maximum value of the interesting error signal when sweeping these other DOFs, within a given interval. This interval is chosen depending on the DOF. For PRCL, CARM and DARM it is their FWHM, so the region around the resonance until the power is decreased by a factor 2. For MICH, it has been chosen in a slightly different way: the width of the interval has been chosen equal to the region around the Dark Fringe that increases the power in the ASY port by a factor 2. Then this interval is applied around the corresponding working point at the different MICH offsets. These intervals are a pessimistic limit, because the control loops do not allow such

a high residual motion, but it allows us to evaluate the evolution of the couplings in a systematic way.

Figure 5.23 shows the coupling evolution of the PRCL and CARM DOFs. The PRCL error signal is decoupled from the other DOFs as it can be seen in the left plot. Notice however, that in the critically-coupled configuration the coupling becomes more relevant, and so it will be a sensible point.

Regarding the CARM error signal, we can see that even if at the beginning the DARM coupling is important up to Step 3 and it decreases during the offset reduction. As the UGF of the CARM control loop is very high (few kHz), this coupling is not very worrying.

The coupling evolution of the differential DOFS is shown in Figure 5.24. The MICH error signal is dominated by the DARM coupling during all the offset reduction process. In the case of DARM, in the right plot, the coupling is relevant only at the beginning, and it decreases towards DF.

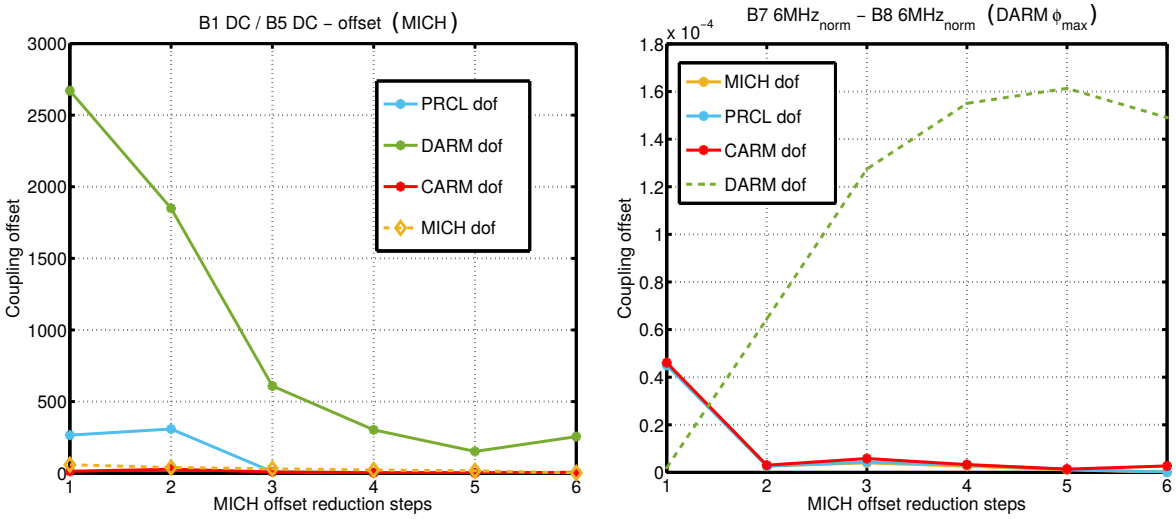

FIGURE 5.24: Coupling evolution of the Differential DOFs during the MICH offset reduction. The continuous lines are the offsets produced by the non-interesting DOFs to the error signal tuned for the interesting DOF at several MICH offsets. The dashed line represents the maximum of the linear region of the error signal for the interesting DOF, providing a reference to evaluate the coupling.

This coupling of DARM to MICH can be solved by implementing a hierarchical control, where the UGF of DARM is higher than the one of MICH. This way MICH will see a smaller movement of DARM within its control bandwidth, reducing the impact on the MICH error signal.

In the previous section we have explained the need of a **higher modulation frequency** in order to deal with the power fluctuations expected due to the marginally stable PRC. The study has been made in DF, where the PRC reaches its maximum finesse. However, at the beginning of the lock acquisition the PRC has a low finesse since the Michelson is on its Half-Fringe. At this point, the losses are already very big and the sensitivity to alignment will be low with a low impact on the OG.

The interesting thing to determine is at which Michelson offset the PRC has enough finesse so that the extra losses due to the coupling of HOMs start to be

relevant. For this reason we have made a simple calculation of the OG of the sidebands inside the PRC during the MICH offset reduction, increasing the losses up to 5%. The results are shown in Figure 5.25.

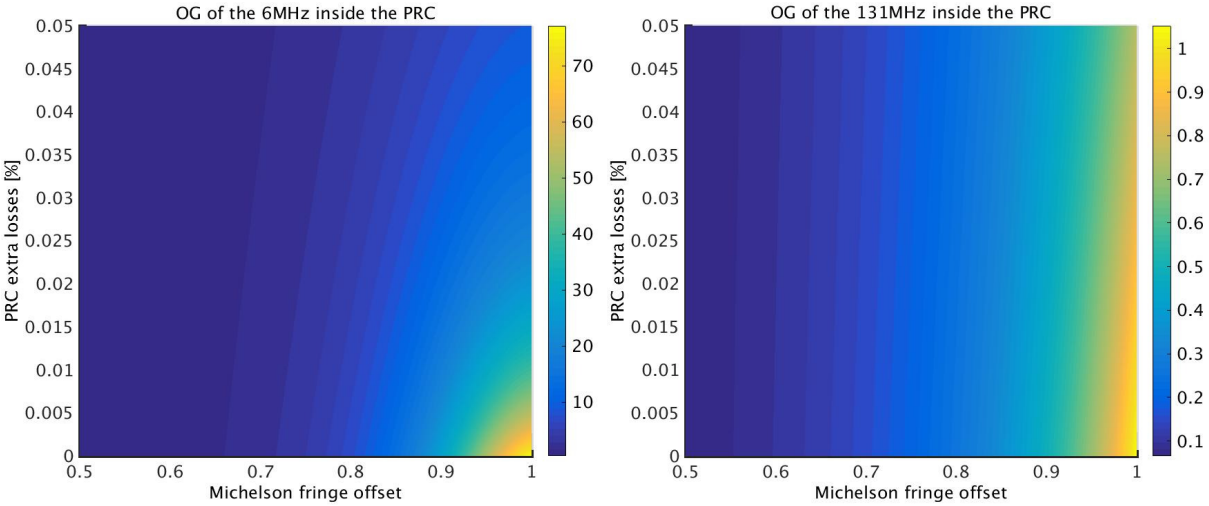

FIGURE 5.25: Variation of the OG of the 6MHz and the 131 MHz inside the PRC as a function of the losses and the MICH offset. In the x-axis 0.5 corresponds to Half-Fringe and 1 corresponds to Dark Fringe.

In the case of the 6 HMz, it is not until 80% of the MICH offset (almost in dark fringe) that the losses start to have an impact on the OG of the sidebands starting to be more and more critical. This indicates that it will not be until the last steps that we will need to use the modulation frequency foreseen to survive to the OG fluctuations due to alignment drifts. On the other hand, we can see that the 131 MHz is much less sensitive to the losses even in Dark Fringe.

There is a last interesting point to consider, which is the **transition of the MICH control from the DC powers to an RF signal**. The tricky point of this hand-off is that you need to make the transition between two signals that are not valid simultaneously. If you try to use the RF error signal out of its linear region, the control loop will bring the Michelson towards the wrong direction. For this reason it is important to make the change inside the linear region or very close to it. Figure 5.6 shows the linear region of B4 6MHz, which starts approximately 3° far from resonance, which is equivalent to 98% of DF, in terms of wavelength.

5.2.7 Summary: Longitudinal control sensing

The most important part of a good control is to have good error signals. This means to fulfil several conditions:

- High OG
- Wide linear region
- Good zero-crossing
- Low coupling from other DOFs

The lock strategy that allows us to reach the working point defined in the previous section is called Variable finesse, and it is summarized in Table 5.10. It consists on engaging the control far from the working point, where it is less critical, and then go towards the dark fringe passing through a series of steady states, always with all the DOFs controlled.

We have made a study of the sensing used in the past during the different steps of the lock acquisition sequence, finding alternatives when necessary. This has been done using the results of Optickle and Finesse simulations. Notice that during this process the priority was to find robust error signals, and so well decoupled. Another important point is to normalize the error signals, since the power inside the interferometer changes as the optical configurations evolve towards the final one. The results for Step 3 and 4 are summarized in Table 5.11.

Step 3	MICH: $B1_{DC}$ / $B5_{DC}$ - offset	DARM is strongly coupled
	CARM: B7 $6MHz_{norm}$ + B8 $6MHz_{norm}$	
	SSFS: B4 6MHz	
	DARM: B7 $6MHz_{norm}$ - B8 $6MHz_{norm}$	MICH is well decoupled, no problem
Step 4	PRCL: B2 3Ω	To survive the change in optical configuration
	MICH: $B1_{DC}$ / $B5_{DC}$ - offset	DARM is strongly coupled
	SSFS: B4 6MHz	
	DARM: B1 $6MHz_{norm}$ or B1 $131MHz_{norm}$	Alternatives less coupled to MICH

TABLE 5.11: Summary of the error signals proposed for each DOF in Step 3 and Step 4.

The last part of the analysis was the evolution of these error signals during the fringe offset. Regarding the change of the demodulation phase during this process it has been seen that it is only relevant in the case of DARM due to the unbalance of the sidebands at the carrier resonance. This forces us to discard the B1 $131MHz_{norm}$ error signal since it changes sign during this process. So for DARM the candidates are B7 $6MHz_{norm}$ - B8 $6MHz_{norm}$ (MICH couples significantly) and B1 $6MHZ_{norm}$ (it is necessary to tune the demodulation phase to prevent sign flips).

Regarding the coupling evolution, the DOFs are intrinsically coupled, especially in Half-Fringe, where it is less problematic due to the lower finesse of the PRC. This coupling becomes more and more critical with the increase of the finesse, but it is easier to decouple the sensing closer to the Dark Fringe. The most critical coupling is DARM to MICH, which can be solved by using a hierarchical control.

We have also estimated that the PRC stability will become a problem around 80% of DF, where it might be necessary to use error signals coming from high modulation frequencies as the 131 MHz. Finally the hand-off to Dark Fringe is a critical step, since the error signal are not valid simultaneously. The linear region of he MICH RF signal starts at 98% of fringe offset.

We have studied several options for each DOF, but the optimal ones at each step will be decided depending on experimental observations. Once in DF the error signals used during the lock acquisition will be handed-off to the optimal ones, which have been chosen in order to have the best sensitivity possible, and so the highest SNR. The chosen error signals for DF are shown in Table 5.12. It exists also the possibility of using B4 6MHz P and Q projections for CARM and MICH, since would improve the phase noise of these error signals.

PRCL	B2 8MHz
CARM	B2 6MHz
MICH	B4 6MHz
DARM	B1 6MHz

TABLE 5.12: Summary of the error signals proposed for the working point of the interferometer.

5.3 SSFS: Second Stage of Frequency Stabilization

So far we have mentioned that the common degree of freedom is a particular one, because it has two contributions: the common cavity length and the laser frequency. The frequency noise is also a common noise, since it couples to the interferometer through the laser, and unlike the seismic noise, it is broadband. In an ideal symmetric interferometer, the frequency noise is perfectly cancelled at the ASY port. However, in practice due to the Schnupp asymmetry, it couples to the asymmetric port. The detection of a gravitational wave depends on this common phase noise that reaches the dark port to be smaller than the $\delta\phi$ produced by the signal to be detected. Moreover, it needs to be smaller in all the measurement frequency bandwidth.

At first the frequency stabilization is done by the pre-stabilization loop, which locks the frequency of the laser to the length of the IMC cavity up to 300 kHz (see Section 3.4). Subsequently, the length of the IMC is controlled by the Reference Cavity up to ∼180 Hz. In order to improve further the control of the frequency stabilization a better reference is necessary.

The CARM error signal provides the frequency reference for the *Second Stage of Frequency Stabilization*. However, the optical TF of CARM limits the control bandwidth that can be reached. This is because at each Free Spectral Range, the TF experiences a change of phase of -180°, which can not be compensated by a filter, creating an instability. This rule is applied as well for a sideband resonance, which were chosen to be almost antiresonant.

For Advanced Virgo the FSR of the arm cavities is approximately 50kHz, which means that the first sideband resonance is at ∼25 kHz, which will be the limit to the UGF. Figure 5.26 shows an Optickle simulation of the TF between CARM and B4 6MHz photodiode for several of the steps of the Variable Finesse lock acquisition sequence, where this phase jump can be observed [32]. For this reason, a second control loop is needed in order to reduce the frequency noise above 25 kHz. This is the role of the pre-stabilization analogical loop.

As it was already mentioned, the error signal to be used comes from either B4 or B2 photodiodes. This is because they measure the Common noise that is cancelled at the ASY port and comes back towards the SYM. Previously we have talked about the leakage of frequency noise to the Dark Fringe through the Schnupp asymmetry. However, it is worth noticing that any asymmetry in the interferometer will increase this coupling: asymmetry between the arm cavities finesse, between the arm cavities losses, between the radius of curvature of the cavity mirrors... All this information is gathered in the so-called Common Mode Rejection Factor of the interferometer. It is a limiting factor of the performance of the frequency stabilization, and some constraints have been put on the most relevant parameters in order to reach the required sensitivity [51]. The finesse asymmetry can be at most 1% and the losses asymmetry at most 40 ppm.

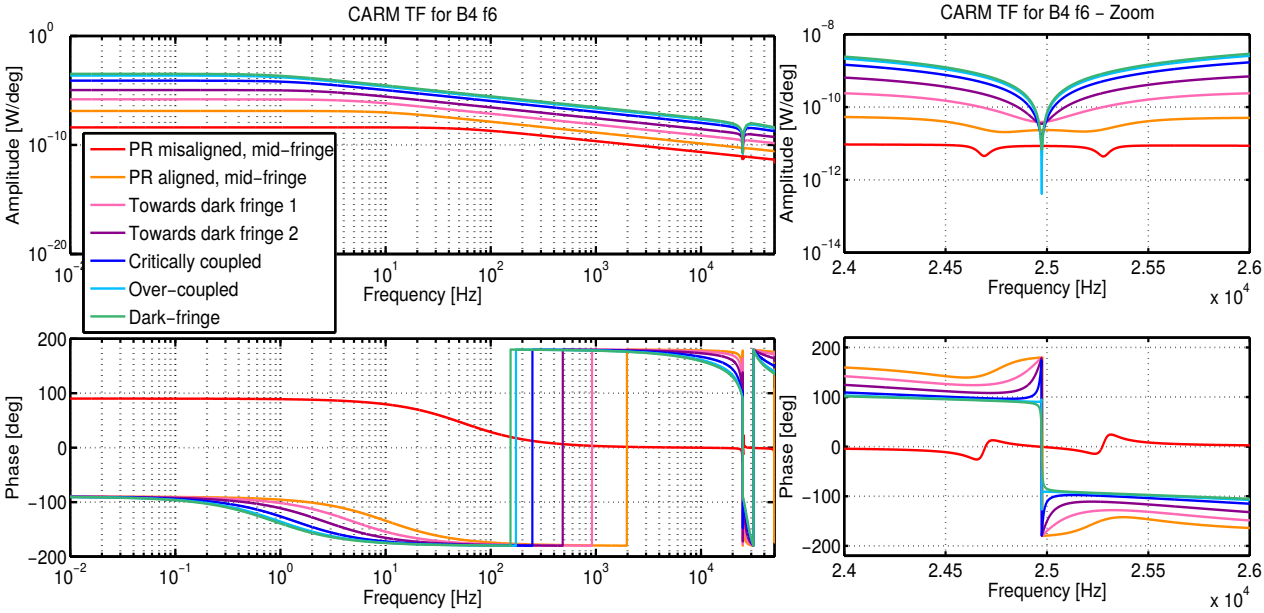

FIGURE 5.26: Optical TF of the interferometer common DOF, CARM and the B4 6MHz error signal for several stages in the lock acquisition strategy.

5.3.1 SSFS architecture

The need of two nested loops makes the architecture of the SSFS quite complicated. In the following, we will describe in detail the different loops and their interaction as well as the considerations needed in order to design the control filters and make the overall system stable.

Figure 5.27 shows a scheme of the SSFS architecture. On it they are represented all the relevant noises in this loop: the laser frequency, ν_0, and the mirrors movement due to the seismic noise of the IMC, the RFC and the common movement of the arm cavities. No sensing noise has been taking into account.

As mentioned before, the pre-stabilization loop is working normally over the UGF of the CARM loop, 20 kHz. This means that the laser frequency is locked to the IMC length using as an error signal the IMC reflection with a control filter F_P. The control filter is analogic in order to reach a very high UGF, 300 kHz. In this frequency bandwidth there is no interaction between the loops.

Up to 20 kHz is the CARM error signal which provides information about the frequency noise. This information is then split in two, the low frequency is sent to the IMC mirror, and the high frequency to the laser itself through the pre-stabilization filter, F_P. This split is done because the IMC control bandwidth is limited to several hundreds of Hzs by the delay due to the digital nature of the filter. This means that there are two filters that use the same error signal, and so they interact in a non-trivial way and they need to be designed very carefully.

Finally, the Reference Cavity still acts as a frequency reference at very low frequencies. This loop has a very low bandwidth, of several Hzs and it prevents slow drifts of the laser frequency.

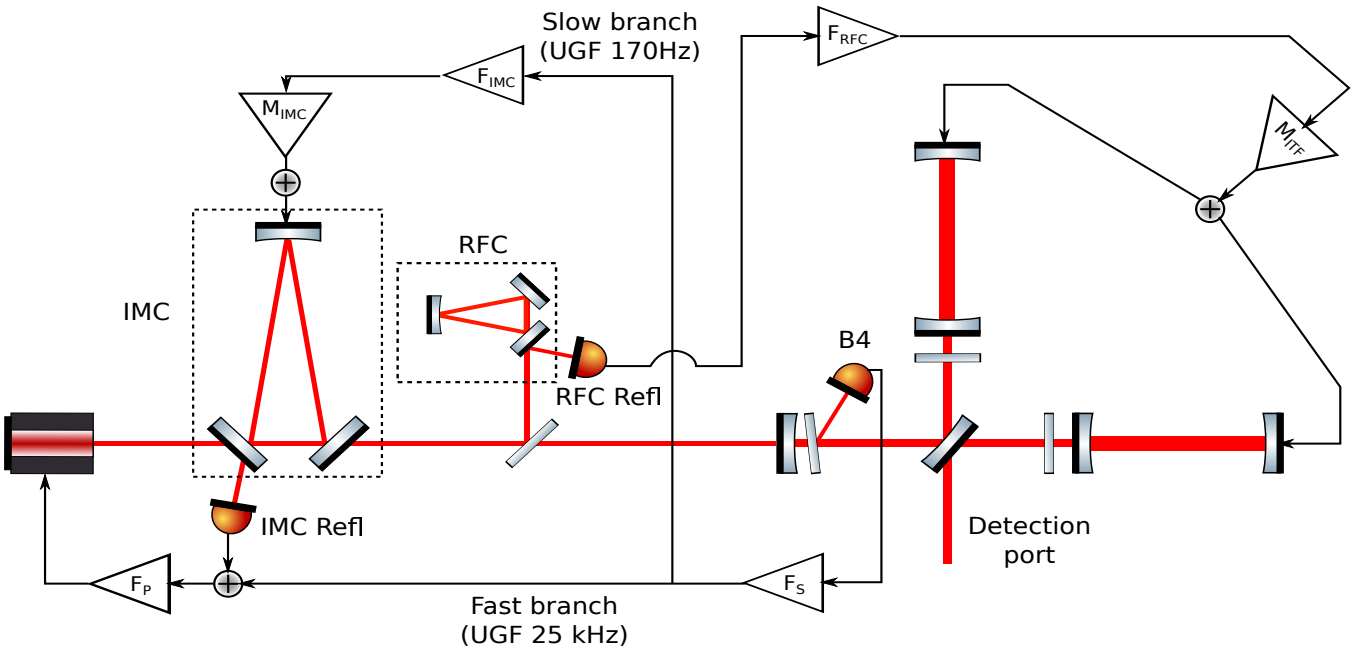

FIGURE 5.27: Scheme of the Second Stage of Frequency Stabilization.

In order to better understand the interactions of these loops, the global open loop of the system can be calculated [51]:

$$CLTF = \frac{T^{\nu}_{IMC}}{(1 - O_P)\,(1 - O_N)} \tag{5.25}$$

where T^{ν}_{IMC} is the optical TF of the transmission of the IMC for a frequency noise, 0_P is the OL of the pre-stabilization loop and 0_N is the OL of the nested CARM loops.

Before entering into details the CLTF gives already information about the stability of the overall system, which will diverge if any of the OL is unstable. The OL of the pre-stabilization is already implemented at the beginning of the lock acquisition and so it is stable. It depends on the analogical filter, the different laser actuators and the optical TF of the reflection of the IMC for a frequency noise. It is well known and shown in Figure 5.28.

Regarding the OL of the nested loops, its expression is more complicated:

$$\begin{aligned} O_N =& T^{z}_{IMC} M_{IMC} F_{IMC} F_S (G_{ITF} + G_{RFC}) + \\ & \frac{T^{\nu}_{IMC}}{1 - O_P} (1 - O_{IMC}) F_S F_P (G_{ITF} + G_{RFC}) \end{aligned} \tag{5.26}$$

where F_S is the SSFS filter and T^{z}_{IMC} and R^{z}_{IMC} are the optical TFs of the transmission and reflection of the IMC for a length variation. M_{IMC} is the TF of the actuator and the suspension of the mirror of the IMC, F_{IMC} is the control filter of the IMC and $O_{IMC} = R^{z}_{IMC} M_{IMC} F_{IMC}$ is the open loop of the IMC mechanical lock. Finally G_{ITF} is the optical TF of the Interferometer Common mode for a frequency noise, seen by the error signal to be used and $G_{RFC} = G^{z}_{ITF} M_{ITF} F_{RFC} R^{z}_{RFC}$ is the coupling of the frequency noise to the error signal through the RFC loop.

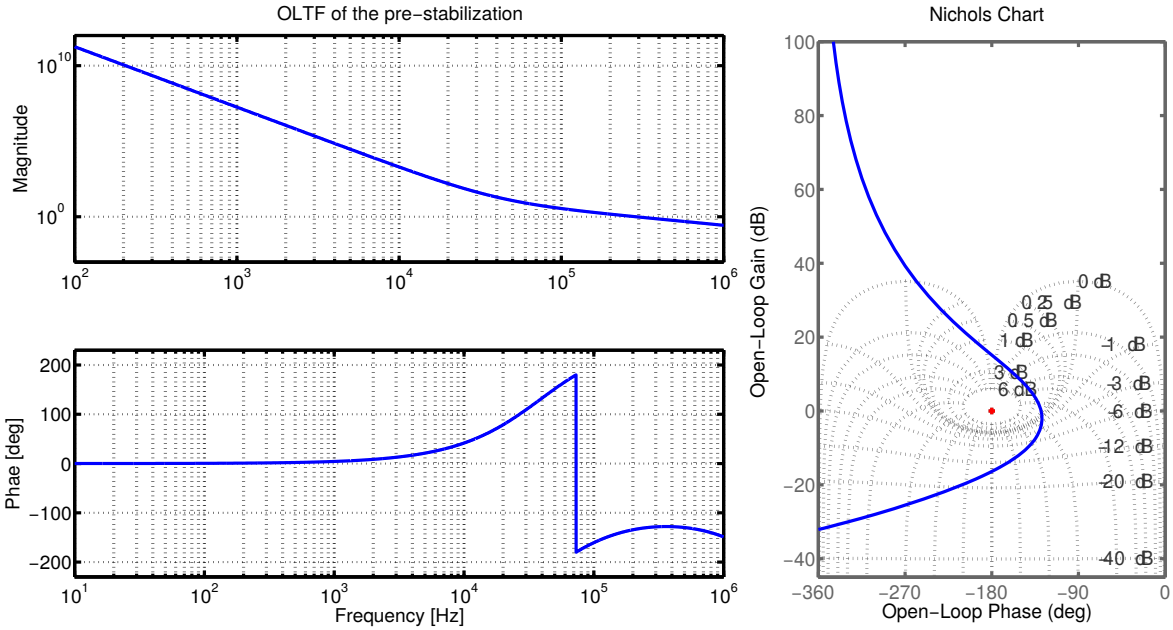

FIGURE 5.28: OLTF of the pre-stabilization loop that locks the frequency of the laser to the IMC length.

This expression accounts for the two branches of the loop. The first term in the sum corresponds to the **slow loop**, which takes the correction of the fast filter, F_S, and filters it again by F_{IMC}, applying the correction to the IMC. The second term corresponds to the **fast loop**, the one that goes to the laser directly. This part is a bit more complicated because apart from the frequency noise coming from the interferometer which is filtered by the SSFS loop, F_S, it considers as well the closed loop of the pre-stabilization, and the interaction with the slow loop. It can be proved [52] that the nested loop will be stable if both terms on the global OLTF, the slow and the fast one, are stable individually. However, notice that the filters to be designed, F_{IMC} and F_S are mixed in these terms, which complicates their design.

5.3.2 SSFS commissioning: CARM to MC

Before entering into the details of these two loops, the scheme can be slightly simplified. This could be advantageous both for the loop design and the commissioning. The commissioning of this loop is very complicated, especially since for AdV the scheme was different than in Virgo and we had to start its commissioning from scratch. However, the fact that the SSFS is now digital (it was analogical in the past), allowed us more flexibility during the process and allowed us to simplify the scheme as it will be presented here.

It can be proven that, when using analogical control filters, a single error signal can not be shared between two loops if both of them have gain at DC because there is always a residual offset that will end up saturating the control [52]. A way to avoid this is to send the error signal to the fast filter and then send the correction to the slow filter. This is the reason why the correction of the SSFS filter is send to the IMC instead of the error signal.

Now that the SSFS is implemented digitally, this is not a problem anymore and we can decouple the IMC branch by sending the error signal itself instead of the correction of the SSFS filter. This allows us to make an intermediate state in the commissioning of this subsystem by engaging first the slow branch only. The lock of the CARM DOF on the IMC will allow us to debug the system and easy the commissioning process. Also in order to simplify further the process, the RFC loop is not yet engaged, it will be the last step of the process.

In the OL of the nested loop, the F_S parameter will disappear from the first term, which decouples more both branches and simplifies the filter design. The first loop to be engaged then is the slow one, that sends CARM error signal to the IMC. Figure 5.29 shows its OL, which has an UGF of ∼180°. The control filter used is the same used to control the length of the IMC with the error signal of the RFC, apart from a compensator for the ITF optical TF.

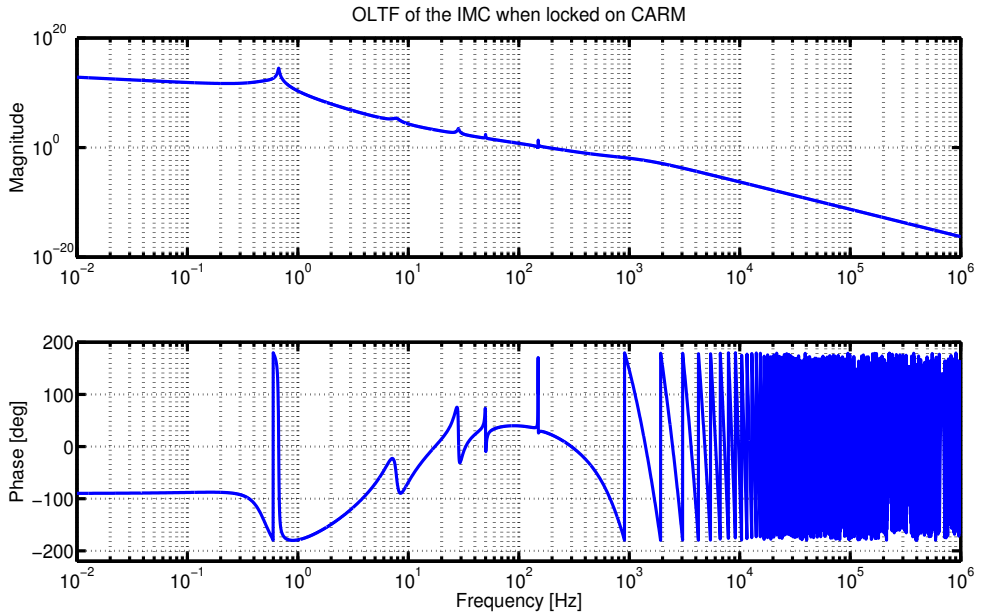

FIGURE 5.29: OLTF of the IMC control loop when it uses the CARM error signal.

The following step is then the engagement of the SSFS loop itself, the fast loop. So far the loops were decoupled, it is at this moment that they start interacting, and we need to consider it for the design of the filter. However, the process is now relatively simple since the other filter is already designed and stable. There are two factors to take into account: the **stability of the crossing point** between the two filters, which is achieved when both filters have a relationship of 1/f at the cross-over frequency, and the **stability of the SSFS loop** itself.

Figure 5.30 shows the IMC OLTF, the SSFS OLTF and the Global SSFS OLTF, which is the sum of both loops, as indicated in Equation 5.26. The cross-over frequency is chosen by tuning the gain of the SSFS filter, and it has been fixed around 150 Hz. At this point the stability criteria is fulfilled since the SSFS OLTF is flat, and the behaviour of the IMC OLTF is f^{-1}.

Once the ratio between both filters is fixed, the global gain is used to adjust the UGF of the system. In Figure 5.30 it has been chosen at 5 kHz, but it can be seen that there is phase margin up to ∼15 kHz. In this example the phase is

limited by a pole placed at 20 kHz, which is used decrease the gain of the filter at high frequencies. However, as it was mentioned before, we are anyway limited by the arm cavities FSR at 25 kHz, and so for lock acquisition purposes this filter gives us enough actuation range.

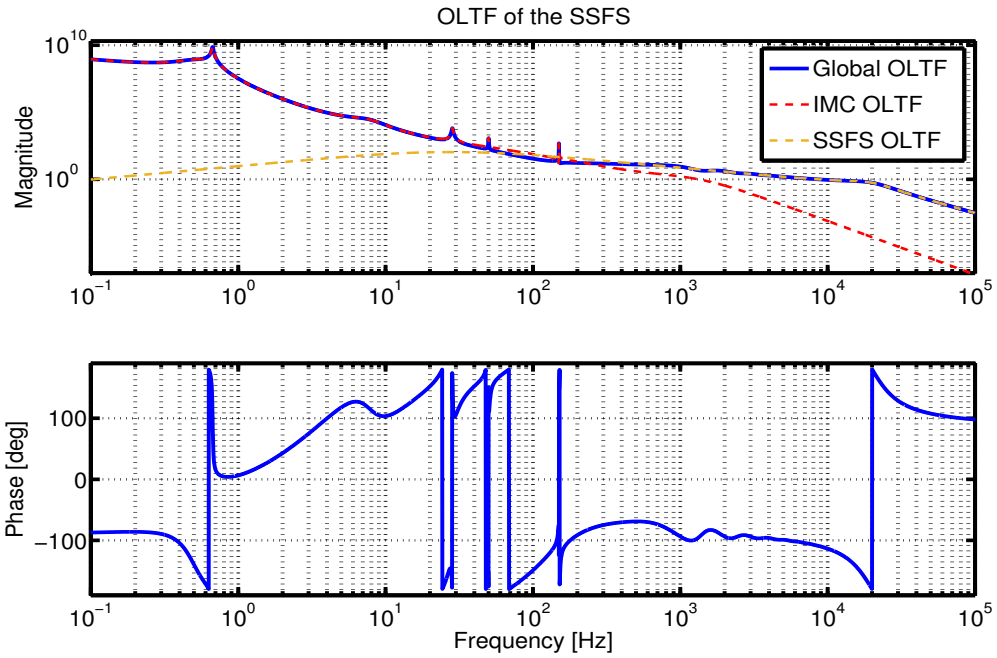

FIGURE 5.30: Global OLTF of the system. The contributions of the fast loop (SSFS) and the slow loop (IMC) are shown as well in the plot.

Once the these two loops are engaged, the very slow loop that uses the error signal of the Reference Cavity is engaged. This loop is not critical from the stability point of view but it is important in order to prevent big drifts of the main frequency of the laser. Figure 5.31 shows the OLTF of this loop, which has an UGF of 2 Hz.

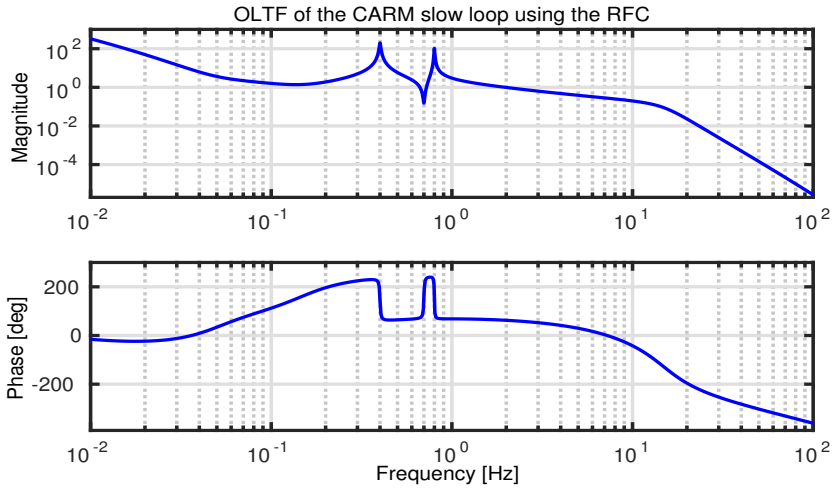

FIGURE 5.31: Global OLTF of the CARM slow loop that uses the error signal of the RFC.

5.3.3 Impact of HOMs on the optical TF

The target UGF of the SSFS control filter is 20 kHz. However, it has been observed in the past that the presence of HOMs has an impact on the Optical TF of the Common DOF of the interferometer. In particular, the first HOMs of the sidebands will be very close to the UGF, and they might cause instabilities if the filter does not take them into account.

A Finesse simulation has been made in order to anticipate the impact of this HOMs, and the shape of the appearing structures. Figure 5.32 shows the Optical TF of the Common DOF of the interferometer at B4 6MHz in Dark Fringe when some mirrors are misaligned.

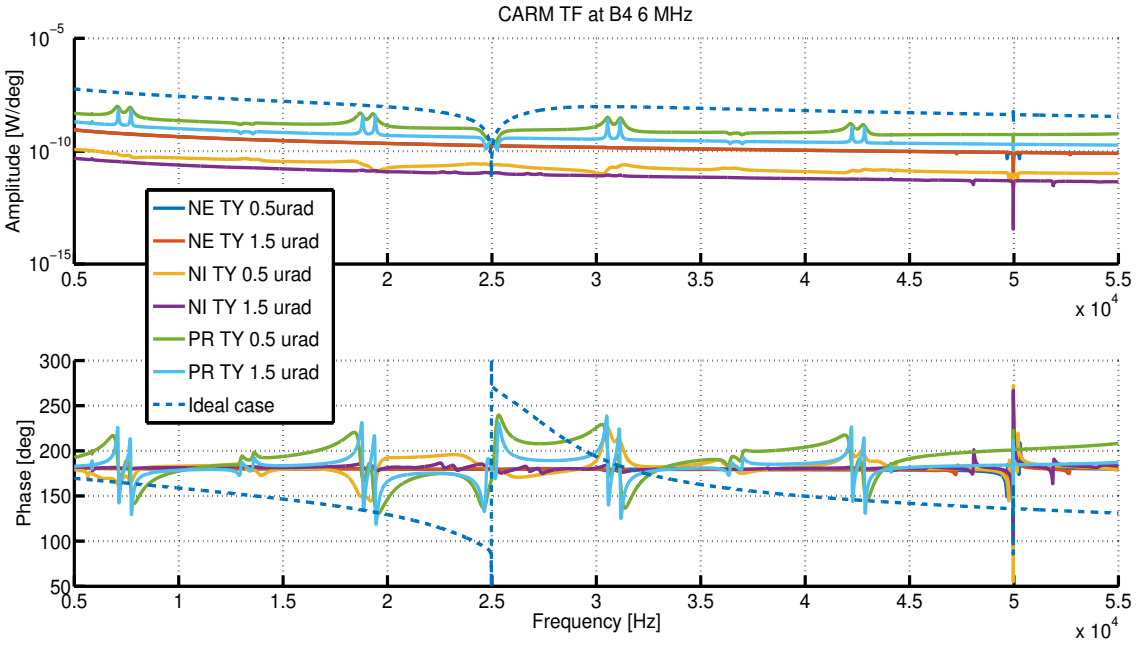

FIGURE 5.32: Optical TF of the interferometer common DOF, CARM, and the B4 6MHz error signal in Dark Fringe. It is shown for different misalignments of several of the mirrors.

In the ideal case there are two notches. The first one corresponds to the sidebands, which are so close (∼300 Hz) that they have merged into one single notch. The second one at 50 kHz corresponds to the carrier. The phase in both cases experiences a jump that will cause the instability of a filter, as it was mentioned previously.

The misalignments of the arm mirrors do not cause significant structures. When the PR mirror is misaligned, the first HOMs of the sidebands appears quite strongly (±5860 Hz), as well as the third order ones (±17580 Hz) as peaks. The second order modes do not appear strongly, since they are not resonant in the interferometer (±11720 Hz), and they appear as notches instead.

At the level of the phase, there are jumps of 90°, which can be compensated with the filter if necessary. With this information it is clear that the alignment of the PR mirror will be critical for the stability of the SSFS filter, and that it is important to measure the Optical TF of the Interferometer in order to push the UGF of the filter at the maximum possible.

5.4 Angular control

So far we have talked about the longitudinal control and the frequency stabilization of the Power Recycling Interferometer. In this section we are going to present the last stage, the angular control. In Chapter 4 the eigenvectors of the alignment of an optical cavity have been described, tilt and shift. However, the PRITF configuration is more complex and there are more angular DOFs, in particular 16, to be controlled.

First of all we are going to define these angular DOFs:

- **PRM**: tilt of the PR mirror.
- **BSM**: tilt of the BS mirror.
- **Comm(+)**: common tilt of both arm cavities which makes their optical axis to recombine in the same spot of the BS mirror.
- **Comm(-)**: common shift of both arm cavities which makes their optical axis to recombine in the same spot of the BS mirror.
- **Diff(+)**: differential tilt of both arm cavities which makes their optical axis to recombine in opposite sides of the BS mirror.
- **Diff(-)**: differential shift of both arm cavities which makes their optical axis to recombine in opposite sides of the BS mirror.

Notice that each of this DOFs have two planes of angular movement, θ_x and θ_y.

Figure 5.33 shows a scheme of the Common and Differential modes. We do not expect any radiation pressure inside the Central part of the Interferometer, because the power is not high enough.

Regarding the requirements on the loops performances, the target is to control them so that the power fluctuations of the carrier and the sidebands on the different cavities are smaller than 10^{-3}. This translates into a control of the cavities mirrors around 2 nrad and of the Power Recycling mirror of $\sim$25 nrad.

5.4.1 Sensing and driving

There are two quadrant photodiodes separated by 90° of Gouy phase at each Detection bench. They are all demodulated digitally except for the ones located in transmission of the arms which are only available in DC. The simulation done in [41] with Finesse, studies the optimal sensing for the alignment DOFs, which is summarized in Table 5.13.

PRM	B2 8MHz (Q)
BSM	B1 6MHz (Q)
Comm(+)	B2 8MHz (P)
Comm(-)	B1 6MHz (P)
Diff(+)	QPD B7 DC + QPD B8 DC
Diff(-)	QPD B7 DC - QPD B8 DC

TABLE 5.13: Quadrant photodiodes that provide the optimal sensing to control the angular DOFs of the PRITF configuration.

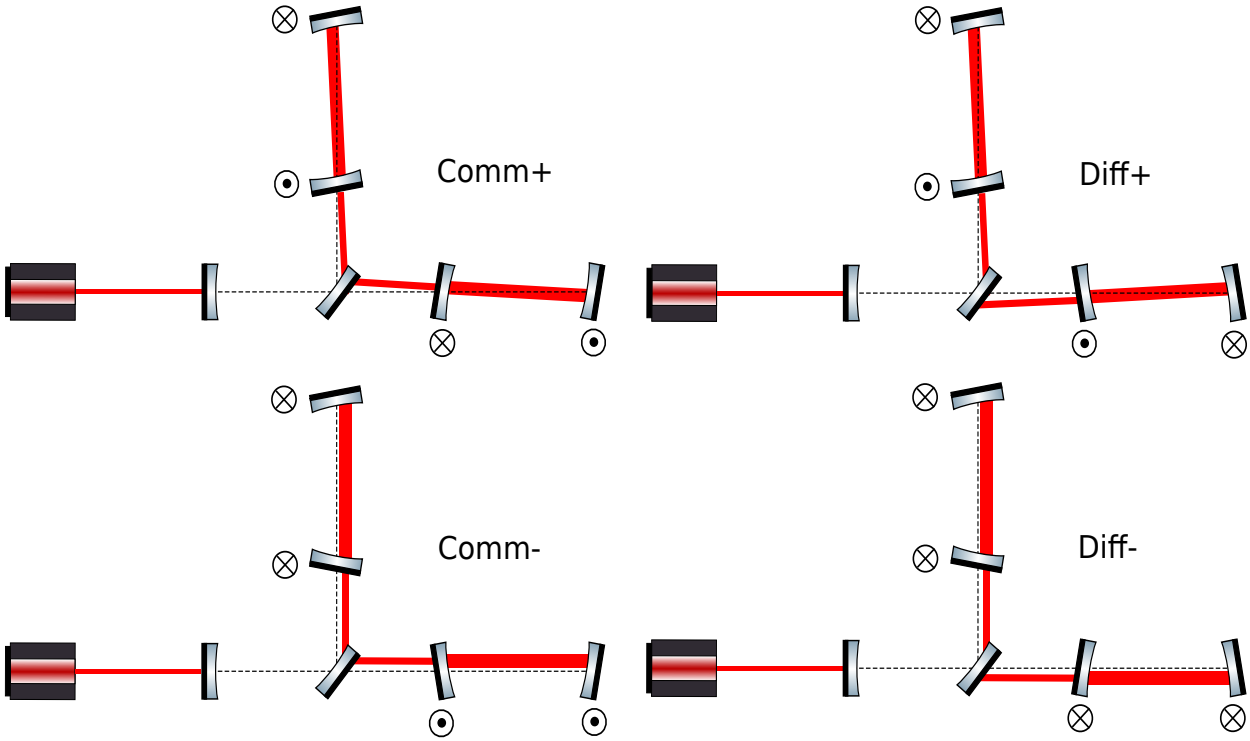

FIGURE 5.33: Scheme of the four angular DOFs of the arm cavities in the horizontal plane. The direction of the rotation of each mirror is indicated with the standard vector notation which indicates if the rotation axis is going in or out of the plane. The dashed line indicates the reference Optical Axis.

This sensing is decoupled, which allows all the DOFs to be closed in full bandwidth without the need of a hierarchical control.

Regarding the driving, the PRM and BSM are trivial, since there is only a mirror involved on each. However, the arm cavities DOFs depend on four mirrors, which might be difficult to implement in practice. The theoretical driving matrix is based on the one calculated for the tilt and shift DOFs of a simple Fabry Perot cavity in Matrix 4.82:

$$Comm(+) = \frac{(-\theta_{NI} + \alpha \cdot \theta_{NE}) \pm (\theta_{NI} - \alpha \cdot \theta_{NE})}{2} \tag{5.27}$$

$$Comm(-) = \frac{(\theta_{NI} + \alpha \cdot \theta_{NE}) \pm (-\theta_{NI} - \alpha \cdot \theta_{NE})}{2} \tag{5.28}$$

$$Diff(+) = \frac{(-\theta_{NI} + \alpha \cdot \theta_{NE}) \pm (-\theta_{NI} + \alpha \cdot \theta_{NE})}{2} \tag{5.29}$$

$$Diff(-) = \frac{(\theta_{NI} + \alpha \cdot \theta_{NE}) \pm (\theta_{NI} + \alpha \cdot \theta_{NE})}{2} \tag{5.30}$$

where $\alpha = (R_1/R_2)$ and $R_{1/2}$ stands for the RoC of the input and end mirror respectively. The $\pm$ accounts for the reversing reflection of the BS mirror, the $+$ corresponds to the yaw direction (θ^y) and the - corresponds to the pitch direction (θ^x).

This is the design of the alignment at the Dark Fringe, in the Steady State of the interferometer. However, the alignment is the most difficult part of the control.

This is mainly because there are a lot of DOFs to control, because they are mostly slow loops which are difficult to tune due to their also slow response and because they need all the longitudinal loops to be working properly.

As the lock acquisition of the longitudinal control is relatively fast with respect to the slow drifts of the alignment, if the system is aligned at the beginning of the lock sequence it will remain reasonably aligned until reaching the DF. For this reason it is not fully engaged since the beginning, only the DOFs that are limiting the longitudinal lock as the PR mirror one. In Virgo+ for example, during the lock acquisition only the PR mirror was engaged, the rest were engaged when in DF.

The commissioning of the angular automatic alignment will be explained in detail in the next Chapter (see Sections 6.2.4, 6.4.4 and 6.5.3), together with the difficulties caused by the coupling of the HOMs inside the interferometer.

5.5 Summary

In this chapter we have analysed the Power Recycling Interferometer configuration, which is the nominal one for the scientific run. We have presented its optical configuration and the longitudinal DOFs to be controlled. Then we have defined the working point of the carrier inside the interferometer as well as the role of the different sidebands and the conditions they need to fulfil.

Next we have presented the results of the Finesse simulation of the error signals in Dark Fringe. As this is the working point, the error signals needs to be as sensitive as possible while remaining decoupled. The optimal sensing has been showed, as well as the driving necessary to keep the DOFs decoupled.

We have also explained that since the Power Recycling Cavity is marginally stable, the HOMs are very close to the carrier and couple a lot to the interferometer. This makes the PRC especially sensitive to alignment, which might cause fluctuations on the OG of the error signals making the longitudinal loops unstable.

The solution proposed is to use the high frequency sidebands which, due to the Schnupp asymmetry, see huge losses and so a lower finesse inside the PRC. For this reason, any extra losses due to couplings of the HOMs will be negligible, and so the error signal will be more robust, although less sensitive.

The uncontrolled interferometer moves due to the seismic and frequency noise, too much to engage the lock of the four DOFS in Dark Fringe at the same time. For this reason a lock acquisition strategy is needed. The one used in Virgo and Virgo+ has been presented: Variable finesse. It proposes to control the longitudinal DOFs far from the working point, where the finesse is very high and the DOFs are very coupled, in order to easy the process. The lock strategy can be summarized in the following steps:

- **Step 1:** With the PR mirror misaligned, and the Michelson uncontrolled, bring the North cavity to resonance.
- **Step 2:** Bring the West arm to resonance.
- **Step 3:** Lock the Michelson interferometer in Half-Fringe by adding an offset to its error signal. Change the arm cavities control basis into CARM and DARM.
- **Step 4:** Align the PR mirror and engage the control of the PRC.

- **Step 5:** Decrease the MICH offset until reaching Dark Fringe.

These steps has been simulated using Optickle and Finesse in order to better understand the behaviour of the error signals during the lock acquisition, in particular the ones used in the past. The target of this study was to check that they behave as expected, to evaluate the performance of the new photodiode B4 and to anticipate any potential problem and look for solutions if needed. In this case the priority is to find robust error signals that survive the lock acquisition.

We have studied the quality of the error signals, which in the intermediate steps is not always good due to the asymmetry of the sidebands, and the coupling between DOFs, which is quite complex and evolves during the lock acquisition. We have studied the potential signals in Step 3 and 4 and then their evolution during the MICH offset reduction, in particular the impact of the demodulation phase. No major changes have been introduced with respect to the sensing used in Virgo and Virgo+ except for the use of B4 6MHz for CARM.

The control loop of the CARM dof has been addressed in a dedicated section because it is very complex due to its two contributions, the seismic and the frequency noise. However, the frequency noise requires a high bandwidth control, that can not be achieved by mechanically actuating on the end mirrors. Instead the corrections are used to modify the laser frequency. At the end the frequency control is split in several frequency bands: at high frequency, above 25 kHz is the pre-stabilization loop that locks the frequency of the laser to the IMC length; below 25 kHz is the Second Stage of Frequency Stabilization which uses the CARM error signal and splits it in two, the low frequency is sent to the IMC mirror (up to $\sim$200 Hz) and the high frequency to the laser itself, by summing it to the pre-stabilization loop. Finally the corrections at very low frequencies, up to several Hzs, are provided by the RFC and sent to the end mirrors.

The last step is the angular control. This is the most complex stage because there are 16 DOFs to control. For this reason, the strategy is to close only the DOFs that prevent the longitudinal control to reach DF. Finally, the alignment depends as well on the presence of HOMs inside the interferometer, which can spoil the error signals coming from the quadrant photodiodes. This means that some kind of thermal compensation might be needed in order to get proper error signal and close all the DOFs in full bandwidth.

Chapter 6

Advanced Virgo Commissioning

So far we have described in detail the PRITF and how it can be controlled from the theoretical point of view with the help of simulations and past experience. Notice that the aim of all the preparatory work that has been presented in the previous chapters was to better understand the behaviour of the Advanced Virgo interferometer and to anticipate potential problems.

In this chapter we are going to present the practical implementation of the process described in the previous section: the *commissioning*. In particular we will present the commissioning of Advanced Virgo until the first lock in Dark Fringe, which is the target configuration of this work. The different stages of the commissioning will be described in detail, as well as the problems encountered and the solutions implemented. We will put the emphasis on describing the logic of the process. It was not only based on theoretical considerations but also on experimental observations and in many cases on hardware constraints.

6.1 Commissioning timeline

First of all it is important to give an overview of the Commissioning chronology, focusing in particular on the time I have worked for the ISC subsystem. For this reason the timeline that will be presented here will begin with the first light reaching a photodiode in transmission of the North Arm, until the first lock in Dark Fringe.

It is important as well to mention the technical issues encountered that have caused major disturbances to the normal development of the commissioning activity to better understand the process. The target of the commissioning was to join O2. However, due to installation problems, the time margin for commissioning was dramatically reduced, which had a strong impact on its development.

The most relevant thing to take into account is the problem with the monolithic fibers that were used to suspend the mirrors. Since the 11th of November of 2015, they have broken on six different occasions, with the mirrors falling as a consequence. The chronology is shown in Table 6.1, although the last one was broken while pumping the vacuum in order to replace the fibers. This was a major issue because it requires to break the vacuum of the tower containing the mirror, extract the mirror to check for possible damage, send it to be cleaned if necessary, cleaning of the towers, replacing the fibers, mounting the mirrors in the payloads and putting them under vacuum again. This operation requires at least one week of work, during which the commissioning activities are very limited.

11-Nov-2015	WI fiber broken
11-Dec-2015	NI fiber broken
26-Feb-2016	NI fiber broken (2nd)
18-Jun-2016	WI fiber broken (2nd)
21-Jun-2016	WE fiber broken
13-Oct-2016	NE fiber broken

TABLE 6.1: Dates when the different fibers broke.

For this reason the commissioning of the CITF was postponed, even if historically it has been a good way to start commissioning different hardware and software elements. The CITF is a relatively simple configuration from the control point of view that it is well understood; therefore, it can provide preliminary diagnosis on the good operation of different components: photodiodes, demodulation, communication between different elements, actuation on the mirrors... However, this configuration has been commissioned later on in order to test different subsystems such as the Thermal Compensation System (TCS) or to test different procedures such as the hand-off of MICH error signal at DF.

These fibers were installed and used during the Scientific Run of Virgo+, so in the first two occasions we re-installed the mirrors with the same suspensions, since the technology was well tested. After the third fall it was decided to replace the fibers by steel wires, since the problem was not understood. The last mirror in replacing its fibers was the NE, which was the only one that had not experienced any problem. However its fibers broke during the venting process. After a big effort to understand the causes of this problem, they have been identified and a project to solve them is being prepared [53].

The delay caused by this problem postponed the beginning of the commissioning, reducing considerably the time available for this purpose. For this reason, the commissioning activity has been intensified, with the priority of joining the Scientific Run as soon as possible.

Another issue that we faced during the installation period is that the BS was manufactured with the wedge in the vertical direction instead of in the horizontal one as foreseen. This had an important impact on the design of the detection bench, in particular on the beam separation between B1 (beam at the detection port) and B5 (beam reflected by the North cavity). The bench needed to be adapted in consequence, but there was not a lot of margin so the priority was given to the quality of the B1 beam, which is the one used for the detection of GWs [54].

Figure 6.1 shows a timeline of the commissioning of Advanced Virgo since the North cavity was aligned for the first time the 24th of May of 2016 until the first lock in DC readout the 30th of March of 2017. The main source of delay, apart from the silica fibers, was the actuation of the BS. Already in Step 3 the MICH control loop was sending very high corrections, which were almost saturating. The gain of the loop was not enough to survive the full alignment of the PR mirror which means that more actuation was necessary for a good control.

We tried to mitigate this lack of actuation at the level of the mirror by implementing a hierarchical control where the high frequency corrections were sent to the marionetta. However the gain in dynamics was not enough and the decision to add an extra magnet to the mirror was taken the 21st of December. Once done, the lock of the PRITF was achieved within one day.

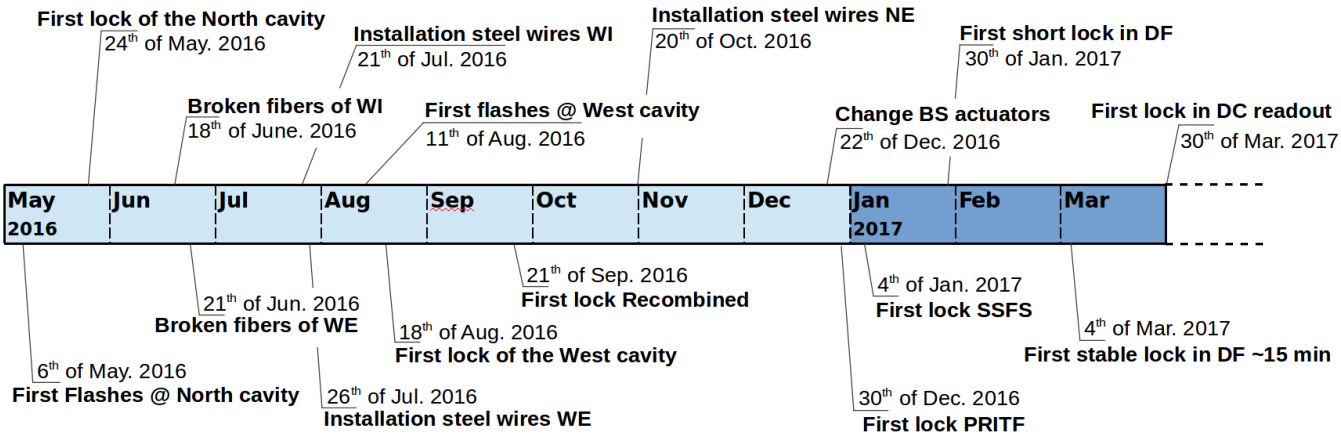

FIGURE 6.1: Timeline of the ISC commissioning of the interferometer from the first light arriving to the photodiode in transmission of the North arm to the first lock in DC readout. This is the period during which I have worked on the commissioning of Advanced Virgo.

Finally it is worth mentioning as well the impact of the TCS on the commissioning, even if it did not cause a direct delay. The PR mirror is pre-curved by 47 m far from the nominal value, in order to compensate for the thermal lens that will be induced by the High Power laser (125 W) that will be installed in the near future. However, the cold RoC makes the PRC "marginally unstable" which means that the cavity is not able to select the fundamental mode and the coupling of HOMs inside the interferometer is very high.

In principle this could be solved by using the Ring Heater (RH) to change the RoC of the PR mirror and bring the cavity to stability. However, due to a manufacturing problem, the ears of the PR were bigger than designed and so the mirror was mounted 7.5 mm closer to the RH, and so to the coils used to actuate the mirrors. The result is that turning on the RH heats up these coils more than usual, in particular it has been estimated that in order to reach the good RoC the coils will work at $\sim 67°$. This is not recommended because the outgassing of the coils could damage the coating of the mirrors [55].

For safety reasons the RH can work only at half power, which means that in order to make the PRC stable it is necessary to act on the input masses with the Central Heating. However the commissioning of the thermal compensation subsystem is delicate because thermal constants are very long (several hours) and it is necessary to have an already working system in order to tune it properly.

So it is important to keep in mind that the commissioning of Advanced Virgo so far has been done without any TCS, and so we have worked with an unstable cavity. Apart from the extra losses and the high presence of HOMs inside the interferometer, an additional difficulty is that modal simulations are not able to simulate unstable cavities. The software that describes unstable cavities is still under development and it is not able to reproduce error signals yet. For these reasons the behaviour of the interferometer might deviate from what theory and simulations predict, especially for the alignment as will be detailed later.

6.2 Steps 1 and 2: Arm cavities control

The commissioning started with the arm cavities, in particular the North one. This is because the North arm cavity defines the alignment of the beam, since it is not affected by the BS position. The first step was to find a pre-alignment of the cavity that allowed light to reach the photodiode in transmission. It took several days because we could not see the beam except in some particular places. Once this was done, it took approximately two weeks to engage the longitudinal control and another two weeks to have the first version of alignment.

At the beginning one of the most time consuming tasks was the pre-alignment of the cavities. It consists on finding the good angular positions in order to have enough light on the photodiodes to engage the control. When the mirrors are only under the Local Controls (LC) and there is no cavity alignment, the angular DOFs can drift by several μrad in relatively short time scales: several hours are enough to lose the light in transmission of the cavities. For this reason it was necessary to align the mirrors periodically by hand, which was very time consuming.

Once the cavity alignment was engaged, this problem was fixed since it prevents the angular DOFs from drifting away in an uncontrolled way. After this we were able to keep the cavities on resonance during long periods of time. Two months later the West cavity was available, and it was quite straightforward to implement a full control as the one of the North arm. In this section we will describe in detail this commissioning process.

6.2.1 Velocity and Finesse measurements

The first work that was needed in order to engage the longitudinal control was to **monitor the velocity of the cavity**, since it is the key point of the Guided Lock technique (see Section 4.4.3). Simulations had shown that the derivative of the PDH error signal was a good probe for the cavity velocity in the expected range of the cavities of Advanced Virgo. However, it was still necessary to find the calibration of this error signal that would give the velocity in physical units.

In order to do this we need an alternative method to calculate the velocity in physical units to be used as a reference. In the past, the distance between two TEM_{00} had been used, since we know that they are separated by an FSR (see Section 4.1). One source of error of this method is that it supposes that the velocity is constant, so the acceleration due to the seismic noise is not taken into account. However, it could provide a first estimation of the calibration factor.

The disadvantage is that the presence of HOMs makes the identification of the fundamental mode very difficult. In order to clearly do so it is necessary to excite the mirrors so that they cross very often the resonances allowing to distinguish between consecutive FSRs. The problem is that at this range of velocities ($>$ 2μrad) the derivative of the PDH signal needs a power law correction [37], which introduces uncertainty in the measurement.

Instead we decided to use the distortion of the power inside a FP cavity due to dynamical effects to obtain the velocity. Equation 4.24 gives its expression taking into account the movement of its mirrors. It depends on two parameters: the velocity of the cavity, v_m, and the storage time of the cavity, τ. This expression can be easily adapted to the transmitted power, which can be measured, by taking into account the transmission of the end mirror. Then it can be used to fit the transmitted power of the cavity which will provide the value of the velocity at which the resonance is crossed. An example is shown in Figure 6.2.

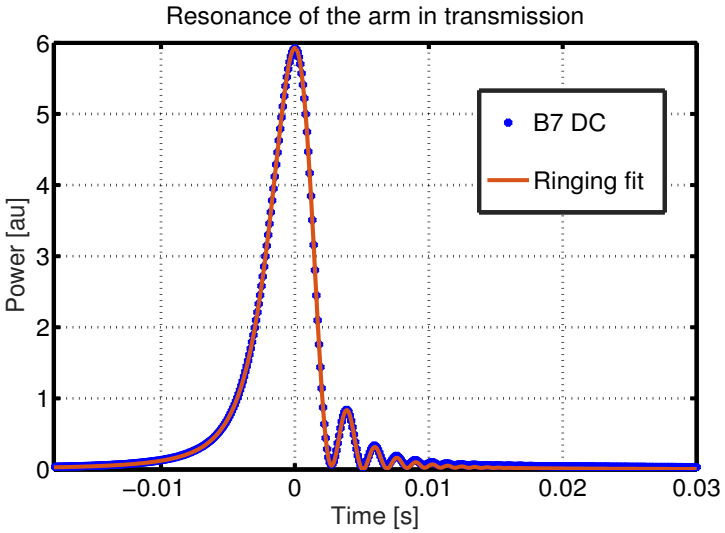

FIGURE 6.2: Resonance in transmission of the North arm fitted using the analytical expression. In this example the fitted velocity is 1.61 μm/s and the fitted finesse is 453.

The comparison between the velocity obtained with the fit and the derivative of the PDH signal allows us to obtain a first estimation of the calibration factor. In the early stages of commissioning it was the error signal in reflection of the cavity, B4 6 MHz, the one used for the longitudinal control. Using a set of data of 120 s and discarding the fits with a normalized residual higher than 30, the **calibration factor obtained is** $\mathbf{C_v = (3.64 \pm 0.15) \cdot 10^{-7}\ ms^{-1}au^{-1}}$. The error included here comes only from statistical considerations.

With the same analysis we obtain as well the **storage time of the cavity** which allows us to calculate the finesse. This provided a preliminary check that the cavities behaved as they should and that there were no major problems. Figure 6.3 shows the histogram of the finesse fitted using this method for the North and West arm cavities. Again, only statistical errors have been taken into account. However in this case the uncertainty on the alignment is an important source of error since it could lead to underestimate the real finesse. The fitted values are consistent with the target finesse which is $\mathcal{F}_{arm} = 454$, so no major problems were suggested by this preliminary analysis.

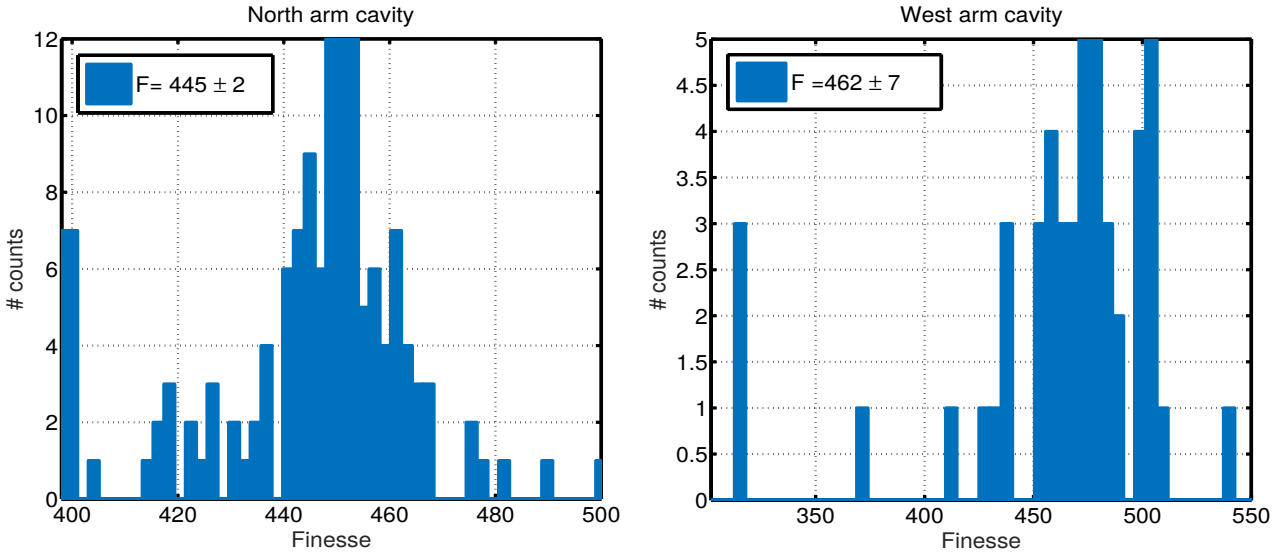

FIGURE 6.3: Histogram of the finesse fitted from the resonances in transmission. **Left plot:** North arm cavity, F = 445±2. **Right plot:** West arm cavity, F = 462±7.

6.2.2 Guided Lock implementation

The calibration factor measured previously, C_v, gave us a starting point to work on the Guided Lock technique (see Section 4.4.3). Notice however that even if time domain simulations had been made, the implementation in a programming language compatible with real-time computing was not straightforward. For this reason, the first version of this control technique was not very efficient and it was needed to wait for several minutes in order to engage the lock of the cavities. Figure 6.4 shows the first lock of the North Arm cavity the 24th of May, 2016.

The plot in the left shows the power in transmission of the north arm cavity, which fluctuates around its maximum power. The plot in the right shows the correction sent to the end mirror in order to keep the cavity on resonance. We see clearly the guided lock process: two short impulses one at -10 V and the next one at 10 V before engaging the linear lock. Notice, however that the strategy was not very well optimized yet. The trigger of the linear lock was not well adjusted since the second resonance was slow enough for engaging it, but a second impulse was sent instead before engaging the control.

The key points to adjust were the **velocity estimation**, the **duration of the impulse** and the **moment of engaging the linear lock**. For the first point we used the results of the simulation showed in Section 4.4.3. The lock algorithm would initialize a counter when the cavity reaches 10% of the maximum transmitted power (we used as a reference the power when the cavity is controlled on resonance) and that stops when reaching 40%. This parameter, GL_{count} contains the information about the cavity velocity and we use it to take a decision.

As mentioned in the corresponding section, the chosen target velocity after the continuous impulse was 0.3 μms^{-1}. This velocity roughly corresponds to 50 counts and when GL_{count} exceeds this value, we know that the cavity is slow enough that our PDH error signal will not suffer from important ringing effects and the linear lock can be engaged.

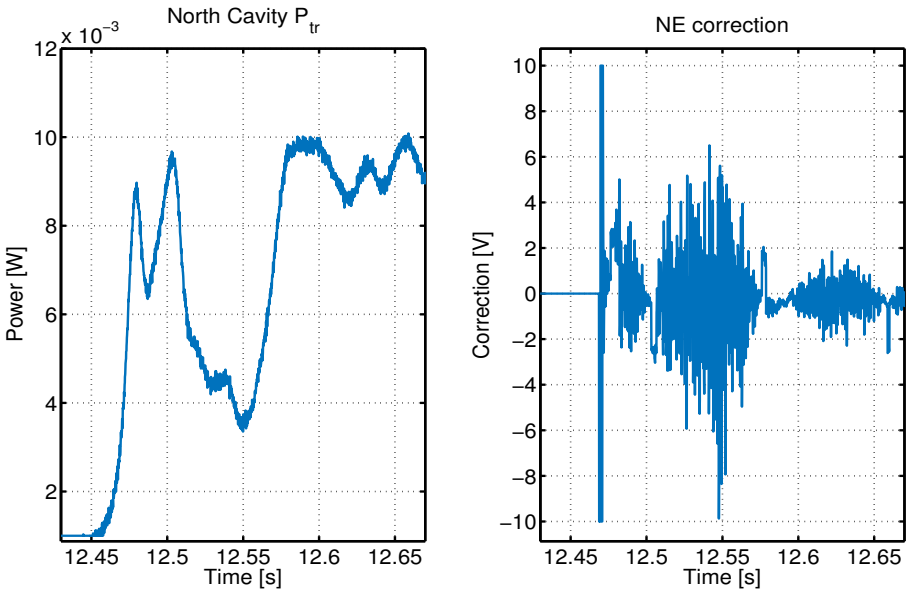

FIGURE 6.4: First lock acquisition of the North arm cavity. **Left plot:** Power in transmission of the cavity. **Right plot:** Correction sent to the NE mirror.

Notice that normally we would need to take in consideration the level of transmitted power before engaging the linear lock as the error signal is linear only when the power is higher than $P_{max}/2$. However as the error signal that we are using is normalized, its linear region is much wider and there is no need of specific power triggers.

On the other hand, if GL_{count} is lower than 50 after reaching 40% of P_{max}, we know that the cavity is going too fast and an impulse is needed in order to slow it down. Equation 4.66 shows the time that the pulse has to be applied knowing that the maximum force available is 2.5 mN (10 V), the mass of the mirrors is 42.3 kg and the target velocity, v_{fin} is 0.3 μms^{-1}.

For the direction of the impulse we use the sign of the error signal before the zero crossing. The equivalence between the sign of the impulse and the sign of the error signal needs to be tuned empirically since it depends on the demodulation phase as well. However, it is not difficult to correctly tune it since a wrong sign will "accelerate" the cavity.

Then the impulse is sent during the calculated time and with the good sign, and a new iteration starts when the cavity crosses the next resonance until the cavity lock is engaged.

An example of this process is shown in Figure 6.5. It shows the power in transmission of the arm cavity, and two resonances can be seen before the lock is engaged. The first resonance presents ringing effects but not the second one, which indicates that the second resonance was crossed with a lower velocity.

From the error signal slope it can be seen that the first and the second time that the resonance is crossed, it is done in opposite directions. Also in this case the ringing is well visible in the first resonance-crossing and less in the second one. The change in the direction is due to the pulse shown in the lower plot. The time that the pulse was applied was shorter the second time that the resonance was crossed, which also indicates a slower velocity.

When the linear lock is engaged, the correction sent saturates. In Section 4.4.1 we saw that the step response might oscillate before reaching a stable state in the presence of an overshoot. In this case the transient is due to the noise in the error signals. After a small amount of time the correction stabilizes within the dynamic range of the actuators, reaching the steady state.

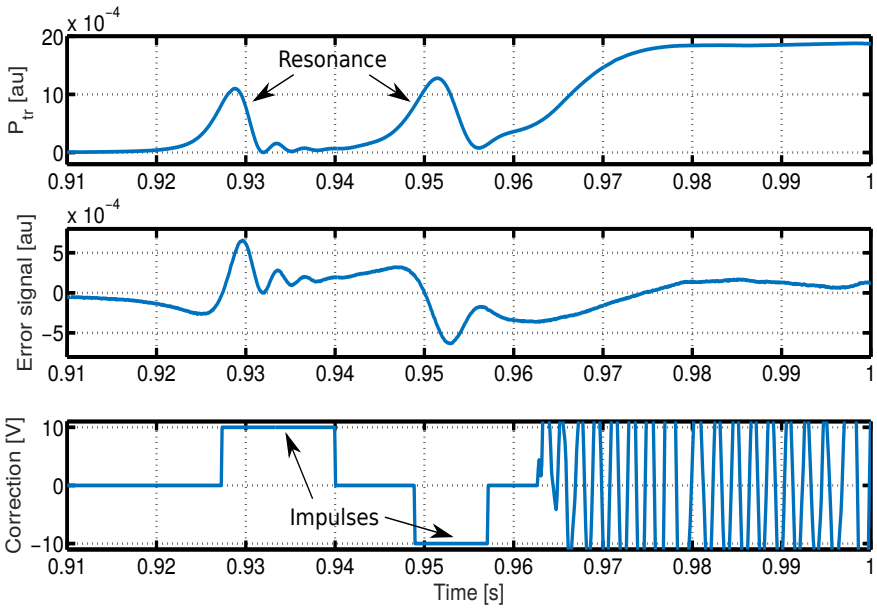

FIGURE 6.5: Lock acquisition sequence using the Guided Lock technique optimized in the Nort Arm cavity. **Upper plot:** power in transmission of the cavity. **Central plot:** error signal, B7 6MHz. **Lower plot:** correction sent to the end mirror.

Finally a second impulse is sent, in the opposite direction and shorter, since the second resonance is crossed more slowly, in order to bring the cavity back to the resonance a last time, when the linear lock is engaged.

6.2.3 Error signal calibration

As it was mentioned before at the beginning we used B4 6MHz (the error signal in reflection of the cavities) to control them because it has more signal than the photodiodes in transmission and so it is less noisy. However, as soon as we realized that the lock could be engaged directly in transmission, we started using B7 and B8 6 MHz because they would allow us to engage simultaneously the lock of both arms.

It is easy to **tune the demodulation phases** of these error signals, since we can leave the cavities free-swinging and tune the phases in order to maximize the slope of the signal in-phase (P) and minimize the signal in-quadrature (Q), as it is shown in the left plot of Figure 6.6.

Once the cavities are locked, the FFT (Fast Fourier Transform) of both error signals will allow us to tune it in a more precise way, again by maximizing the signal in P and minimizing the signal in Q. Once within a range of $\pm 10^{\circ}$ around the optimal demodulation phase, the effect of the tuning is hard to see on the projection we are trying to optimize. Instead, at this stage is easier to minimize

the other projection, until reaching the electronic noise of the photodiode. The plot on the right of Figure 6.6 shows an example when the North cavity is locked.

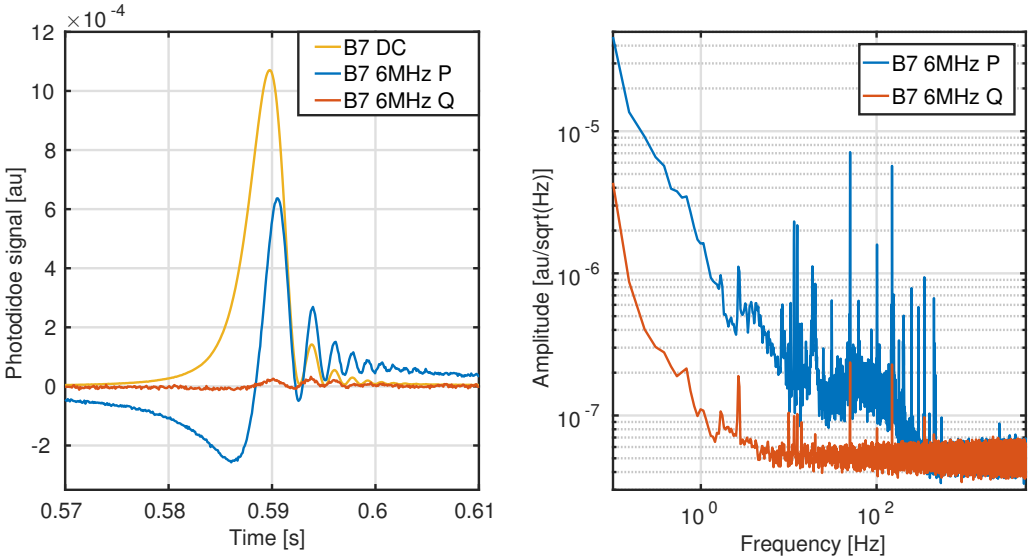

FIGURE 6.6: **Left plot:** DC power and P and Q projections of the error signal in B7 photodiode (arm transmission) when crossing a resonance. **Right plot:** FFT of the error signal P and Q projection while the cavity is controlled.

The **error signal provides information about the quality of the lock** since it carries information about how far is the cavity from resonance. This means that when the cavity is controlled, the error signal basically represents the residual length fluctuations, and so if we calibrate it, we will know the precision of the longitudinal control.

In order to calibrate the error signal, we will use the knowledge we have of the OLTF of the feedback loop of the cavities. As exposed in Section 4.4.1, the feedback loop of a simple Fabry Perot cavity depends on:

- **The Plant**, which in our case is the Optical TF of the arm cavity (W/m).
- **The Sensor** Transfer Function (V/W).
- **The Control Filter** (V/V).
- **The Actuators** (μm/V), which comprises the Mechanical TF of the suspension of the mirror and the TF of the coils, which are already calibrated in physical units.

The error signal can be calibrated by measuring experimentally the Open Loop TF of the arm cavity and comparing it to the model. The gain of the control filter and the calibration factor of the actuator TF are known, so the extra factor needed in order to make the model agree with the experimental measurement will be the calibration factor that we are interested in. It contains the gains of the Optical TF and the Sensor TF, always under the supposition that the photodiode has a flat TF in the region of interest.

In order to **measure experimentally a transfer function** it is necessary to inject noise in a strategic point of the feedback loop while it is closed. This way the response of the system can be monitored. The point of injection (Input Y(s)) and the point where we measure the system's response (Output X(s)) are chosen depending on the TF we are interested in. As we want to measure the OLTF of the system, the noise will be injected at the level of the error signal and the response will be studied after the control filter, as shown in Figure 6.7.

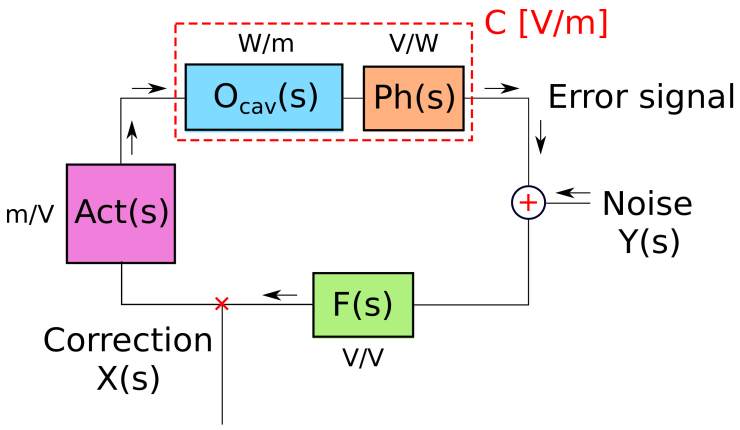

FIGURE 6.7: Scheme of the feedback loop of a cavity showing where to inject noise in order to measure the OLTF.

In order to make a good measurement we need to be sure that the level of injected noise is high enough to have coherence between the Input and the chosen Output. For this reason the noise has to be adapted to the shape of the correction sent to the actuators of the loop in the frequency bandwidth that we want to study. On the one hand the noise needs to be high enough to have coherence, but on the other hand it has to be low enough not to saturate the controls which would provoke a loss of the control. This usually means that the noise injected can not be simply white noise, but it has to be shaped to fulfil this requirements.

Figure 6.8 shows the measurement of the OLTF of the North arm. It has an UGF of 28 Hz, and it can be seen that the model (already presented in Section 4.4.1) and the measurements are in agreement in the region where the coherence is good (> 0.8). Notice however that in order to have a good agreement for the phase of the filter, an additional delay of 800 μs has been considered.

This delay comes from the propagation of the error signal from the photodiode to the actuator. This includes the delay due to the passage through several digital processes, which typically is 200 μs per process, and the delay from the actuator itself, which have been measured by the calibration team and is typically of the order of 400 μs [56]. It plays a key role on the stability of the filters since a time delay is seen in the frequency domain as a phase loss [57] which will limit the phase margin and so the bandwidth that can be reached. Indeed, the maximum UGF that can be achieved is limited by the delay since at 200 Hz there is no phase margin anymore (less than 45°).

In order to improve the performance of the filter, an extra integrator (a pole) has been added at low frequencies, also known as *boost*. It can not be seen on Figure 6.8 because it is out of the frequency range shown. Its role is to have a more stringent control at low frequencies, where there is a higher presence of noise, mainly seismic one. It reduces the stability margin at low frequencies, but it

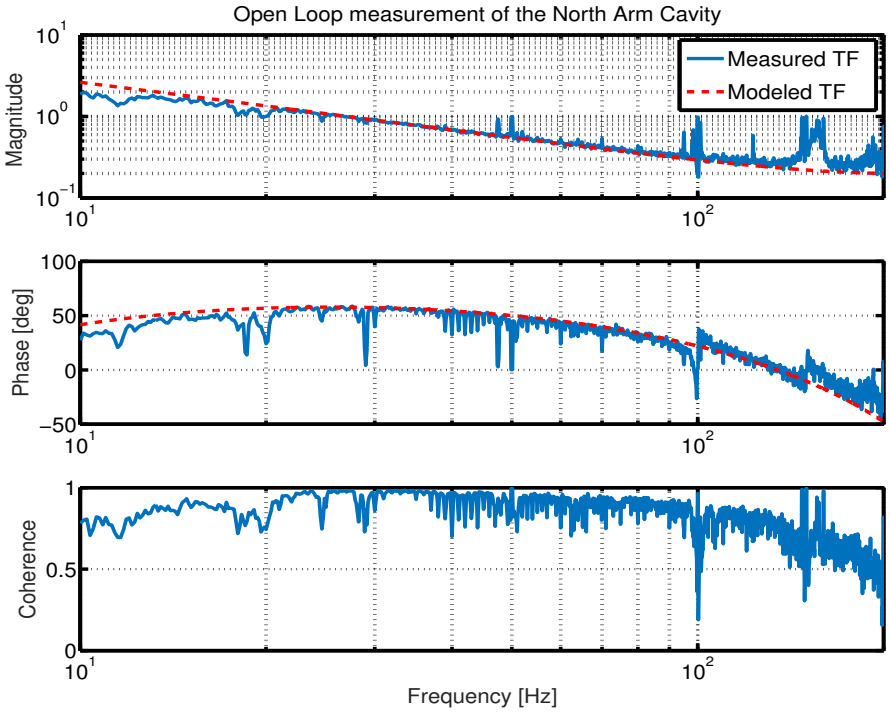

FIGURE 6.8: OLTF of the North arm cavity comparing measurement and model. The coherence of the measurement is shown in the lower plot.

provides a better control. For this reason, the control is engaged without the boost, and once the transients have passed (few seconds) and the cavity is controlled, the boost is turned on.

From this measurement we have been able to derive the **calibration factor for the North Arm and for the West Arm** by doing an equivalent noise injection.

- $\mathbf{C_{north} = 2.15 \cdot 10^{-7} m/V}$
- $\mathbf{C_{west} = 2.66 \cdot 10^{-7} m/V}$

The discrepancies between both can come from slightly different optical transfer functions. The maximum power measured is not the same for both arms, so either the finesse is not exactly the same or there is some diffused light on one of the benches. Regarding the uncertainty on the calibration factors, there are two main sources. One comes from the fit, which has been done with an accuracy around 15%. The second one comes from the measurement itself, and the conditions of the interferometer during the data taking. When the PR is misaligned the interferometer is in a quiet state, so we are limited by the fit error. However, the aim of these measurements is a check of the loops correct behaviour, not precision. For this reason we will not take into account errors in the calibration factors.

Finally, applying this coefficient to the corresponding error signals, we can calculate the residual motion of the cavities when they are controlled with the rms of their power spectral density (PSD). For the north arm it is 25 pm and for the west arm it is 27 pm, as we can see in Figure 6.9. The performances are very

similar between them, as expected, since the controllers are the same and they are affected by the same noise sources. The UGF of the control loop when the PSD of the error signals was done was ∼55 Hz.

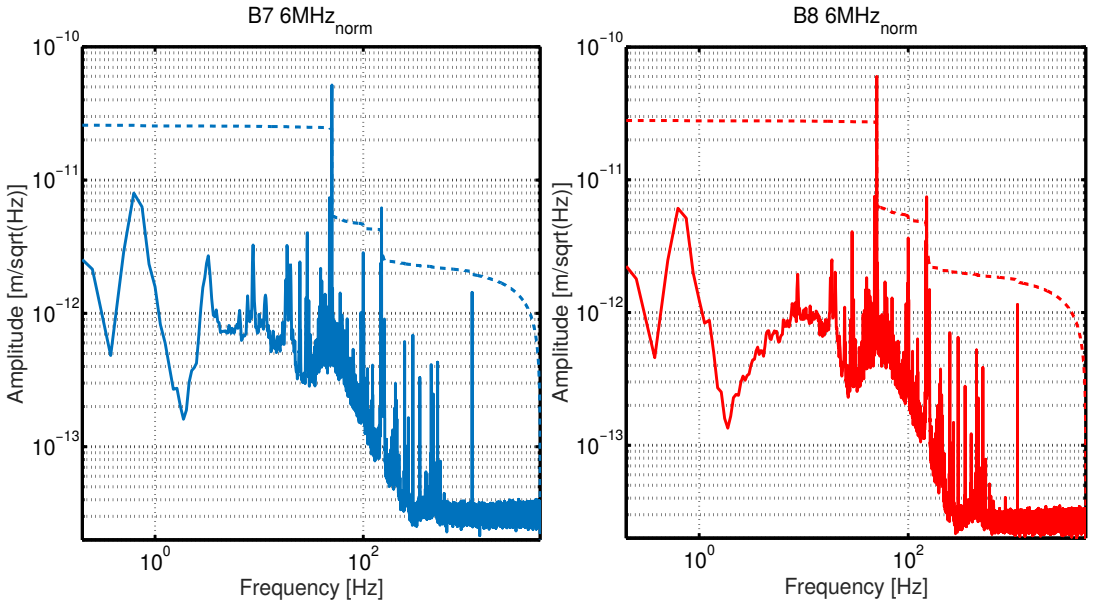

FIGURE 6.9: FFT of the error signals used for the arm longitudinal control calibrated. **Left plot:** B7 6MHz normalized error signal, rms = 25 pm. **Right plot:** B8 6MHz normalized error signal, rms 27 pm.

The rms is mainly dominated by peaks at 50, 100 and 150 Hz, which come from electronic coupling. In this case the solution would be to reduce the coupling of these lines to the error signal, which would allow us to improve the quality of the lock. This work will be done at the DF during the noise hunting period while trying to improve the sensitivity.

If the correction needed to compensate these lines is larger than the actuator dynamics, the control might become unstable. In this case it is possible to add a *notch*[1]at these frequencies on the filter. This could be a problem for the 50 Hz frequency since it is close to the control UGF and it could reduce the stability margin.

6.2.4 Angular control

As it was mentioned in Chapter 4, the mirrors suffer from slow angular drifts, which couple to the longitudinal control introducing noise and spoiling the coupling of the input beam to the optical resonator. For this reason an active angular control is needed both to align the beam to the optical axis of the cavity and to center the cavity axis with respect to the mirror actuation.

Several methods were presented in Section 4.5.2 and it was decided that the mechanical modulation was the best for the arm cavities. It does not provide a high bandwidth control, its UGF is normally of the order of tenths of mHz, but it is easily implemented and very robust, which makes it perfect for the beginning of

[1]A notch is a special type of band-stop filter that attenuates a very narrow frequency range.

the commissioning. A control loop which such a low bandwidth is also known as *drift control*.

Sensing

As explained in the previous chapter, the **mechanical modulation** takes advantage of the coupling between the longitudinal and the angular motion. Its working principle is to add a sine on the angular degree of freedom to be controlled at a particular frequency, $f^{\theta_i}_{drift}$. This movement will cause a length change, δL, when the optical axis is not perfectly aligned. The δL will be corrected by the longitudinal control in order to keep the cavity on resonance. This means that the presence of a signal at $f^{\theta_i}_{drift}$ in the longitudinal correction will tell us that the oscillating DOF is misaligned. This information can be extracted by demodulating this correction at $f^{\theta_i}_{drift}$ and then use as an error signal.

For the alignment of the beam with respect to the cavity axis the rationale is very similar. A line at $f^{\Delta_i}_{drift}$ is placed into the DOF of the beam to be controlled. However in this case it is the transmitted power that contains information, because the alignment of the beam with respect to the optical axis modifies the power that resonates inside the cavity (see Section 4.5). The presence of a line at $f^{\Delta_i}_{drift}$ on the spectrum of the transmitted power will be minimum when the beam and the optical axis of the cavity are well aligned so the demodulation of P_{tr} at $f^{\Delta_i}_{drift}$ can be used as an error signal for the control of the beam alignment.

The first step was the **centering of the beam** on the PR and the NI mirrors. Mechanical modulation was used also for this purpose. A dithering line was added to both PR and NI angular DOFs and then the low finesse cavity PR-NI was locked. The beam's tilt and shift were adjusted in order to minimize the dithering line on the spectrum of the longitudinal lock correction and to maximize the resonating power.

This provides a pre-alignment of the beam with respect to the interferometer plane. This step is very important because the actuators of the beam alignment which have large dynamics are components of the Injection telescope 3.4 and they can not be used inside a control loop since they are very sensitive. For the shift DOF this is especially critical since it can only be adjusted with this telescope or by adjusting the height of the mirrors with the suspensions, but none of these actions can be made within a control loop.

On the other hand, the tilt of the beam can be fine tuned taking advantage of the fact that the PR mirror is curved. In this case the angle of the output beam will be different depending on where it impinges on the PR mirror and so a translation will cause a tilt of the beam that impinges on the North cavity. For the same reason, a translation of the BS mirror will tilt the beam that impinges on the West arm cavity. Notice that the beam impinging on the North arm cavity depends only on the input beam alignment while the one impinging on the West arm cavity can be further adjusted with the BS. It is for this reason that the PR-NI cavity is used as a reference.

The next step was to **choose the frequency of the dithering signals**. The aim was to tune them to be as low as possible while keeping them visible in the correction spectrum. The frequencies were chosen to fall into a quiet part of it, but within the bandwidth of actuation of the marionetta. As its TF behaves as $1/f^2$, more actuation is necessary to actuate at higher frequencies. To avoid saturation, the bandwidth can be at most 20 Hz. It turned out that the region around 10 Hz is

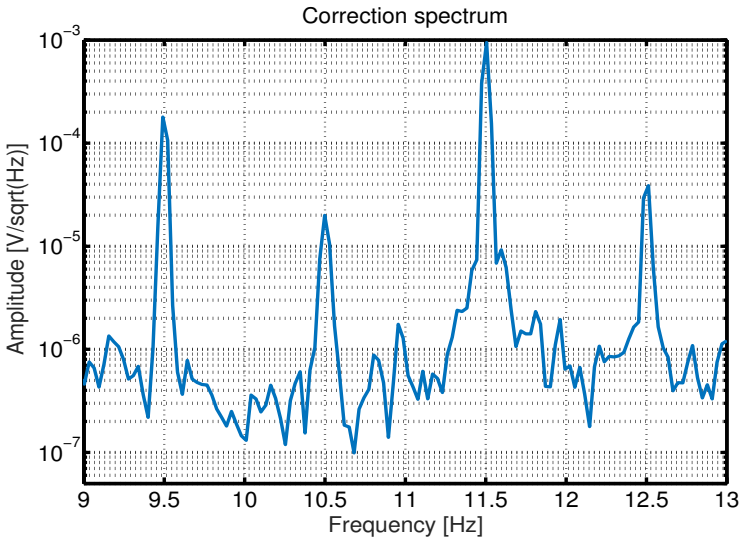

FIGURE 6.10: Zoom of the power spectral density of the correction of the longitudinal lock of the North Arm cavity once the dithering lines are added to the mirrors angular DOFs.

the most quiet one and so the lines chosen were: 9.5 Hz for the NE θ_x, 10.5 Hz for NE θ_y, 11.5 Hz for NI θ_x and 12.5 Hz for NI θ_y. They can be seen in Figure 6.10.

Once the lines were injected, the correction of the lock was demodulated at the chosen dithering frequencies in order to build the error signals of the four angular DOFs of the cavity. At this point it was necessary to **check if these demodulated signals were good error signals**. First of all we checked if they could sense the corresponding mirror movement. In order to do this, during one lock of the North Arm cavity, each of the mirrors was misaligned in an independent way. Then the correction of the longitudinal control is demodulated at each $f_{drift}^{\theta_i}$ to get the angular error signals. The demodulation phases were tuned offline in order to maximize the effect of the angular movement. The results are shown in Figure 6.11.

The plots on the left of Figure 6.11 show the signals from the LCs which represent the misalignment experienced by each angular DOF. On the right plots we can see the optimized demodulated signals. It is clear that they sense the misalignment of each mirror, as we expected. The zero-crossing do not agree with the one of the LCs, but this can be tuned by adding an offset.

However, it was also observed that the NE and NI error signals were very coupled between them, as expected from the geometry of the arm cavity (see Section 4.5.1). For this reason, in order to build error signals that are decoupled between them it was necessary to reconstruct the cavity eigenvectors: tilt and shift.

Regarding the tilt of the input beams of the cavities, a similar process has been done. For the North arm cavity, dithering lines have been added to the PR mirror translation and for the West one they have been added to the BS mirror. The error signal are obtained this time by demodulating the transmitted power.

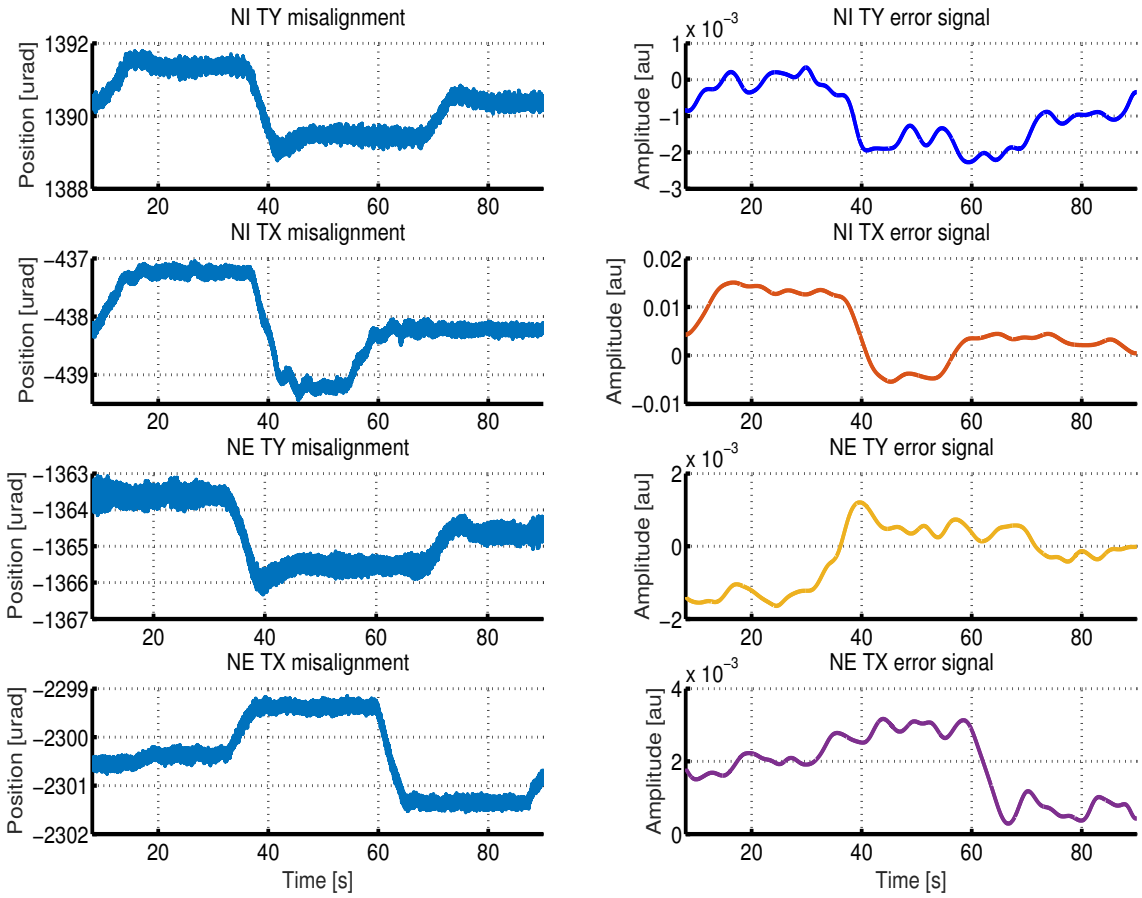

FIGURE 6.11: **Left plot:** angular movement of each mirror of the north cavity. **Right plot:** corresponding error signals with the demodulated phase optimized.

Driving

In Section 4.5.1, the eigenvectors of the cavity alignment were defined in Equation 4.82. However, in real life the ability to actuate on this DOFs depends on the actuators calibration, which is accurate within 10% [58]. In order to decrease this uncertainty we have **measured experimentally the dependence of the transmitted power of the cavity on the single mirrors alignment**.

Starting from an aligned state with the LC engaged but with the cavity unlocked longitudinally, the evolution of the transmitted power resonances or *flashes* has been studied as a function of the misalignment of both mirrors. In order to do so, an angular line has been added to the θ_i of the End mirror at the level of the marionetta, with an amplitude of $\pm 8\mu$rad and at a frequency of 20 mHz. The frequency was chosen under the resonances of the mirror pendulum (600 and 800 mHz) in order to avoid the attenuation due to the mechanical transfer function which decreases as $1/f^2$ above the resonances. Otherwise, in order to make such an important angular movement, the correction sent would be too high.

At the same time the angular position of the North Input mirror was changed by applying a slow ramp at the marionetta (several minutes to do $\pm 35\mu$rad). This

action was repeated for different alignments of NE θ_i (always with the angular line on) until the misalignment was too important to see any flash on the B7 photodiode. When this happened, the mirrors were repositioned in order to find an alignment that allowed to have light resonating on the cavity. This process was iterated in order to make several complete scans of the cavity alignment. An example of this scan for the North arm cavity in the Y-plane is shown on Figure 6.12.

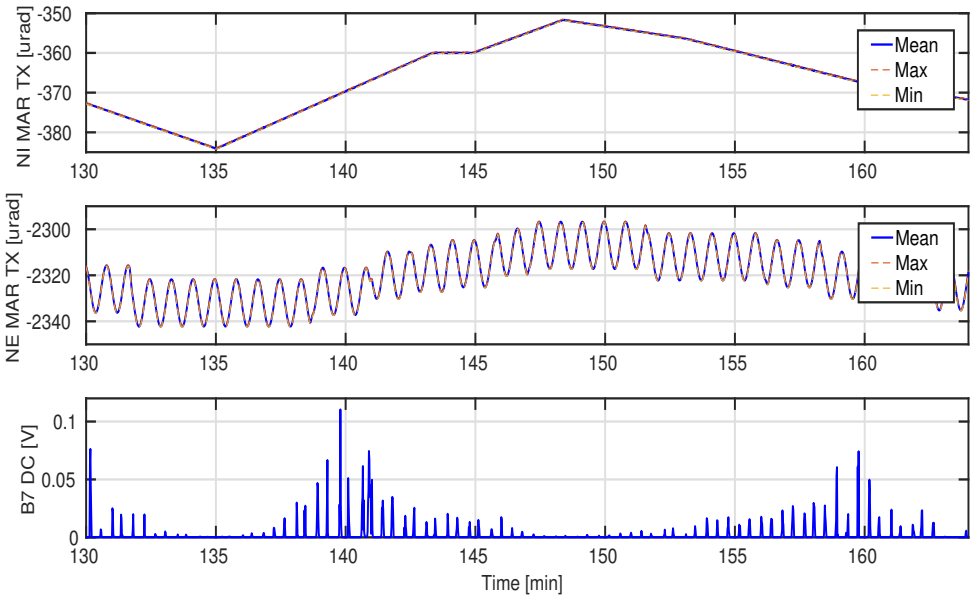

FIGURE 6.12: Scan of the transmitted power of north arm by misaligning the NE and NI mirrors on θ_x by acting on the marionetta. The flashes on the transmitted power, B7 DC, are resonances of the cavity. It is shown how they increase and decrease depending on the angular position of the cavity mirrors. The data shown are sampled at 1Hz (trend data).

With the collected data, an analogue plot to Figure 4.28 was done for the arm cavities of Advanced Virgo. The analysis has been made with the trend data (stored at 1Hz), and in order to have more statistics the mean, maximum and minimum values of the mirrors alignment positions have been used. For each alignment position, the maximum power of the transmission peaks of each scan has been taken into account. Notice that as we are using the data at 1 Hz, there are several transmission peaks at each position. Taking the maximum value of the power guarantees that we are selecting the slowest peak (as explained on Section 4.4.3).

In order to be sure that the maximum peak is always a 00 and not a HOM due to a high misalignment, we made a simulation and we checked that in the studied interval the 00 carries always the most power (see Figure 6.13).

As there were made several complete scans of the cavity alignment, for each alignment position there were several power values. This way the impact of the cavity velocity on the power of the transmission peaks was minimized. The analysis has been done by taking the maximum value of all of them and by taking the mean value obtaining an equivalent result for both configurations. Figure 6.14 shows the configuration where the maximum values are taken.

According to Equations 4.76 and 4.77 the slope of Figure 6.14 should give us the ratio between both radius of curvature that is used in order to change basis.

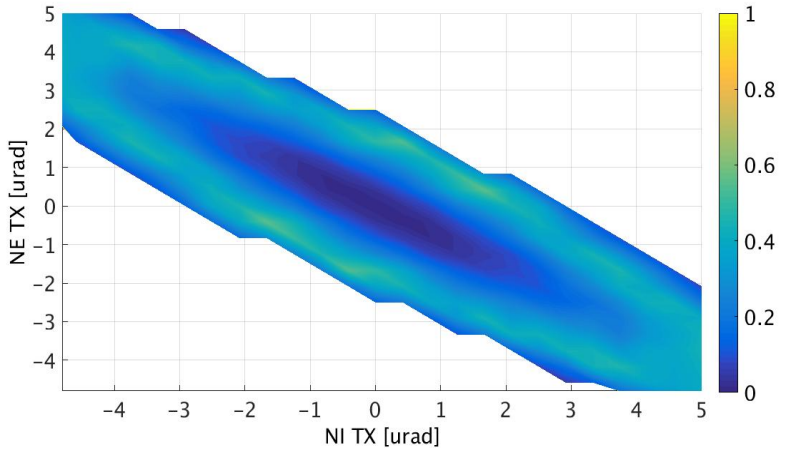

FIGURE 6.13: Power ratio between the HOMs due to the misalignment and the 00 as a function of θ_x of NE and NI mirrors (P_{HOM}/P_{00}). The power ratio goes from blue (when there is no HOM) to yellow (when the 00 and the HOM have the same power).

Figure 6.14 has been fitted to a line with a slope of 0.92 to be compared with the theoretical one which is 0.84. The discrepancy comes from the cross-calibration between the actuators of the NE mirror and the NI mirror which are expected to be identical within a 10% error [58]. Taking into account this uncertainty the experimental measurement is well in agreement with the values predicted by the theory.

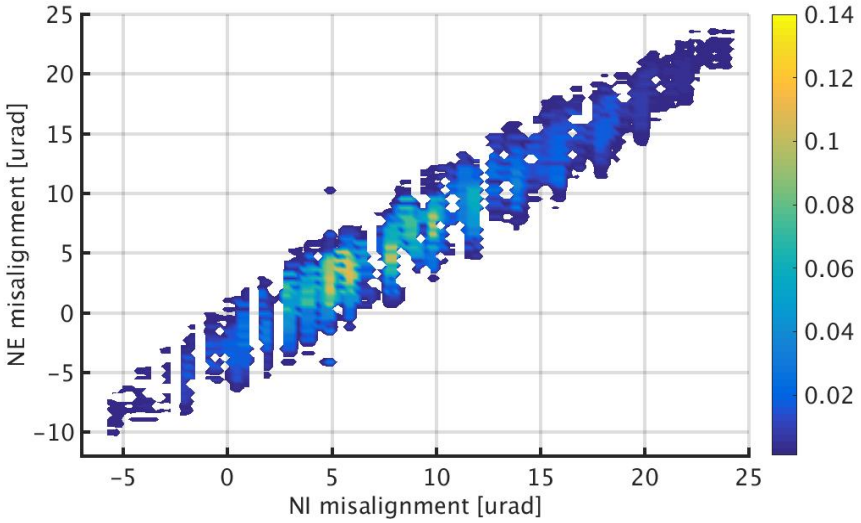

FIGURE 6.14: Measurement of the transmitted power of north arm as a function of the mirrors misalignment on θ_x. The power distribution is represented in a color scale which goes from blue (minimum power) to yellow (maximum power).

This measurement has been done for the two cavities and in the two planes X and Y. Table 6.2 shows the measured driving of the arm cavities angular DOFs. In particular, the coefficients shown correspond to a pure tilt. In order to reconstruct

the shift it is enough to change the sign of the end mirror coefficient. All the values are within 10% of discrepancy from the theoretical value except the X-plane of the North arm cavity, where this discrepancy is of the order of 30%.

	North Arm θ_x	North Arm θ_y	West Arm θ_x	West Arm θ_y
End mirror	-0.92	1.09	-0.89	-0.72
Input mirror	1	1	1	1

TABLE 6.2: Driving of the cavities that produces a pure tilt. In order to drive a shift it is only necessary to change the sign of the End mirror coefficient. These coefficients correspond to the matrix elements of Equation 4.78

The relative sensitivity to a shift or to a tilt can be extracted from Figure 6.15. The ratio between both DOFs can be calculated as done for the simulation: in this case for the photodiode signal to decrease to 0.032 V a pure tilt of 6.7±0.6 μrad and a pure shift of 39.6±0.6 μrad are needed. The ratio between them is in this case 5.9±0.6 which is in agreement with the result of the simulations taking into account the actuators calibration uncertainty of 10% previously mentioned.

Using the slope found experimentally the change of basis to tilt / shift has been made as well as its calibration and it is shown on Figure 6.15.

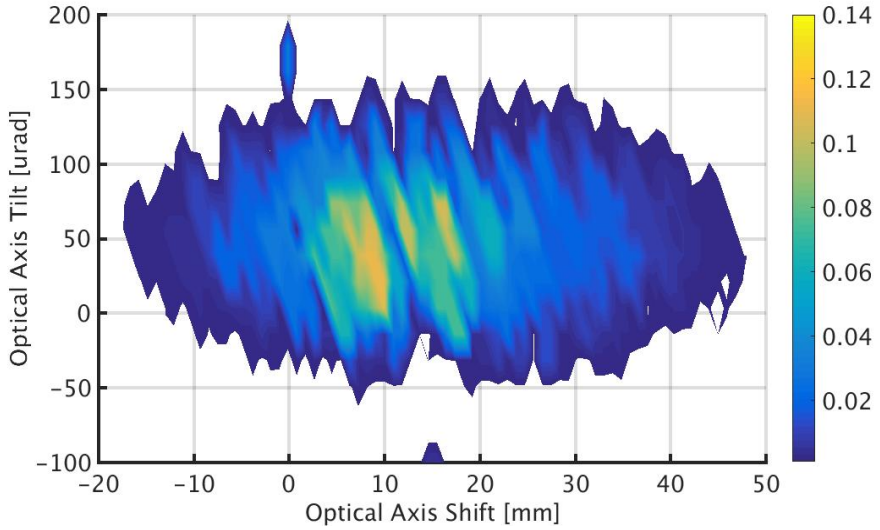

FIGURE 6.15: Measurement of the transmitted power of north arm as a function of the optical axis angular degrees of freedom. The power distribution is represented in a color scale which goes from blue (minimum power) to yellow (maximum power).

Implementation

At this point we have all the information needed to **engage the loop**. First of all the error signals obtained from each mirror (4 in total) are combined in order to recreate the tilt and shift degrees of freedom using Equation 4.78. Then, they are sent to the control filter which for a drift control consists of a simple integrator whose gain is adjusted in order to have an UGF around several tenths of mHz.

The limiting part of this control is the precision of the actuators, because the cavity angular DOFs need a particular driving matrix in order to be decoupled. In order to simplify this problem we have implemented a hierarchical control between tilt and shift. Knowing that the tilt is the most relevant DOF, it has the highest bandwidth and so it is the fastest loop. The shift is the slow loop, with a lower bandwidth than the tilt. As it is the less sensitive DOF, we have simplified the driving and used only the input mirror to correct it. This way any coupling from the slow loop can be quickly corrected by the fast one.

Regarding the beam tilt, this loop has also a high bandwidth, since it is a relevant one as well. In this case there is no problem of driving, since only one mirror is involved.

This control scheme has allowed us to reach very long periods of lock (several hours). Also an advantage is that with a rough pre-alignment of the arm cavities, the drift control is able to bring them to an aligned state in a short period of time, saving a lot of commissioning time. Figure 6.16 shows a lock period of the North arm cavity. It is first locked longitudinally while being misaligned (half of the maximum power) and then the drift control is engaged.

In Figure 6.16 the angular control acts on the alignment of the cavity mirrors and the beam until reaching the aligned state, where the power is maximum. As mentioned previously, we will use the translation of the PR mirror as actuator of the beam alignment. Within one minute most of the power is recovered. So in principle even if the control it is not very precise, it is very robust and provides a stable alignment over extended periods of time, which was the target.

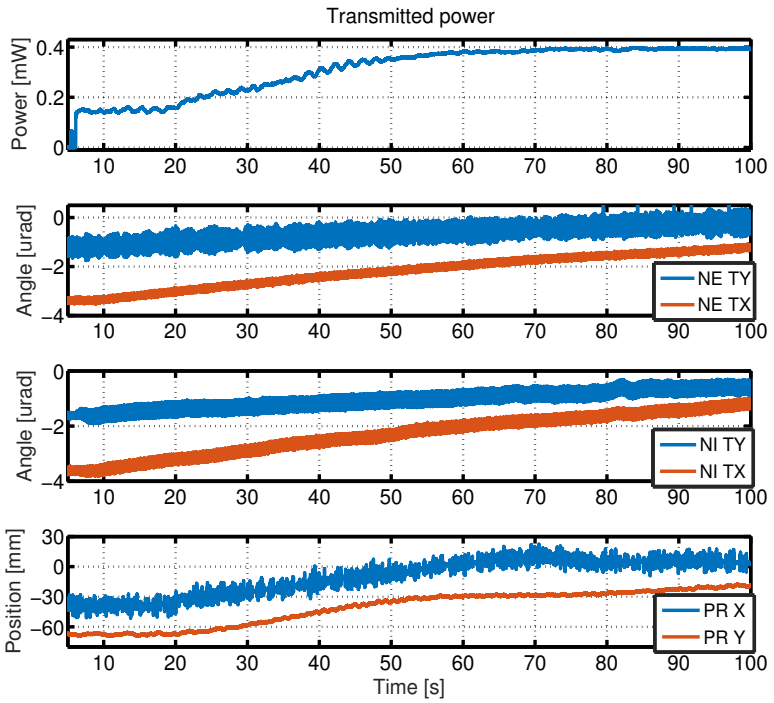

FIGURE 6.16: Alignment of the North Arm cavity thanks to the drift control. **Upper plot:** power transmitted by the cavity. **Central plots:** angular position of the end and input mirrors in both the X and Y-planes. **Lower plot:** position of the PR mirror both in the horizontal and the vertical planes.

6.3 Step 3: Recombined

As presented in the previous chapter, in this step all the loops are engaged in a sequential way, except the PRCL one because the PR mirror is misaligned at this stage to minimize the coupling. As a reminder, the Michelson is locked on its Half-Fringe in order to decrease the finesse of the PRC when it will be aligned. Then, there is a change of basis and we pass from controlling the arm cavities in an independent way to control the Common and Differential arm lengths, CARM and DARM. This allows us to engage the Second Stage of Frequency Stabilization, decreasing the frequency noise in preparation for the next step.

6.3.1 MICH loop

Once the arm cavities are controlled and aligned, the next step in the lock acquisition scheme is to control the Michelson interferometer. Two error signals had been studied for this DOF using the simulations: B1/B5 and B1/B4, with an offset to change the interference condition. The conclusion was that both error signals were valid but that the B1/B5 would provide a wider linear range.

Unfortunately, in practice the B5 photodiode was the last one to be available, and the B5 DC signal was not very stable. This signal is extracted from the same Detection bench as the B1 photodiode and the separation of both beams is very tricky, as we mentioned in Section 6.1. For this reason we discarded the use of B5 as a normalization in favour of B1 beam, which is the priority.

As the normalization by B4 had a very narrow linear range, we decided to try another possibility: **B1+B4**. The DC signal at the B4 photodiode gives the power reflected back from the symmetric port and the B1 photodiode gives the power arriving to the antisymmetric port. The power distribution between these two photodiodes gives information about the Michelson interference condition and so the sum of both gives the total power interfering at the BS.

This new error signal is shown in Figure 6.17, where we can see that even if the slope is lower than for the error signals studied in the past section, the linear region is similar (B1/B4 linear range is $5.7{\cdot}10^{-8}m$ as shown in Figure 5.12), and so it is a robust error signal as well. Again the linear region has been calculated as the region within which the error signals deviates less than 10% from the linear fit. Regarding the coupling between DOFs, it is essentially the same as for B1/B4 and B1/B5.

In practice we need to calibrate the B1 and B4 error signals, since each detection bench has a different telescope. The target is to equalise the power in B1 photodiode at Bright Fringe and the power in B4 photodiode in Dark Fringe, which is the good behaviour. The B1 photodiode was taken as reference and a calibration factor was applied to the B4 signal to fulfil this condition.

An advantage of this error signal is that it gives us direct information about the **fringe offset**. This signal has a value of 1 at bright fringe and a value of 0 at dark fringe. So at Half-Fringe the MICH offset will be 0.5. This is very convenient from the coupling point of view because it allows us to adjust the offset properly, minimizing the coupling of the other DOFs as explained in Section 5.2.5.

The fringe evolution given by the power distribution is not equivalent to the interference condition given by the length difference between the arms (MICH) when the PR mirror is aligned. This can be appreciated in Figure 6.18 that shows the relationship between them once the PR mirror is aligned. At 0.6 they are

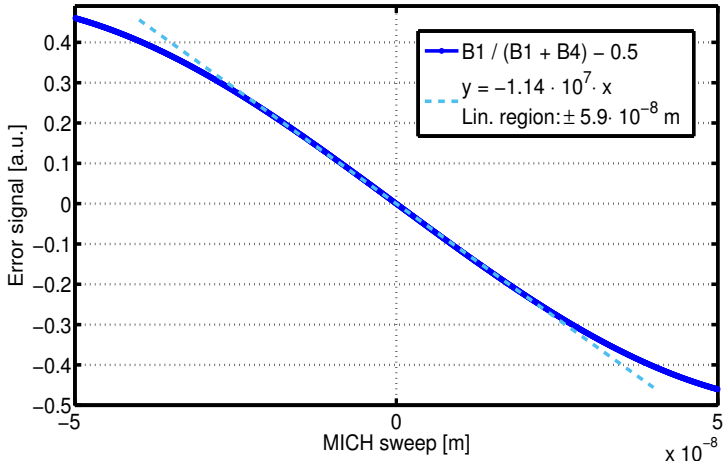

FIGURE 6.17: Simulation of an alternative MICH error signal, B1/(B1+B4). The plot shows as well a fit of the linear region.

almost equivalent and the difference between them increases when getting close to the DF and to the Bright Fringe.

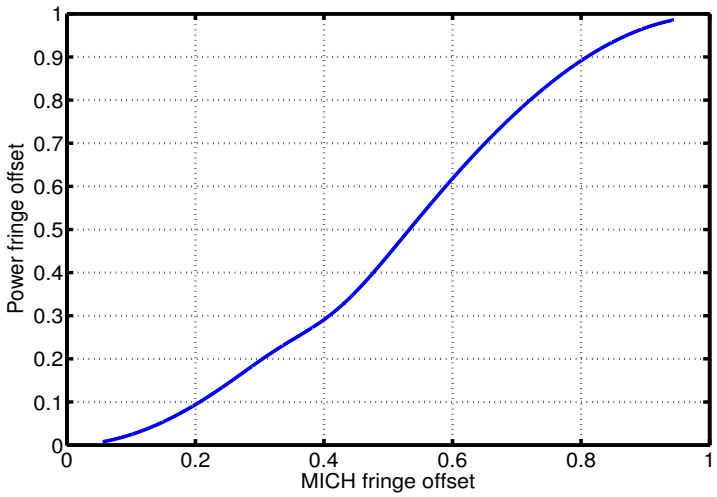

FIGURE 6.18: Relationship between the fringe offset as a function of the wavelength and as a function of the power that recombines at the BS, B1+B4.

However, this error signal is very useful since it provides straightforward information about the fringe offset. For this reason, from now on the MICH offset will be defined as a function of the power and not the length difference between the short arms.

An important parameter when we want to engage a control loop is the *trigger*. It is a **switch that is turned on when we are in the good conditions to engage the linear lock and turned off when the conditions are not good anymore**. Usually the good range is within the linear range of the error signal. In the case of the arm cavities, the trigger was the counter on the rising time of the

transmitted power. For the Michelson, a simple trigger on the power will be used to know when we are in the good region.

The signal that is used as trigger is the error signal itself, without any offset applied. The value chosen was an interval of ±0.1 around the working point, which is within the linear range, as seen in Figure 6.17, and close to the working point. So the trigger that will be used for MICH will be $0.4 < \text{B1} / (\text{B1} + \text{B4}) < 0.6$. An example of the lock engagement is shown in Figure 6.19.

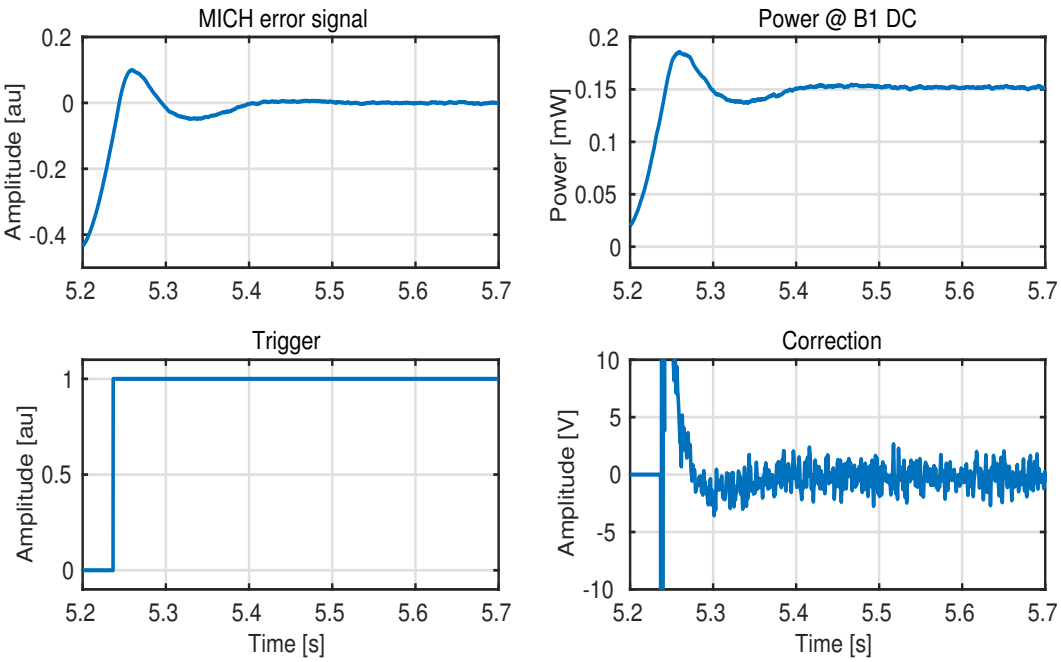

FIGURE 6.19: Example of a lock of the MICH DOF. The plots shown are: the error signal (Up-right), the power in the antisymmetric port (Up-left), the trigger (Down-right) and the correction (Down-left).

The trigger is 0 when we are outside the region of interest and it becomes 1 when the error signal becomes smaller than 0.1. At this point, the linear lock is engaged, and corrections start to be sent to the mirror actuators, in this case the BS.

It can be observed that during the first instants of the lock, the correction saturates, since the dynamic of the actuators is only ±10 V. This is normal during the transient that takes place when the lock is engaged, which corresponds to the step response presented in Section 4.4.1. After this transient the correction stabilizes around normal values, and so does the power at its Half-Fringe value.

Once the lock is engaged, the trigger parameters are changed in order to anticipate the PR alignment. A relevant increase of the power is foreseen so the range of the trigger is broadened to allow some fluctuations caused by the lock acquisition transients. This is done to avoid that the control is turned off by the trigger during this process or during the MICH offset reduction.

At this point we can **measure the OLTF of the MICH loop** by injecting noise, and the results are shown in Figure 6.20. The TF of the actuators is the same as for the arm cavities, but the optical transfer function is flat instead of

having a pole as in their case. The measurement of the OLTF is well in agreement with the model.

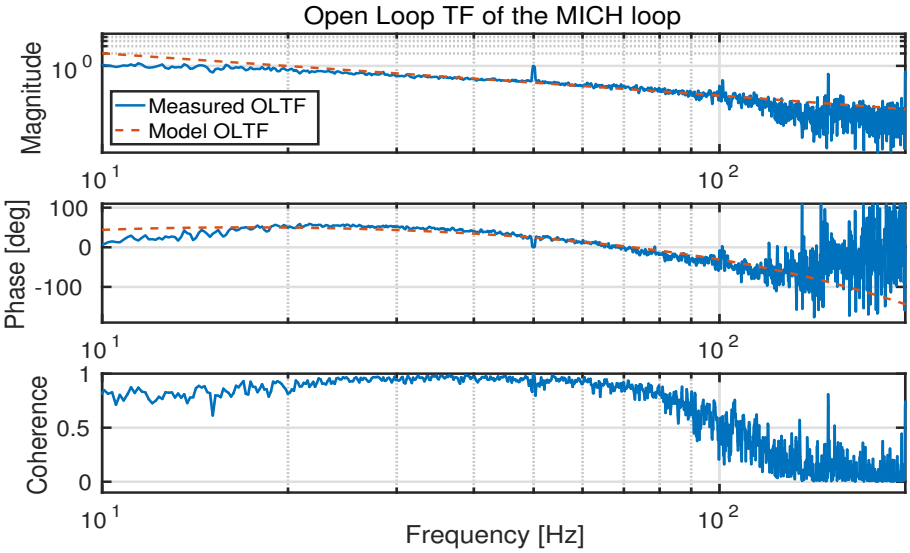

FIGURE 6.20: Comparison of the measurement and the model of the OLTF of the MICH DOF. It has an UGF of 20 Hz and a delay of 2400 μs.

The UGF of the MICH loop is 20 Hz. As we have mentioned in the previous chapter, it is convenient to have a hierarchical control between MICH and DARM loops since they are highly coupled. MICH loop is the slow one which is the reason why the UGF is so low. The DARM loop has priority since is the DOF that will detect the passage of a GW.

In order to fit the phase, a delay of 2400μs was needed. This delay is very high with respect to the actuators one which is of the order of 400μs. In order to check if there was a problem with this loop, we made a different kind of noise injection, also known as *sweep sine*. It consists on injecting a sine and change its frequency in the range of interest. This does not provide a precise measurement of the shape of the OLTF because it has information only in a discrete set of frequencies, but it assures an almost perfect coherence at each frequency.

We made a measurement on the frequency range corresponding to the high limit of the phase margin to check the delay. When the measurement is done with a sweep sine, the phase is better adjusted and the measured delay is 650μs which is consistent with the known delay sources. The extra delay might come from the process that generates the white noise in real time computers, which decreases when we are injecting only a sine.

Again, with this measurement we can calibrate the error signal used to control the MICH DOF. The calibration factor obtained is $\mathbf{C_{MICH} = 3.3 \cdot 10^{-10} m/V}$ and the PSD is shown in Figure 6.21. It has an rms of 140 pm, which is higher than for the arm cavities, but also the UGF is lower for this DOF. Again, the rms is dominated by the 50 Hz line. In this case the 100 and 150 Hz lines do not appear because there are a specific notch for it and all the harmonics of the 50 Hz up to 500 Hz. These notches were implemented to decrease the correction of this loop, which was close to saturation.

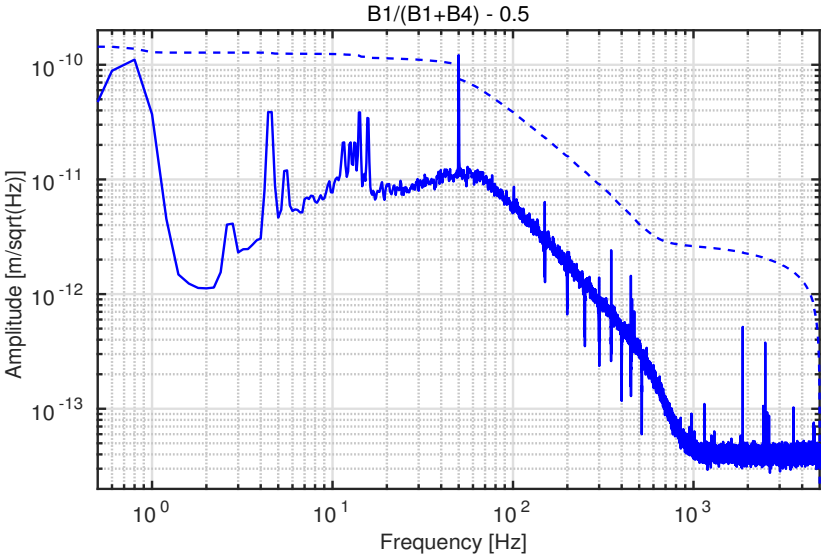

FIGURE 6.21: Calibrated power spectral density of the MICH error signal, while locked in the Recombined configuration. The residual length fluctuation is given by its rms, 140 pm.

Notice however that the maximum UGF that can be achieved does not depend only on the digital delay of the signals inside the control loop (phase margin). The dynamics of the corrections can also have an impact on this value. This was a problem for the MICH loop, whose control was saturating even on steady state. In this case, an increase of the bandwidth would mean an increase of the correction sent as well, leading to a bigger saturation. A non invasive solution was tried by implementing the so called *marionetta reallocation*. This consists on splitting the control between the mirror itself and the higher stage in the suspension chain, the marionetta. This usually helps because it increases the actuation range.

In this case this was not enough, and it proved to be a limiting factor when aligning the PR mirror since the control needed more bandwidth but at the same time the actuation was saturating. For this reason, the 22nd of December it was decided to increase the gain of the actuation by a factor 6. This was an invasive operation because it implied the opening of the BS tower, but it allowed the first lock of the PRITF in Half-Fringe with the PR mirror fully aligned, as it will be seen later on in this chapter.

6.3.2 CARM / DARM loops

Once all the DOFs are controlled (the PR mirror is still misaligned) we make a change of basis between controlling the arms length independently and controlling the Common and Differential arm lengths. In order to do this, we build the error signals with the transmission of the arms, as explained in Equation 5.24. The only modification was to take into account the gain of the arm loops (G_{north} and G_{west}) when reconstructing the **sensing**, this way both error signals have the correct weight in the sum, and so the sensing becomes:

$$
\begin{aligned}
CARM &= \frac{G_{north} \cdot B7\ 6MHz}{B7\ DC} + \frac{G_{west} \cdot B8\ 6MHz}{B8\ DC} \\
DARM &= \frac{G_{north} \cdot B7\ 6MHz}{B7\ DC} - \frac{G_{west} \cdot B8\ 6MHz}{B8\ DC}
\end{aligned}
\tag{6.1}
$$

Finally, notice that the relative phase between the error signals is important in order to assure that we are summing or subtracting. The sum of two error signals de-phased by π is a subtraction instead. In order to check this we made the TF between both error signals and its phase will tell us the phase difference between them. We have adjusted this relative phase to 0 by changing the demodulation phase of one of the error signals by π in order to preserve the expression of the sensing.

Regarding the driving, it is the one shown in Table 5.7, which shows the actuation that decouples the CARM and DARM DOFs.

The control filter is the same as the one for the single cavities at this early stage of the commissioning. However, the transition needs to be done carefully, in order not to open the control of the arm cavities. As the arm loops are already closed, the integrator of the controller (the poles) is already charged with information. For this reason we are going to initialize the CARM and DARM filters before making the change of basis. This means that the error signal is sent to the filter, which calculates the corrections, but they are not sent to the actuators yet. Once the filter has been charged for several seconds, the correction from the arm loops is stopped and the ones from CARM and DARM are sent. The transition between both error signals is done progressively over several seconds and it is is shown in Figure 6.22.

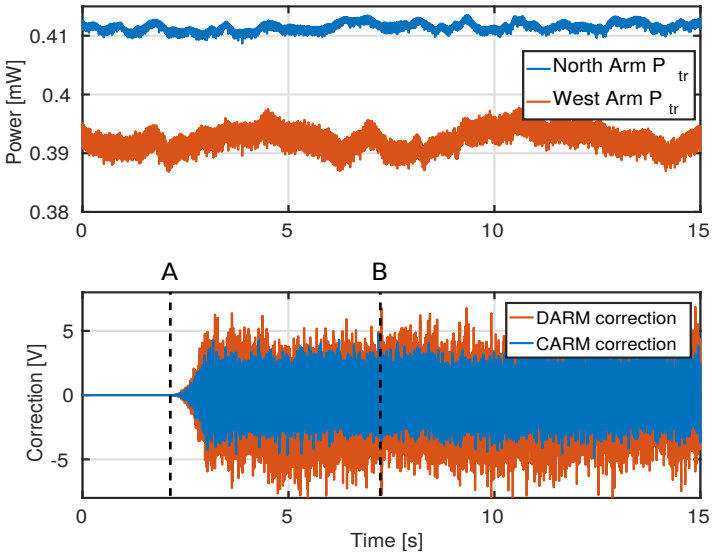

FIGURE 6.22: Transition between controlling the length of the arms independently, to control the common and differential length, CARM and DARM. The figure shows the arms transmitted power and the correction applied to each DOF. From point A, the corrections are calculated but not sent yet. At point B the transition is done progressively.

The figure shows an example of the **hand-off to CARM and DARM DOFs**. The CARM and DARM corrections start to be calculated at point A and 5 seconds after the hand-off is done (point B), that is, the corrections start to be sent. The transmitted power of the arms remains unchanged, as expected, since this basis is equivalent to the previous one.

6.3.3 Second Stage of Frequency Stabilization

At this point we are ready to engage the Second Stage of Frequency Stabilization using the CARM error signal coming from the B4 photodiode. As mentioned in Section 5.3, we have tried to decouple the slow and the fast branches of the frequency stabilization, by sending the error signal to both the IMC and the SSFS. This allows us to pass through an intermediate state before engaging the control in full bandwidth which is the lock of the slow branch only, sending the CARM error signal to the Input Mode Cleaner (IMC).

Slow loop: CARM to IMC

The OLTF of the IMC is well known, since it is engaged from the beginning using the error signal coming from the Reference Cavity. So in principle the commissioning of this slow branch is straightforward, it is only necessary to add a compensation for the Optical TF of CARM (zero @ 50 Hz), which is characterized by the pole of the arm cavities at this stage. In order to keep the loop stable after the compensator, an extra pole is added (pole @ 2000 Hz), and the resulting OLTF was shown in Figure 5.29.

So in practice it is only necessary to **calibrate the CARM error signal**, B4 6MHz normalized by B4 DC, with respect to the error signal of the RFC. Even if it was not necessary to normalize it because the gain margin was large enough, we did it to simplify the MICH offset reduction process.

In order to do this calibration we started from the TF between the B4 6MHz$_{norm}$ error signal and the correction sent to the IMC when the loop is closed with the RFC error signal. This TF was chosen because it gives the extra calibration factor needed in order to substitute the RFC error signal by the CARM error signal while keeping the filter in the stability region.

First of all notice that no specific noise injection was done in this case, since the frequency noise is dominant above the UGF of the IMC (171 Hz) up to 1 kHz. Then, when we make the TF between the error signal (Output) and the correction calculated by the filter (Input) we are measuring:

$$TF_{B4-Corr} = TF_{Act} \cdot TF_{CARM} \cdot TF_{Ph} \tag{6.2}$$

The calibration factor that we are looking for comes from the different optical TF and the different photodiode. By taking into account the mechanical TF of the actuator and the mirror suspension, which is already calibrated, and the shape of the CARM TF we obtain this extra factor that needs to be taken into account when using B4 6MHz$_{norm}$ error signal. The measured calibration factor was $\mathbf{C_{B4} = -1.9 \cdot 10^{-5} V/V}$. The minus sign comes from the fact that the global phase of the TF was π, meaning the error signals have opposite signs, which has to be compensated by the filter gain.

Once the calibration was done it was straightforward to make the **hand-off**[2] **between the error signals**. The only change was to add a couple zero-pole

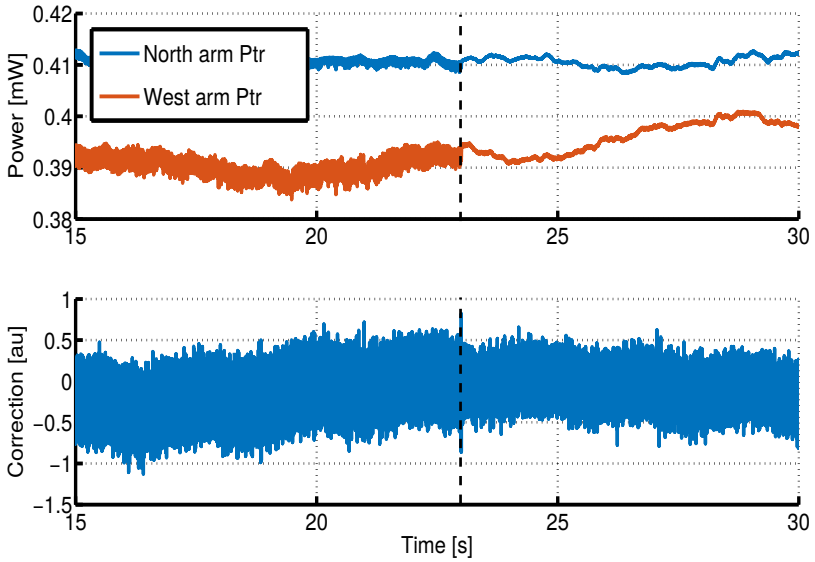

FIGURE 6.23: Lock sequence of the slow branch of the SSFS loop. The control is engaged using a manual trigger at the moment marked by the dashed line and the transition is instantaneous. The figure shows: arms transmitted power (Upper plot) and correction sent to the IMC mirror (Lower plot). The improvement on the frequency noise can be clearly observed on the transmitted power.

to the filter and the calibration factor to the filter gain. This is done at the same time as the error signal is changed, being an instantaneous transition, triggered by a manual switch. The transition can be seen in Figure 6.23 and the beginning is marked by the dashed line. The improvement on the control after the transition is clear by looking at the stability of the transmitted power. The transition is almost transparent for the IMC as it can be seen from the continuity of the correction sent.

A noise injection can be done in order to measure the OLTF of the slow branch of the SSFS as done for the arm cavities. As the actuation of the IMC mirror is calibrated in μm, we can calculate the calibration factor in this case as well by comparing the measurement with the theoretical model presented in Section 5.3. Figure 6.24 shows both the measurement and the model of the OLTF of the IMC when locked using CARM error signal which has an **UGF of 171 Hz**. In order to match the phase to the measurement a delay of 800μs needed to be added. This delay is still within reasonable values.

The calibration factor extracted from the measurements is $C_{cal} = 1.9{\cdot}10^{-11}$ m/V. However, as we are dealing with frequency stabilization, we are more interested in calculating the residual frequency variation. This operation is straightforward according to $\delta\nu/\nu = \delta L/L$ (Equation 2.2) where L is the arm cavity length (3 km). We can then transform the calibration factor into a more convenient unit, $\mathbf{C^{\nu}_{cal} = 1.79Hz/V}$. The calibrated PSD of the B4 6MHz$_{norm}$ error signal when used by the IMC loop is shown in Figure 6.27. In the plot it is compared to the

[2]We call hand-off to the process of passing from one error signal to another one while the system remains locked.

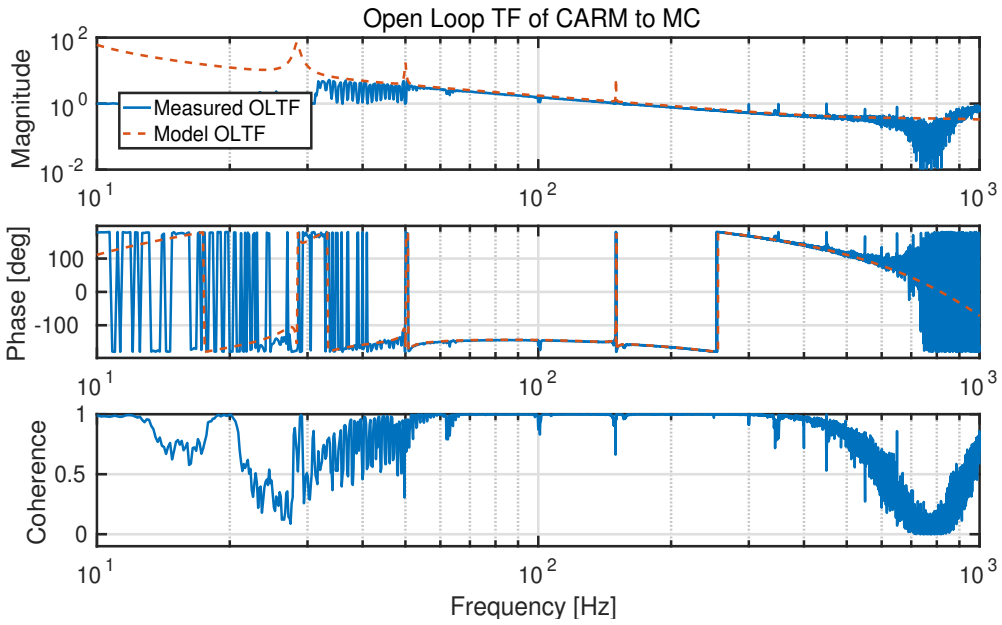

FIGURE 6.24: Comparison of the measurement and the model of the OLTF of the slow branch of the SSFS: the IMC lock using the CARM error signal. The UGF is 171 Hz and the fitted delay 800μs.

PSD when the loop is closed with the Reference Cavity error signal and with the SSFS fast branch closed.

Fast loop: SSFS

Once the slow branch was engaged, the only missing part was the commissioning of the fast branch of the SSFS. The first thing we did was to estimate the **gain of the filter** necessary to assure the filter stability. In principle we are interested in the TF between the error signal that we want to use, B4 6MHz$_{norm}$, and the correction sent to the laser. This is analogous to the noise injection done in order to calibrate the MC loop. The tricky part is that in this case, the error signal is already in closed loop in the IMC, so we need to take it into account and compensate for it. In fact this is not a problem, since the OLTF of the slow branch is well known from the model and the measurements.

Since the loop is not yet closed, the noise has been injected instead of the correction of the SSFS and sent to the pre-stabilization filter. The injection was done while the IMC was controlled using the RFC. As the calibration factor between the RFC error signal and the B4 6MHz$_{norm}$ is known (C_{B4}), the conversion is straightforward. The measured OLTF after compensating for the IMC loop was flat, as expected, with a level of $C_{SSFS-RFC} = 10^{-4} V/V$. If we take into account the calibration factor C_{B4}, the OLTF has an approximate value of 5 V/V, that will need to be compensated by the control filter in order to reach the stability.

This calibration factor is used to fix the cross-over frequency between the IMC loop and the SSFS loop. As it is shown in Section 5.3, the target cross-over frequency is 150 Hz. Then the UGF of the system is further increased by tuning both gains at the same time so that the cross-over frequency is not modified.

Once this was done, we tried to **engage the SSFS** without success. The origin of the problem was not clear from the data since the unlocks were very fast, of the order of a few miliseconds. In such a short time is very hard to extract information. For this reason we changed the strategy, we turned on the SSFS at very low gain so that at the beginning it had no impact on the system. Progressively we started to increase the gain of the SSFS control filter, and we found that the system would unlock due to instabilities at very low frequency (tenths of Hz).

The explanation for these oscillations was the presence of some structures that were not included in the model. The first lock on the 4^{th} of January was achieved by compensating these structures inside the SSFS filter, which had a very complicated behaviour. Further investigations showed that these structures were coming from a coupling between the SSFS and the Automatic Alignment (AA) of the IMC.

The SSFS loop modifies the working point of the IMC, which is seen by the longitudinal error signal of the IMC. If the beam is not perfectly centred in the quadrants, when the information from the individual quadrants is subtracted not all the fundamental mode disappears. This allows some information about the longitudinal control to leak into the quadrant photodiodes used for the AA. So in practice the engagement of the SSFS control was provoking a malfunctioning of the alignment loop, creating unexpected structures. As they were placed at higher frequencies than the bandwidth necessary for the AA (several Hz), an optimization of this filter to discriminate them solved completely the problem.

At this point, with the system behaving as expected, we could remove all the compensators added to the control filter, returning to the initial shape. A measurement of the **OLTF of the SSFS** in this configuration is shown in Figure 6.25. Two separate noise injections have been done in order to cover a wider bandwidth. If we try to do the same in only one noise injection there are more risks of saturating the control and the noise shape has to be finely tuned.

The measurement shown in Figure 6.25 agrees well with the model: it has an UGF of 2 kHz, and with the Digital Signal Processor (DSP) running at 200 kHz the phase agrees with a delay of 27.5 μs. This delay has two different origins: one is linked to the digital processes sampling frequency and the other one to the physical link between processes. The first one has two contributions: the SSFS DSP itself, and the demodulation process. In principle they contribute with one sample of delay each so, $t_{sample} = 2 \ / \ \mathrm{f}_{sampl} = 10 \ \mu s$. This delay can be reduced by increasing the sampling frequency.

Regarding the physical link, there is an optical fiber that allows communication between the demodulated signals and the DSP, which introduces a delay that depends on its length. There are 50 m of optical fiber, which corresponds to approximately 2.5 μs of delay, which can not be reduced. According to this, there are 5μs of not-understood delay. The team that develops the DSP is confident that this delay can be reduced by a better synchronization of the different elements on the digital chain. The delay of this loop is significantly less than the others because both the actuators and the digital processes involved have a lower delay.

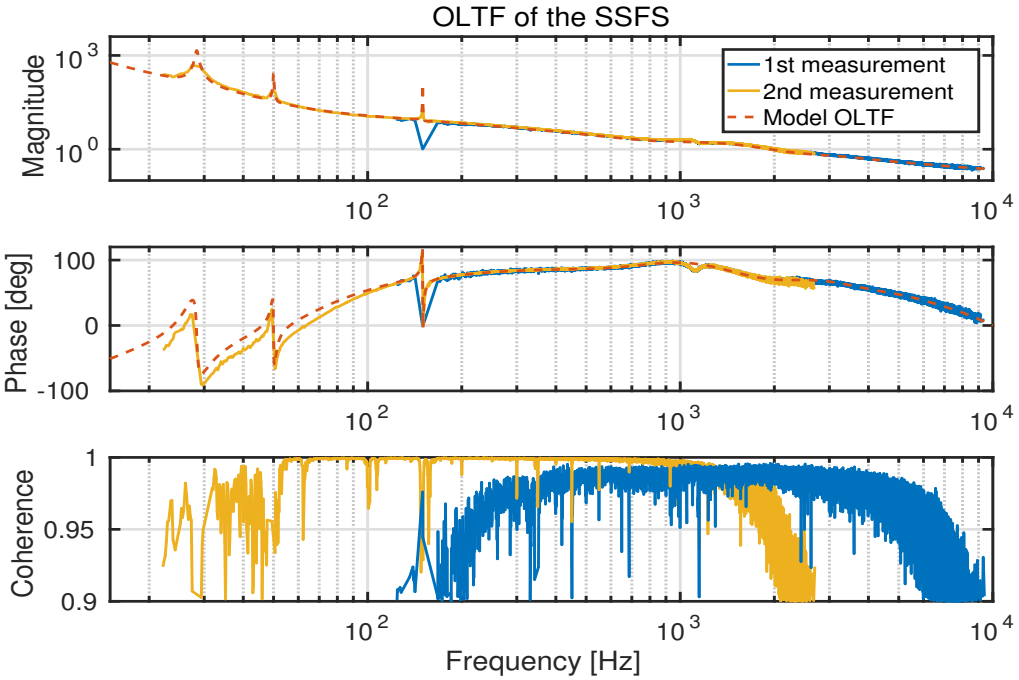

FIGURE 6.25: Comparison of the measurement and the model of the OLTF of the fast loop of the SSFS. Its UGF is 2 kHz and the fitted delay is 17.5 μs.

An interesting feature is the small oscillation seen both in the magnitude and in the phase around 1 kHz. This results from an interaction between both SSFS branches, the slow and the fast one. This allows us to determine the exact cross-over frequency, and the delay of the IMC loop. The filter still has gain margin (up to an UGF of 6kHz). It was decided not to adjust the UGF in the recombined interferometer and do it once the PR is aligned instead. This way we can take advantage of this gain margin to deal with the increase of power.

The **UGF is limited by the delay in the loop**. This is because the amplitude margin is limited by the delay introduced to the system, which changes the behaviour of the phase. The part concerning the number of samples inside the DSP depends on the sampling frequency, so by increasing it, the delay can be reduced. This phenomena can be seen in Figure 6.26. It shows the same filter for two different sampling frequencies, 200 and 500 kHz. The phase crosses 180° at higher frequencies in the second case, giving more phase margin and allowing to increase the UGF. The same filter at 500 kHz allows us to reach an **UGF of 8-9 kHz**.

The third curve of Figure 6.26 shows a more adapted filter for 500 kHz of sampling frequency with a roll-off at higher frequencies, which would allow us to increase further the UGF, up to 10 kHz. From now on, the results shown will be with the DSP running at 500 kHz, which was the best configuration available during the commissioning.

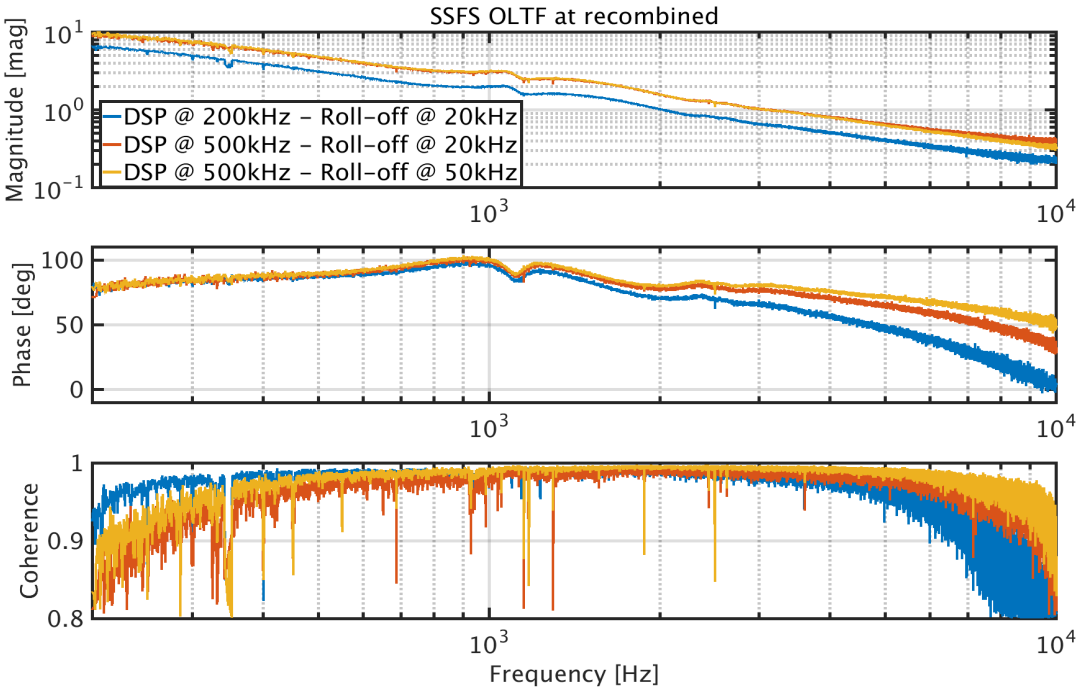

FIGURE 6.26: Measurement of the OLTF of the fast loop of the SSFS. The blue and red lines show the same control filter at two different sampling frequencies. It has an impact on the phase margin, which increases with the sampling frequency. The blue line shows the same filter, with a roll-off at a higher frequency, with 500 kHz of sampling frequency. The phase margin is even bigger in this case.

It is interesting to compare the residual frequency variations of the Common DOF, for the different controls. Figure 6.27 shows the PSD of the B4 6MHz$_{norm}$ error signal in the recombined configuration, when the CARM DOF is controlled mechanically, with only the slow branch engaged (CARM to the IMC) and with the SSFS engaged.

The noise is considerably reduced (around a factor 10) in the region between 10 and 100 Hz when using the CARM error signal to lock the IMC, passing from an rms of 35 mHz to 16 mHz. These rms are dominated by the lines at 50, 100 and 150 Hz, which explains why it is only reduced by a factor 2 between both cases. When the full SSFS is engaged, the noise is further reduced, especially at low frequency and in the region 200-400 Hz. In this case the curves are significantly reduced, lowering the overall rms to 3 mHz.

RFC loop

Finally there is one more control loop to complete the SSFS. This loop is engaged once the SSFS fast loop is already engaged. Its role is to control the frequency of the laser at very low frequency using the error signal of the Reference Cavity. When the SSFS is engaged, the common length of the arm cavities is the reference used for the laser frequency stabilization. For this reason the RFC error signal, which is very stable at low frequencies, is used to control the CARM DOF at very low

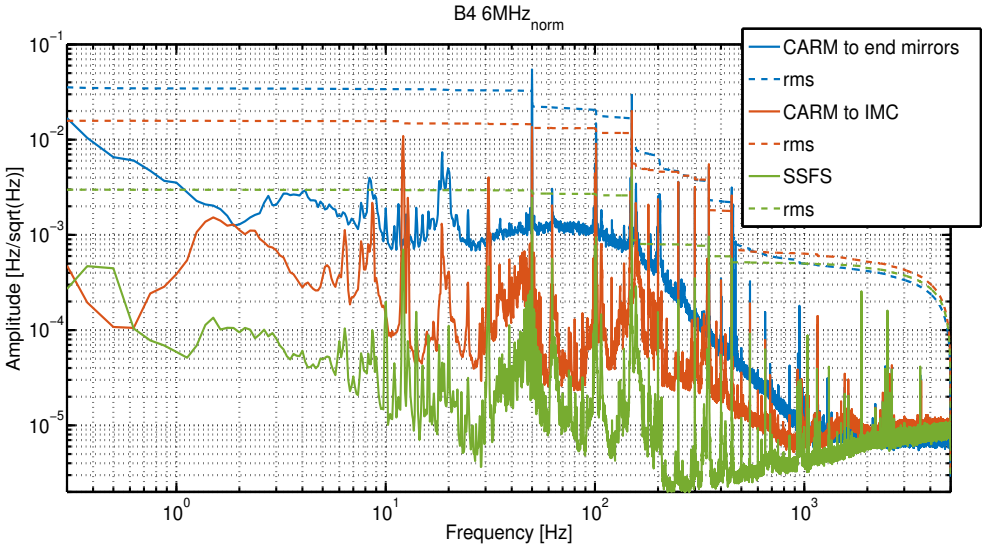

FIGURE 6.27: Calibrated power spectral density of the SSFS error signal, B4 6MHz normalized by B4 DC. Three different cases are shown: CARM locked actuating on the end mirrors, 35 mHz of rms, CARM locked actuating on the IMC, 16 mHz of rms and CARM locked with the full SSFS engaged, 3 mHz of rms.

frequencies by acting on the end mirrors with the proper driving (see Table 5.7). A measurement of this loop is shown in Figure 6.28.

As we can see in this figure, the **UGF of this loop is 2 Hz**. This measurement has been done using a sweep sine. It does not provide a perfect shape, but it agrees very well with the model. The delay used to fit the phase was 750μs, which is coherent with the expected values.

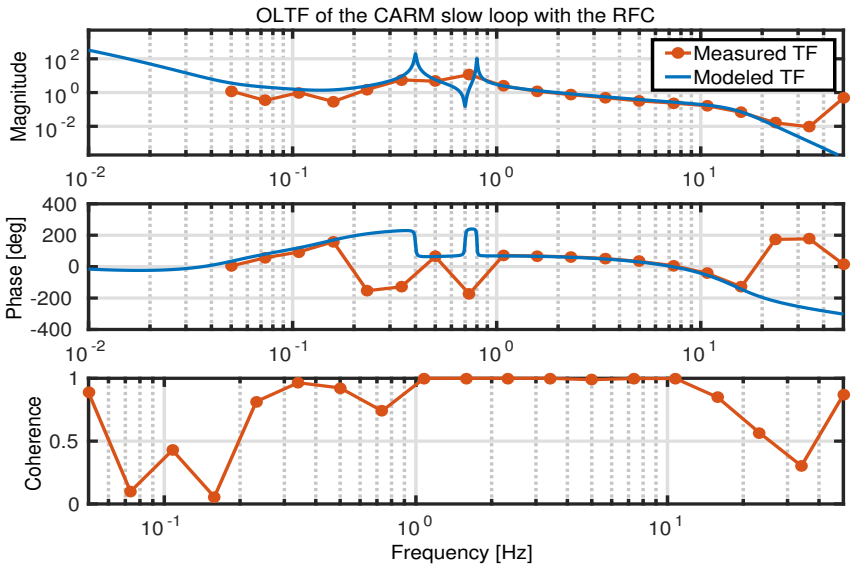

FIGURE 6.28: Comparison of the measurement and the model of the OLTF of the RFC loop that actuates on the end mirrors, fixing the laser frequency at very low frequencies. It has an UGF of 2 Hz and the fitted delay is 750 μs.

6.4 Step 4: PR alignment

During the Step 3, all the DOFs are engaged except PRCL, since the PR mirror is misaligned. At Step 4 it is aligned and the control of the PRC is engaged. This step is very critical since there is an important increase of the power circulating inside the interferometer and as a consequence, of the OG of the different error signals. To minimize this effect, the error signals used in Step 3 are normalized by the relevant powers, as presented the previous section and in Chapter 5.

Also after the alignment of the PR, the coupling between the different DOFs will increase and the behaviour of the sidebands becomes more complicated. Once the PR is aligned it is convenient to engage the alignment of the PR mirror, since it will become a limiting factor for the longitudinal controls later on the locking sequence.

6.4.1 PRCL loop

As presented in the previous chapter, there are two candidates for the PRCL error signal: B2 3Ω and B2 8MHz. It was shown that the 3Ω is less sensitive to changes of the PRC optical parameters as expected during the MICH offset reduction. However, we do not expect big changes until the point where the PRC passes from under-coupled to over-coupled, which happens when very close to DF (97.6% of the MICH power offset). So it was decided to use initially the 8MHz, since it has a better SNR, and hand-off to the 3Ω error signal closer to the critically-coupled point. It was also decided to normalize the error signal in order to anticipate for the OG change during the MICH offset reduction. The same normalization as for the MICH error signal has been used: the sum of B1 DC and B4 DC.

The next step is to **tune the demodulation phase** of the error signal. This is not a straightforward process since we need to optimize it before aligning the PR mirror. For this reason we will use the lock of the PR-NI cavity as a reference. In this configuration, the 8 and 18 MHz sidebands are not resonant, acting as a phase reference, while the carrier is resonant inside the PR-NI cavity (the end mirrors are misaligned).

When we pass to the PRITF configuration, the sidebands are still not resonant, but the carrier is now resonant inside the arm cavities as well so the phase of the reflected field changes by 180°. For this reason the same phase can be used for the PRCL DOF, taking into account that the sign of the filter gain will have opposite sign.

At this point the PR mirror can be brought to its aligned position. This time the **trigger** that starts the control depends on the intra cavity power, B4 DC. This parameter indicates the moment when the PR is enough aligned, i.e. when the cavity build-up is enough close to the final one that the control loop can be engaged. This value has been fixed empirically to B4 DC > 0.025 mW. At this moment the filter starts to send corrections to the PR mirror and the lock is engaged. Even if the sign of the filter gain was obtained during the tuning of the demodulation phase, the value of the gain was obtained empirically, starting from the value used for the PR-NI cavity. Figure 6.29 shows the process of alignment of the PR mirror and the engagement of the PRCL loop.

The PR mirror starts to move towards its aligned position at the beginning of the sequence shown in the plots. At first the effect on the power is negligible, however once the PR is more or less 5μrad far from the aligned position, there are oscillations that start to appear in the B4 photodiode due to the crossing of

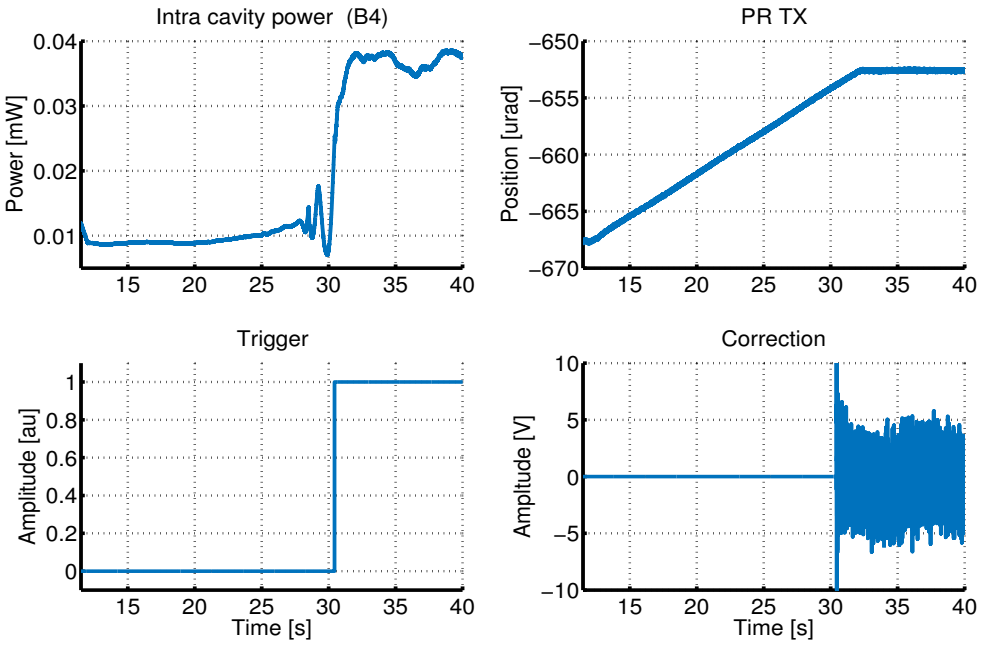

FIGURE 6.29: Alignment of the PR mirror and lock of the PRCL DOF. The figure shows: the power inside the PRC, B4, the angular position of the PR mirror, the trigger and the correction sent to the PR mirror. It can be seen how, while the PR is being aligned, the cavity build-up starts, and once it is high enough, the trigger is activated and the corrections start to be sent.

different resonances of the carrier and the sidebands, similar to what was shown by the simulation. It is not until the PR is 2μrad far from the target angular position that the power starts to increase significantly, triggering the engagement of the control loop. By the time the PR is aligned the PRCL loop is already engaged.

Notice that at the beginning due to some experimental difficulties to engage this loop it was decided to engage the control in a slightly brighter fringe, since the finesse of the PRC would be lower. For this reason we engage the lock at 70% of Bright Fringe instead of exactly at Half-Fringe (50%).

Once the loop is engaged the trigger is broadened as in the case of the MICH loop. In this case it is necessary since the trigger is on the intra-cavity power, which is going to increase during the MICH offset reduction. For this reason the higher threshold (DC $<$ Trigger$_H$) has to be increased to a higher value than the value of B4 DC in DF.

A **measurement of the OLTF** of this loop can be done by injecting noise as for the other DOFS, and the result is shown in Figure 6.30. The optical TF of the PRC can be considered flat since it has a pole at 100 kHz. The **UGF is at 70 Hz** and the delay needed to fit the phase was 400μs. This DOF is already controlled with a boost, i.e. with an extra integrator at low frequencies that makes the filter to correct more in that region.

Also from this measurement the calibration factor of the error signal can be extracted, $\mathbf{C_{PRCL} = 1.4 \cdot 10^{-9} m/V}$. Figure 6.31 shows the PSD of the error signal used, B2 8MHz normalized, with an rms of 71 pm.

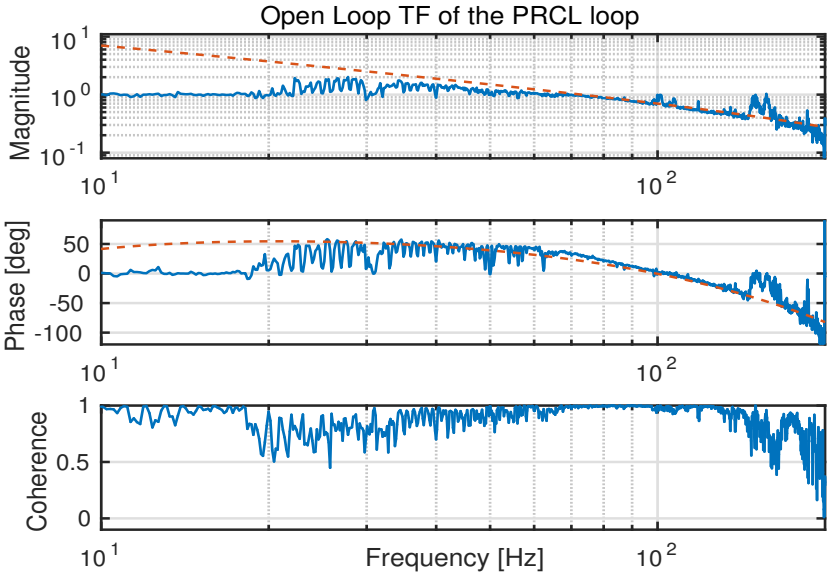

FIGURE 6.30: Comparison of the measurement and the model of the OLTF of the PRCL loop. The UGF is at 70 Hz

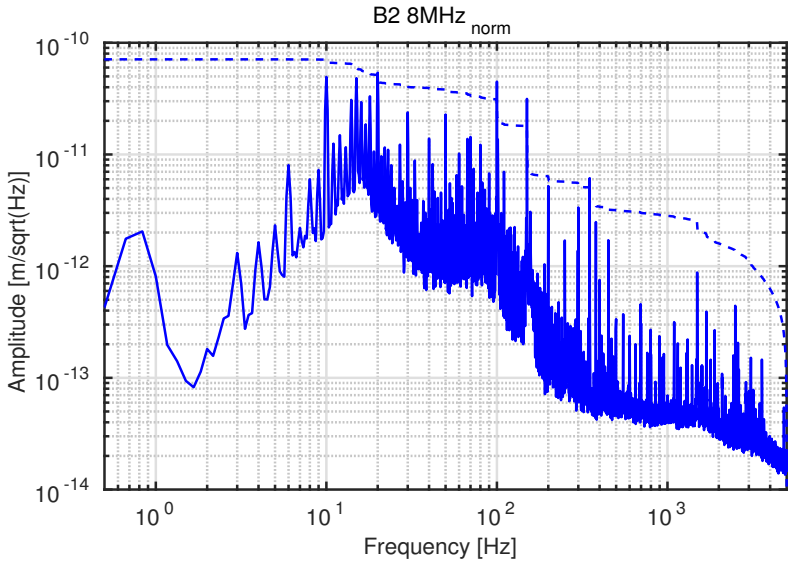

FIGURE 6.31: Calibrated PSD of the PRCL error signal, B2 8MHz normalized by B1+B4. The remaining length fluctuations are 71 pm rms.

6.4.2 MICH driving matrix

There is an extra factor to take into account when the PR mirror is aligned: the driving matrix of the MICH DOF. So far it was driven using one mirror only, since the PR was misaligned and it did not play a role yet. However, once the PRC is locked, it is necessary to use both mirrors. Otherwise we would send the MICH correction to the PRCL DOF as well. We decided to measure experimentally the driving matrix, by minimizing this coupling of the MICH DOF to the PRCL DOF.

The ideal driving matrix was presented in Table 5.7 and we obtained:

$$MICH = 0.7 \cdot BS + 0.5 \cdot PR \tag{6.3}$$

In order to monitor the coupling, we injected a line in MICH at 11.1 Hz and we made the driving matrix vary until this line disappeared from the PRCL correction. So we fixed the coefficient of the BS to 0.7 and we made a sweep of the PR mirror coefficient. The transfer function between MICH and PRCL and the injected line has been monitored during this sweep. The ratio between both TFs as a function of the PR coefficient is shown in Figure 6.32.

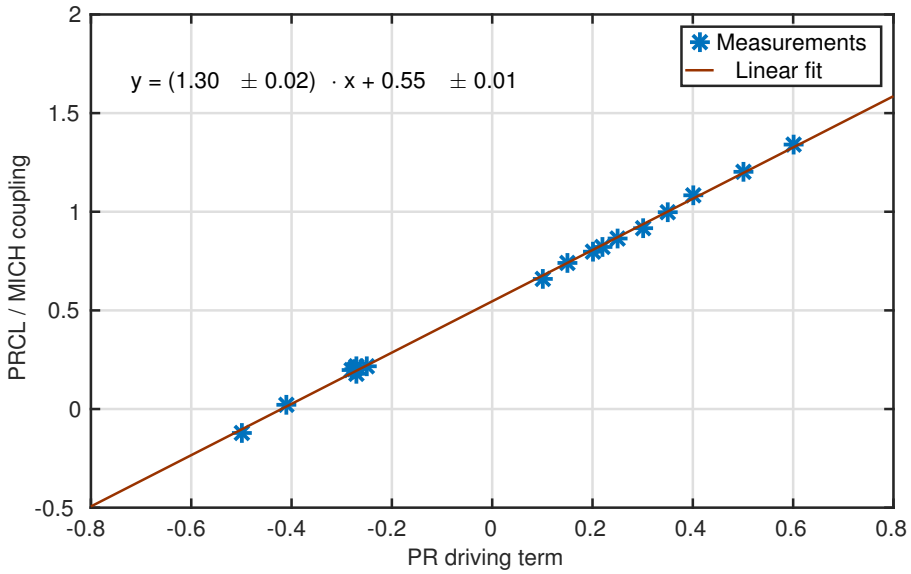

FIGURE 6.32: Ratio between the TF of the injected line and PRCL and the TF of the injected line and MICH as a function of the PR driving coefficient when actuating on MICH DOF. The figure shows the measurements done and the linear fit whose zero-crossing gives the PR driving coefficient that suppresses the coupling of MICH to PRCL.

We see that there is a linear relationship between both magnitudes that can be well fitted. According to this measurement, the diagonal driving term for the PR mirror is -0.42±0.01. This measurement supposes that the coupling only comes from the driving term and so that the sensing is completely decoupled. This is a safe assumption since the PRCL error signal is very decoupled from the other DOFs, as it was shown by the simulations in Figure 5.19.

6.4.3 Longitudinal loops after the PR alignment

As it was anticipated in the previous chapter, the alignment of the PR mirror supposes an increase in the power impinging on all the photodiodes of a factor 10, and of a factor 100 on the B2 photodiode. It is interesting to study the changes that experience the longitudinal loops and check the efficiency of the chosen normalizations.

The **MICH DOF** does not suffer any particular change, its gain is tuned by 20% in order to keep a **UGF of 25 Hz**. The DARM DOF tuning is a bit more

critical instead. As we have anticipated in the previous section, both differential DOFs are very coupled, and the way to mitigate this effect is to implement a hierarchical control.

In order to study this phenomena we have measured the OLTF of the DARM DOF for two gains of MICH, separated by a factor 2 corresponding to UGF of 16 and 8 Hz. The measured DARM OLTFs are shown in Figure 6.33 and they have an UGF of 28 Hz.

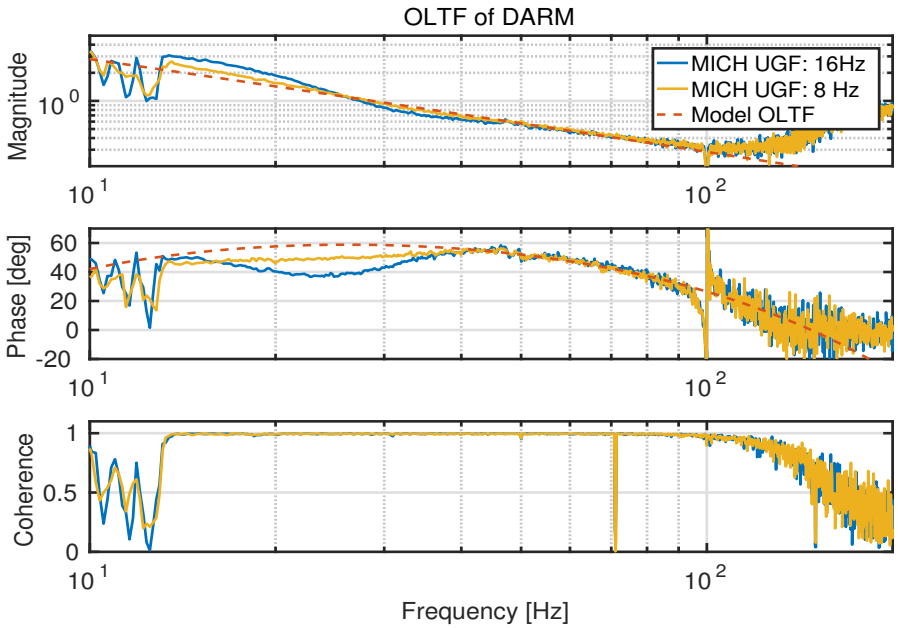

FIGURE 6.33: Comparison of the measurements and the model of the OLTF of the DARM loop. The UGF is 25 Hz for a fitted delay of 800 μs. Two measurements are shown, one when the MICH loop has an UGF of 8 Hz an another one when it has an UGF of 16 Hz. The coupling between MICH and DARM affects the shape of the OLTF, both the magnitude and the phase.

Both the magnitude and the phase are deformed for both cases due to the coupling of both loops in a very similar way as in the SSFS loop. The effect is very small for the case where MICH UGF is lower, and it becomes worse when both UGFs are closer. This proves the need of a hierarchical control between these two DOFs. We can consider that around a factor 3 between both UGFs is a safe factor in terms of coupling. For this reason it was decided to fix **DARM UGF at 70 Hz** (remember that MICH UGF was fixed at 25 Hz). Thanks to the normalization the gain of the DARM loop needs to be adjusted only by 20%.

Regarding the **SSFS loop**, the gain remains unmodified during the PR alignment, since this loop has a very high phase margin. The **loop passes from 3 kHz to 6 kHz of UGF** once the PRCL DOF is locked. It is only modified by a factor 2 because it is also normalized. The SSFS is a key loop when trying to go further during the lock acquisition scheme since the frequency noise couples strongly to the rest of DOFs and so we are interested in having the highest gain available, always keeping a safe margin.

To illustrate this, Figure 6.34 shows the error signal used for the control of the SSFS, B4 6MHz, when the SSFS is engaged before and after the PR alignment

and the same when the SSFS is off. When it is not engaged, the frequency noise couples more when the PR is aligned, as expected. Once it is engaged, the noise is reduced by two orders of magnitude in the interesting region (from 10 to 1000 Hz), which will simplify the lock acquisition process.

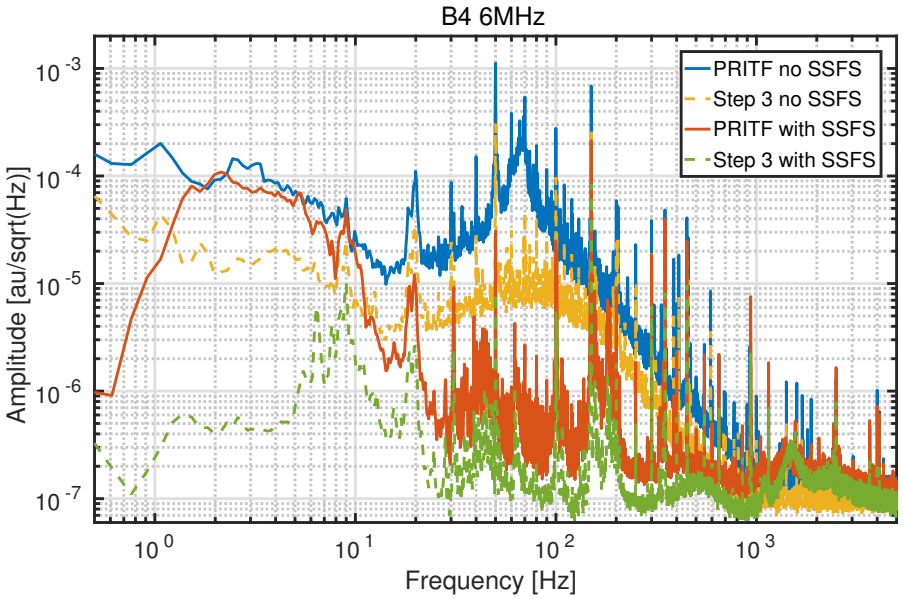

FIGURE 6.34: PSD of the error signal used for the SSFS loop, B4 6MHz. A comparison of its behaviour when the SSFS is engaged and when it is not is shown both in the recombined configuration and with the PR aligned.

6.4.4 Alignment using quadrant photodiodes

As mentioned in the previous section, the alignment of the PRITF is the most complex part of the control of the interferometer. There are a lot of angular DOFs, 16 in total, which have complicated couplings during the lock acquisition. For this reason only the most critical ones are engaged before reaching the Dark Fringe: the PR and the BS.

So far all the mirrors are angularly controlled via the Local Controls, which provide a local reference for the mirrors position, independently of the other optical elements. However, at this point we are interested into the alignment with respect to the rest of the interferometer. For this reason we want to use the quadrant photodiodes, because they indicate the working point where there are no first order HOMs generated.

Let's start by the **PR mirror alignment**, which is a key point in the lock acquisition sequence since it causes the sidebands gain to fluctuate due to the stability of the PRC. As a reminder, the best error signals for the PR mirror alignment are the ones coming from the B2 quadrant photodiode (in reflection of the PRC) demodulated at 8 MHz (see Section 5.4).

At each detection bench there are two quadrant photodiodes, separated by 90° of Gouy phase. However, they are not placed at 0 (waist) and 90° (far field), but at a random position, since it is simpler from the optical bench design point of view. This only means that the information they carry about the different angular

DOFs is mixed in both quadrants and we need to find the good sensing matrix in order to separate them.

In order to determine the **sensing matrix** we made a noise injection on each DOF (θ_x and θ_y) at 2 Hz. Then we tuned the phases of the quadrant photodiodes[3] in order to maximize the injected line. The amplitude of the TF between the noise and the error signal gives us the sensing matrix.

In order to check the quality of the error signal we have used the sensing matrix in order to reconstruct the noise injection. The results of the reconstruction are shown in Figure 6.35.

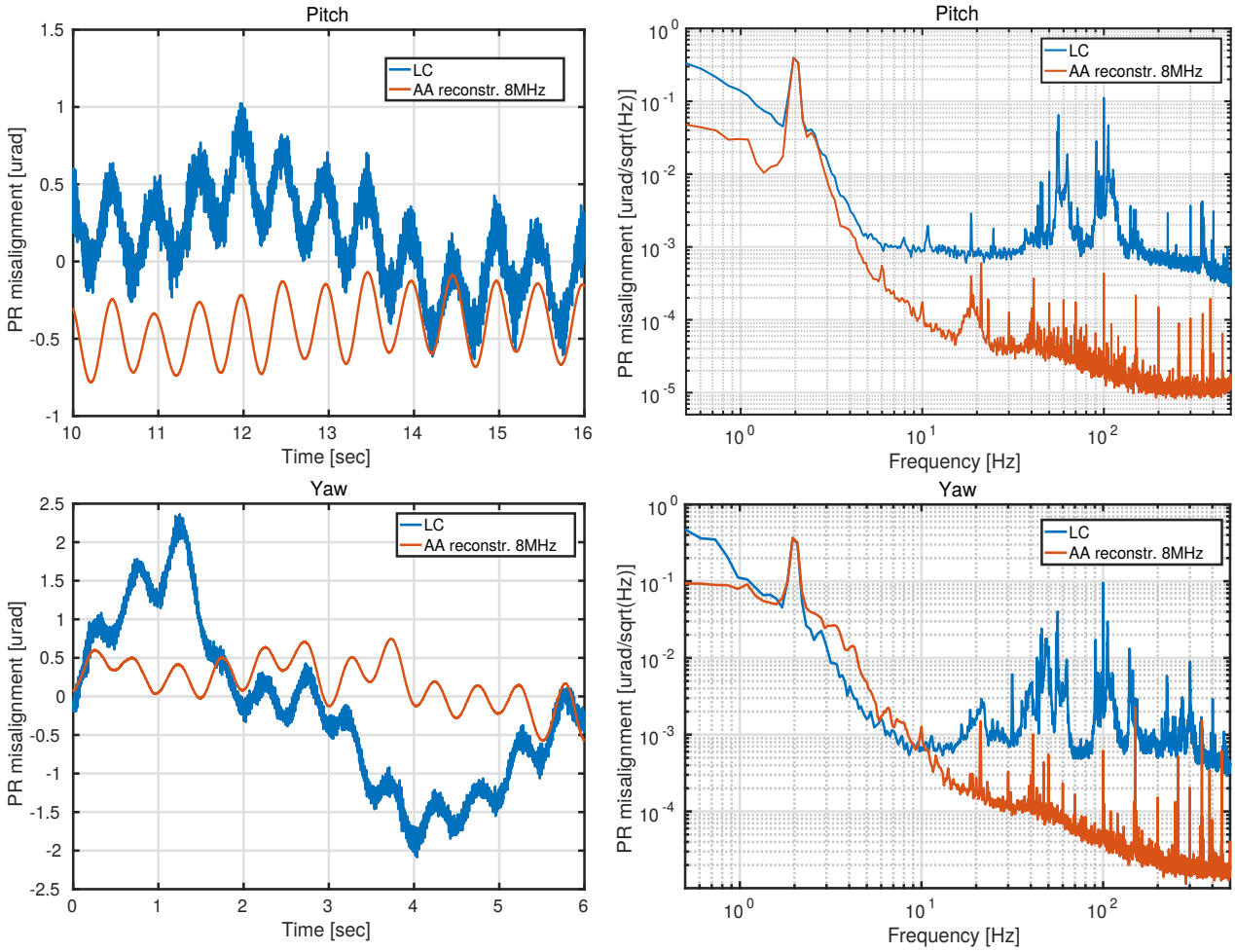

FIGURE 6.35: Reconstruction of the angular noise injection performed on the PR mirror compared to the reconstruction from the Local Controls. The plots on the left show the time domain reconstruction while The plots on the right show the frequency domain reconstruction of the PR angular noise injections.

The plots in the left of Figure 6.35 show the reconstruction of the injected sine at 2 Hz in the time domain, and the plots in the right the reconstruction of the error signal in the frequency domain. In the same plots the error signal from the Local Controls is also shown as a reference.

[3] In a quadrant photodiode there are two error signals and so two demodulation phases to tune: the horizontal and the vertical one.

The time domain plots give information about the zero of the error signal: the working point. It is interesting to compare them with the ones from the LC because during Step 3 the drift control brings the interferometer to an aligned state. As the alignment drifts occur at low frequencies, the LC positions are still good after aligning the PR mirror during several minutes (∼15 min) and so they are a good reference.

The θ_y (yaw)[4]reconstructed from the quadrants agrees with the one from the LC while the θ_x (pitch) from the quadrants is shifted by half a μrad. It is not negligible, but it could be due to a misalignment of the beam with respect to the PR mirror, so in principle we will consider it as physical.

Regarding the frequency domain it can be seen that the frequency is well reconstructed, having a similar SNR to the LC signal. However, over 2 Hz, the noise of the reconstructed error signals is of the same order of magnitude or even bigger. This is a problem for engaging the alignment in full bandwidth (UGF around 2 Hz). It is not the case for the LC because the system is very stable (it is independent from the interferometer, it is insensitive to its fluctuations) and so the controller can be designed to cut the error signal above the UGF in a very efficient way. This is not the case for the error signals from the quadrants since they extract information from the interferometer. The optical gain fluctuates in this case, which requires more phase margin and so the cut has to be less aggressive than in the case of the LC.

However, even if an alignment in full-bandwidth seems too challenging, the error signals are good enough to engage a drift control. A loop was closed at this stage without any problem.

The same process has been conducted for the **BS angular DOF**. This degree of freedom is less critical, but it is also important since it impacts on the recombination of the beams at the antisymmetric port. We injected the same line at 2 Hz, this time to the BS mirror. The results are shown in Figure 6.36.

First of all notice that the LC are very noisy in this case, which can be understood from the presence of very big lines at 50 and 150 Hz. From the time domain plots we can see that the Pitch has a good zero. However, this is not the case for the Yaw, which is shifted by 1.5 μrad. This offset is too high to be real, since, as it was just mentioned, the alignment does not have time to drift so much in a short time. Also, such a big misalignment should be macroscopically visible in the cameras that monitor the beams at the different detection benches, in this case the one that is placed in the antisymmetric port.

For this reason, we decided to add an offset to this error signal, choosing ourselves the working point with the help of the cameras. The loop was engaged without any problem, but the evolution of this offset was monitored in case it drifts during the MICH offset reduction. Finally, the frequency domain signals show an up-conversion of the line injected (there are peaks at 4, 6 and 8 MHz) which is not physical and will spoil the error signal.

[4]Yaw and Pitch are a name convention for an angular movement around the y-axis (θ_y) and the x-axis (θ_x) respectively.

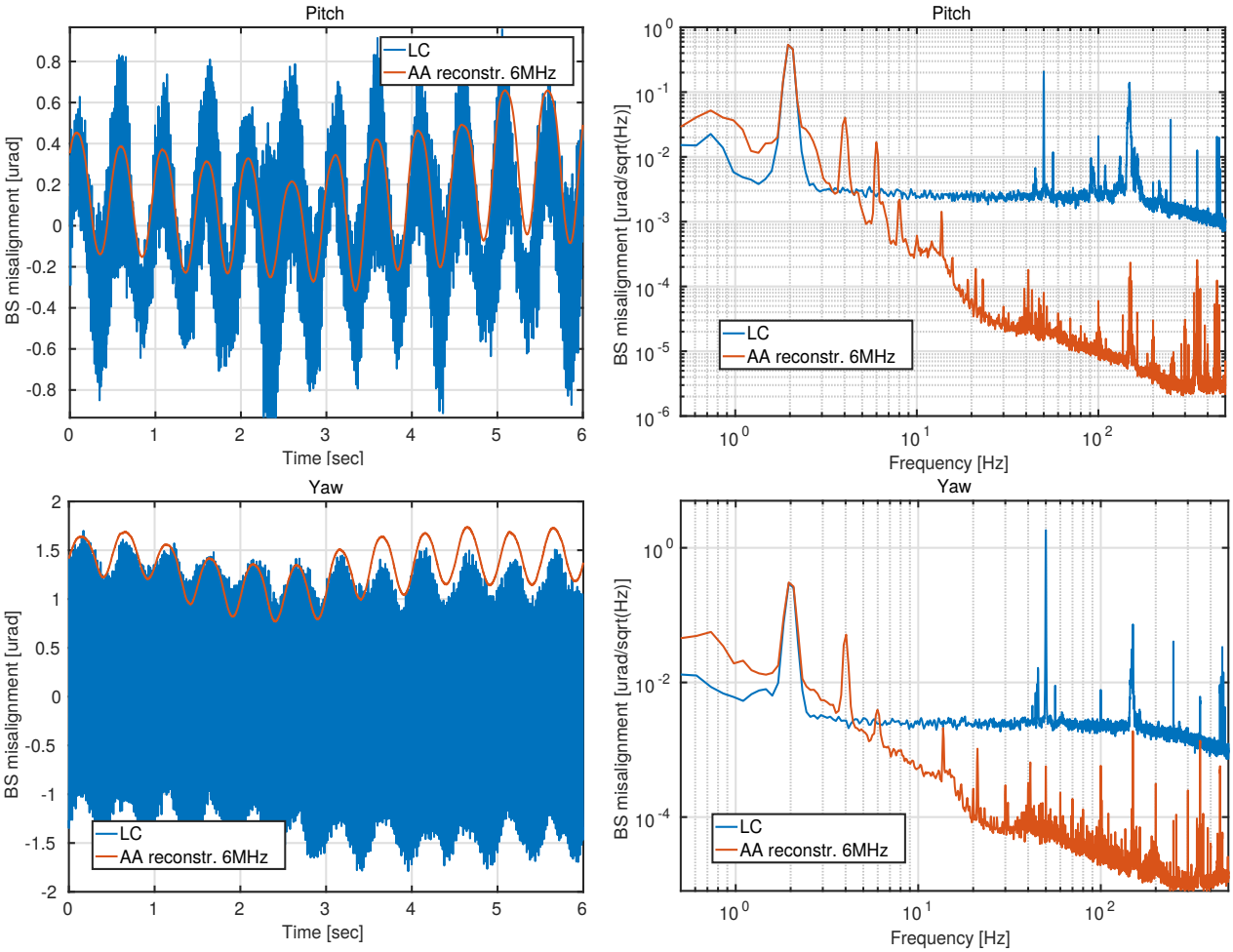

FIGURE 6.36: Reconstruction of the angular noise injection performed on the BS mirror compared to the reconstruction from the Local Controls. The plots on the left show the time domain reconstruction while The plots on the right show the frequency domain reconstruction of the BS angular noise injections.

6.5 Towards Dark Fringe

At this point we have all the DOFs controlled and their UGFs have been chosen carefully. Now we need to decrease the MICH offset to pass from 0.7 of bright fringe to Dark Fringe. The tricky part of this transition is the fact that the power in all photodiodes will change during this process as well as the optical configuration, and in consequence also the OG of the different error signals. If this variation is too important, the loops may become unstable causing an unlock of the whole interferometer.

6.5.1 Optical Gain evolution

Figure 6.37 shows the evolution of the power inside the interferometer during a lock where a MICH offset of 0.07 was reached, compared to the simulations presented in Section 5.2.3. The power at the antisymmetric port, B1, the power at the symmetric port, B2, and the power inside the PRC, B4 are shown in Figure 6.37.

In order to be able to compare simulation and measurements, they have been normalized to the power at a MICH offset of 0.4

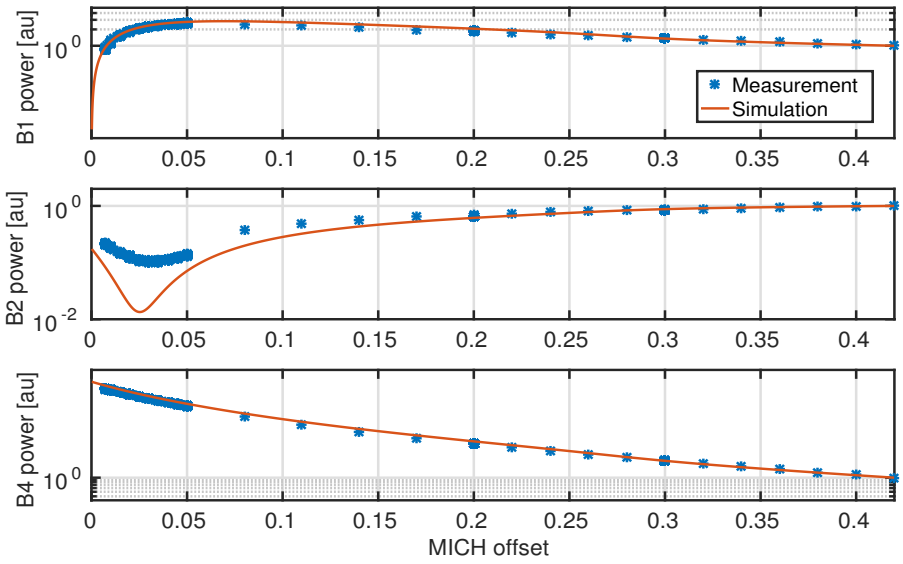

FIGURE 6.37: Power evolution during the MICH offset reduction. **Upper plot:** power in the antisymmetric port. **Central plot:** power reflected by the PRC. **Lower plot:** PRC intra-cavity power.

The power at B1 and B4 is more or less in agreement with the simulation, which represents the ideal case. However, the power on B2 does not agree with the simulation near the DF, which gives us information about the optical configuration of the interferometer.

The first interesting thing is the MICH offset at which the **PRC is critically coupled**. This happens when the Round Trip Losses (RTL) of the PRC are equal to the transmission of the PR mirror. So this parameter gives information about the losses inside the interferometer. The RTL of a FP cavity depend on the transmission and the losses of the input and end mirrors [59]. In the case of the PRC it depends on: the PR mirror transmission (T_{PR}) and losses (L_{PR}), the MICH interference condition (T_{MICH}), and the losses inside the Fabry-Perot cavities (L_{arm}). The total expression can be written as:

$$RTL_{PRC} = T_{PR} + T_{MICH} + L_{PR} + L_{arm} \tag{6.4}$$

From Figure 6.37 in the ideal case the PRC is critically coupled at $\text{Offset}^{cc}_{simu} = 0.025$, while in the real interferometer this happens at $\text{Offset}^{cc}_{real} = 0.031$. Knowing that the simulations have been done with the measured transmission of the PR [60], it can be concluded that the PRC has smaller losses than in the design. For the simulation we considered $L_{arm} = 75$ ppm and $L_{PR} = 35$ ppm[5].

Another interesting information that can be extracted from Figure 6.37 comes from the **depth of the minimum of the power on B2**. In the simulation this minimum is much lower than in the real interferometer (a factor 10). The fact that there is more reflected power in the real interferometer when we approach Dark Fringe implies the presence of HOMs that are generated but do not couple

[5]These are the maximum losses accepted to reach the nominal sensitivity [14].

to the interferometer. This is not surprising taking into account that the only alignment engaged is the PR mirror loop in drift control and that the input beam is mismatched with respect to the PRC since the PR mirror RoC is 70m away from the nominal value.

So far we have seen how the power inside the interferometer varies with the MICH offset reduction in a non-negligible way (more than 2 orders of magnitude). In practice this causes problems of saturation in the photodiodes. In particular the photodiodes in transmission of the arm cavities that are used for controlling DARM are exchanged during the lock acquisition (at 0.3 of MICH offset) from the PD1 that receives 90% of the light entering into the detection bench to PD2 which receives only 10%.

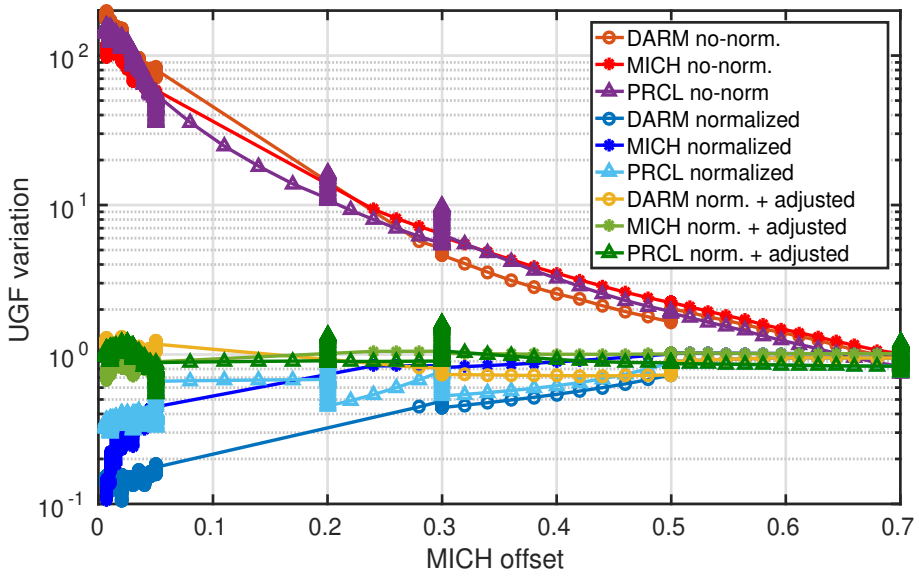

FIGURE 6.38: Variation of the UGF during the MICH offset reduction for DARM, MICH and PRCL. Three cases are shown: when the error signals are not normalized, when they are normalized and once their gain is adjusted during the process.

Regarding the longitudinal loops performance, all the error signals were normalized to deal with the PR alignment, which is convenient for the MICH offset reduction as well. In Figure 6.38 the **variation of the UGF of the longitudinal loops** with respect to the MICH offset is shown, except for the SSFS that will be shown later.

Without any normalization all the UGFs increase very rapidly. It would be impossible to compensate dynamically for such an important variation of OG even for a very slow offset reduction. Instead when the error signals are normalized, the variation is less important, around a factor 10 at most during the last stages of the offset reduction process.

Still, a factor 10 is too high for a control loop to survive and so further adjustment is necessary. For this purpose the *UGF servo* was implemented. The idea of this technique is to add a permanent line to the sensing of each DOF above their UGF (67.1 Hz for PRCL and 87.1 Hz for DARM). This allows us to calculate the OLTF of each loop at the frequency of the lines. As their shape is known, it is possible to monitor the variation of the UGF of the longitudinal loops.

Thanks to it we were able to adjust finely the gains of the loops in order to keep the filters within their stability ranges and to keep the hierarchy between the DARM and MICH loops. The third set of curves in Figure 6.38 shows the UGF variation after the adjustment of the gains using the information provided by the UGF servo. The UGFs remain stable within a factor 3, which is manageable by the longitudinal loops.

The SSFS loop was studied independently, because at the early stages of the commissioning it was not possible to implement the UGF servo due to software constraints of the SSFS DSP. Instead, we opted for finding an optimized normalization. Figure 6.39 shows the UGF variation with the standard normalization, B4 DC, which fluctuates by a factor 10. The red curve is the result of the adjustment of the gain done by hand and the variations are at most a factor 2, but they are a bit violent. Using this data we found an empirical normalization, $P_{B4DC}^{0.67}$, that minimizes the gain fluctuations and the result is shown in the yellow curve. The residual variation in this case is a bit less than a factor 2, and it changes in a smooth way.

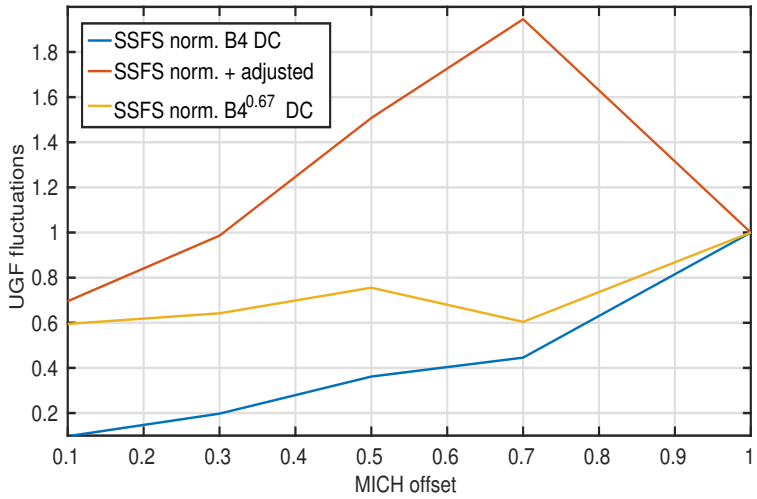

FIGURE 6.39: UGF variation during the MICH offset reduction of the SSFS loop. Three cases are shown: when the error signal is normalized by B4 DC, when it is normalized and its gain is adjusted by hand and once it is normalized with an empirical signal, $P_{B4DC}^{0.67}$.

Another interesting question that affects the OG is the **demodulation phase variation**, as it was already mentioned in Section 5.2.6. A variation of more than 10° starts to have an impact on the OG since the cosine used for the demodulation is not anymore on its maximum. Figure 6.40 shows the variation of the demodulation phases of the error signals that are used to control DARM, CARM and PRCL.

First of all notice that we do not tune the demodulation phases during the lock acquisition sequence, so the fluctuations shown in Figure 6.40 contribute to the OG variations shown in Figure 6.38. For the CARM error signal (B4 6MHz) and for PRCL error signal (B2 8MHz) there is not a significant variation of the demodulation phase.

In the case of DARM DOF we see variations up to 30°. This is not unexpected, since we had already mentioned that the differential DOFs were very sensitive to

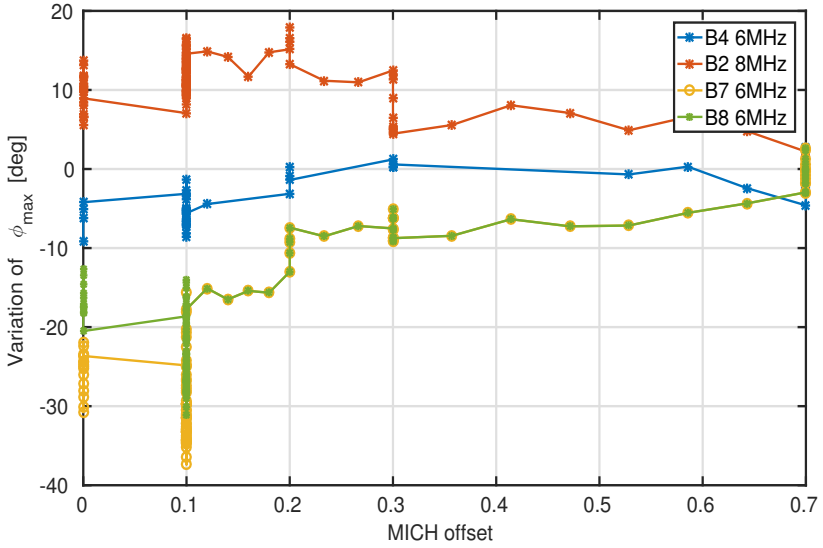

FIGURE 6.40: Variation of the optimal demodulation phase of the used error signals during the MICH offset reduction. The B7 and B8 6MHz demodulation phase is tuned separately and then they are combined to build-up the DARM error signal.

the MICH offset reduction, since the sidebands are very unbalanced. This ϕ_{max} variation translates in a higher fluctuation of the OG for DARM than for the other DOFs, as shown in Figure 6.38. However, this is not very worrying since the DARM error signal will be handed-off to the B1 photodiode in Dark Fringe.

The initial idea was to start with the 8MHz error signal and then hand-off to the 3Ω when getting closer to the critically-coupled point. However, a sign flip was detected in this error signal, that prevents us from using it. The behaviour of the demodulation phase can be seen in Figure 6.41.

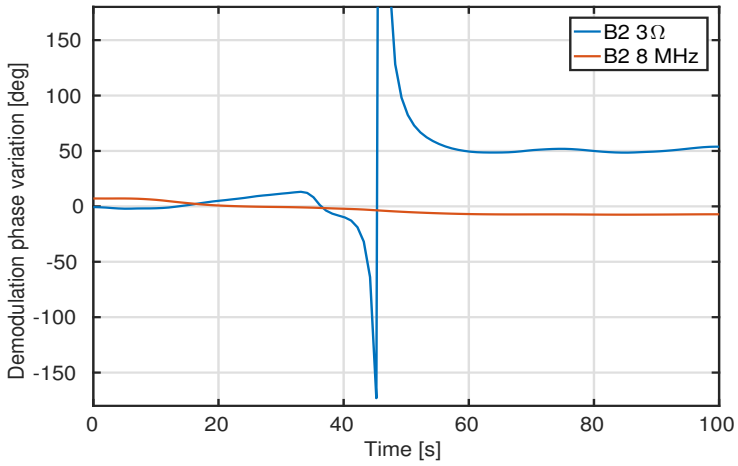

FIGURE 6.41: Optimal demodulation phase evolution of the B2 8MHz and 3Ω during the MICH offset reduction. It can be seen how the ϕ_{max} of the 3Ω experiments a big jump when crossing the critically-coupled point.

This phenomenon is unexpected and it is not well understood. The critically coupled point is crossed at 41s, and then the phase starts to drift, having a very violent change that would be impossible to compensate. This was not the case in Virgo+, since it was used all the way to Dark Fringe.

The fact that the phase changes at such low MICH offsets might suggest that the HOMs that couple into the interferometer have an impact into the 3Ω error signal, which is a very weak signal. The carrier is cleaned from HOMs by the arm cavities while the sidebands are not. As the 3Ω signal depends only on the sidebands information, it is understandable that it is more sensitive to them.

6.5.2 Recycling Gain

We know that there are HOMs generated due to misalignment and mismatch on the PRC. Since it is very close to the instability, their coupling to the interferometer will be very high, as it was already detailed in Section 5.2.2. A good way to evaluate the impact of this coupling is to monitor the Recycling Gain of the carrier and the sidebands. However it is not a straightforward operation, since the B4 photodiode can not decouple carrier, sidebands and HOMs.

In the **carrier** case we will use the B7 and B8 photodiodes because the arm cavities are able to select the fundamental mode better than the PRC. As the sidebands are not resonant inside the arms, we are sure that we have information only about the fundamental mode of the carrier.

As we do not know the input power at the photodiodes we need to take as a reference the power impinging on them at the recombined configuration (Step 3). Notice however that we need to compensate for the transmission of the PR mirror. At Step 3 it is misaligned, but the light that traverses it is attenuated by T_{PR}. This is not the case anymore when the PRC is aligned, since the light resonates inside it instead. We do not need to compensate for the Optical Gain of the FP cavities since it is constant during all the lock acquisition.

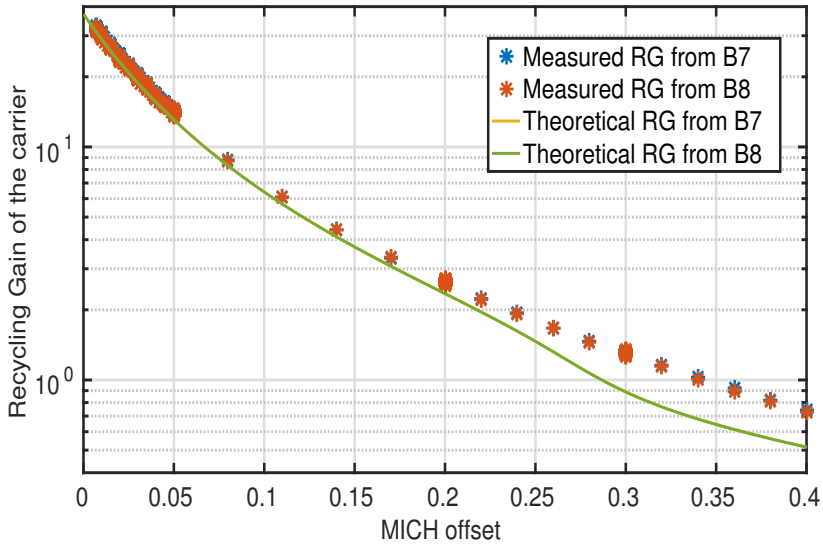

FIGURE 6.42: Recycling Gain of the carrier obtained using the arms transmitted power. The plot shows a comparison of the value obtained from the simulation and from the experimental data.

Figure 6.42 shows the increase of power on the photodiodes in transmission of the arms during the MICH offset reduction process, taking the power in Step 3 as a reference. It agrees very well with the simulation below a MICH offset of 0.25, which reaches an OG for the carrier in Dark Fringe of $OG^c_{PRC} = 37.09$. Above 0.25 of MICH offset the measurements are approximately a factor 2 higher than the simulations.

The origin of this discrepancy has not been further investigated. As the simulation and the measurement agree close to the working point it is not likely to come from a bad modelization of the optical parameters in the simulation. Since it is quite clear that we are dealing with an anomalous PRC, it is more likely to come from the coupling of HOMs leaking to the photodiode in transmission. For this reason we will not worry about it until the nature of the PRC is better understood.

The case of the **sidebands** is a bit more complicated because they are not resonant in the arm cavities. The fundamental mode resonates inside the PRC together with the HOMs, and so they are very sensitive to the optical configuration of the interferometer. For this reason they are an important figure of merit of the interferometer good functioning.

In order to evaluate the Recycling Gain of the sidebands we need to find a probe that senses them independently from the carrier. For this purpose we use the 2Ω signal, which results from demodulating the signal read by the photodiode at twice the modulation frequency, in our case at 12 MHz. This signal contains information about the beating between the components of the beam separated by 2Ω. It contains a term which depends of $4J_0J_2$ and another term that depends on $2J_1^2$. When we are at the working point they depend as well on their Recycling Gain. For this reason the first term can be neglected, since the 2Ω component is not resonant inside the interferometer.

However in practice we need a normalization since we do not know the input power on the photodiodes. In principle we can use the power at the recombined state as in the carrier case, but then we can not neglect the term $4J_0J_2$.

Following an analogous reasoning as in the carrier case, the RG of the sidebands at the B5 photodiode can be written as [61]:

$$RG^s_{B5} \approx T_{PR} \cdot 2 \cdot \frac{P^{2\Omega}}{P^{2\Omega}_{HF}} \tag{6.5}$$

where $P^{2\Omega}$ is the power of the 2Ω error signal, $P^{2\Omega}_{HF}$ is the power of the 2Ω error signal at the recombined configuration and the factor 2 comes from evaluating $(2J_1(m)^2 + 4J_0(m)J_1(m))/2J_1(m)^2$, where m is the demodulation depth.

Regarding the B4 2Ω we also need to take into account the reflectivity of the Michelson interferometer towards the symmetric port, and so we can obtain the RG as [61]:

$$RG^s_{B4} \approx T_{PR} \cdot \frac{R^{HF}_{SYM}}{R_{SYM}} \cdot 2 \cdot \frac{P^{2\Omega}}{P^{2\Omega}_{HF}} \tag{6.6}$$

However, it is a bit tricky to calculate the RG during the lock acquisition since the modulation depth of the 6 MHz is decreased when approaching the DF in order to avoid the B4 phootdiode to saturate. While we use the 56 MHz to control the SSFS and MICH DOFs, the 6 MHz is free. Due to its high recycling gain, it increases a lot close to the DF, causing the B4 photodiode to saturate. For this reason it is better to make the calculations directly in DF, which will be presented later.

During the offset reduction we can see that after 0.3 of MICH offset, the sidebands start to fluctuate a lot. Figure 6.43 shows the 2Ω signal when the interferometer is locked at 0.1 of MICH offset. They vary more than a factor 3. This confirms the hypothesis of the high coupling of the HOMs to the interferometer, which has a big impact in the behaviour of the sidebands. It also explains the misbehaviour of the 3Ω signal, as it was pointed out before. This increases the complexity of controlling the interferometer, since all the longitudinal loops will suffer from UGF fluctuations and it is very difficult to predict the behaviour of the interferometer.

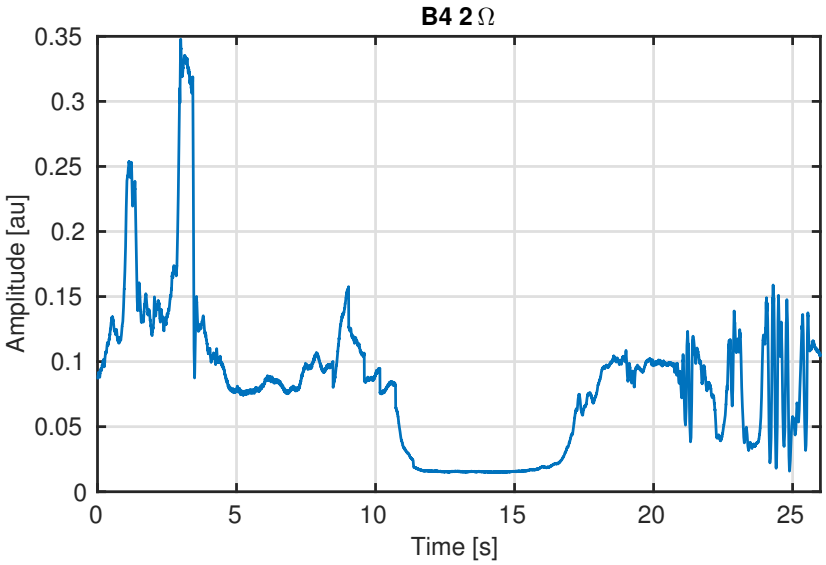

FIGURE 6.43: 2Ω error signal at the B4 photodiode at 0.1 of MICH offset. It depends on the sidebands power, and it fluctuates up to a factor 4.

6.5.3 Alignment

In Step 4 we have engaged the PR and BS loops, since they are the most simple angular DOFs, and they improve significantly the performance of the interferometer. The problem that was observed in the previous step was the presence of offsets on the error signal with respect to the positions indicated by the LC. They have been compensated by adding an offset to the error signals. For this reason it is important to check that these offsets do not evolve during the MICH offset reduction process, as well as the sensing.

First of all we have found a good **normalization** for the four loops. In the case of the PR loop we have normalized by the square root of the DC power impinging on the B4 quadrant photodiode (QPD). This is because we are using the 8 MHz and so only the carrier experiments the increase of the optical gain due to the optical configuration of the interferometer.

For the BS, as both the sidebands and the carrier are resonant inside the PRC, we normalize by the DC power impinging on B1 DC. We do not use the power on the QPD in this case, since it saturates close to DF, which is not the case for the photodiode used for the longitudinal control. Figures 6.44 and 6.45 shows the evolution of the error signals of both loops with and without the normalization

during the fringe offset reduction. We see that it remains stable thanks to the normalization.

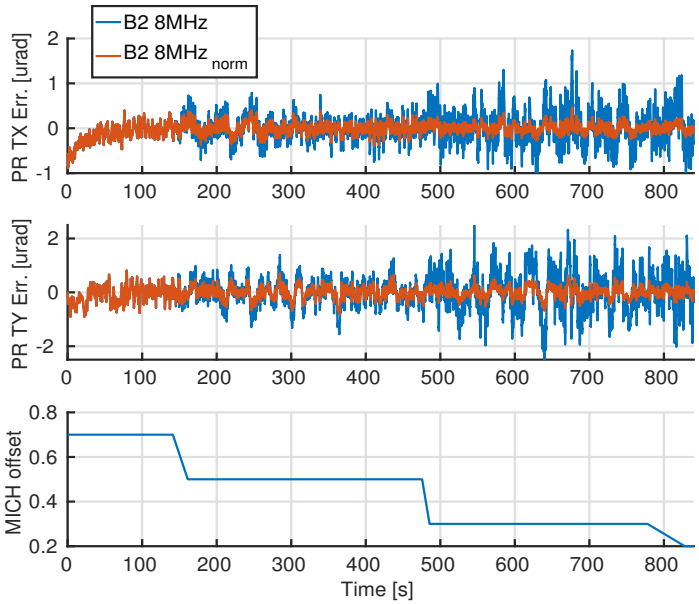

FIGURE 6.44: Error signal from the B2 quadrant photodiode (QPD) demodulated at 8MHz during the MICH offset reduction. **Upper plot:** error signal of the PR θ_x DOF with and without normalization. **Central plot:** error signal of the PR θ_y DOF with and without normalization. **Lower plot:** MICH offset.

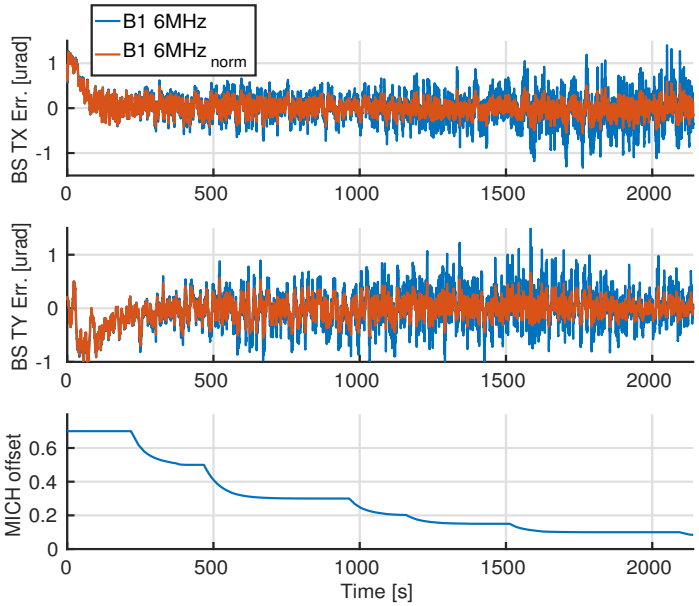

FIGURE 6.45: Error signal from the B1 quadrant photodiode (QPD) demodulated at 6MHz during the MICH offset reduction. **Upper plot:** error signal of the BS θ_x DOF with and without normalization. **Central plot:** error signal of the BS θ_y DOF with and without normalization. **Lower plot:** MICH offset.

Now regarding the **evolution of the offset** we found that for the PR loop, the working point given by the error signals is not good all over the MICH offset reduction process. During the lock acquisition sequence it was clear from the cameras that the beams at B4 where not well superposed, meaning that the alignment was fixed at a bad point.

We tried to add an offset to the error signal during the MICH offset reduction, tuning the working point by hand. However, this offset would change from one day to the other, which would oblige us to tune it almost daily. Somehow it was practical to have this loop engaged, since, once the offset tuned, it would remove a variable from the lock sequence, which was already very complex.

In the case of the BS, we had added an offset to the yaw DOF from the beginning, since the zero of the error signal was more than 1μrad away from the aligned position. The same problem of the offset of the error signal that changes over the offset reduction process was found for this loop, but also an extra problem on the yaw DOF. The sensing would change as well, which does not allow to close a stable loop on it. It is not surprising that one DOF works differently from the other, which could be caused by the presence of astigmatism on the beam. In this case the beam profile is not the same in 2 orthogonal directions, modifying the response of the quadrant photodiodes.

This behaviour of the QPDs signals which fluctuate depending on the optical configuration of the interferometer is compatible with the presence of HOMs inside the interferometer. Remember that the working principle of the automatic alignment is based on the supposition that the first order mode is dominant over the HOMs. If this is not the case, as it seems to indicate the sidebands behaviour, the information seen by the quadrants will be a mixture of the different HOMs and it will be impossible to disentangle the relevant information.

The only solution to this problem is to use the Thermal Compensation System to bring the PRC to the most stable condition possible and to reduce the presence of HOMs. However, as it was not possible at that moment, we decided to find an alternative to control the alignment, since the quadrants were not reliable.

So we recovered the mechanical modulation technique used at the recombined configuration. It was decided to turn off the mechanical modulation lines once the interferometer is aligned on Step 3. Then the lock acquisition continues without alignment until a MICH offset of 0.1. At this point the lines are turned on again, but this time with a smaller amplitude, since the system is much more sensitive at this point. This does not provide an absolute alignment, since this technique only centers the beam into the optics in order to minimize the coupling between the angular and longitudinal controls, but it stabilizes the interferometer in a repeatable way.

We modified the BS and PR loops with respect to Step 3 though. We only succeeded to use the quadrant photodiodes in a reliable way for the PR loop, even if the offset is set by hand, using the same error signal as in Step 4, B2 8 MHz. Regarding the BS, the same angular lines as before are added, but now we use as error signal the demodulation of B1 DC at $f_{drift}^{\theta_i}$. This is used to align the recombination at the antisymmetric port. Once the system had time to get aligned, the alignment loops are turned off and we are ready to make the passage to DF in an aligned position.

6.6 Dark Fringe

So far we have presented the lock strategy up to reaching 0.1 of MICH offset. The missing step is the **hand-off of MICH error signal**: it is necessary to pass from the DC error signal to the Radio Frequency error signal. As it was explained in the previous chapter, this step is critical since the hand-off is done between two error signals whose validity does not overlap. As it was shown by the simulation, the linear region of the MICH error signal starts at 98% of fringe in terms of wavelength or 99.9% in terms of power.

However the DC error signal is not a good error signal anymore so close to the DF. Moreover the fluctuations of the sidebands make difficult the approach to the DF in a stable way. For this reason the hand-off is done before, at 90% of fringe in terms of power, as it was done in Virgo+. This is a state that was reached in a repeatable way, and thanks to the alignment we could keep the interferometer controlled during relatively long periods of time.

Regarding the demodulation phase, it does not need to be tuned since the in-phase projection of the error signal is used to control the SSFS. To find the correct gain is more difficult, since we do not have information about the values of the signals in DF. The strategy was to study the unlocks close to the working point, since occasionally the interferometer would cross the DF which would allow to make a rough estimation of the scaling factor needed. Finally, the hand-off needs to be instantaneous, without any transition. The aim is to avoid as much as possible the zone where the error signals are not good and to pass from a controlled state to another one.

At the beginning we tried to make the hand-off directly with the 6MHz. However due to the enormous fluctuations of the sidebands, this transition was not reliable. Even though we succeeded several times, the control in DF was very unstable lasting only few minutes. We tried then to use the solution proposed in Section 5.2.2, that is to use an error signal generated by a higher modulation frequency. Due to technical problems, the 119 MHz was not available and so the only option was the 56 MHz, which in any case has a lower Recyling Gain than the 6 MHz (13 vs 77).

This test was successful and in spite of the sidebands stability the control was much more stable, providing longer periods of lock. Moreover, this error signal would allow to reach the DF in a reliable way. An example of the MICH hand-off is shown in Figure 6.46. The offset reduction is done quasi-instantaneously (in one second), and we can see the drop of power in the antisymmetric port, at B1 DC.

In the same figure we can see the error signal used for MICH, which transitions from the old one, B1/B1+B4 to B4 56MHz Q. Finally the last signal shown is B4 56 MHz Q, which is free until 10.5s. Then the transition to Dark Fringe starts, and it can be seen that instead of going straight towards zero, the error signal goes first towards more negative values and then it reaches zero at DF. This is because when the hand-off is done, we are not yet within the linear region of the error signal.

At this point the error signals do not need normalization anymore, and so B4 56MHz is not normalized.

Once it was confirmed that this error signal was more reliable than the 6 MHz, we took the decision of changing the error signal of the SSFS as well to its 56 MHz version (B4 P). This had two advantages: the first one the robustness regarding the sidebands fluctuations and the second one to reduce the phase noise, as explained in Section 5.2.4.

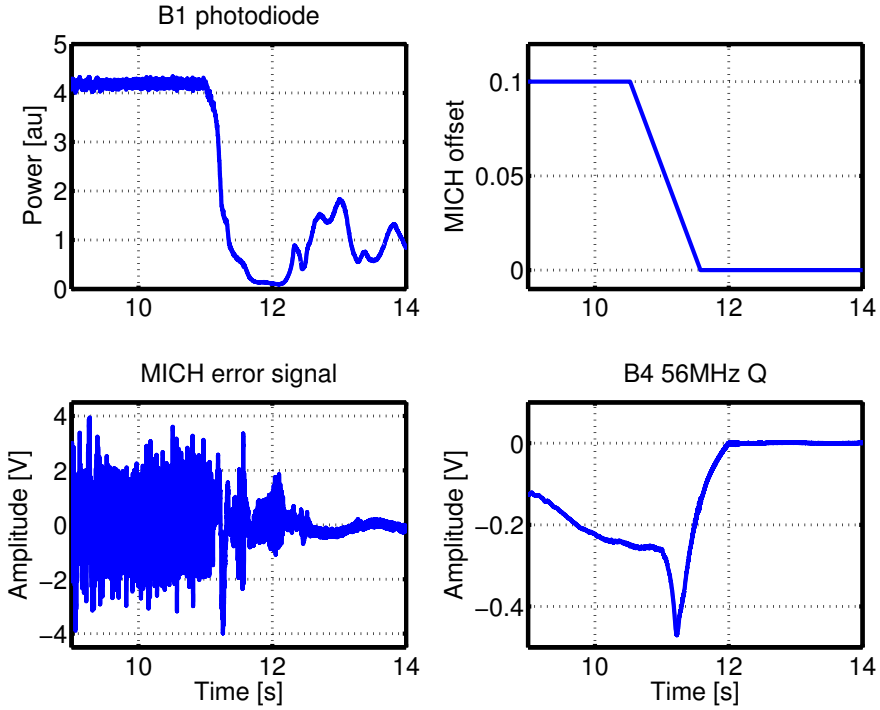

FIGURE 6.46: MICH hand-off to an RF signal and lock in DF. The power in the antisymmetric port is shown as well as the MICH offset, the signal showing the transition between both error signals and the B4 56 MHz Q which is the target one.

The final step is to **change the DARM error signal**. So far it is locked using B7 6MHz$_{norm}$-B8 6MHMz$_{norm}$ which are very unstable as well due to the sidebands fluctuations. The target is to change the error signal to B1 56 MHz since the 6MHz will suffer the same problem.

As DARM is already controlled is straightforward to tune the demodulation phase and the gain. For the first one it is enough to minimize the spectrum of the quadrature, B1 56MHz Q. For the gain instead we can make the TF between the current error signal and the one we want to use. If ϕ_{max} is well tuned, both signals are coherent and the TF is flat. Its value gives the factor that needs to be taken into account in order to transition between the two error signals. The transition is done in a smooth way, ramping up the new error signal while ramping down the old one.

An example of the transition is shown in Figure 6.47. The MICH hand-off can be seen both in the B1 power and in the DARM error signal. Then, at the second 11, the DARM hand-off is done, and the control is improved, since the error signal is reduced.

Regarding the **alignment**, the dithering lines have been tuned for this configuration, but the scheme is the same as at 0.1 of MICH offset. The only difference is that in this configuration the PR AA does not work anymore, and so two lines have been added to the angular DOFs and the error signals are extracted from the correction of the PRCL DOF. In spite of this effort, the fluctuations of the sidebands did not improve.

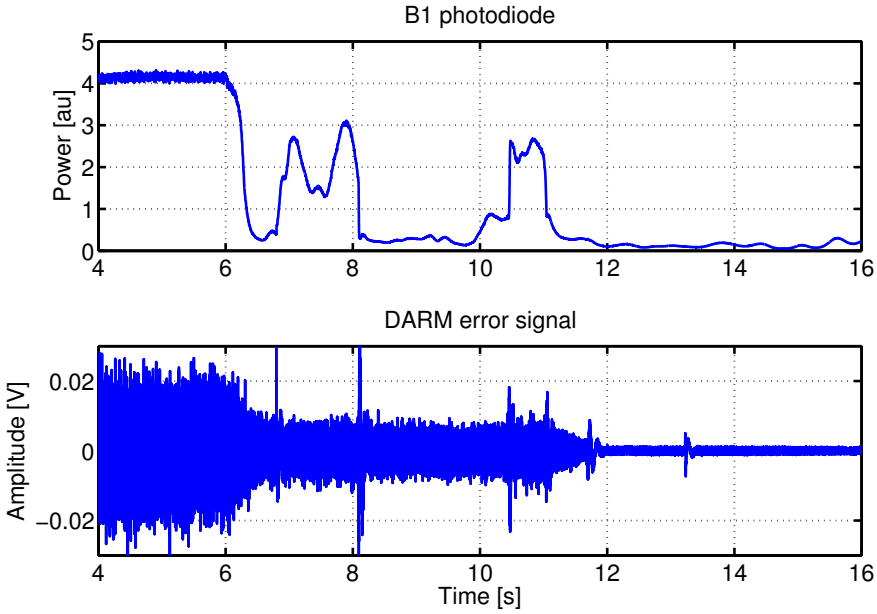

FIGURE 6.47: DARM hand-off once in DF from the B7 6MHz$_{norm}$-B8 6MHz$_{norm}$ to the B1 56 MHz which is mores stable. We can see the MICH hand-off first, and then the DARM one.

A fraction of lock in Dark Fringe is shown in Figure 6.48. We have used the photodiodes in transmission in order to calculate the Recycling Gain of the carrier. We have used Equations 6.6 and 6.5 to calculate the Recycling Gain using the 2Ω error signal. The carrier remains stable, while the RG of the sidebands fluctuates up to a factor 5. Notice that the target sidebands RG is 77, and so the maximum is still under this value. Even if the 2Ω signal allows us to separate information between the sidebands behaviour and the carrier, it does not separate the behaviour of the HOMs. This means that its value might be affected by the presence of HOMs so we can not take it as a final result. However, it will be useful for the commissioning of the TCS, to determine if there are improvements or not.

An overview of the **lock acquisition sequence** is shown in Figure 6.49, from the lock of the arms to the DARM hand-off in Dark Fringe. The power on the different photodiodes (B1, B4, B7 and B8) is shown as a function of time and the different stages of the process are indicated in different colors. The overall sequence takes almost four minutes unlike in Virgo+ where the lock acquisition sequence was much longer ($\sim 30min$) to deal with thermal transients that we do not yet experience.

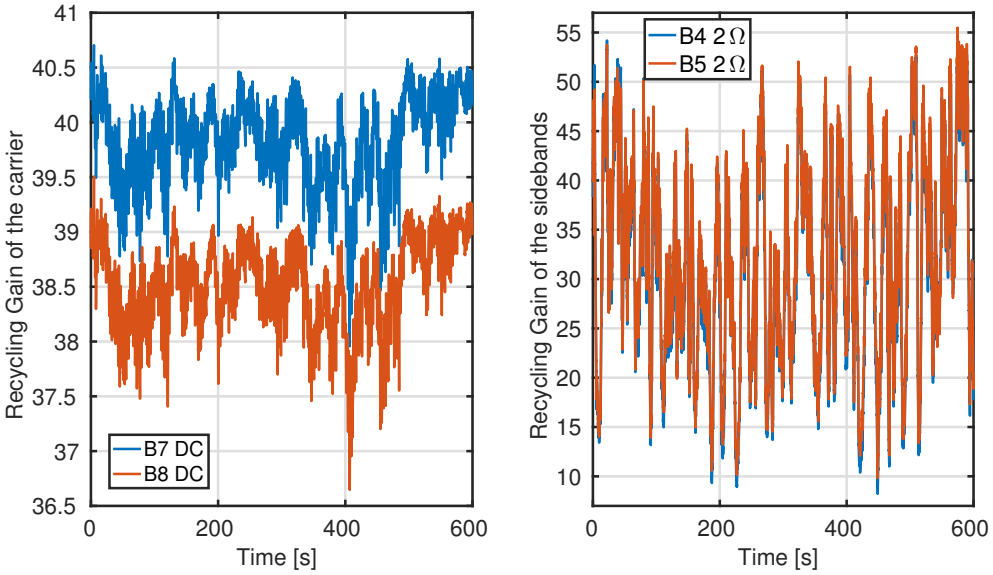

FIGURE 6.48: **Left plot:** Recycling Gain of the carrier calculated from B7 and B8 DC. **Right plot:** Recycling Gain of the sidebands calculated from B4 and B5 2Ω

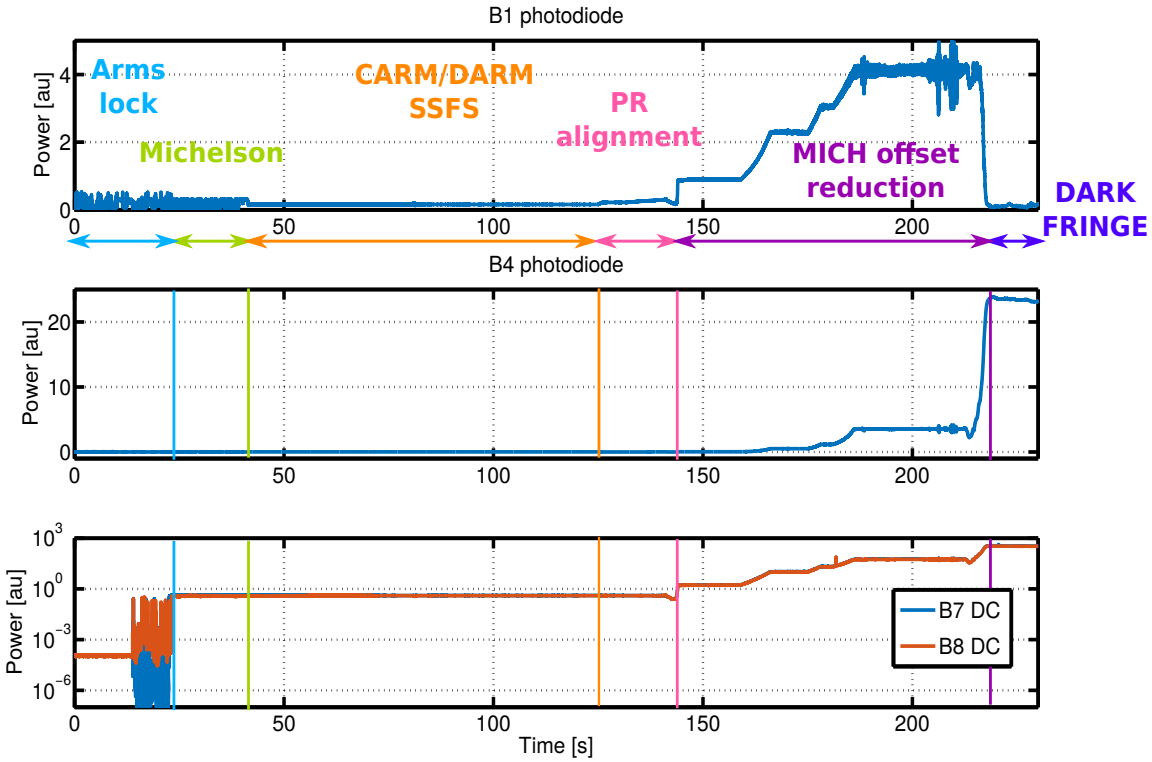

FIGURE 6.49: The Variable Finesse control strategy is shown here, from the arm cavities lock to the DARM hand-off in DF. The power at the antisymmetric port, inside the PRC and in transmission of the arms is shown in the figure. The different steps are indicated with different colors.

Once the DF is reached, the two Output Mode Cleaners are locked in order to clean the beam that is detected by the detection photodiode. Figure 6.50 shows the images of the cameras installed in the detection bench and monitoring the B1p photodiode (the one used for the longitudinal control, that we have called B1 during the thesis) which is placed before the OMCs and the B1 photodiode placed after the second OMC and which is used for the DC readout. The image in the left corresponds to the B1p camera and it shows a beam which is not gaussian due to an important presence of HOMs and the sidebands. The image on the right shows instead the B1 camera, where the fundamental mode of the carrier has been selected. The beam quality has improved significantly after passing through the OMCs.

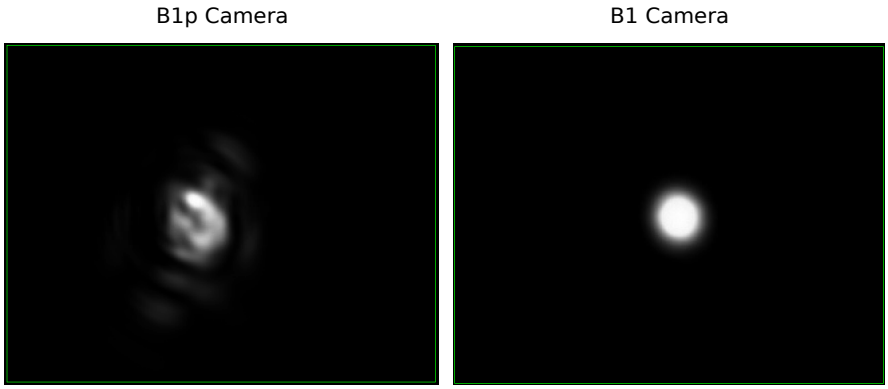

FIGURE 6.50: Camera images from the detection bench in DC readout. **Left image:** B1p camera, which monitors the beam before entering into the OMC. **Right image:** B1 camera, transmission of the second OMC, after the two of them have been controlled.

A global scheme of the longitudinal and angular controls that are engaged in Dark Fringe is shown in Figure 6.51. The sensing and driving of each loop are indicated with continuous lines. The angular loops are indicated using dashed lines. This is because they are not systematically engaged in Dark Fringe since they are not always reliable.

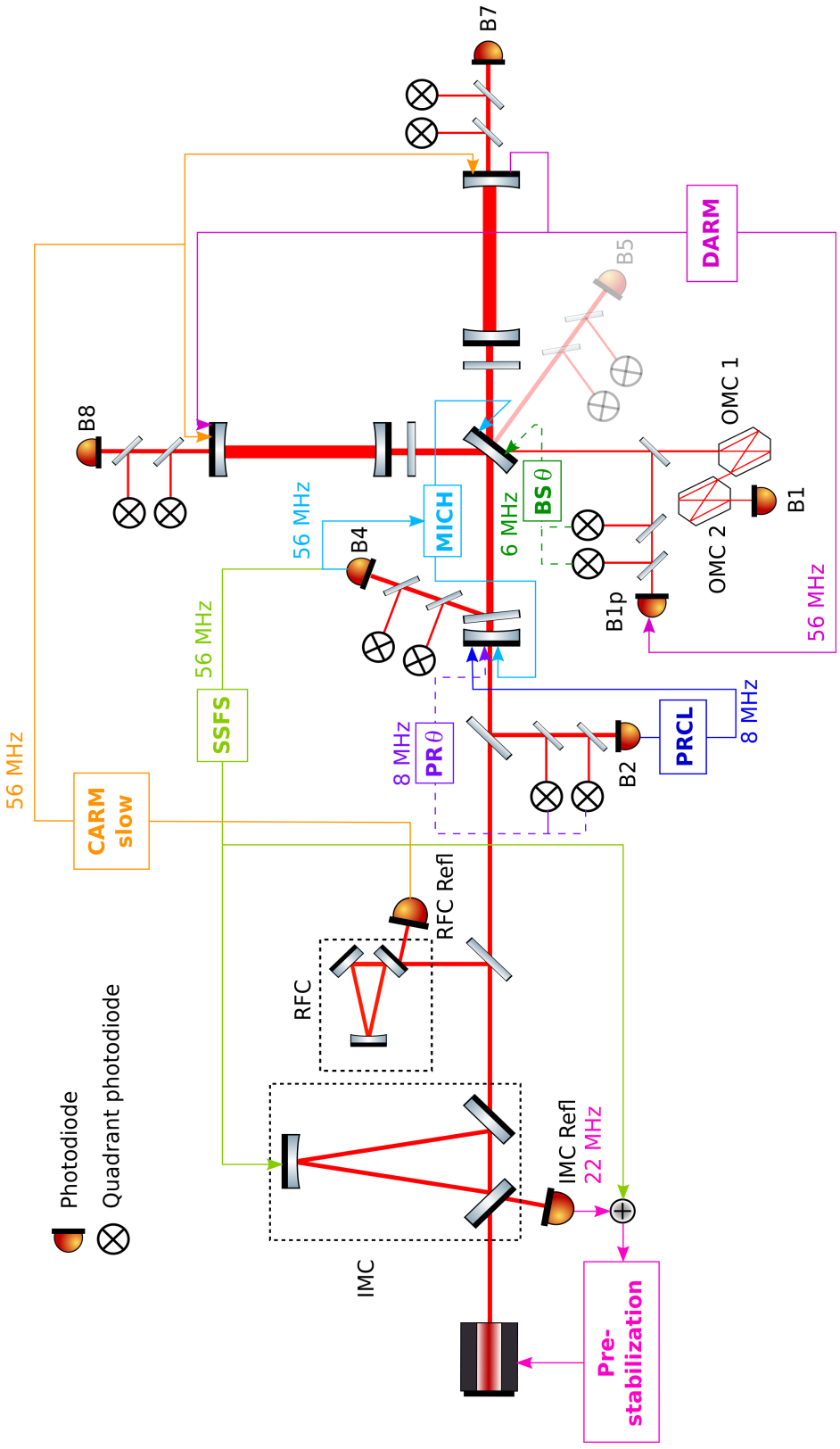

FIGURE 6.51: Scheme of the longitudinal and angular loops that are engaged in DF. The angular loops are represented by dashed lines because they are engaged systematically.

Once at the working point, the controls are fine tuned in order to reach the best sensitivity possible. This implies mainly to add boosts to the controls, since the most problematic region is the low frequency, where the noise is higher. This is the case for DARM and SSFS loops. However, the boost implementation has not been successful for the MICH DOF since the error signal is too noisy and the controls saturate. In the case of PRCL, the boost was engaged from the beginning.

In this state we have made a set of noise injections to measure the OLTF of the longitudinal control loops. This measurements are shown in Figures 6.52 and 6.53, together with the old filter without the boost for comparison for DARM and SSFS. Even if the shapes are correct, the UGFs are not accurate since they fluctuate with the sidebands.

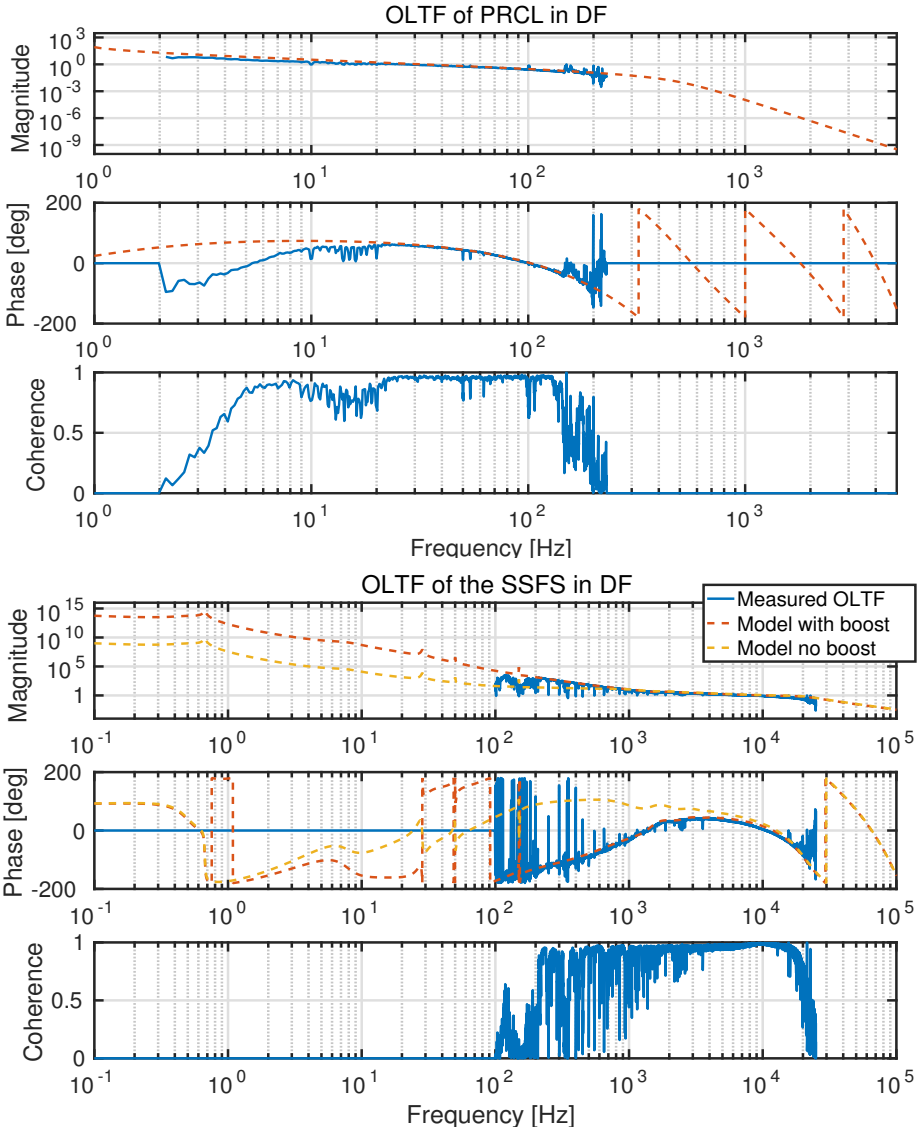

FIGURE 6.52: Comparison between the measurement and the model of the OLTF of PRCL and SSFS loops. In the case of the SSFS the model with and without boost is showed for comparison.

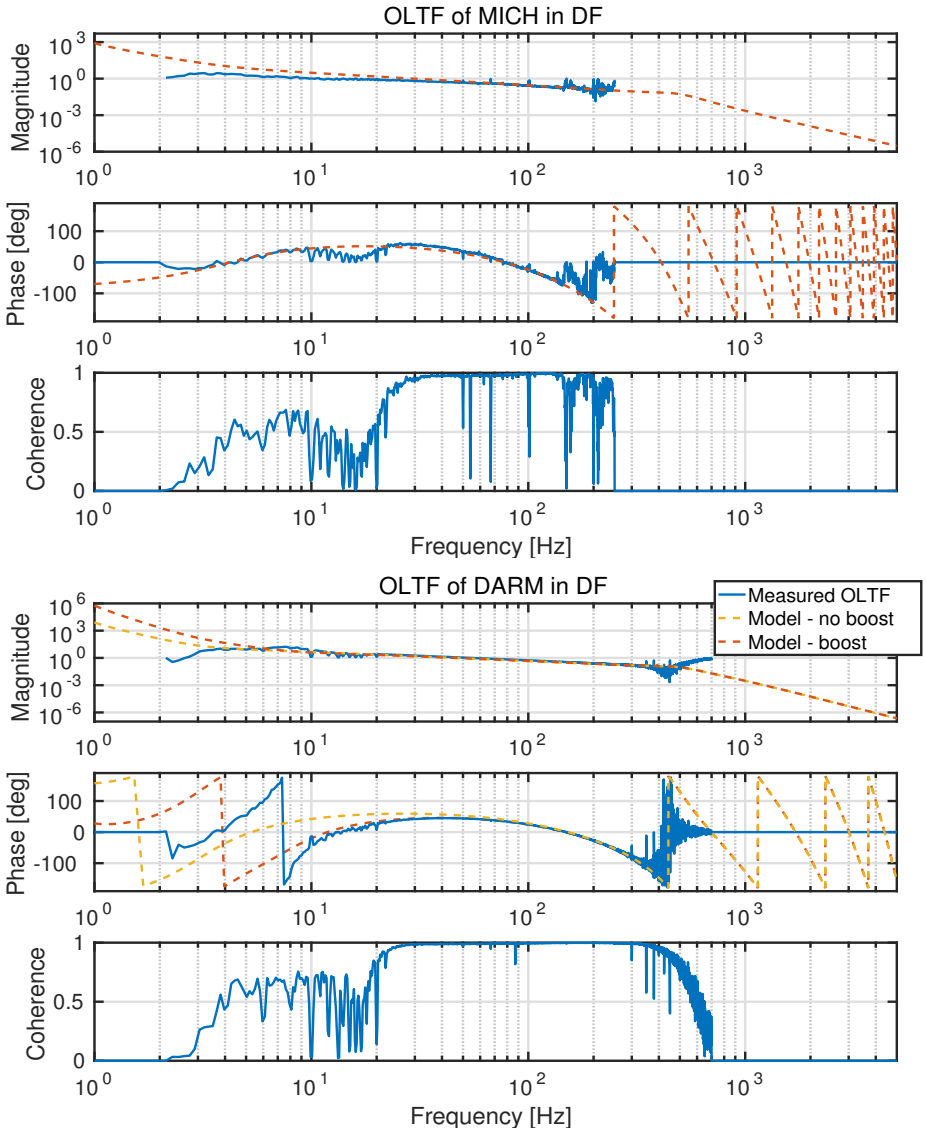

FIGURE 6.53: Comparison between the measurement and the model of the OLTF of MICH and DARM loops. In the case of DARM the model with and without boost is showed for comparison.

Just as before, we can use the OLTF measurements to calibrate the error signals, and so to estimate the quality of the longitudinal controls. The calibration factors estimated in the previous sections are not correct anymore since they take into account the optical gain, which changes during the MICH offset reduction.

In this case, it makes even less sense to evaluate the errors of the calibration factors, since the measurement is highly affected by the instability of the interferometer. Taking into account the sidebands fluctuations, the measurements are more an averaged behaviour of the loops.

The calibration of the SSFS is done in a slightly different way this time. When we measure the OLTF of the SSFS loop the actuation is applied to the laser and so we need its calibration factor in Hz/V. When doing the commissioning of the SSFS loop we had already measured the $C_{SSFS-RFC}$ in V/V. Using the calibration of the error signal of the RFC $C_{RFC} = 6.57 \cdot 10^4 Hz/V$ [62] we obtain the calibration of the actuation of the SSFS in physical units, $C_{Act-SSFS} = 6.57 Hz/V$. Figure 6.54

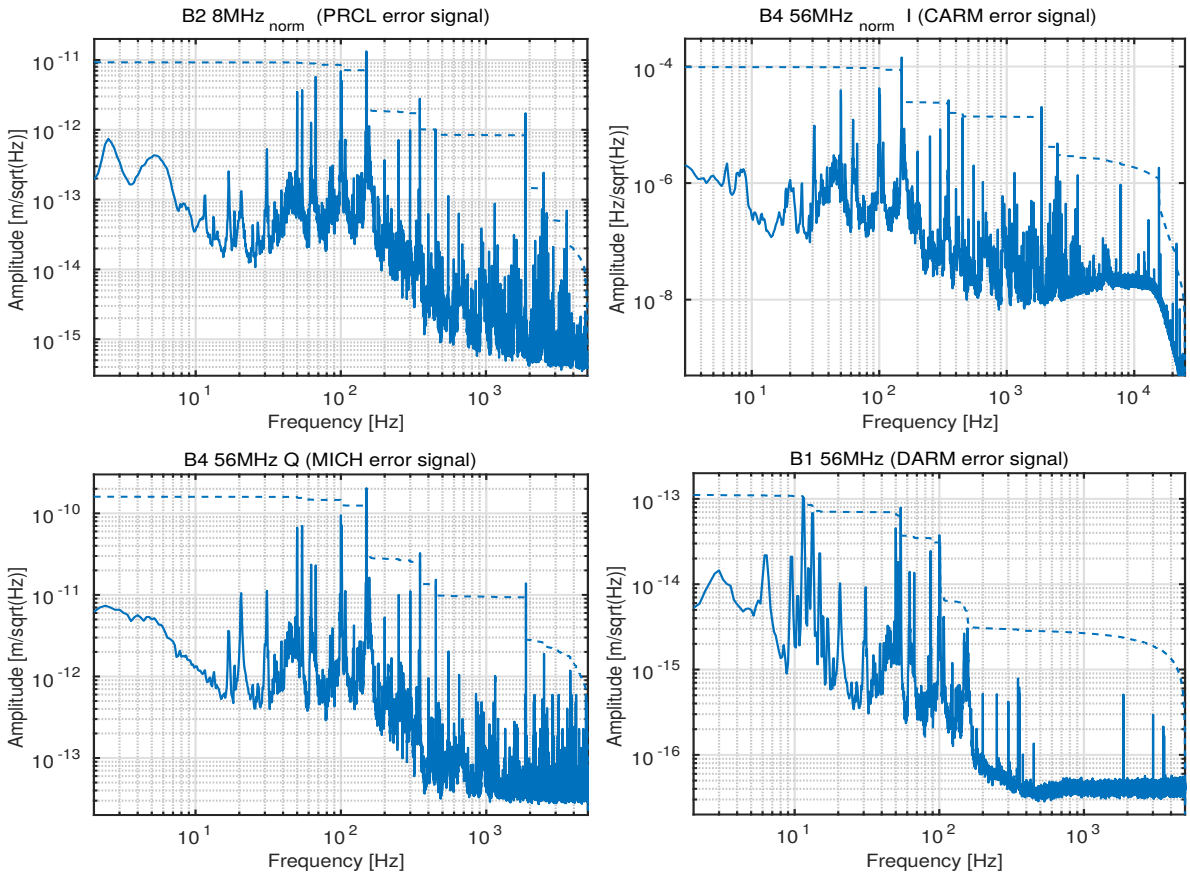

FIGURE 6.54: Calibrated PSD of the error signals used in DF for the longitudinal DOFs.

shows the PSD of the calibrated error signals. The information of the loops is summarized in Table 6.3.

	PRCL	MICH	CARM	DARM
UGF [Hz]	35	30	8000	55
Delay [μs]	400	650	11	700
Precision	9 pm	160 pm	0.009 mHz	0.1 pm

TABLE 6.3: Properties of the longitudinal loops in DF. The precision of the SSFS loop is given in Hz since it is a frequency stabilization.

First notice that the measured UGFs are not the target ones. It was necessary to find a compromise between the target UGFs (which provide the best control), the actuators dynamics (the control saturates if the error signals are noisy) and the control stability (due to the sidebands fluctuations we need some extra phase margin). In particular, the target UGF of the DARM control is 75 Hz and the gain of this loop was adjusted after this measurement accordingly.

The precision of the controls is improved in the case of DARM and the SSFS due to the boosts ($\text{DARM}_{0.5}$ = 27 pm, $\text{SSFS}_{0.5}$ = 3 mHz). In the case of PRCL DOF the filter has not been adjusted, but the control precision has improved ($\text{PRCL}_{0.5}$ = 71 pm). This is because the SSFS boost has decreased the frequency

noise, which couples strongly to the PRCL DOF, as it was shown in Figures 5.6 and 5.19. Finally the MICH control has stayed at the same level ($MICH_{0.5}$ = 140 pm). Its filter has not been changed, since its UGF can not be increased. Even if the DARM loop coupling has been reduced significantly, which should have improved the performance, the photodiode used now is different. We suspect an important presence of diffused light on this photodiode (even with the bench under vacuum), based on some specific measurements made by the noise hunting group. This would worsen the error signal and so the control performance.

Conclusion

The commissioning of the ISC subsystem of the Advanced Virgo detector started on May 2016 with the lock of the first arm cavity. However, it was not until November that the installation of the steel fibers was finished and the full interferometer was available on its final configuration. The commissioning done during the last year together with the preparatory simulations performed have allowed to bring the interferometer to its working point in a reliable and robust way. Advanced Virgo joined the Advanced LIGO detectors on the scientific data taking O2 the 1st of August until the 25th of August. During this time its duty cycle has been ∼83% with a sensitivity of 26 Mpc of BNS horizon. The performance of the Advanced Virgo detector allowed to make the first triple detection of a Binary Black Hole the 14th of August [63].

We have seen that Advanced Virgo has incorporated several upgrades to its design in order to improve the sensitivity with respect to Virgo. Among them, the increase of the finesse of the Fabry-Perot cavities on the arms, the change on their geometry and the stability of the Power Recycling Cavity. These upgrades in particular have a direct impact on the control of the interferometer and have obliged us to adapt the control strategies.

The first stage of this work has been to study these problems using simulations. We have seen that the new finesse of the cavities induces dynamical problems that require a new lock acquisition technique. Using simulations we have adapted the Guided Lock technique to our needs. In particular we have obtained the analytical expression that relates the time that the transmission power takes from reaching 10% of its maximum power to reaching 40% of it, to the velocity of the cavity. This allows us to estimate the velocity of the cavity online and in physical units without any calibration factor. This method allows to engage the control of the arm cavities in a very short period of time and reliably.

The arm cavities geometry was modified in order to maximize the beam size in both mirrors. This has increased the complexity of the alignment control, since the driving matrix that relates the angular DOFs of the cavity with the actuators is not diagonal. We have simulated the impact of the alignment on the transmitted power, confirming that the driving matrix can be extracted from this information. When the input power will be increased, radiation pressure effects will appear and it will be necessary to adapt the controls in consequence, adding more complexity to the alignment loops.

Regarding the PRC stability we have studied the impact of misalignment on its Optical Gain. We have verified that for being very close from instability, the HOMs couple strongly, decreasing dramatically the Optical Gain of the cavity, specially for the sidebands. This has important effects in the stability of the control loops (both longitudinal and angular) and the quality of the error signals, so we have explored a solution: the use of a higher modulation frequency. The presence of the Schnupp asymmetry makes the finesse of the PRC dependent on the modulation frequency. This way, the higher is the modulation frequency, the lower is the finesse. We have simulated the impact of alignment on the Optical Gain for different modulation frequencies, using the Central Interferometer. Our results confirmed that higher

frequencies are less sensitive to misalignments. We confirmed it also experimentally using a low finesse cavity, the PR-NI. Our studies provided an alternative error signal to control the interferometer until the alignment is stabilized. We have also proved that the effects of the HOMs will become relevant in the last steps of the control strategy, when close to the Dark Fringe.

We have also studied the impact of HOMs on the Optical Transfer Function of the CARM degree of freedom and the photodiode used for its control (B4). We have confirmed that both the sidebands and the HOMs create structures on the Optical TF which should be compensated for in the control filter of the SSFS for being very close to the target UGF.

Finally we have simulated the different steps of the old acquisition strategy with the new optical design. We have checked the robustness of the error signals used in the past during the lock acquisition and studied the optimal sensing for the final state, the Dark Fringe, taking into account both precision and coupling. We have verified that no major problems arose from the upgrades, and we have found alternative error signals for the signals potentially problematic. These studies have provided a better understanding of the process of lock acquisition and a reference for the ideal behaviour of the interferometer.

Then we have applied all the knowledge acquired with the simulations on the commissioning process. We have successfully implemented the Guided Lock technique using the new method of calculating the velocity online. We have engaged the angular control of the arm cavities using mechanical modulation and it has proved to be very robust.

However, the commissioning has not always been straightforward and we had to deal with experimental limitations. First of all the absence of reliable signals coming from the B5 photodiode forced us to find an alternative normalization for the MICH error signal. We came up with a combination of signals, B1+B4, that had the extra advantage of providing direct information of the MICH offset. Once this was fixed, the normalization proposed was able to keep the control loops within stability during the alignment of the PR mirror, as expected. The addition of an intermediate state in the SSFS was successful and allowed the commissioning of the interferometer to advance while working on the full bandwidth control. After solving the coupling with the IMC alignment, the SSFS was engaged and functional.

The pre-curvature[6] of the PR mirror made the PRC even more unstable than foreseen in the design. The fluctuation of the sidebands reaching a factor 3 when close to the Dark Fringe. This spoiled the error signals on the quadrant photodiodes, and most probably the 3Ω signal as well.

The use of a high frequency modulation was a success and thanks to it we reached the Dark Fringe in spite of the alignment fluctuations. To be able to control the interferometer during long periods of time we implemented a basic angular control adapting the mechanical modulation technique used for the arms.

We have implemented a control strategy that allows the interferometer to reach its working point in a reproductive and robust way, that is with a high duty cycle. There are no explicit specifications on the precision of the loops since the important factor is how do they couple to the sensitivity. The impact of the different DOFs (angular and longitudinal) on the sensitivity is not straightforward and depends strongly on the noises present on the interferometer. In order to improve further the sensitivity an iterative process is necessary between noise hunting and tuning of

[6] It is optimised for 125 W.

the controls. The control loops performance depends strongly on the error signals quality. An improvement on the sensing noise would allow to optimize the controls without saturating the actuators.

In particular, to be able to use the nominal modulation frequency (6 MHz) it is necessary to implement a reliable alignment. We have explored the possibility of applying the same solution as for the longitudinal control, which is to use the 56 MHz. The signals from the Quadrant photodiodes at this frequency look promising and had a much better SNR. The first tests prove that the stability of the sidebands improves dramatically using these signals. Then it is necessary to evaluate if the angular control provided by these signals is enough to hand-off the longitudinal controls to the 6 MHz. Otherwise, the Thermal Compensation System (under commissioning) will be necessary to improve the stability of the cavity, allowing us to engage the alignment with the nominal modulation frequencies and reducing the presence of HOMs in the interferometer.

Another important aspect in the improvement of the sensitivity is the SSFS, because the frequency noise couples strongly to the interferometer. However, the requirements of the frequency stabilization depend on the arms finesse asymmetry (impact at low frequency) and the arm losses (impact at high frequency). A precise measurement of these parameters will allow to better understand the performance of this loop.

Also at present the UGF of this loop is limited by a loop oscillation around 10 kHz. We need to understand if it is due to the sidebands fluctuations that bring the control out of its phase margin, or if it comes from the presence of structures on the Optical TF. A measurement of the Optical TF of the CARM degree of freedom would allow to determine the cause. In case of the presence of structures we should first determine whether the SSFS needs a better performance and if so we should evaluate if the phase margin we have is enough to compensate for the structures. If it is not possible, we will need to consider alternatives to reduce the delay, including the possibility of implementing an analogical solution.

List of Abbreviations

AA	**A**utomatic **A**lignment
ADC	**A**nalog to **D**igital **C**onverter
AdV	**Ad**vanced **V**irgo
ASY	**A**nti**SY**mmetric (port)
BBH	**B**inary **B**lack **H**ole
BH	**B**lack **H**ole
BNS	**B**inary **N**eutron **S**tar
BPC	**B**eam **P**ointing **C**ontrol
BS	**B**eam **S**plitter
BSM	**B**eam **S**plitter **M**irror tilt (angular DOF)
CARM	**C**ommon **ARM** (length)
CH	**C**entral **H**eating
CITF	**C**entral **I**n**T**er**F**erometer
CLTF	**C**losed **L**oop **T**ransfer **F**unction
Comm(+)	**Comm**on tilt (angular DOF)
Comm(-)	**Comm**on shift (angular DOF)
CP	**C**ompensation **P**late
DAC	**D**igital to **A**nalog **C**onverter
DAQ	**D**ata **A**c**Q**uisition
DARM	**D**ifferential **ARM** (length)
DET	**DET**ection
DF	**D**ark **F**ringe
Diff(+)	**Diff**erential tilt (angular DOF)
Diff(-)	**Diff**erential shift (angular DOF)
DOF	**D**egree **O**f **F**reedom
DSP	**D**igital **S**ignal **P**rocessor
EOM	**E**lectro **O**ptical **M**odulator
FFT	**F**ast **F**ourier **T**ransform
FP	**F**abry-**P**erot (cavity)
FSR	**F**ree **S**pectral **R**ange
FWHM	**F**ull **W**idth at **H**alf **M**aximum
GW	**G**ravitational **Wave**
HF	**H**alf-**F**ringe
HOM	**H**igh **O**rder **M**ode
IMC	**I**nput **M**ode **C**leaner
INJ	**INj**ection
ISC	**I**nterferometer **S**ensing and **C**ontrol
ITF	**I**n**T**er**F**erometer
LC	**L**ocal **C**ontrol
MICH	**MICH**elson (Degree of Freedom)
MIR	**MIR**ror
NE	**N**orth **E**nd (mirror)
NI	**N**orth **I**nput (mirror)
NS	**N**eutron **S**tar

OG	**O**ptical **G**ain
OLTF	**O**pen **L**oop **T**ransfer **F**unction
OMC	**O**utput **M**ode **C**leaner
OSD	**O**ptical **S**imulation and **D**esign
P	In-**P**hase
PDH	**P**ound-**D**rever-**H**all (technique)
POP	**P**ick-**O**ff **P**late
PR	**P**ower **R**ecycling (mirror)
PRC	**P**ower **R**ecycling **C**avity
PRCL	**P**ower **R**ecycling **C**avity **L**ength
PRITF	**P**ower **R**ecycling **I**n**T**er**F**erometer
PRM	**P**ower **R**ecyling **M**irror tilt (angular DOF)
PSD	**P**ower **S**pectral **D**ensity
PSL	**P**re**S**tabilized **L**aser
Q	In-**Q**uadrature
RH	**R**ing **H**eater
RF	**R**adio **F**requency
RFC	**R**e**F**erence **C**avity
RMS	**R**oot **M**ean **S**quare
RoC	**R**adius **O**f **C**urvature
RTPC	**R**eal **T**ime **PC**
SLC	**S**tray **L**ight **C**ontrol
SNR	**S**ignal-to-**N**oise **R**atio
SOS	**S**econd **O**rder **S**ection
SR	**S**ignal **R**ecycling (mirror)
SSFS	**S**econd **S**tage of **F**requency **S**tabilization
SUSP	**SUSP**ensions
SYM	**SYM**metric (port)
TCS	**T**hermal **C**ompensation **S**ystem
TEM	**T**ransverse **E**lectromagnetic **M**ode
TF	**T**ransfer **F**unction
TT	**T**ensor **T**raceless
UGF	**U**nity **G**ain **F**requency
VAC	**VAC**uum
WE	**W**est **E**nd (mirror)
WI	**W**est **I**nput (mirror)

Bibliography

[1] P.R. Saulson. *Fundamentals of interferometric Gravitational Wave detectors.* World Scientific, 1994.

[2] J.D.E. Creighton and W.G. Anderson. *Gravitational-Wave Physics and Astronomy.* Wiley-VCH, 2011.

[3] B.P. Abbott and et al. Observation of gravitational waves from a binary black hole merger. *Phys. Rev. Lett.*, 116, 2016.

[4] B.P. Abbott and et al. Gw151226: Observation of gravitational waves from a 22-solar-mass binary black hole coalescence. *Phys. Rev. Lett.*, 118, 2017.

[5] B.P. Abbott and et al. Gw170104: Observation of a 50-solar-mass binary black hole coalescence at redshift 0.2. *Phys. Rev. Lett.*, 116, 2016.

[6] B. Abbott and et al. Beating the spin-down limit on gravitational wave emission from the crab pulsar. *The Astrophysical Journal*, 683, 2011.

[7] B. Abbott and et al. Beating the spin-down limit on gravitational wave emission from the vela pulsar. *The Astrophysical Journal*, 737, 2011.

[8] R. A. Hulse and J. H. Taylor. Discovery of a pulsar in a binary system. *Astrophysical Journal*, 195:L51–L53, 1975.

[9] M.A. Bizouard and N. Christensen. Gravitational wave detection. Moriond 2017 proceedings, Virgo, 2017. VIR-0242A-17.

[10] G. Vajente. Readout, sensing and control. VESF School on Advanced Gravitational Wave Detectors, 2012.

[11] G. Vajente. *Analysis of sensitivity and noise sources for the Virgo gravitational wave interferometer.* PhD thesis, Universita de Pisa, 2008.

[12] E. Black and R.N. Gutenkunst. An introduction to signal extraction in interferometric gravitational wave detectors. *American Journal of Physics*, 71, 2003.

[13] The LIGO collaboration. A gravitational wave observatory operating beyond the quantum shot-noise limit. *Nature Physics*, 7, 2011.

[14] The Virgo collaboration. Advanced virgo technical design report. Internal note, Virgo, 2012. VIR–0128A–12.

[15] G. Vajente. Interferometer configurations. VESF School on Advanced Gravitational Wave Detectors, 2012.

[16] R.W.P. Drever and J.L. Hall et al. Laser phase and frequency stabilization using an optical resonator. *Applied Physics B: Lasers and Optics*, 13(1), 1983.

[17] A. Freise and al. Frequency domain interferometer simulation with higher-order spatial modes. *Class. Quant. Grav.*, 21(5), 2004.

[18] Optickle website: https://github.com/optickle/optickle.

[19] B. Bhawal, M. Evans, E. Maros, M. Rahman, and H. Yamamoto. Overview of end-to-end model. Technical note, LIGO, 1997. https://labcit.ligo.caltech.edu/ e2e/.

[20] F. Acernese et al. Measurements of superattenuator seismic isolation by virgo interferometer. *Astroparticle Physics*, 33, 2010.

[21] G. Pillant and E. Genin. Isys training session. Presentation, Virgo, 2017. VIR-0215A-17.

[22] F. Riehle. *Frequency standards basics and applications.* Wiley-VCD, 2004.

[23] A. Freise and K.A. Strain. Interferometer techniques for gravitational-wave detection. *Living Reviews in Relativity*, 31(2), 2010.

[24] M. Rakhmanov. *Dynamics of Laser Interferometric Gravitational Wave Detectors.* PhD thesis, California Institute of Technology Pasadena, California, 2000.

[25] N. Ismail, C. C. Kores, D. Geskus, and M. Pollnau. Fabry-pérot resonator: spectral line shapes, generic and related airy distributions, linewidths, finesses, and performance at low or frequency-dependent reflectivity. *Optics Express*, 24(15), 2016.

[26] A.E. Siegman. *Lasers.* University Science Books, 1986.

[27] O. Svelto. *Principles of Lasers.* Springer, 2010.

[28] C. Carr. Course on principles of instrumentation. Imperial College of London, 2012.

[29] J. Doyle, B. Francis, and A. Tannenbaum. *Feedback control theory.* Macmillan Publishing Co., 1990.

[30] E. Black. Notes on the pound-drever-hall technique. Internal note, LIGO, 1998. LIGO-T980045-00- D.

[31] L. Barsotti. *The control of the Virgo interferometer for gravitational wave detection.* PhD thesis, Universita degli studi di Pisa, 2006.

[32] F. Bondu. *L'interferometre Virgo : proprietes optiques, stabilisation en frequence du laser.* PhD thesis, Universite de Nice Sophia-Antipolis, Observatoire de la Cote d'Azur, 2008. Memoire d'habilitation a diriger des recherches.

[33] S. Kreckelbergh. *Dynamics of Laser Interferometric Gravitational Wave Detectors.* PhD thesis, Universite de Paris Sud, Centre d'Orsay, 2005.

[34] B. Swinkels and P. Ruggi. Lock acquisition of the advanced virgo arm-cavities with reduced force. Internal note, Virgo, 2012. VIR-0019A-12.

[35] M. J. Lawrence and B. Willke et al. Dynamic response of a fabry–perot interferometer. *J. Opt. Soc. Am. B*, 16(4), 1999.

[36] J. Camp, L. Sievers, R. Bork, and J. Heefner. Guided lock acquisition in a suspended fabry–perot cavity. *Optics letters*, 20(24), 1995.

[37] K. Izumi. Lock acquisition of fabry-perot cavity with guided lock. Gravitational Wave Advanced Detector Workshop, 2008.

[38] D. Bersanetti. *Development of a New Lock Acquisition Strategy for the Arm Cavities of Advanced Virgo.* PhD thesis, Universita degli studi di Genova, 2015.

[39] D.Z. Anderson. Alignment of resonant optical cavities. *Applied Optics*, 23(17), 1984.

[40] J.A. Sidles and D. Sigg. Optical torques in suspended fabry-perot interferometers. *Physics Letters A*, 354(3), 2016.

[41] M. Mantovani. Automatic alignment sensing and control scheme for advanced virgo msrc configuration. Internal note, Virgo, 2011. VIR-0201A-11.

[42] L. Barsotti and M. Evans. Modeling of alignment sensing and control for advanced ligo. Technical note, LIGO, 2010. LIGO-T0900511-v3.

[43] S. Solimeno et al. Fabry-pérot resonators with oscillating mirrors. *Physical Review A*, 43(11), 1991.

[44] N. Mavalvala. *Alignment issues in laser interferometric gravitational-wave detectors.* PhD thesis, Massachusetts Institute of Technology, 1997.

[45] E. Morrison, B. J. Meers, D. I. Robertson, and H. Ward. Automatic alignment of optical interferometers. *Living Reviews in Relativity*, 33(22), 1994.

[46] G. Vajente. Advanced virgo length sensing and control steady state design. Internal note, Virgo, 2011. VIR-0738A-11.

[47] G. Vajente, R. Day, and J. Marque. Adv optical layout: new parameters proposal. Presentation, Virgo, 2011. VIR-0377B-11.

[48] A. Allocca, A. Chiummo, and M. Mantovani. Locking strategy for the advanced virgo central interferometer. Internal note, Virgo, 2016. VIR-0187A-16.

[49] K. Arai and M. Ando et al. New signal extraction scheme with harmonic demodulation for power-recycled fabry–perot–michelson interferometers. *Physics Letters A*, 273(1-2), 2000.

[50] A. Staley and et al. Achieving resonance in the advanced ligo gravitational-wave interferometer. *Classical and Quantum Gravity*, 31(24), 2014.

[51] G. Vajente and E. Calloni. Conceptual design of the second stage of frequency stabilization for advanced virgo. Internal note, Virgo, 2012. VIR-0013C-12.

[52] F. Bondu. Some issues with multiple servo loop systems. Internal note, Virgo, 2003. VIR-NOT-OCA-1390-234.

[53] P. Rapagnani. Monolithic suspension update. Presentation, Virgo, 2017. VIR-0199A-17.

[54] R. Gouaty for the DET subsystem. Impact of bs wedge on sdb1 bench. Presentation, Virgo, 2015. VIR-0226A-15.

[55] A. Allocca, E. Genin, M. Mantovani, and B. Swinkels. Thermal effect of the ring heater in the power recycling mirror. Internal note, Virgo, 2016. VIR-0183A-16.

[56] V. Germain. Advanced virgo calibration. Presentation, Virgo, 2017. VIR-0326A-17.

[57] L. Mirkin. Introduction to time-delay systems. Lund University, 2012.

[58] Personal communication with paolo ruggi.

[59] F. Bondu. Gravitational wave interferometer optics. Presentation, Virgo, 2006. VIR-0801A-06.

[60] L. Pinard. Advanced virgo power recycling mirror characterization report-pr01 (coatings c14097+c14101). Internal note, Virgo, 2015. VIR-0029A-15.

[61] I. Nardecchia. Chs tests and considerations on sb gain. Presentation, Virgo, 2017. VIR-0372A-17.

[62] E. Capocasa and et al. Advirgo injection system frequency noise. Presentation, Virgo, 2016. VIR-0212A-16.

[63] B.P. Abbott and et al. Gw170814: A three-detector observation of gravitational waves from a binary black hole coalescence. *Phys. Rev. Lett.*, 119, 2017.

université PARIS-SACLAY | ÉCOLE DOCTORALE PHENIICS

Titre: Contrôle du détecteur interférométrique d'ondes gravitationnelles Advanced Virgo

Mots clés: *ondes gravitationnelles, Virgo, cavités suspendues*

Résumé: La première détection d'une Onde Gravitationnelle (OG) a été faite le 14 Septembre 2015 par la collaboration LIGO-Virgo avec les deux détecteurs de LIGO. Elle a été émise par la fusion de deux Trous Noirs, fournissant ainsi la première preuve directe de l'existence des Trous Noirs. Advanced Virgo est la version améliorée de l'interféromètre Virgo et il va rejoindre les détecteurs LIGO dans les mois qui suivent.

Le passage d'une OG induit un changement différentiel de la distance entre masses-test (uniquement sensibles à la force gravitationnelle). Cette variation de distance est proportionnelle à l'amplitude de l'OG, néanmoins le déplacement le plus grand qui peut être observé depuis la Terre est de l'ordre de 10^{-19} m/sqrt(Hz) en terme de densité spectrale. C'est pour cela que l'interféromètre de Michelson est l'instrument idéal pour détecter cet effet différentiel. Les détecteurs d'OG utilisent des miroirs suspendus, qui se comportent comme masses-test. Le passage d'une OG va produire un changement dans la distance entre les miroirs qui va modifier la condition d'interférence et donc une variation de puissance lumineuse mesurée par la photodiode de détection. Cependant, un Michelson simple n'est pas assez sensible et des améliorations ont été ajoutées. La première génération de détecteurs a ajouté des cavités Fabry-Perot dans les bras pour augmenter le chemin optique. De plus un nouveau miroir a été ajouté pour recirculer la lumière réfléchie vers le laser et augmenter la puissance effective, en créant une nouvelle cavité connue comme Power Recycling Cavity (PRC). Son effet est d'autant plus important que le Michelson est en fait optimalement réglé sur une frange noire.

Touts les miroirs du détecteur ressentent le bruit sismique et les longueurs des cavités, entre autres, changent en permanence. Il est donc nécessaire de contrôler activement la position longitudinale et angulaire des cavités pour les maintenir en résonance. Pendant ma thèse j'ai étudié le contrôle de Advanced Virgo d'abord en simulation puis pendant le commissioning lui-même. D'abord j'ai simulé la stratégie de contrôle utilisée dans Virgo avec des simulations modales. L'objectif était de vérifier si la même stratégie pouvait être appliquée à Advanced Virgo ou s'il fallait l'adapter. Avec Advanced Virgo les cavités Fabry-Perot ont une finesse plus grande ce qui entraîne de nouveaux effets dynamiques et qui demande une stratégie de contrôle spéciale, stratégie que j'ai modifiée pour l'adapter aux besoins du commissioning. Concernant la PRC, j'ai étudié l'impact de sa stabilité dans le fonctionnement de l'interféromètre. Comme elle est très proche de la région d'instabilité, l'onde lumineuse être très sensible à l'alignement et a l'adaptation du faisceau à la cavité. J'ai vérifié avec les simulations son impact sur les contrôles longitudinaux, qui peuvent devenir instables, et une solution a été validée. Ensuite j'ai utilisé cette information pour le commissioning d'Advanced Virgo. Dans cette thèse les détails du commissioning des contrôles longitudinal et angulaire de l'interféromètre sont présentés. La stabilisation en fréquence est aussi présentée, puisqu'elle joue un rôle très important dans le contrôle de l'interféromètre car étant le bruit dominant.

Title: Control of the gravitational wave interferometric detector Advanced Virgo

Key words: *gravitational waves, Virgo, suspended cavities*

Abstract: The first detection of a Gravitational Wave (GW) was done on September 14 th of 2015 by the LIGO-Virgo collaboration with the two LIGO detectors. It was emitted by the merger of a Binary Black Hole, providing the first direct proof of the existence of Black Holes. Advanced Virgo is the upgraded version of the Virgo interferometer and it will join the LIGO detectors in the next months.

The passage of a GW on Earth induces a change on the distance between test masses (experiencing only the gravitational interaction) in a differential way. This distance variation is proportional to the amplitude of the GW however the largest displacement observable on Earth will be of the order of 10^{-19} m/sqrt(Hz). Taking this in account, a Michelson interferometer is the ideal instrument to detect this differential effect. GWs detectors will use suspended mirrors to behave as test masses. The passage of a GW will cause a change on the distance between the mirrors that will spoil the interference condition, allowing some light to leak to the detection photodiode. However, a simple Michelson interferometer does not provide enough sensitivity. For this reason the first generation of detectors added Fabry-Perot cavities in the arms, in order to increase the optical path. A second change was the addition of an extra mirror in order to recycle the light that comes back towards the laser, to increase the effective power, creating a new cavity also known as Power Recycling Cavity (PRC). Its effect is more important when the Michelson is tuned in an optimal way in a dark fringe.

All the mirrors of the detector are affected by the seismic noise and so their distance is continuously changing. It is necessary to control the longitudinal and angular position of the cavities in order to keep them at resonance. During my thesis I have studied the control of Advanced Virgo using simulation and during the commissioning itself. First of all I have simulated the control strategy used in Virgo using modal simulations. The aim was to check if the same strategy could be applied to Advanced Virgo or if it needs adaptation. In Advanced Virgo the Fabry-Perot cavities have a higher finesse, which arises new dynamical problems and requires a special control strategy that I have modified to match the commissioning needs. Regarding the PRC, we have studied the impact of its stability on the performance of the interferometer. As it is very close from the instability region, the electrical field inside will be very sensitive to alignment and matching of the laser beam. We have checked using simulations its impact on the longitudinal controls, which can become unstable, and a solution has been validated. Then I have used this information during the commissioning of the Advanced Virgo detector. In this thesis the details of the commissioning of the longitudinal and angular control of the interferometer will be presented. It includes the frequency stabilization, which has a key role in the control of the interferometer, since it is the dominant noise.

Université Paris-Saclay
Espace Technologique / Immeuble Discovery
Route de l'Orme aux Merisiers RD 128 / 91190 Saint-Aubin, France